SPIM

Thèse de Doctorat

école doctorale **sciences pour l'ingénieur et microtechniques**

UFC UNIVERSITÉ DE FRANCHE-COMTÉ

Optical design and development of building blocks for a new generation of vertically integrated on-chip confocal microscopes

Maciej Kamil BARANSKI

SPIM

Thèse de Doctorat

école doctorale **sciences pour l'ingénieur et microtechniques**

UFC UNIVERSITÉ DE FRANCHE-COMTÉ

THÈSE présentée par

Maciej Kamil BARANSKI

pour obtenir le

Grade de Docteur de
l'Université de Franche-Comté

Spécialité : **Sciences pour l'ingénieur**

Optical design and development of building blocks for a new generation of vertically integrated on-chip confocal microscopes

Unité de Recherche :
FEMTO-ST

Soutenue publiquement le 12 decembre 2013 devant le Jury composé de :

Hans-Peter HERZIG	Rapporteur	Professeur à EPFL, Neuchâtel, Swiss
Alain BOSSEBOEUF	Rapporteur	Directeur de Recherche CNRS, IEF, Université Paris Sud
Katarzyna CHAŁASIŃSKA-MACUKOW	Examinateur	Professeur à l'Université de Varsovie, Faculté de Physique
Véronique BARDINAL-DELAGNES	Examinateur	Directeur de Recherche CNRS, LAAS-CNRS
Maik WIEMER	Examinateur	Chef de Groupe, Fraunhofer Institut - Elektronische Nanosysteme ENAS
Christophe GORECKI	Directeur de thèse	Directeur de Recherche CNRS, FEMTO-ST
Nicolas PASSILLY	Co-encadrant	Chargé de Recherche CNRS FEMTO-ST
Sylwester BARGIEL	Co-encadrant	Chercheur à l'UFC, FEMTO-ST

Acknowledgements

I would like to express my gratitude to my thesis supervisor prof. Christophe Gorecki for giving me the opportunity of work in his group, the trust and support during my PhD study and research. Equally, I want to thanks to my co-supervisors: dr Nicolas Passilly and dr Sylwester Bargiel for their patience and for large amount of shared knowledge.

I thank the examination jury, especially the jury president professor Véronique Bardinal-Delagnes, the reviewers prof. Alain Bosseboeuf and prof. Hans-Peter Herzig, as well as examiners: dr Maik Wiemer, prof. Katarzyna Chałasińska-Macukow and dr Patrick Sandoz.

Many part of research presented within this thesis was performed within DWST-DIS project, so I would like to thanks our project partners from Fraunhofer Institute ENAS: dr Maik Wiemer, dr Chenping Jia, Jörg Frömel and Dirk Wünsch. Also, many thanks to Dominique Buoncuore the project coordinating officer from Programme Inter Carnot Fraunhofer for the support and great enthusiasm for DWST-DIS project.

My sincere thanks to all members of the MOEMS group for their help, many advises and numerous discussions about my research work: dr Jorge Albero, dr Ravinder Chutani, dr Madoka Hasegawa, dr Etienne Herth, dr Karolina Laszczyk and dr Artur Zarzycki. Special thanks to the three PhD students: Stéphane Perrin, Justine Lullin, Vincent Maurice who joined the group in the final year of my PhD studies for their enthusiasm, optimism and important help in finishing my work. Additional thanks to Patricia Gorecki for much help in various organization tasks and to Sophie Marguier for great support during the writing this manuscript.

The large part of experimental work presented in this thesis was performed in TEMIS cleanroom, in here I would like to acknowledge the important impact of my work to the technical staff of the cleanroom (the "MIMENTO") especially: Valérie Petrini, Jean-Yves Rauch, Blandine Edouard-Guichardaz, Denis Bitschene, Laurent Robert.

Many thanks to other colleagues from FEMTO-ST for their help and company in everyday work in the institute, in particular to I want to name: Olivier Gaiffe, Sarah Benchabane, Luc Froehly,

Franck Chollet, Vincent Armbruster, Emmanuel Dordor.

Also, I express my sincere thanks to all the professors and colleagues from the University of Warsaw where I have started my research in optics. Special thanks to dr Rafał Kasztelanic and prof. Katarzyna Chałasińska-Macukow who encourage me in my decision on pursuing PhD studies.

Many part of the work presented within this manuscript was performed by the use of free software. The acknowledgments are addressed to all developers of the software tools that allowed me an efficient work on my research projects. In particular, I would like to thanks all the contributors of the following software: Python (especially numpy, scipy, sympy, matplolib and IPython packages), KLayout, ImageJ/Fiji, LightPipes, Emacs, Inkscape, LaTeX and the GNU/Linux operating system in the form of the Arch Linux distribution.

The three years I have spent in Besançon would not be the same without my friends that I have met during this period thanks to: Ivan, Eva, Clara, Fred, Popuxu, Viki, Lu, Gina and Arnaud, Anas, Emilia, Elisa, Laura, Katia, Lamin, Sebastian, Justyna, Irmina. The special thanks to the two "Belettes" for their presence and great support during my struggle with writing this manuscript. And finally, I thank to my whole family for their continuous support.

Contents

Title Page i

Acknowledgements v

Table of contents xi

General Introduction 1

1 Confocal microscopy and challenges of miniaturization 5

1.1 Principles of confocal microscopy 5

1.1.1 Image formation 6

1.1.2 Optical Sectioning and 3D Imaging 8

1.1.3 Different types of confocal microscopes 10

1.2 Imaging Quality: Contrast and Resolution 12

1.2.1 Definitions 12

1.2.1.1 Two-Point Resolution Criteria 13

1.2.1.2 Frequency Domain Resolution Analysis 16

1.2.1.3 Axial resolution 17

1.2.2 Resolution in non-perfect optical system 18

1.2.2.1 Aberrations 19

1.2.2.2 Noise 19

1.2.2.3 Sampling 19

1.2.3 Resolution improvements in confocal microscopy 21

1.2.3.1 Apodization 21

1.2.3.2 Theta configuration 22

1.3 Beam scanning in confocal microscopy 24

1.3.1 Beam scanning techniques . . . 25
1.3.2 Dynamical modes of scanning . . . 27
1.4 MOEMS for confocal microscopy . . . 29
1.4.1 Wafer-level microfabrication . . . 30
1.4.2 Integration, assembly and packaging . . . 31
1.5 Miniature Confocal microscopes: State of Art . . . 33
1.5.1 Motivation of miniaturization: Why miniature confocal microscope? . . . 33
1.5.1.1 Applications of miniature confocal microscopes . . . 34
1.5.1.2 Beam scanning for optical micro-manipulation . . . 36
1.5.2 Fiber-optics based confocal microscopes . . . 38
1.5.3 MEMS confocal microscopes . . . 39
1.5.3.1 MEMS-enabled confocal microscopes . . . 40
1.5.3.2 MOEMS approach to miniature confocal microscopes . . . 43
1.5.4 Review of performances of miniature confocal systems . . . 45
1.6 Motivations . . . 47

2 Optical Design **49**
2.1 Design Specifications . . . 50
2.1.1 MEMS-based system . . . 50
2.1.2 Micro-Optics . . . 51
2.2 Beam scanning by lens displacement . . . 53
2.2.1 Single Lens Scanning Relations . . . 53
2.2.2 Afocal doublet for 3D beam scan . . . 56
2.3 Four lens system for scanning and focusing . . . 58
2.3.1 Paraxial Description - ABCD-EF formalism . . . 59
2.3.2 The scanning performance . . . 61
2.3.3 Conclusions of paraxial analysis . . . 63
2.4 Scanner implementations . . . 64
2.4.1 First demonstrator: ball-lens based scanner . . . 64
2.4.2 Advanced system I: plano-convex scanning lenses . . . 69
2.4.3 Advanced system II: Anastigmatic focusing block . . . 72
2.5 Summary . . . 76

3 Characterization of focusing components **79**

3.1 Topography measurements . . . 79

3.1.1 Dicing and SEM imaging . . . 80

3.1.2 Scanning profilometry . . . 81

3.1.3 Interferometric methods . . . 82

3.2 Direct Optical Characterization . . . 84

3.2.1 Characterization setup for transmisive elements . . . 85

3.2.1.1 Theory . . . 85

3.2.1.2 Implementation . . . 86

3.2.1.3 Data analysis and example measurements . . . 88

3.2.2 Characterization setup for reflective elements . . . 90

3.2.2.1 Theory . . . 91

3.2.2.2 Implementation. . . . 94

3.2.2.3 Data analysis and example measurement. . . . 94

3.3 Conclusion and perspectives . . . 100

4 Microoptical components **101**

4.1 Technology of micro-mirrors and micro-lenses . . . 102

4.1.1 Wet etching of silicon with KOH solution . . . 102

4.1.1.1 Theory . . . 102

4.1.1.2 Fabrication . . . 104

4.1.1.3 Experimental results and discussion . . . 107

4.1.2 Isotropic wet etching of silicon . . . 110

4.1.2.1 Wet etching models . . . 110

Chemistry of HF/HNO_3 silicon etching process: . . . 112

Kinetics and geometry of masked etch. . . . 114

Limits of mass-transfer regime approximation. . . . 117

Effects of agitation. . . . 118

4.1.2.2 Fabrication . . . 118

Mask material choice. . . . 119

Agitation. . . . 124

Process control. . . . 125

Microlenses molds and micromirrors. . . . 126

Arrays. . . . 129
4.1.2.3 HF/HNO_3 etching: conclusions . . . 131
4.1.3 Silicon etching in SF_6 plasma . . . 133
4.1.3.1 Basic etching mechanisms in plasma process . . . 133
4.1.3.2 Plasma etching of silicon for mirrors/mold fabrication . . . 134
4.1.3.3 Experiment . . . 135
Gas pressure. . . . 136
Substrate temperature. . . . 136
Aspherical Structures. . . . 137
Surface roughness. . . . 138
4.1.3.4 Conclusions and future work . . . 138
4.1.4 Molding . . . 140
4.1.4.1 Glass replication . . . 140
4.1.4.2 Polymer replication . . . 141
4.1.5 Microlenses and Micromirrors: Conclusions . . . 142
4.2 Micro Schwarzschild Objective . . . 144
4.2.1 Two-mirrors anastigmat . . . 144
4.2.2 Fabrication within Si/Glass μtechnologies . . . 148
4.2.2.1 Architecture . . . 148
4.2.2.2 Tolerances . . . 149
4.2.2.3 Influence of Glass Support . . . 152
4.2.3 First Demonstrator . . . 154
4.2.3.1 Specifications . . . 155
4.2.3.2 Fabrication . . . 155
4.2.3.3 Characterization . . . 158
4.2.4 Conclusions/Perspectives . . . 159
4.3 Micro-Beam-Splitter . . . 160
4.3.1 Classical Beam-Splitting . . . 160
4.3.2 Wafer-Level Cube-Type Micro-Beam Splitter . . . 161
4.3.3 Realization of MBS . . . 162
4.3.3.1 Architecture . . . 162
Stack design . . . 163
Advanced polarizing MBS . . . 164

4.3.3.2 Fabrication . . . 167
Glass dicing. . . . 167
Dicing optimization . . . 167
Roughness impact. . . . 168
Dielectric mirror . . . 171
4.3.4 Characterization . . . 171
4.3.5 Conclusions and Perspectives . . . 172

5 Toward first demonstrator of scanning confocal microscope 175
5.1 Introduction . . . 175
5.2 General architecture . . . 176
5.3 MEMS microscanner for confocal microscope . . . 177
5.4 Opto-mechanical design . . . 178
5.4.1 MEMS/Mechanical constraints, technological limitations . . . 179
5.4.1.1 Bonding methods and materials selection . . . 179
5.4.1.2 Thickness limitations . . . 181
5.4.1.3 Micromachining methods and process availability . . . 181
5.4.2 Sensitive components, hermetic packaging . . . 181
5.5 Components tolerance analysis . . . 182
5.6 Integration methods . . . 183
5.6.1 Ball lens bonding . . . 184
5.6.2 Electrical connections . . . 184
5.6.3 Multi wafer anodic-bonding . . . 186
5.7 Conclusions and perspectives . . . 188

A SEM Profiles Analysis 191
A.1 Profile extraction . . . 191
A.2 Profile analysis . . . 193
A.3 Example . . . 197

General Conclusions and Perspectives 203

Bibliography 209

Author's publications 230

General Introduction

Biological imaging for medical diagnosis is nowadays still typically based on histopathology after a resection of tissues, consisting in the analysis of specimens with bulky bench-top (and often expensive) optical instruments. Despite its efficiency, this approach is limited by sampling errors, processing costs, preparation time and thus, by the amount of tissue that can be analyzed. Moreover, artifacts such as tissue sectioning, paraffin embedding and histochemical staining can widely affect the accuracy of diagnosis. In the medical research framework, this also constrains to the examination of tissues out of context, or post-mortem samples preventing longitudinal studies.

Consequently, there is a strong need for real time *in vivo* imaging in order to refine diagnosis tools. To be applied in pathologic conditions, new methods based on small devices presenting sub-cellular resolution are currently developed. Among all the different methods, optical microscopes are extensively employed and within them, a particularly interesting method is confocal microscopy. Confocal microscopy is a powerful imaging technique especially adapted to *in vivo* imaging, due to its capability to perform high resolution imaging and optical sectioning in both reflectance and fluorescence modes. Reflectance imaging is well suited for non-invasive diagnosis since extrinsic contrast agents are not required. Whereas reflectance imaging provides information on cell and tissue micro-morphology, fluorescence imaging allows the study of cell function by using targeted fluorescent probes and dyes. Both methods can provide clear images from optically thick biological tissues with sub-cellular resolution. Thanks to a "pinhole" placed in between the objective lens and the detector, confocal microscopy rejects out of focus light and detects backscattered photons only from a tiny focal volume within the tissue to be measured. Hence, it is necessary to move the point source with respect to the specimen in order to collect a full image. Despite advantages of confocal imaging, *in vivo* applications have been constrained by bulk optics. Consequently, as it is shown with this example of biological imaging, size reduction and portability of confocal imaging systems

are desired. This is also the case for applications such as handheld micro total analysis systems.

One way to achieve such miniaturization is to rely on MEMS and MOEMS technologies. They are based on wafer-level microfabrication that allows generation of micro-actuators and/or micro-optical components such as microlenses, micromirrors and miniature beam-splitters. Moreover, since planar wafer-level technology is used, components can be fabricated in dense arrays and many identical systems can be produced in parallel. Consequently, such characteristic of batch micromachining approach can reduce significantly the cost of the final device if large volume production is reached and then lead to unanticipated applications. Moreover, sensor arrays, performing parallel measurements, could be produced. But if planar technology allows the natural array-ability of the system, more complex optical systems require additional vertical assembly of the system elements.

During the last three years, I had the opportunity to work in the framework of DWST-DIS (The Development of multi-Wafer Stacking 3D Technology for Displays and Imaging Microsystems), a project funded within the Programme Inter Carnot Fraunhofer (PICF) and involving FEMTO-ST institute and Fraunhofer ENAS (Chemnitz, Germany). This project (October 2010-March 2014) is aimed at the development of a vertically integrated micro-optical scanner, suitable for a wide number of imaging systems such as confocal microscopes or optical coherent tomography (OCT) probes. Within this thesis, focus is mainly on confocal microscopy application.

Then, association of refractive microlenses and MEMS actuators is considered in order to implement a miniature confocal microscope. One of the most critical obstacles for achieving cost-effective solutions is the complete integration of such optical microsystems. The integration requires numerous hybrid technologies, positioning with tolerances of few microns, and complex packaging. To match this ambitious objective, we identified three important challenges: - to develop an appropriate optical design, in order to find the optimal optical architecture based on a stack of microoptical and MEMS wafers, taking into account optical resolution as well as optical aberrations, - to propose fabrication technologies for wafers of planar microoptical components adapted to our vertically integrated optical micro-instrument, and - to investigate technological issues of 3D packaging by using multi-wafer vertical assembly, combining heterogeneous technologies (microoptical and micromachining technologies; glass and silicon technologies).

In consequence, the thesis manuscript concerns optical design and development of a vertically integrated MEMS-based confocal microscope. Different optical architectures are proposed that aim

to combine optimal optical design and the numerous technological constraints linked to the batch fabrication of the different building blocks. The latter, made by hybrid technologies and packaged by vertical assembly using multi-wafer bonding, allow the construction of a complete microsystem for instrumentation. Special emphasis is placed on the minimization of optical aberrations generated by the different microoptical components to ensure measurements with good resolution.

The manuscript contains five chapters:

Chapter 1 presents the principle of confocal microscopy and declines its different configurations. It also reviews the state of the art on miniaturization of laser scanning confocal microscopes. In addition, the principles of MOEMS are introduced along with the approach of vertical multi-wafer assembly.

The **second chapter** deals with optical design of the vertically integrated MEMS-based optical scanner adapted to the application of confocal microscope. The 3D microoptical scanner, which is based on axial and lateral microlens displacements, is analyzed. Three different configurations are shown, that differ in difficulty level of technological realization. The first scanner design that relies on discrete micro-optical components (ball-lenses) is targeted for the preliminary demonstrator of the integrated scanner. Further two designs are optimized, aiming at improving optical performance, in order to be better adapted for application of the scanner to confocal microscopy. However, better optical performance requires high quality optical elements like aspherical microlenses and reflective micro-objective.

In the **Chapter 3**, techniques employed for the characterization of micro-optical components are presented. A method based on direct optical characterization is proposed that allow quality assessment of high numerical aperture components based on simple experimental set-up and data interpretation.

Then, the **fourth chapter** concerns the development of the different building blocks of the microscope. Namely, we refer to a batch-fabricated cube-typed beamsplitter, different silicon molded refractive microlenses and a miniature reflective objective. For all the different building blocks, special attention is paid on the possibility to generate high quality components by batch fabrication. In particular, three different techniques of silicon etching that allow generation of spherical geometries, are analyzed. They are the double step anisotropic wet etching, isotropic wet etching and plasma etching.

Finally, the **Chapter 5** presents a conception of the technological realization of a vertically integrated optical scanner. Mechanical construction, wafer bonding technology and electrical interconnection technologies are presented. The application of the scanner in a confocal microscope within hybrid (fiber-optics based) approach is discussed.

1

Confocal microscopy and challenges of miniaturization

1.1 Principles of confocal microscopy

Invented in 1957 by Minsky [1] confocal microscopy is an optical imaging technique that relies on point-by-point image formation. A confocal system is based on a point source imaged by an illumination objective whereas the light reflected/scattered by the object is imaged by a collection objective onto a point detector (figure 1.1). The coupled point source and point detection in the imaging system assure that only single point of the object is imaged. To generate 2D or 3D image of an object the optical scanning is required to sequentially interrogate the volume of the object. Indeed, the image is not formed directly by the optical system but has to be reconstructed from data collected during scanning procedure. Then, point-by-point image formation allows imaging of thick specimens by reconstruction of 3D images from data obtained by scanning through the volume of the object.

Scanning microscopy originally targeted the imaging of thick specimens that cannot be well resolved using conventional microscopes [1, 2]. In the conventional wide-field microscope, the entire specimen is illuminated through a condenser lens 1.2a and the image can be projected directly onto detector (photographic film or pixel array detector). However, when a point detector is used instead of a 2D detector (figure 1.2b), only the response corresponding to a specific point of the specimen is recorded. The inverse situation is also possible: 2D detector and point illumination (figure 1.2c) also leads to better imaging of thick specimens. The confocal system can be seen as a combination of two scanning systems so that both source and detector are scanned simultaneously [3, 4]. The important

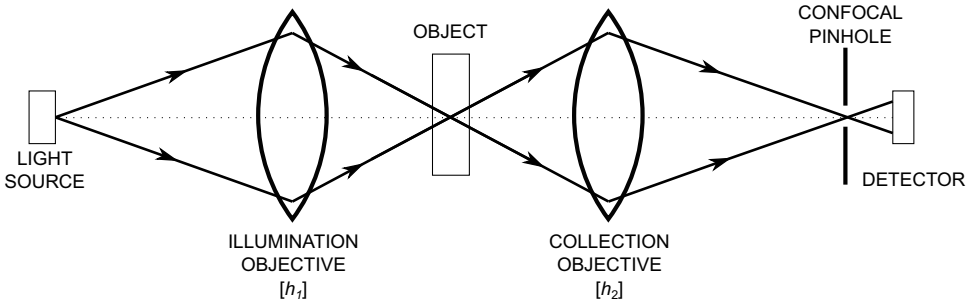


Figure 1.1: Working principle of the confocal microscope - Point illumination and point detection made by pinhole filtering allows 3D imaging of the object.

difference from the point of view of optical architecture of any of this optical systems is different contribution of illumination and collection blocks into imaging performances of the systems. In the case of conventional microscopy, the condenser lens has a minor impact onto imaging quality of the system as for all microscopes where wide-field illumination is used (figure 1.2b). In case of point illumination system (figure 1.2c) the illumination objective is mostly responsible for optical quality of the generated image whereas collection lens is of minor importance. In the confocal systems both objectives (illumination and collection) are equally contributing to the image formation. In consequence, this "double imaging" leads to an important improvement of imaging performances of confocal systems in respect to the conventional microscopy.

1.1.1 Image formation

The evaluation of performances of the imaging systems requires a precise model of image formation. One of the most common method for analysis of optical systems is the point spread function (PSF) formalism. PSF represents the impulse response of the system, ie, it is a functional (2D or 3D) representation of an image of a point object generated by the considered optical system. The image formation of extended objects can be then described by convolution of PSF of the optical system with the function describing the object interaction with illumination light. The definition of convolution is given by equation 1.1.

$$(h * o)(x) = \int h(\vec{x}')o(x - x')\mathbf{dx}' \tag{1.1}$$

where $*$ represent convolution operator, h and o are convolved functions.

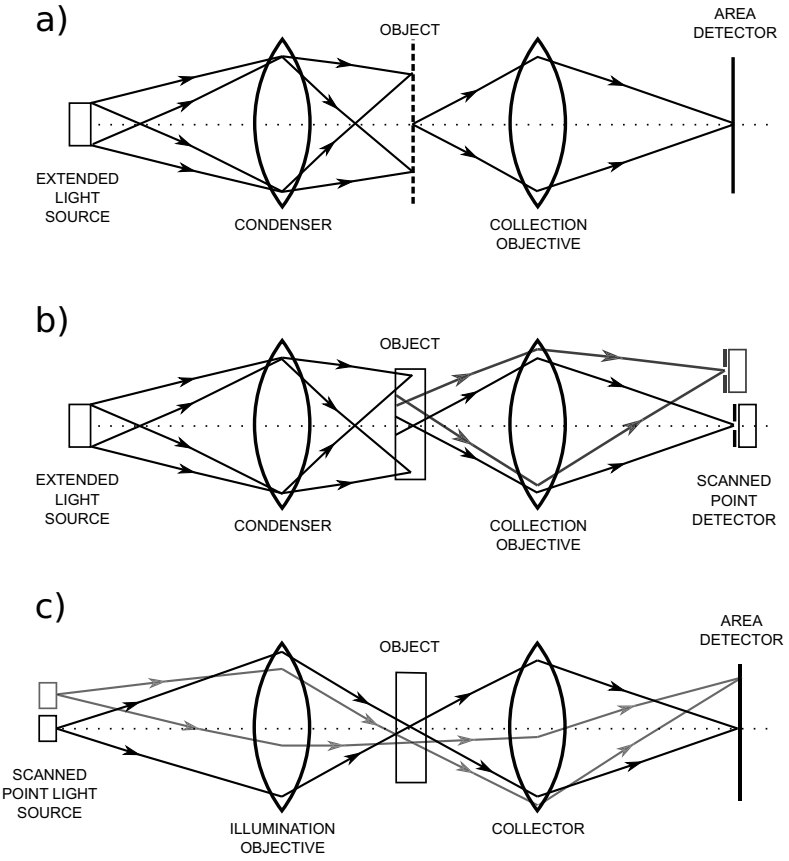


Figure 1.2: Evolution of scanning microscopy - (a) conventional wide-field microscope; (b) microscope with scanning point detector; and (c) scanning point illumination system. Combination of (b) and (c) leads to confocal system presented on figure 1.1

The effective PSF of the optical system depends strongly on the configuration of used optical system. The conventional wide-field microscopes and confocal microscopes build-up using same optical elements are characterized by different effective PSF's. The wave nature of light requires consideration of both an amplitude and phase when considering imaging properties of optical systems.

Indeed, classical[1] imaging system, image formation can be described by a convolution operation [3, 5]:

$$I_{classical} = |h_2|^2 * |o|^2 \tag{1.2}$$

[1] wide-field, incoherent microscopy

where h_2 is the amplitude point spread function (PSF) of the imaging lens, $*$ is the convolution operator, and o represents the object transmitance function.

In case of confocal imaging system, both objectives contribute to the image formation, so that:

$$I_{confocal} = |(h_1 h_2) * o|^2 \tag{1.3}$$

where h_1 is the PSF of the illumination lens. Here, it is clearly visible that illumination system equally contribute to the image formation which is contrary to the conventional microscopy where h_1 does not appear[1].

Although, equations 1.2 and 1.3 have similar form - the effective PSF's of both system is different. Moreover, the image formation (or convolution realization) is different between the two systems. In wide-field system the image is generated at once - all points are imaged in parallel, in confocal system imaging is sequential - point-by-point.

The concept of intensity PSF (IPSF) can be used to make a direct comparison between a wide-field imager and confocal imager in terms of intensity image recorded by the detector in the case of imaging a point object. Thus, figure 1.3 shows the resolution improvement offered by confocal system over conventional wide-field system by comparing intensity response functions of both systems.

1.1.2 Optical Sectioning and 3D Imaging

The potential of confocal microscopy lies in the efficient imaging of thick specimens. When 2D in-plane scanning is performed, the image obtained within a confocal system is a so-called "optical section" (z-section) of the specimen. On the one hand, point illumination assures that only a small volume of the sample is illuminated, on the other hand the point detector collects the light only within this limited focal volume. In consequence confocal system is characterized by strong localization of the observation volume.

The confocal detection is performed by a point detector. However, a true point detection can not be realized physically (the power reaching the detector have to be reasonable), moreover existing detectors have always finite sizes. In practice, confocal systems often utilize a pinhole filtering to realize small area detection (figure 1.4). Important issue in the design of confocal microscope is the choice of the pinhole size. From one hand, the pinhole has to be large enough to transmit enough signal from the sample to detector. From other hand enlarging the pinhole decrease the confocality

[1] In here we did make same sort of simplification, precise analysis shows that in wide-field microscopy condenser lens influence image formation, however this impact is minute comparing to the case of confocal microscopy. Precise theory of image formation in classical microscopy is given for example in [6].

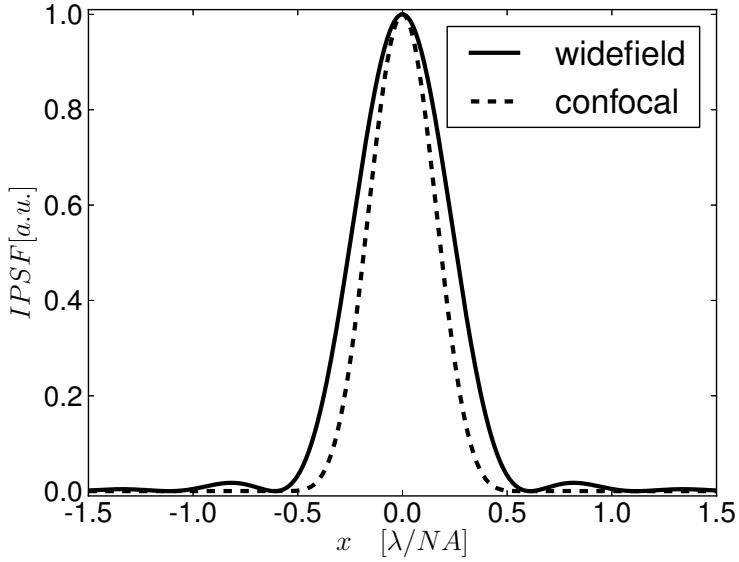


Figure 1.3: Comparison of latral IPSF of wide-field and confocal system - Improvement of the resolution of confocal system visible by narrower IPSF than in case of wide field case.

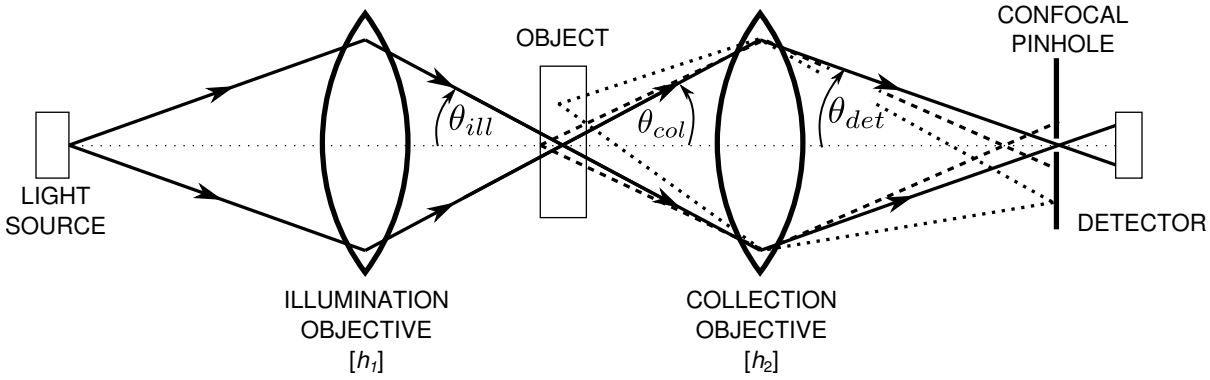


Figure 1.4: Optical sectioning - The point illumination assure that only small volume is illuminated whereas point detection realized by pinhole filtering defines the volume from which signal is collected, when 2D in-plane scanning is performed, confocal system images specific z-section of thick specimen.

of the system - the observation volume increase (resolution decrease) when too large pinhole is used. In conclusion, the best performance of confocal system (in terms of optical resolution) is achieved when pinhole diameter satisfy condition given by equation 1.4 [3].

$$d < \frac{2.5}{\pi} \frac{\lambda}{NA_{det}} \tag{1.4}$$

where d is the diameter of the pinhole and NA_{det} is numerical aperture of the system in the detector plane ($NA_{det} = sin(\theta_{det})$). The resolution of the confocal system is usually anisotropic (different in axial and lateral directions) (figure 1.5) and is defined by the numerical aperture (NA) of the objectives and the wavelength of the light source. In the case on symmetric system (same objective in the collection and illumination blocks $\theta ill = \theta_{col}$) the optical resolution can be expressed as (equations 1.5-1.6):

$$\delta x, y_{fwhm}^{cfl} = 0.37\frac{\lambda}{NA} \tag{1.5}$$

$$\delta z_{fwhm}^{cfl} = 1.26\frac{\lambda}{nNA^2} \tag{1.6}$$

where λ is working wavelength of the microscope, NA is objective numerical aperture ($NA = nsin(\theta_{ill})$), n is refractive index of object space, $\delta x, y_{fwhm}^{cfl}$ and δz_{fwhm}^{cfl} are lateral and axial resolution respectively.

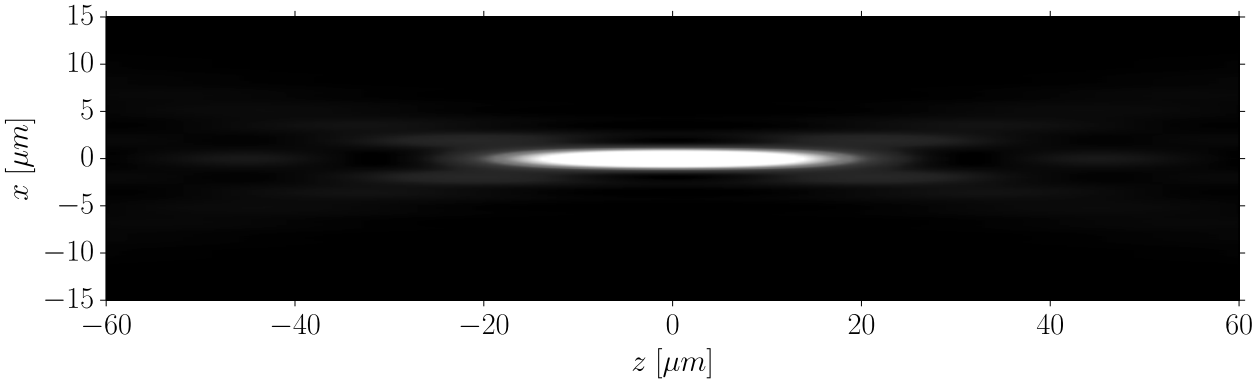


Figure 1.5: Anisotropic resolution - The XZ cross section of $|h|^2$ in case of ideal objective. The 3D shape of image of a point object takes form a pot that is elongated in the direction of the propagation axis. In here example for NA=0.2 is shown for which $\delta_x^{fwhm} = 1.6\mu m$ and $\delta_z^{fwhm} = 30\mu m$, if the same optical system would be used for confocal imaging ($|h|^4$) resolution would be improved to: $\delta_x^{fwhm} = 1.1\mu m$ and $\delta_z^{fwhm} = 20\mu m$.

1.1.3 Different types of confocal microscopes

Many configurations of confocal microscopes have been proposed, each of them adapted to specific imaging applications. Classical monochromatic modes are used when investigated specimen poses intrinsic contrast variation due to light absorption or scattering, i.e. structure of the sample can be analyzed by observation of variation of light intensity caused by absorption/scattering within the

sample. However, in case of many biological specimens where sample contrast is low (sample weakly absorbs/scatters the light), fluorescence technique is often employed. In the fluorescence systems, illumination wave λ_{il} excite the specific molecules in the sample that emits fluorescence signal at different wavelength λ_{em} that is observed by the microscope. Fluorescence system can be divided into two groups: first one relies on so-called auto-fluorescence of the sample, that is molecules of the sample are excited to generate the fluorescence signal. In the second group, fluorescence signal originates from the special marker that sample is labeled with[1]. The optical architecture of fluorescence confocal microscope is presented in figure 1.6, from the point of view of optical implementation the origin of fluorescence does not define the optical configuration, however the light source and the detection block that have to be adopted to the specific excitation and emission wavelengths of the observed fluorescence.

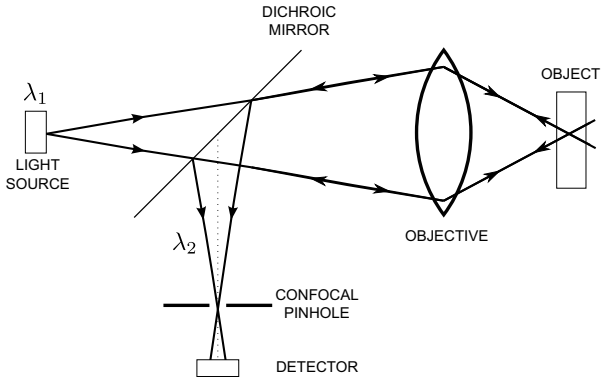


Figure 1.6: Confocal fluorescence microscope - Fluorescence confocal microscope illumination (λ_1) excite the fluorescence in the sample and only fluorescence signal (λ_2) is detected.

The confocal systems can operate in transmission or reflection modes, in the transmission mode the investigated sample is sandwiched between the illumination and collection objectives (figure 1.1). In the reflection mode, illumination and collection are performed with the same objective (figure 1.7a), the sample scattering signal being redirected to the detector by a beam splitter located before the objective.

Reflectance, differential confocal microscopy is a special type of confocal system adapted to topography measurements of reflective surfaces (figure 1.7b). The concept is based on the high-sensitivity of confocal response function when the reflective object is located on the slope of axial

[1] sample labeling sometimes considered as invasive technique, however fluorescent labeling is a common technique allowing observation desired structures within the specimen, for this reason fluorescence confocal microscopy is a common tool even when "in-vivo" imaging is performed [7]

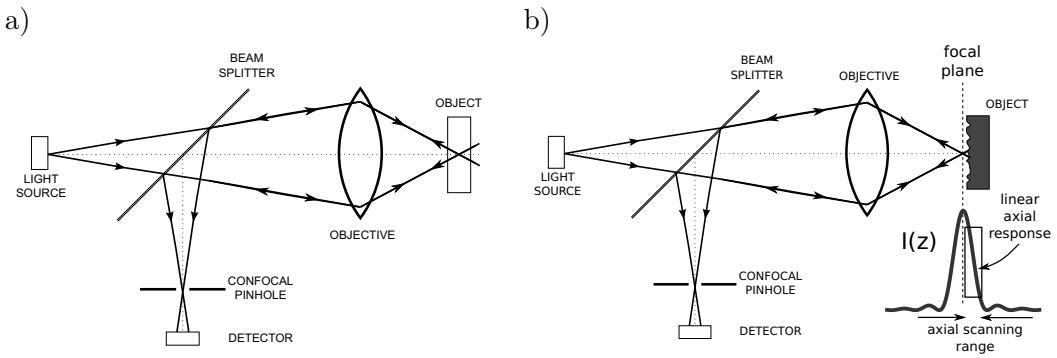


Figure 1.7: Confocal imaging in the reflection mode - (a) the most popular confocal systems are based on the reflective configuration, (b) differential confocal system - specific design for measurement of micro/nano-topography of reflective specimens.

response function. This system allows achieving high axial resolution without the need of high NA objectives. Authors of the method reported [8] 2nm axial resolution using NA=0.85 which is much above the limit of conventional confocal microscopy given by equation 1.6. This particular "super-resolution" is due to the specific relation between the signal level (recorded by the detector) and the sample axial position relatively to illumination focus maximum in case of uniform reflection/scattering of the sample. In the case of non-uniform sample reflectivity, architectures that allow monitoring of the varying reflectivity as well as the topography using two detectors in the collection block has been also proposed [9, 10], leading to similar improvements.

1.2 Imaging Quality: Contrast and Resolution

In this section we discuss basic properties of optical systems in the context of imaging quality. In particular, optical resolution definitions are reviewed and same specific configuration of confocal systems aiming at improvement imaging quality are discussed.

1.2.1 Definitions

Resolution of on optical system describes is the ability to resolve fine detail in the object that is imaged. In practice, several criteria are used to define the resolution of the optical system depending on the object that is used for investigation of system imaging characteristics. Two cases are mainly considered, the first class are the so called two-point criteria that defines the resolution on a basis

of distinguish-ability of two close point-like objects imaged by the optical system. The second commonly used formalism is based on frequency domain image analysis. This approach use the optical transfer function (OTF) formalism to analyze the contrast transfer of spatial frequencies through optical system. The advantage of this method is its applicability to imaging of extended objects in contrary to two-point criteria for which resolution is well defined for point-like objects only.

1.2.1.1 Two-Point Resolution Criteria

The resolution of an optical imaging systems is eventually limited by diffraction effects (related to the wave nature of light). In the ideal case (aberration-free optics) of axially symmetric system with circular aperture, image of a point at the focal plane has a form of an Airy disk (eq. 1.7). Then the size and shape of the point response define the resolution of the optical system.

$$h(r, z = z_f) \quad = \quad \frac{2J_1(v)}{v} \tag{1.7}$$

where λ is the wavelength, v is unit-less radial coordinate defined as $v = \frac{2\pi}{\lambda} rNA$, r and z is axial coordinates respectively, z_f is axial focus position, and $J_1(v)$ is a Bessel function of the first kind of order one.

The basic resolution criteria relay on the so called "two points resolution criteria". This approach defines the resolution of the system as the smallest distance between two point objects that can be distinguished (resolved) in the imaging plane of the optical system. Quantification of this rather imprecise definition was made firstly by Rayleigh [11] and later by Sparrow [12], that leads to two different resolution criteria. Rayleigh resolution definition is based on the functional shape of the airy disk, and says that two points can be resolved when distance between them corresponds to the position of the first dark ring (first zero value) of the Airy disk (figure 1.8a). Sparrow resolution criteria sometimes called "true limit of resolution" is defined as object separation for which combined image intensity distribution has two first derivatives equal to zero (figure 1.8c). Finally, the third criterion which has become one of most the used alternative to Rayleigh and Sparrow criteria is one based on full width half maximum (FWHM) (figure 1.8c). These different approaches, employed to define the resolution show that resolution is never the same strictly defined value. Equations 1.8-1.10 show the expressions for resolution defined by the three mentioned criteria. Visibly different definitions result in resolution values that can differ by more than 20%.

$$d_{Rayleigh} = 0.61\frac{\lambda}{NA} \tag{1.8}$$

$$d_{FWHM} = 0.51\frac{\lambda}{NA} \tag{1.9}$$

$$d_{Sparrow} = 0.48\frac{\lambda}{NA} \tag{1.10}$$

Rayleigh criterion is directly based on the functional form of focal spot of ideal (aberration free) incoherent imaging system. Consequently it cannot be directly applied to all optical systems. In order to extend Rayleigh resolution definition to arbitrary system the contrast value is used (eq. 1.11).

$$c = \frac{I_{max} - I_{min}}{I_{max} + I_{min}} \tag{1.11}$$

Where I_{max} is the peak intensity in the image and I_{min} is the intensity value at mid distance between images of the two points. Contrast value can lead to an alternative definition of Rayleigh resolution expressed as the object separation that produces contrast equal to 26%. Generalization of resolution criterion based on the image contrast leads to a more general formulation of resolving power of optical systems. As discussed in [13] a more general way to define the resolution is to define the detectable contrast and consequently the resolution as: *"the distance of two objects at which a certain contrast is achieved in their image"*. Thus the different resolution criteria (for Airy disk) given by 1.8-1.8 can be rewritten in the contrast frame as (eq. 1.12-1.14):

$$c_{Rayleigh} = 0.26 \tag{1.12}$$

$$c_{Sparrow} = 0 \tag{1.13}$$

$$c_{FWHM} = 0.05 \tag{1.14}$$

where c_{name} is the contrast value. It can be noted that Sparrow criterion represents the absolute limit of resolution and in this case the contrast vanishes. The FWHM criterion correspond to a relatively small value of contrast (5%) in comparison to Rayleigh one that corresponds to 26%. However, FWHM value is hardly ever translated into contrast values and is used as the first/simplest estimation of resolving power of optical systems basing of the calculated or measured shape of the system IPSF. It is important to underline that equations 1.8-1.14 describe the relations for lateral resolution in the case of wide-field incoherent imaging system and do not represent general rule between resolution criteria and contrast values in different systems. The contrast based reinterpretation of two-points resolution criteria allows its use in arbitrary systems. In confocal

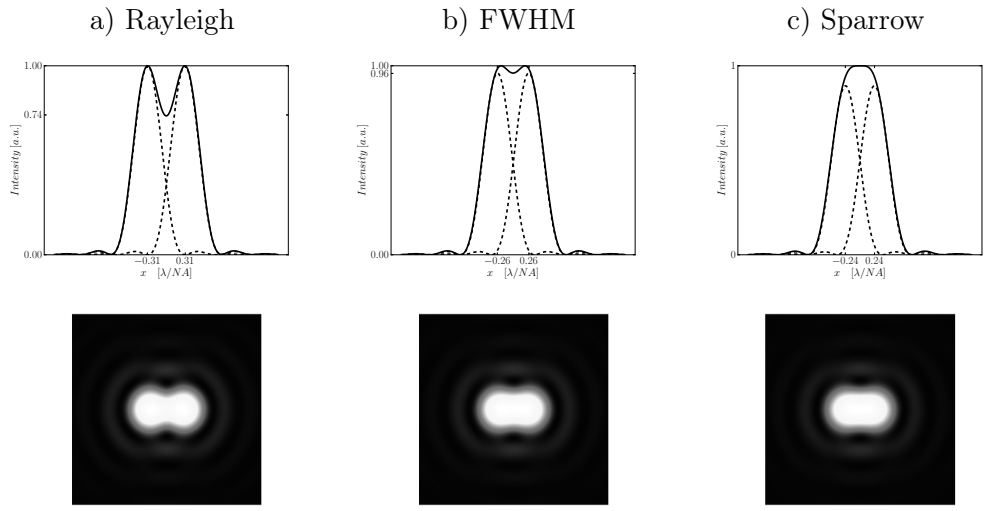


Figure 1.8: Separation of two points imaged by the conventional microscope in case of separation distance equal to Rayleigh a), FWHM b) and Sparrow c) separation distances

microscopy, the "double imaging" leads to an increased resolving power so that resolution can be given as:

$$d^{cfl}_{Rayleigh} = 0.44\frac{\lambda}{NA} \tag{1.15}$$

$$d^{cfl}_{Sparrow} = 0.27\frac{\lambda}{NA} \tag{1.16}$$

$$d^{cfl}_{FWHM} = 0.37\frac{\lambda}{NA} \tag{1.17}$$

$$\tag{1.18}$$

In here, Rayleigh resolution is defined by conserving original 26% contrast, the Sparrow criterion by definition has the limiting value of zero contrast, whereas the FWHM resolution in case is characterized by slightly higher contrast (6%) than in wide-field system (5%).

Finally contrast-based resolution definitions (Rayleigh and Sparrow criteria) are considered as a more general (and more meaningful) definition than shape-based criteria. From one side it is easily extensible to the case of imaging extended objects and from another side it allows taking into account other properties of the imaging system that affects imaging quality, like noise, detector dynamic range or image sampling or optical aberrations [13].

1.2.1.2 Frequency Domain Resolution Analysis

Another formalism to describe imaging performances employs the modulation transfer function (MTF) [5, 6, 14]. MTF is the frequency domain representation of impulse response of the optical system (modulus of Fourier transform of PSF). This method describes imaging quality of extended objects, and is more general than the two-point resolution criterion used to describe imaging of point-like objects.

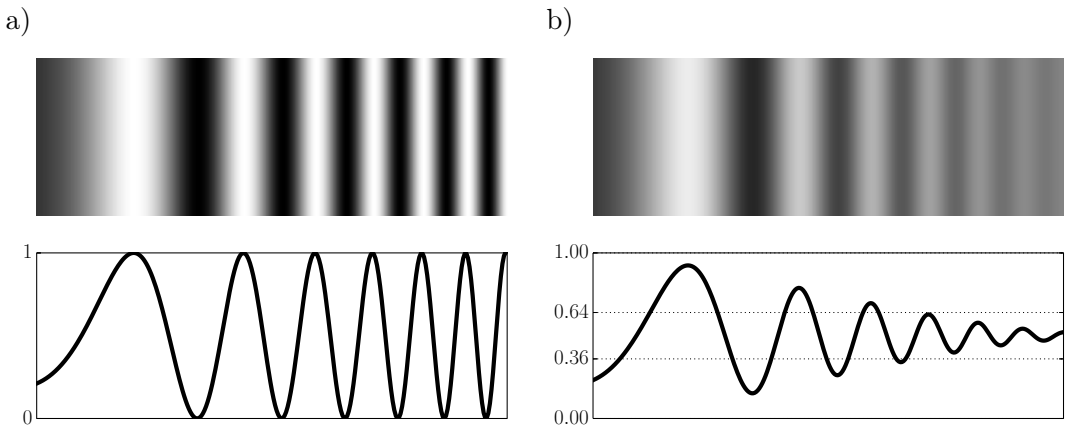


Figure 1.9: MTF contrast interpretation - Test pattern imaged by optical system, resulted image has contrast (modulation) dependent of frequency of the object. a) the object - signal with varying period and its image b) for which contrast decrease with increased frequency. Grid lines in b) correspond to Rayleigh resolution limit defined by contrast value of 26%.

MTF can be interpreted as value of contrast, in function of spatial frequency, in the case of imaging of test pattern (figure 1.9). In this context, high frequencies represent fine detail of the object whereas low and mid frequencies describe slow modulation present in the structure. The contrast transfer in the region of high frequencies defines the resolution of the system. When contrast is too low, some information of the object may not be recorded by the detector. Similarly to the two-point criteria in the frequency domain resolution qualification detection limit can be defined in different manners.

In addition to contrast-defined resolution limit (ex. by Rayleigh 26% contrast value) important characteristic of each system is the cut-off frequency. The cut-off frequency is the maximal value frequency that can be imaged by the system with non-zero contrast (similarly to Sparrow criteria). In the spatial domain cut-off frequency is equivalent to the Abbe resolution criteria [15] (first

resolution limit ever defined) that reads $d_{cut-off} = \frac{\lambda}{2NA}$ and $d^{cfl}_{cut-off} = \frac{\lambda}{4NA}$ for conventional and confocal microscopes, respectively (figure 1.10). The cut-off frequency or Abbe resolution limit are often considered as the absolute limit of resolution of classical, far-field, linear imaging systems.

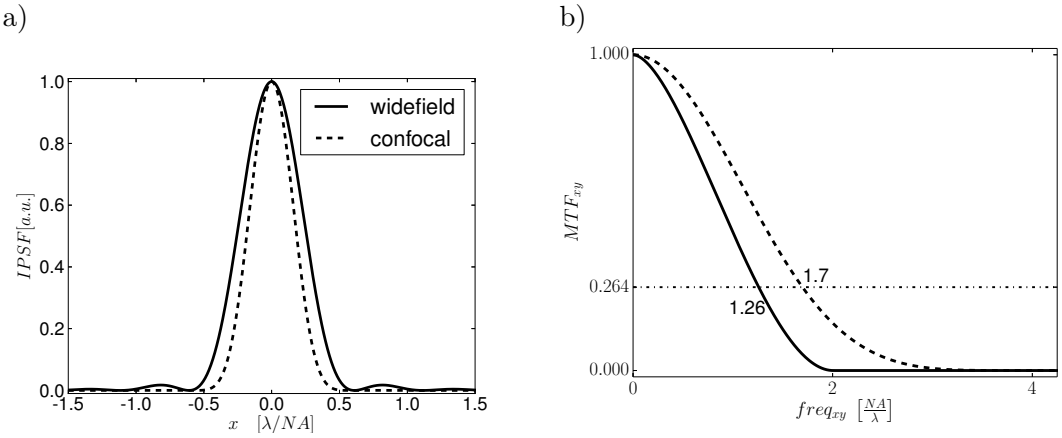


Figure 1.10: Classical wide-field vs confocal imaging system - Lateral resolution comparison via (a) IPSF and (b) MTF, of confocal microscope (dashed line) and wide field system (solid line). It is visible that confocal system has higher resolution since MTF reaches higher spatial frequencies than classical system.

1.2.1.3 Axial resolution

Similar analysis as presented for lateral resolving power can be made to analyze axial resolution. The axial extension of PSF is defined by equation 1.19 [3].

$$h(v=0,u) = \frac{sin\left(\frac{u}{2}\right)}{\frac{u}{2}} \tag{1.19}$$

where u is unitless axial coordinate defined as $u = \frac{2\pi}{n\lambda} z NA^2$, z - is coordinate along propagation axis with coordinates origin at the focal plane and n is refraction index in the object space. From this relation is also possible to derive resolution according to different discussed formalism.

$$\delta z_{c=0.26} = 2\frac{n\lambda}{NA^2} \tag{1.20}$$

$$\delta z_{fwhm} = 1.26\frac{n\lambda}{NA^2} \tag{1.21}$$

$$\delta z_{cut-off} = \frac{n\lambda}{NA^2} \tag{1.22}$$

Equations 1.20-1.22 summarize resolution of confocal system in most useful criteria: $\delta z_{c=0.26}$ - Rayleigh 26% contrast, δz_{fwhm} FWHM and $\delta z_{cut-off}$ cut-off frequency. It is important to note that axial resolution is always worse than lateral, and that it has faster dependence on numerical aperture of the system (NA^2). The MTF for axial frequencies can be also defined in similar way that for lateral ones. In this case confocal systems show also improvement comparing to wide field systems (figure 1.11).

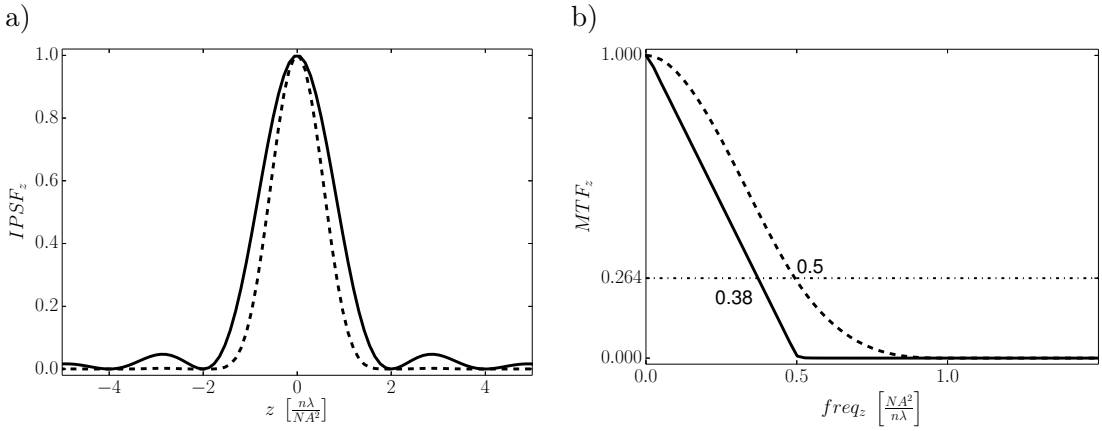


Figure 1.11: Axial resolution IPSF - Axial resolution analysis in confocal microscope (dashed line) compared with wide-field system (solid line). (a) IPSF and (b) MTF.

1.2.2 Resolution in non-perfect optical system

In real system resolution is limited by additional aspects of optical and detection systems, like optical quality (optical aberrations), dynamic range of the detector, noise present in the system (that can originates from the source, sample or the detector) or the digitization procedure of the collected signal influence the final resolution of the complete system. In general all these aspects reduce the theoretical system resolution and should be considered as part of the system design. An additional effect, impacting the resolution in confocal system is In the context of confocal microscopy is the detector size (pinhole size) . In general when perfect optical system is employed and detector size fulfill condition 1.4 the pinhole size do not impact resolution of confocal system.

1.2.2.1 Aberrations

The resolution aspects discussed above quietly assumed perfect optical systems, i.e., without optical aberrations. The perfect imaging system transforms electromagnetic wave introducing the curvature to its wavefront. In the real systems finite size of optical systems add geometrical limitation to the wave that propagate in the system leading to diffraction effects. Another issue that appears in the physical systems is never exactly spherical wavefront generated by optical system. The wavefront deviation from the ideal spherical shape is called the wavefront aberration.

The aim of an imaging system is to form image of the point on the image plane. A perfect point source that emits electromagnetic radiation generate divergent spherical wave[1]. The inverse relation is also valid: a convergent spherical wave should also "focus" into a point. This simple observation based only on the symmetry and time invisibility of wave propagation indicate that perfect imaging system should generate spherical waves. The two mentioned limitations for the physical realization of an optical imaging system will cause degradation in focusing of the optical systems. Firstly limited lateral size of the lenses cause that only part of spherical wave can be generated in consequence focusing to a ideal point is not achievable. Second important issue in the real systems is the precision of the shape of the wavefront generated by the objectives. In the optical systems composed from lenses and mirrors generation of perfectly spherical wavefront is virtually not possible. The aberrations always decrease the contrast of optical systems. The main criteria of optical design is always to minimize the aberrations present in the system. The impact of wavefront deviations to imaging quality is covered by the aberration theory [6, 16].

1.2.2.2 Noise

As was discussed the resolution of optical systems has a strict relationship with the contrast. However, detectable contrast is defined by the detection systems and sample itself. Practically, detectable contrast depends on the noise present in the system or more precisely on signal to noise ratio (SNR). In every optical instrument different system elements contribute to the noise present in the output signal. The detector and light source noise often originates from the driving electronic.

1.2.2.3 Sampling

Digitization is a process of transforming analog system obtained within the optical measurement system into a digital form that can be treated in the digital manner. In practice, confocal mi-

[1] under scalar wave approximation

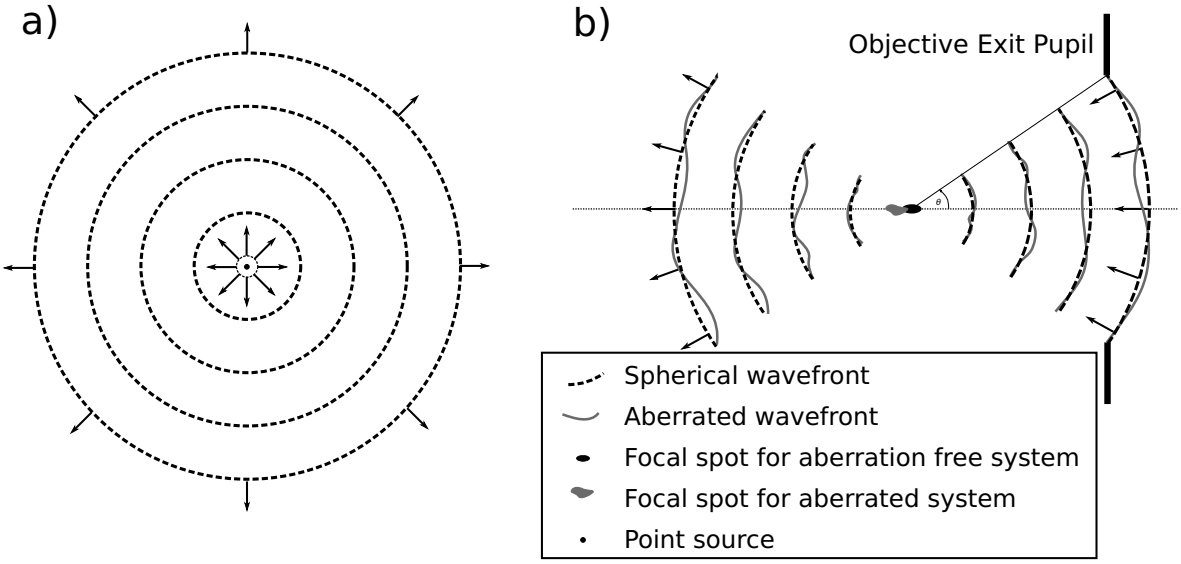


Figure 1.12: Resolution limits in real optical systems - Point source generate spherical wave a), physical optical system b) to focus light (ideally to a point) has to generate convergent spherical wave, however limited size of objective ($\theta < 2\pi$) and wavefront deformations lower the resolution capability.

croscopy that generates the 3D images the data post-processing and analysis is always done in the digital form and the digitization is done directly within the system. Generally, in the context of optical imaging two main parameters of the digitization are important: the sampling rate and the quantization resolution (bits per sample). The sampling rate defines the frequency of the sampling the signal where resolution defines values span of the possible values of the signal. The golden rule for choosing the sampling rate is the Nyquist criterion [5] that states that sampling frequency has to be twice larger then maximal frequency present in the signal to be digitized. In the context confocal microscopy it is interpreted as sampling with frequency twice higher then optical resolution provided by optical system [4]. In the many implementation of laser scanning confocal microscopy systems the so-called oversampling is used, it means that higher than necessary sampling rate is applied and redundant data are used for noise reduction via averaging [17]. The sampling data size defines the number of intensity values that can be recorded within digital signal representation, different confocal systems operates with the depths from 8 to 16 bits that is adapted to required imaging conditions.

1.2.3 Resolution improvements in confocal microscopy

As discussed before, the important advantage of confocal microscopy is an improvement of optical resolution compared to classical microscopy. In terms of Rayleigh resolution criterion, the resolution gain in confocal system is about 20%. However, when considering absolute resolution limit (Sparrow criterion or frequency cut-off) resolving power of confocal microscopy is doubled (figures 1.10 and 1.11). Many investigations have been done to improve the useful resolution of confocal systems. In this section, we discuss two approaches that can be employed in the confocal microscope to improve system resolution without the increase the NA of the objective.

1.2.3.1 Apodization

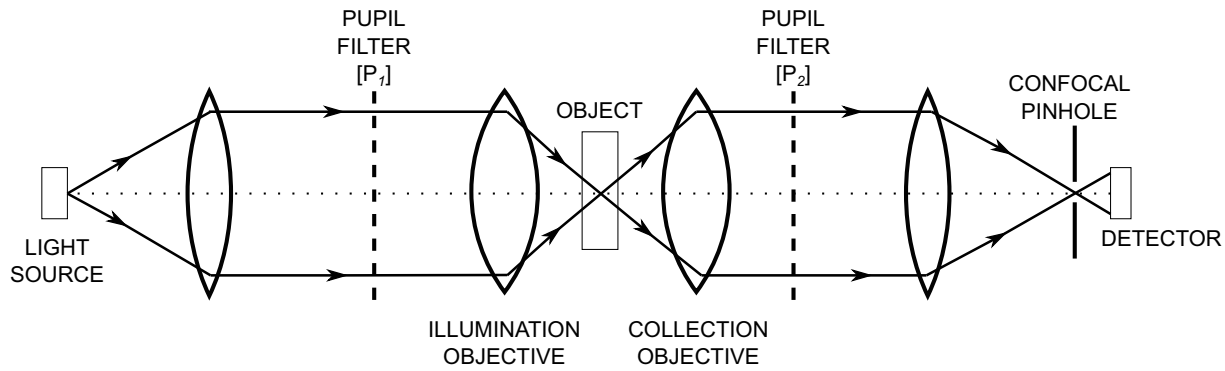


Figure 1.13: Apodization in confocal microscopy - Two pupil filters can be used in confocal microscopy: one in illumination and one in collection part. In the usual configuration apodization filters are placed in the $4f$ arrangement, i.e. located in the focal plane of objectives.

One of the large area of research for improving resolution is so-called PSF-engineering [18, 19, 20]. The basic idea is to change the shape of the PSF (and consecutively MTF) by introducing apodization filters (pupil filters) in the optical system (figure 1.13). This approach aims to increase the contrast of high frequencies that in standard confocal systems are imaged with low contrast and are in practice undetectable. However, the resolution improvement obtained by apodization is achieved through contrast improvement and is always below the frequency cut-off that is defined exclusively by the numerical apertures and wavelengths used in the optical system [21]. In figure 1.14 effect of linear apodization (gray-tone amplitude filter with linear transmittance) is presented in the case of 2D optical imaging system. The PSF (figure 1.14a) of the apodized system has reduced width, however side-lobes are clearly larger than in the system without the filter. The

MTF plot (fig. 1.14b)) illustrates the effects of contrast transfer modification introduced by the apodization filter. We can see an increased contrast in the region of high frequencies (fine detail) which is obtained at the cost of lower contrast for mid and low frequencies [5].

In confocal microscopy, apodization can be applied twice: one filter is located in the illumination objective aiming modification of the illumination response function (h_1), and the second filter in the collection objective modifies the collection PSF (h_2) (figure 1.13). Then, since the effective PSF in the confocal system is defined as a product of illumination and collection impulse responses (eq. 1.3) the system PSF can be improved to higher extent than in the conventional microscopy where only single apodization is possible [22].

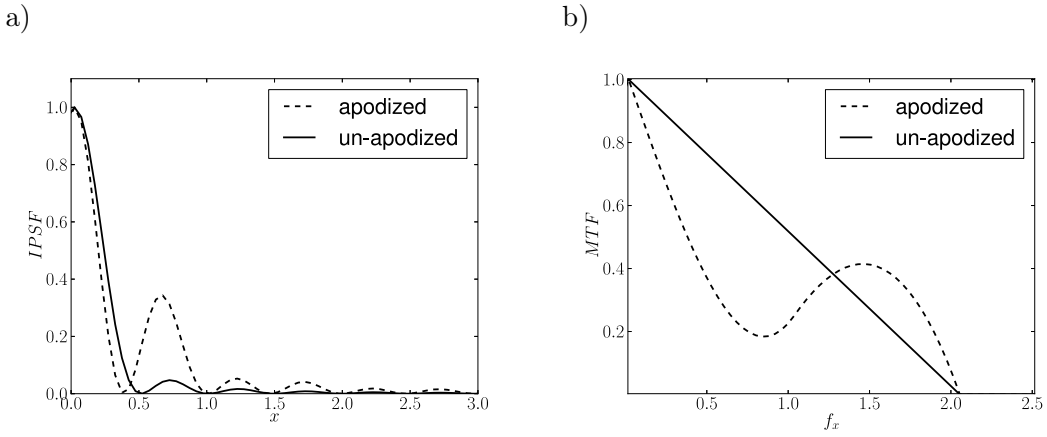


Figure 1.14: Apodization example - A pupil filter introduced into optical path of microscope can change (a) the impulse response function and (b) and transfer function of the optical system. In this example linear apodization filter applied to 2D optical system improves the transfer of high frequencies, however side lobes that appears in PSF due to apodization filter deteriorate imaging of mid-frequencies [5].

1.2.3.2 Theta configuration

One of the main challenge in the construction of confocal imaging system is the requirement of high NA objectives to achieve reasonable axial resolution (eq. 1.6). The high NA objectives that are corrected for optical aberrations are complex systems and difficult to manufacture in miniature system. Moreover, high numerical aperture of the objective also signifies usually a short corresponding working distance of the optical system. The long working distance and low NA objectives are often preferable, especially for miniaturized systems. Low NA always means larger field of view whereas

long working distance allows larger separation between the device and the investigated specimen. Additionally, in the context of miniaturized systems, construction of high NA micro-objectives is very challenging, especially when beam scanning is employed for which off-axis aberrations need to be considered.

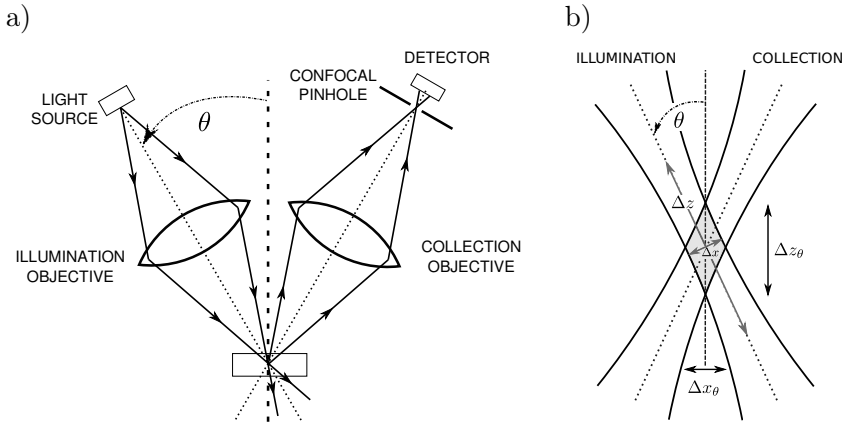


Figure 1.15: Architecture of theta confocal microscopy - Two separate objectives working in reflective confocal mode in the theta-configuration (a), Noncolinear illumination and collection PSF generated by low NA objectives whose optical axes cross at angle 2θ form effective response of theta confocal microscopy that is isotropic in 3D space (b).

Apodization discussed before can modestly improve the system performances. However, it cannot improve axial resolution sufficiently. One system that can provide high 3D resolution without the use of high NA objectives was proposed by Stelzer and Lindek [23]. The architecture baptized as "theta confocal microscopy" (sometimes called "dual-axis" or "bi-axial" confocal microscopy) uses two objectives (one for illumination and second for collection) whose optical axes are inclined at angle θ relative to each other (figure 1.15).

In this configuration, illumination and detection follow different axes and share only a small common part of a focal volume (figure 1.15). This system allows significant reduction of axial resolution compared to the classical systems. In the theta configuration, the resolution of the system is defined not only by NA of the composing objectives but also by the angle between the objectives. Consequently, the 3D resolution in paraxial approximation (low NA) is expressed [24]

as follows (eq. 1.23-1.25):

$$\Delta x_{fwhm} = \frac{0.37\lambda}{NAcos(\theta)} \tag{1.23}$$

$$\Delta y_{fwhm} = \frac{0.37\lambda}{NA} \tag{1.24}$$

$$\Delta z_{fwhm} = \frac{0.37\lambda}{NAsin(\theta)} \tag{1.25}$$

where θ is the half-angle between the objectives axes (figure 1.15). The important consequence of equations 1.23-1.25 is a linear dependence of axial resolution Δz on NA comparing to the classical confocal system (eq. 1.6) where relation is NA^2 dependent. The improvement of axial resolution is achieved in some level in cost of the lateral resolution. However, the resolution is more isotropic (figure 1.15b) with low NA system than in the case of the classical system. Except the use of low NA in this system important feature of this configuration is low impact of optical aberrations onto imaging quality [25]. Moreover, the non co-linear illumination and collection paths improves scattered light rejection in the case of imaging thick samples [26].

The realization of system using with two inclined microscope objectives is relatively complex to setup and use in practice. Several experimental setups were described [24, 27, 28, 29, 30]. However, this system is very attractive for realization in miniature form, especially since low NA objectives can be used. The theta configuration gained more attention in the single objective configuration in particular with the divided aperture technique [28, 31, 32]. The optical configuration of single lens theta system is presented on figure 1.16. In this configuration resolution gain is less important than in case of two objective systems [33, 34]. However, advantages of scattering light rejection and decreased impact of optical aberrations are preserved [25].

1.3 Beam scanning in confocal microscopy

Confocal microscope, in principle, is not more demanding optically than standard microscope systems. The main difference and main difficulty in the construction of confocal systems is related to the requirement of scanning. In general two options are possible: object scanning or beam scanning.

The simplest way to achieve imaging (2D or 3D) based on confocal point-by-point image formation principle is to move the specimen around the stationary focus point of the optical system in order to sample all volume of the specimen. This method allows observation of large volumes without optical limits for the scanning range since objective works in the purely on-axis configuration thus no limits related to off-axis aberrations are present. However, important drawback of this

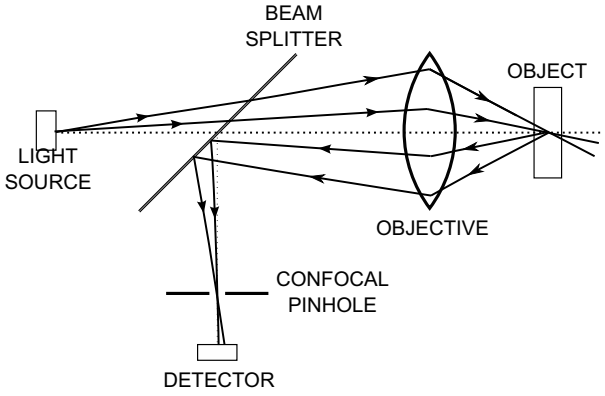


Figure 1.16: Single Lens Theta confocal microscopy - One objective used in theta configuration so called "divided aperture" approach: one part of the objective is used for illumination another for collection.

approach is the bulk size of the instrument in regards to the investigated object. Moreover, sample scanning speed is limited by relatively slow translational stages. In addition, the investigated specimen has to be placed onto a stage limiting the applications of this technique.

1.3.1 Beam scanning techniques

The second scanning option, faster and more convenient in many cases (stationary object) is the beam scanning. In this approach the position of imaged point is controlled by opto-mechanical configuration of the optical scanning module. The most commonly employed scanning devices are made with mirrors or acusto-optic deflectors [37, 38]. Lately, galvanometer mirrors that are commonly used in optical scanning systems are often replaced by MEMS mirrors that allow construction of fast and compact optical scanners [39]. MEMS technology allows miniaturization (figure 1.17) and cost reduction of confocal systems. Miniaturization is not due only to smaller dimensions of the scanners but also to the integration of 2D scanner in the single element. The galvanometer mirror can provide only 1D-scan, so that in-plane 2D-scan needs two mirrors set-up in appropriate configuration. Thus, it requires the use of more complex optical systems and results in larger sizes of the scanning systems. In the case of MEMS-based mirrors, 2D beam deflection can be achieved with a single mirror [40, 41, 42].

Nowadays, the tilted mirror based scanning systems dominate the market of beam scanners in confocal microscopy[1]. However, alternative scanning methods like rotating polygon or acousto-

[1]Spinning disks confocal microscopes are also popular but they are a little different class of systems

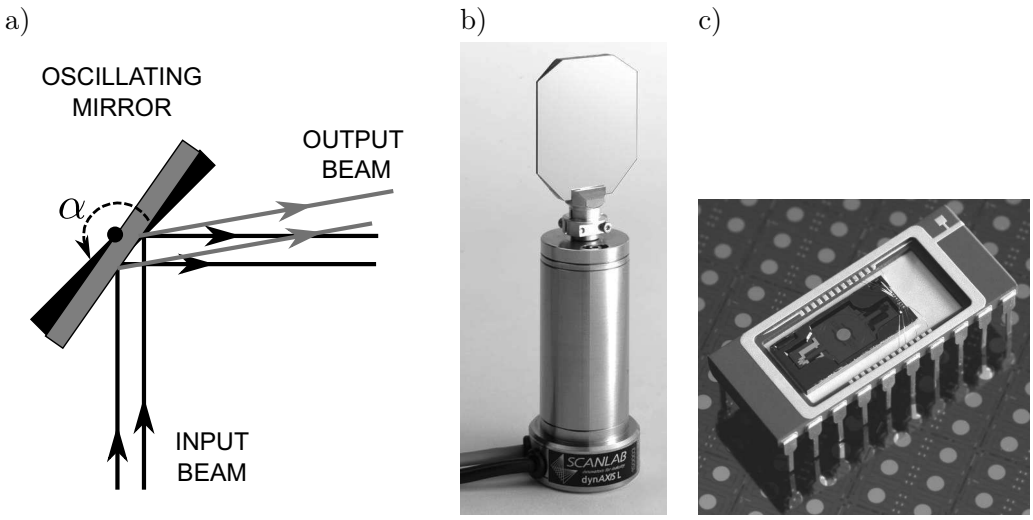


Figure 1.17: Mirror-based optical scanning - Most common scanning method is based on beam deflection by mirrors, (a) optical scheme, (b) classical galvanometer scanning mirror [35] and (c) MEMS-based optical scanner [36].

optic deflectors have demonstrated their potential in specific applications [43]. Figure 1.18 presents scanning principles of those elements. Rotating polygon scanners (figure 1.18a) allow fast scanning without resonance effects present in galvanometer scanners. Acousto-optic deflectors (figure 1.18b) are the only beam scanners that have no moving parts. Instead, it uses acoustic waves in a bulk, transparent medium as a controllable diffraction grating [37].

Currently, most common configurations of beam scanning applies only to the XY plane (perpendicular to the optical axis), whereas the Z-scan (along the optical axis) is still achieved by vertical displacement of the sample. Alternatively, objective lens can be placed on the actuator (axial stage) that allows displacement of the focal plane within stationary sample.

However, current trend in the development of laser scanning confocal microscopy (LSCM) tends to replace this hybrid scanning approach with full 3D beam scanning systems. One of the investigated area to reach this aim is the use of deformable optical components. Shao *et al.* [44] developed a scanner based on MOEMS technology performing 3D beam-scanning. The proposed scanner used a deformable mirror made of SiN membrane that can be independently deformed and tilted around x and y axes. Both deformation (focus scan) and til ting of the mirror are driven by electrostatic actuation. A different approach to 3D optical scanning discussed in literature is based on acousto-optics deflectors that analogically can be used to form an active optical component for very fast

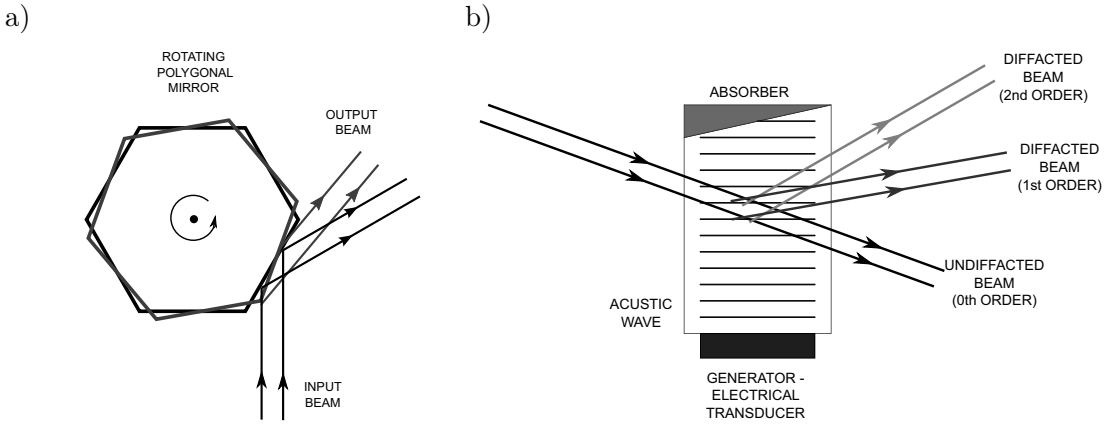


Figure 1.18: Classical beam scanning - Most common scanning modules for fast scanning: rotating polygon mirror a) and by acusto-optic deflectors

optical scanner [45, 46].

An alternative and actually one of the oldest method of confocal scanning system is a spinning disk microscope. Original design by Petran [47] used a rotating disk with spiral pattern of pinholes (a so-called Nipkow disk) to generate in-plane optical scanning (figure 1.19). The high speed spinning movement is easier to realize than mechanical oscillations. Moreover in this system parallel measurements are achieved by use large number of pinholes employed simultaneously and use of arrayed detector. Modern version of spinning disk systems use microlenses coupled with pinholes to improve light efficiency of original system [48].

1.3.2 Dynamical modes of scanning

The interpretation of the data obtained by scanning microscope depends largely on the scanning method. So-called "raster scanning" is the basic method used in most scanning devices (for example in CRT displays). The raster scanning systems employ two orthogonal scanners to perform 2D scan. In this mode the first axis (fast-axis) is driven in sawtooth mode while the second one (slow-axis) is controlled in stepping mode (fig. 1.20). The raster scan is the simplest mode in terms of image reconstruction. The scanning is made with constant speed so that sampling is naturally defined on a 2D Cartesian grid. However, the true (linear) raster scan is not always most appropriate when a fast mechanical scanning is required. Sawtooth driving is often not compatible with fast scans because it requires linear displacement and rapid reset of the scanner position which is difficult to

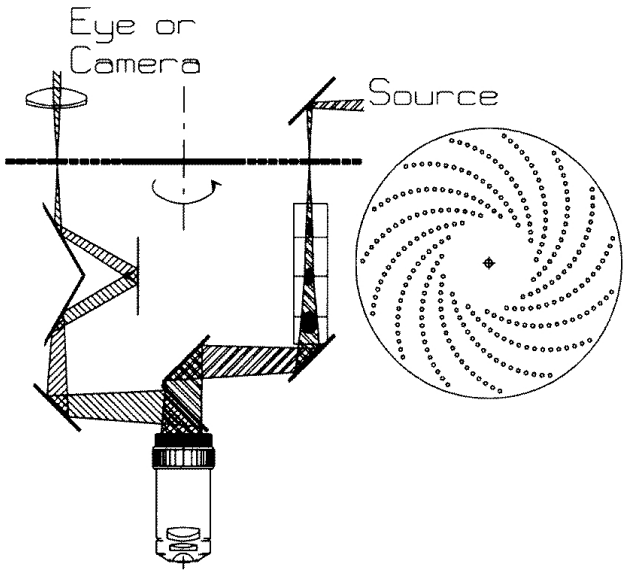


Figure 1.19: Spinning disk scanning microscope scheme - Rotating disk with pinhole pattern used to perform optical scanning. Spiral pattern on the Nipkow disk generates raster scanning in the image plane.

achieve in case of mechanical systems.

Two of the examples of optical scanners that generate sawtooth scanning is the rotating polygon mirror or Nipkow spinning disk described in the previous section. In other mechanical scanning systems it is often preferable to drive the scanners in the dynamic mode, i.e. in resonance. The resonance mode allows fast, stable and power efficient scanning. To be close to the simplicity of raster scanning only the fast axis is often driven at resonance whereas the second uses static stepping like in the raster mode (figure 1.21). The principal drawback of this scanning method is the non-uniform sampling of the image space along fast axis (red circles on the figure 1.21a)). To address this issue non-linear acquisition triggering or post-processing (interpolation of the data to the standard Cartesian grid) has to be performed. Still, this approach allowed reaching a speed of 12kHz for galvanometer scanners [49] and over 22kHz [50] in case of MEMS scanner where scanners that work in static mode (linear displacement) usually operates below 1kHz [51].

In the context of micro-scanners, resonant mode is preferable because it leads to more efficient mechanical performances of the scanning device. In consequence, it is often desirable to have not only fast-axis scanner working in resonance but also the slow-axis. The all-resonance 2D scanning does not speed up the overall system speed (2D) since the scanning speed is defined by the fast-axis speed only. In this case both scanners work in the resonances however their resonant frequencies have

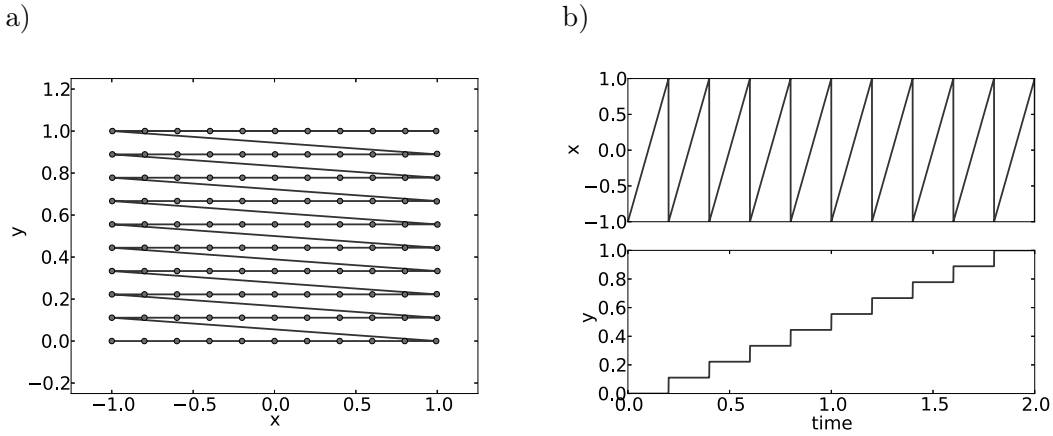


Figure 1.20: Raster scanning - (a) 2D image space scan pattern (line) and sampling (circles) and (b) $x(t)$ and $y(t)$ displacements curves.

to be different. The result of superposition of two sinusoidal movements are Lissajous figures [52]. In this case scanning path is much more complex than in the cases considered before since sampling is nonuniform in both directions (figure 1.22). However, since scanning pattern in both directions is known *a priori* 2D image can be reconstructed in similar manner as in the case of raster scanning mode. This "all resonance" mode makes use of maximal performance of MEMS-based scanners [53]. And as it was demonstrated by several authors [17, 54, 55, 56] that technique can be used for miniaturized confocal microscopes. The most important advantage of Lissajous scanning method is simpler control of the actuators, i.e., driving and position readout of the scanners. Because driving in resonant mode is achieved by single tone sinusoidal signal, the source takes a form of simple sine generator. Moreover, sinusoidal movement of the scanner is often a natural dynamic mode of the mechanical construction of MEMS scanners. This means that feed-back control (closed-loop control) is not necessary and position readout can be largely simplified [57].

1.4 MOEMS for confocal microscopy

Era of Micro-Electro-Mechanical Systems (MEMS) has started during the sixties when active mechanical functional blocks were added to electronic circuits [58]. From then, various mechanical microsystems were demonstrated like accelerometers, gyroscopes and pressure sensors [59]. Later, microsystems for light modulation have been demonstrated [60, 61] and Micro-Opto-Electro-Mechanical Systems (MOEMS) were introduced [62]. The MOEMS allowed to integrate optical

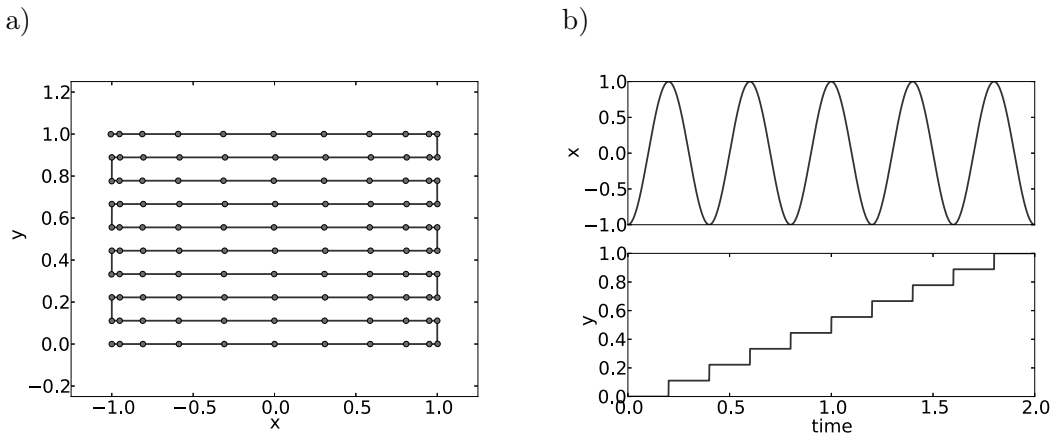


Figure 1.21: Resonant scanning - (a) 2D image space scan pattern (line) and sampling (circles) and (b) $x(t)$ and $y(t)$ displacements curves b).

functionality to the microsystems within the specific MEMS fabrication technology, which is different from the so-called optical-MEMS where optical elements are included to the device in a separate assembly process. The integration of optics with micromachining has lead to miniaturization of various optical devices like interferometers [63], spectrometers [64] and tunable filters [65, 66, 67].

Another family of microsystems are the fluidic-MEMS. Microfluidics has been developed in parallel to the main branch of MEMS. In most cases microfabrication was limited to channels generation where active components (pumps, detection systems) were laboratory scale [68, 69, 70]. Currently, microfluidics is often combined together with MOEMS to form the Lab-on-Chip or microTAS (Total Analysis Systems) [71, 72, 73].

1.4.1 Wafer-level microfabrication

The MEMS term is not only related to miniaturization but also to the fabrication technology. From the origin, fabrication of MEMS is based on wafer processing. The structures are made by etching, layers deposition where pattern transfer is made by means of (photo)lithography.

The wafer level approach allows the so-called "batch fabrication", which means parallel production of many (hundreds to thousands) devices at the same time. This parallelism is the main advantage of MEMS over traditional micro-devices made with classical methods like micro-milling where each device is fabricated separately (serial fabrication). The most common wafer processes are based on the monocrystaline silicon substrates. Silicon is the material most used in MEMS

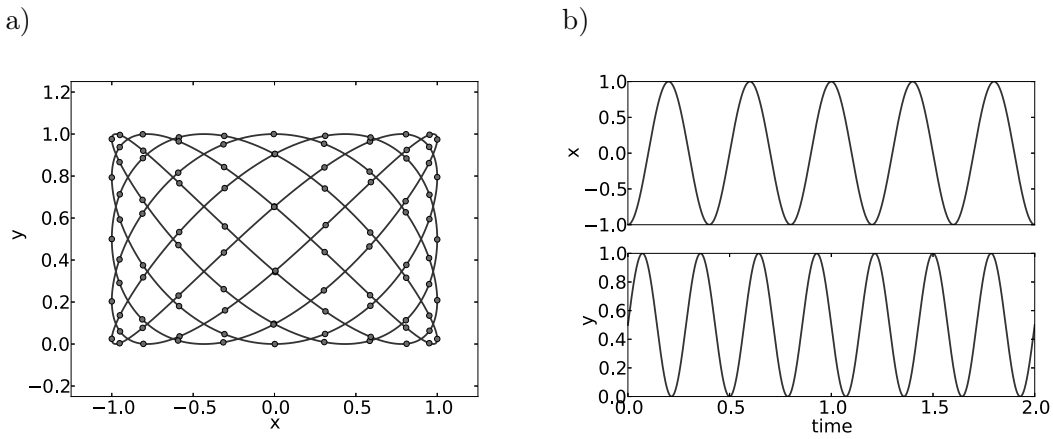


Figure 1.22: Lissajous (2D resonant) scanning - (a) 2D image space scan pattern (line) and (b) sampling (circles) a) and $x(t)$ and $y(t)$ displacements curves.

technologies. It has a well established micromachining technology and very good electric, thermal and mechanical properties. As a many MEMS technologies, silicon as a principal material is directly inherited from the electronics industry. In integrated circuits (IC) industry silicon was chosen as cheap and easy to process semiconductor material, however having good mechanical properties [74] allowing its use as a base material for mechanical devices. Moreover electronic industry developed a large scope of silicon processing techniques e.g. isotropic and anisotropic wet etching, plasma etching, thermal oxidation [75].

1.4.2 Integration, assembly and packaging

The important challenge in MEOMS design and fabrication concerns their assembly and packaging. The assembly is a process of physical positioning and connecting of all components of the microsystem. In the context of wafer-level processing, assembly tends to be replaced by the integration of the system components. This means that the different components are fabricated on the same substrate (by different but compatible processes) and all necessary connections are made by means of microfabrication processing so that there is no need for elements assembly. Only components that cannot be fabricated within system wafer level processing work-flow need to be assembled.

The packaging is the process of interfacing, sealing and isolating the system from environment. From one point of view, microsystem has to be protected from the environment (moisture, dust) and from the other, it has to be connected to the world. Interfacing takes the form of electrical

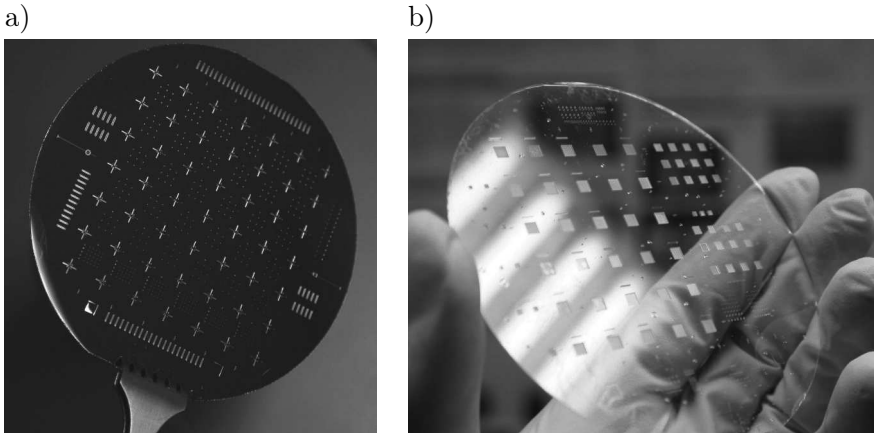


Figure 1.23: Wafer-level microfabrication - Components of the system are fabricated on the substrates much larger than generated elements (typically used wafers has 4,6,8 inches diameter). On the single substrate many elements can be generated, basic material used is silicon however for different transparent materials can be also used when optical properties are important. (a) concave micromirors generated by wet etching of silicon and (b) arrays of microlenses generated in glass.

connections (inputs/outputs) and e.g. optical windows that are necessary for most of MOEMS. The sealing or encapsulation of the device is also necessary to ensure reliability of the devices independently of the environment. The MOEMS packaging is a challenging task because performance of the device often strongly depends on the package construction [53].

Although, assembly and packaging seems straightforward in the case of macro-devices, it is in context of microsystems the bottleneck for industrialization of many microsystems. It was shown that assembly, packaging and testing of MEMS devices often generate more than 70% of their total cost [76, 77, 78]. The important conclusion is that packaging and assembly of MEMS have to be considered from the beginning of the system design, and when it is possible favor integration and wafer level approaches.

As many MEMS technologies originate from microelectronics the assembly and packaging used micromechanical systems is often very different than one used in the case of integrated circuits. The wafer level assembly and/or packaging technologies for micro devices such as pressure sensors, accelerometers or gyroscopes was successfully applied. However, in the context of systems including also micro-optical components, assembly tolerances and packaging methods are often not adequate. Indeed alignment of optical components require precise positioning and external package has to include optically transparent port. From this perspective, the most desirable method for building

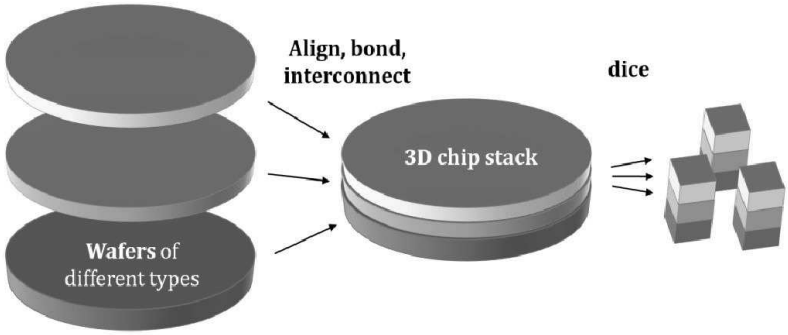


Figure 1.24: Philosophy of wafer-level assembly - The components of the microsystem fabricated on wafer substrates (possibly with different materials) are aligned and bonded into a vertical multi-wafer stack. The bonding process can realize electrical connections and provide hermetic package of fragile elements. The final dicing step separates many systems fabricated on wafer into independent devices.

the system is to rely on the high degree of integration of whole device i.e. wafer-level assembly and packaging. However this approach leads to constraints onto the design and materials used to build the system.

1.5 Miniature Confocal microscopes: State of Art

1.5.1 Motivation of miniaturization: Why miniature confocal microscope?

Confocal microscopy is a powerful imaging technique that has gained popularity in scientific and industrial communities. In particular, confocal microscopy is an everyday characterization tool in the life science and material science.

As it was described before confocal systems are based on point light source and point detection. Consequently, illumination as well as detection can be performed by discrete opto-electronic components. In the context of miniaturization, the use of these discrete components allows higher degree of system size-reduction. The point illumination can be realized by a single laser diode without need of complex illumination system. The same principle applies to the detector, for which single photodiode can be used. The latter is not only smaller but can be much more robust (in terms of sensitivity, speed, internal noise or dynamic range) than arrayed detectors (image sensors) like CCD or CMOS cameras [79, 80] used in conventional wide-field imaging systems.

Today opto-electronic components used within MOEMS are usually fabricated separately and have to be assembled during a separate step. Important trend in the MEMS/MOEMS community is the direct integration of electronics within MEMS [81, 82]. Recently, Huang [83] presented sensing microsystem that integrates polymer micro-optics (microlenses, mirrors) fabricated on a substrate where matrices of avalanche photodiodes were previously generated. The integration of laser source within MOEMS was also demonstrated. In [84], authors presented microlens scanner that was collectively fabricated on top of VCSEL's. These two examples show the potential towards the direct integration of optoelectronic components within MOEMS that can lead to high degree of miniaturization of confocal microscopes. In particular, MOEMS technologies represent a large potential for the implementation of miniature confocal microscopes, putting together the potentials of micro-optics, opto-electronics and MEMS.

The point-by-point image formation principle from the other side requires miniature scanning systems. The MEMS technology developed in last decades has made possible strong miniaturization of micro-actuators that can be used for construction of such miniature optical scanners. MEMS in the form of gyroscopes, accelerometers, scanning mirrors have reached the market and have proved that MEMS can replace traditional fabrications methods. In the field of beam steering, MEMS mirrors have started to replace one of the classical method used for beam scanning i.e. galvanometric mirrors. In particular, micro-mirrors with controlled tilt angle can be actuated by either electrostatically [40, 41, 85], magnetically [86, 87], thermally [88] or piezo-electrically [89, 90] generated forces. Whatever actuation mechanism is employed, micro-devices have inherent advantages over classical macro-devices. The first obvious advantage is clearly the potential of miniaturization, since conventional fabrication technologies are characterized by a limit of size, below which performances of the devices decrease. Secondly micro-mechanisms inherently have low-inertia, it is then easier to generate high speed movement with smaller devices than with larger system. Finally, the third important advantage lies in the technology of MEMS fabrication: wafer-level processing makes possible parallel fabrication of MEMS devices. The so-called batch fabrication can lead to a significant decrease of cost that often is the most important reason for migrating to MEMS-based devices.

1.5.1.1 Applications of miniature confocal microscopes

Confocal microscopy is very often applied in life sciences, however classical confocal microscopy used in biological research are bulky, cumbersome and expensive systems. The 3D visualization of biological specimen on the cellular level that can be achieved by confocal microscopy is especially

attractive when it is performed *in-vivo*. The *in-vivo* imaging has a particular interest in medical diagnostics and in fundamental biological research. The diagnostics targeting devices aim to investigate the living tissues. The confocal systems already proved its usability in the research and diagnosis of cancerous pathologies of skin [91, 92], ovary [93] and colon [94]. The confocal imaging is also used for cornea pathologies diagnosis [95, 96]

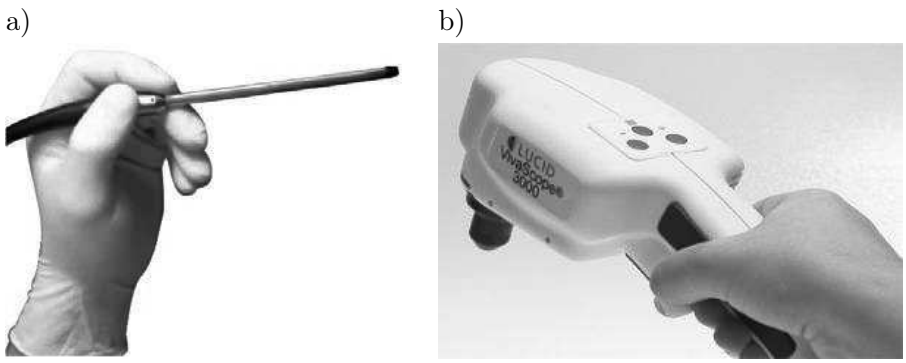


Figure 1.25: Handheld confocal microscopes - Two examples of miniaturized confocal systems already present on the commercial market: a) OptiScan FiveI [97] and b) Vivascope 3000 [98].

Two different types of systems are considered for this task. The first ones are the endoscopic systems which can inspect internal parts of the organism. Endoscopes are instruments which takes the form of a small head that can be directly introduced into the body to have access to the interested tissue. The head of the endoscope needs to be as small as possible to minimize the invasiveness of the method. The main approach employed for the endoscopes construction is usually the separation of the active part of the system (scanning/source/detection) from the part that is actually inserted to the living organism. This approach allows to miniaturize only a part of the system whereas the active part can remain bulk. Most of endoscopic devices are thus fiber-based systems.

The second family of devices that target *in-vivo* imaging are the systems imaging the external tissues of the living organisms. The most common objects under investigation are skin [98, 99], cornea [96] or tissues that can be surgically exposed for the time of investigation [100]. One of the aim of these types of devices is also diagnosis of pathological changes of external human organs (skin cancer, cornea pathologies). Figure 1.25 presents two examples of commercial handheld confocal systems used for *in-vivo* investigations.

Another application of portable imaging instruments targets the fundamental biological research. Confocal microscopy is then used to investigate functioning of living organism on cellular level.

Direct *in-vivo* monitoring of cell behavior is crucial method in many fields of life sciences like: cancer studies [91], drugs development and testing [101], brain studies[100]. For this type of investigation, miniaturization allows more versatile use of the instrument, since, in most cases portability and simplicity of use is a key factor. Figure 1.26 shows examples of *in-vivo* research performed on animals, the first system (fig. 1.26a) is a laboratory-scale instrument, requiring attachment of the investigated animal to be delivered and attached to the instrument. The second system (fig. 1.26b) is a miniature system that allows the object of investigation to move freely during experiment. This system demonstrated the possibility to study correlations of rat behavior with brain activity on the neuron level [100]. However, miniaturization is not yet advanced enough and higher degree of size reduction is consequently needed to allow less invasive *in-vivo* imaging.

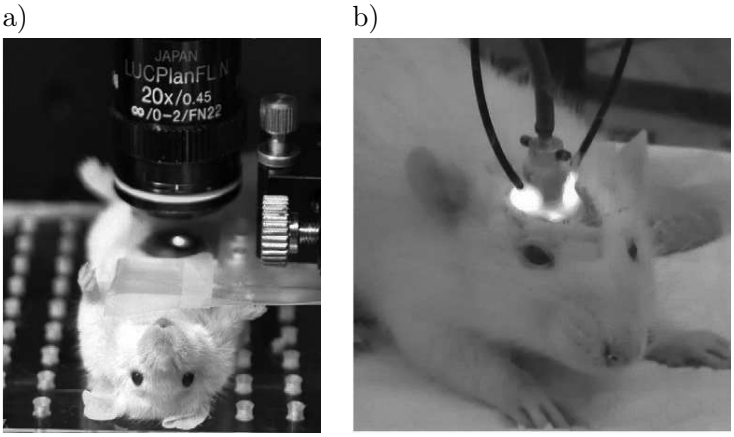


Figure 1.26: In-vivo imaging examples - (a) Standard bulk confocal system [101] and (b) miniaturized (two-photon) imaging system [102] used in *in-vivo* studies.

1.5.1.2 Beam scanning for optical micro-manipulation

The laser scanning used in confocal microscopy can have other applications than only sample imaging. As was demonstrated by Ashkin [103] light can be used for trapping the micro-particles. Since 90s optical trapping has grown into new domain of optics and already has found many applications in biological research and colloids study. The so-called optical tweezers was successfully used for cell trapping [73], sorting [104, 105].

The working principle of optical tweezers is the mechanical interaction between light and matter. The scattering of light by micro-particle effects in momentum redistribution which in consequence

effect in force exerted by light beam on the micro-object. However, the light pressure exist as general phenomena, its minute values the dynamical interaction can be visible only in specific situations. The most common system where optical trapping is performed is a colloidal solution in which micro-particles suspended in liquid are easy to manipulate because eliminated surface interactions and reduced effect of gravity [106]. The trapping effect is achieved within tightly focused laser beams when intensity gradients are large and effective force drag particle to the center of the focused laser spot (figure 1.27). The liquid environment used in the optical tweezers are well compatible with classical biological environments. Recalling that Lab-on-chip devices are often based on microfluidics we can notice that optical tweezers are naturally compatible with those systems. In consequence, coupling optical tweezers technology with Lab-on-chip can found many interesting applications [107].

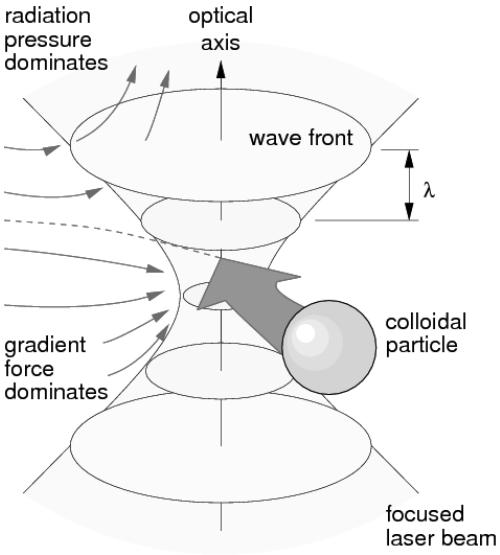


Figure 1.27: Optical tweezers - Optical force can appear when particle is close to nonuniform electromagnetic field, since the force is proportional to the gradient of the intensity the particle is attracted to the center of the focused beam [106].

As this work is focused on miniaturized confocal microscopy, it is easy to notice that laser scanning confocal microscope and optical tweezers system are similar systems. The confocal microscopy relies on fast 3D optical scanning of focused laser beam through the sample volume whereas optical tweezers system use 3D slowly moved focused laser beam to displace the micro-particles. In consequence, miniature optical scanner fabricated for LSCM can be used as well used as optical tweezers systems.

1.5.2 Fiber-optics based confocal microscopes

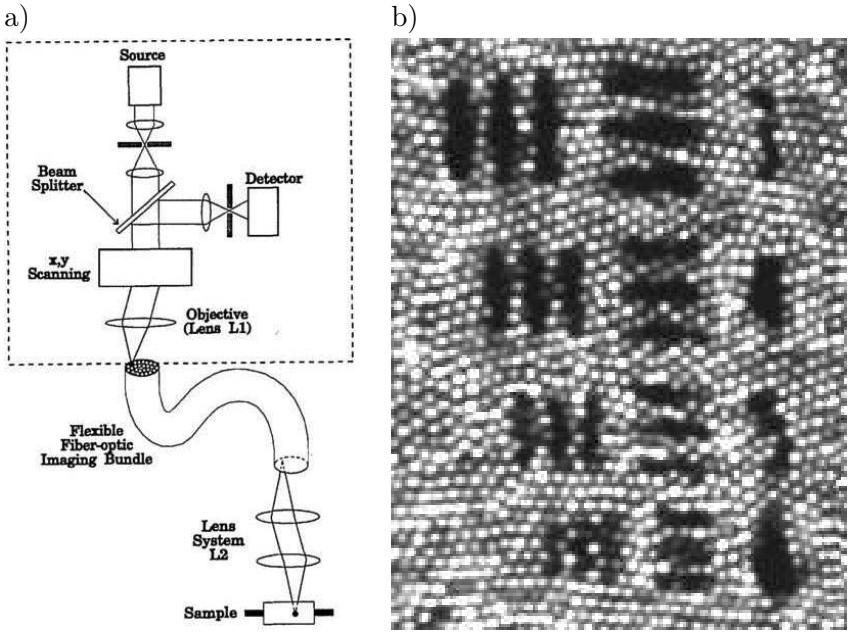


Figure 1.28: Fiber-bundle based confocal microscopy - (a) scheme of the system proposed in [108] the scanning system located at the one end of the fiber bundle (dashed box) can be located far away from the objective, which is located at the other end of the fiber. (b) specific image structure due to sparse location of the fiber in the bundle [109].

Optical fiber technology, developed initially for telecommunication industry has found many applications in the sensing devices [110]. Among those, fiber based endoscopic systems were introduced at first as simple image guiding devices, capable only of visualization of the surface of the specimen. The first confocal system based on a bundle of fibers was proposed by Gmitro and Aziz in 1993 [108], whereas theoretical analysis of confocal imaging using optical fiber was previously addressed by Gu *et al.*[111]. The system proposed by Gimitro and Aziz has become the base for most today's endoscopic confocal systems. The principal idea of this system is to separate the scanning optics from the imaging objective. Scanning system is located at the entrance of the fiber bundle whereas the miniature objective is placed in direct neighborhood of the investigated object (fig. 1.28). The core of the system is the fiber bundle, composed of tens of thousands of single mode optical fibers. Then illumination and scanning systems couple the laser light to an individual fiber for each scanned point. At the other end of the fiber, an objective lens image a point from the

fiber in the volume of the sample. Collection of the light from the sample is done by the same fiber than the one used for illumination. In principle the small core (4-10μm) of single-mode optical fiber can be used also as confocal pinhole [111]. However, since fibers are packed closely in the bundle a second physical pinhole is usually necessary to ensure that signal only from a single fiber reaches the detector (figure 1.28a). The number of sampling points in this imaging system is defined by number of fibers in the bundle. Moreover, finite distance between the fibers add sparse structure to the images obtained with the system (figure 1.28b).

The main advantage of this approach is that the miniaturization problem is bypassed, the only need for miniaturization is the final objective and not the main part of the system. However, fiber-optic scanning method allows only 2D scanning. If axial (in depth) scanning is also necessary, it has to be implemented into the objective location, i.e., on the objective side. The 3D scanning system with fibers-bundle used for 2D scan was realized [7, 97]. In those systems miniaturized axial scanner is added to the micro-objective so that objective lens can be axially displaced (figure 1.29).

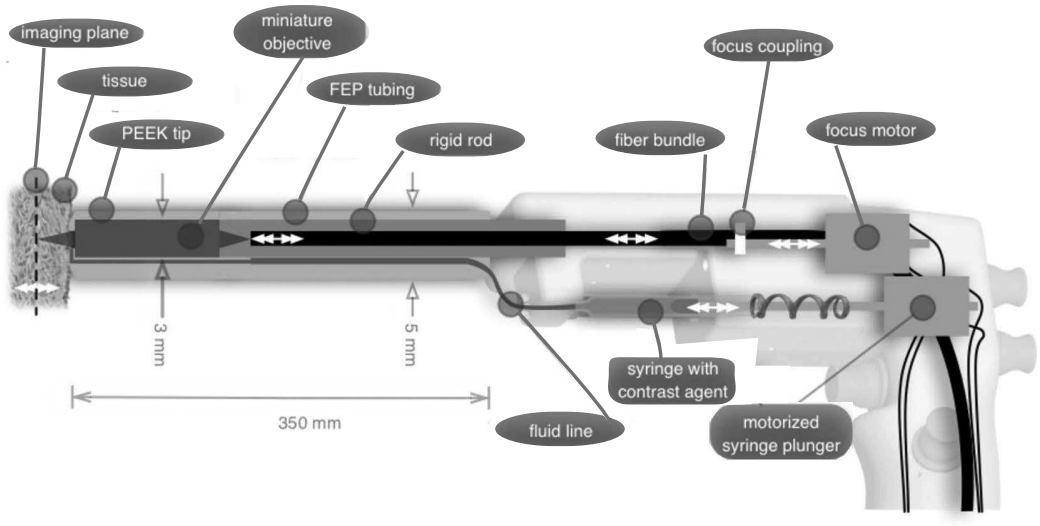


Figure 1.29: Confocal micro-laparoscope - Fiber-bundle based confocal microscope as laparoscope designed for early detection of ovary cancer, 2D scanning is achieved within fiber-bundle external scanning and axial scanning is performed in the objective by motorized lens [7]

1.5.3 MEMS confocal microscopes

MEMS applied were applied to confocal microscopy in two different ways. The first one is the use of micro scanners within classical (large) optical system. This approach allow modest miniaturization

of the system but in the important factor reduce its cost and dynamic performances. The second approach is based on joining MEMS with micro-optics aiming at construction completely miniature imaging system.

1.5.3.1 MEMS-enabled confocal microscopes

MEMS scanners presents an attractive alternative to the conventional scanning methods used in confocal microscopy. Because of improved dynamical characteristic and their high reliability, the microscanners tend to replace classical scanning techniques used in confocal systems.

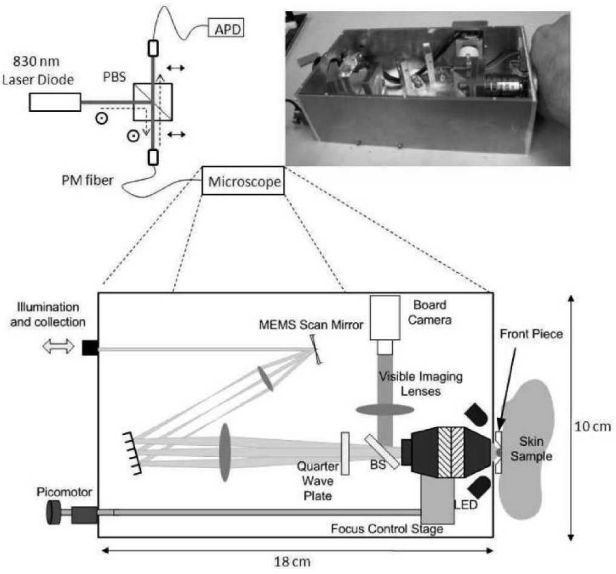


Figure 1.30: Confocal system with MEMS mirrors and bulk optics - Prototype of hand-held confocal system for skin imaging. Miniature in-plane scanning system made of bi-axial MEMS-mirror and axial scanning is performed via miniature stepper motor ("picomotor"), The use of classical optical components defines scale of the device ($18 \times 10cm^2$) [112].

Arrasmith at al. [112] constructed the confocal system that employs micromachined mirrors for in-plane beams scanning. Their construction uses standard optical elements and a stepper motor for axial scanning, that makes the system a hybrid setup combining micro and macro components (fig. 1.30). This types of construction uses MEMS scanner that allows size reduction of the system. This is achieved by simplification of the optical system thanks to two-dimensional scanning system achieved within single element.

The good dynamic performances and compactness offered by MEMS scanning systems important advantage of micro-fabricated devices is the cost. Since MEMS, as was discussed before are

fabricated by the wafer-level processes that can lead to important cost reduction if certain production volume is reached. In consequence, MEMS based systems can significantly reduce the cost of the device in regards to the one based on classical scanning systems.

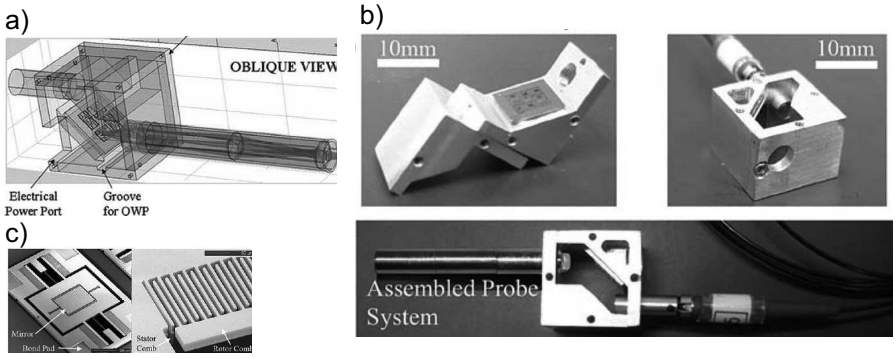


Figure 1.31: Confocal system with MEMS mirrors and miniature optics - Confocal microscope composed by MEMS scanning mirror and miniature optical components. Miniature metal package of the device require precise assembly of the miniature components used in the system. [113]

When the device compactness is targeted, miniature optics has to be employed. Kumar et al. [114] proposed a confocal microscope that uses miniature objective lenses together with MEMS scanning block allowing higher degree of compactness of the device. In this system commercially available miniature lenses were used (usually few mm in size glass molded lenses). The higher degree of miniaturization can be achieved when micro-components are used. Xie [115] proposed confocal system that utilized microlens as an objective. As shown in figure 1.32a, this system uses axial displacement of a microlens mounted on top of an actuator for beam scanning.

The lens scanner allows to simplify the optical system - optical path is linear in contrary to mirror based scanners where beam have to be deflected one or more times. This simplification makes easier and more tolerant the assembly and packaging of the microsystems 1.32b).

The simplification of the optical design always tend to help the miniaturization of the optical system. However, often this is made at the cost of the lower performance of the device. As was discussed before confocal system to perform 3D imaging require high NA objective. A single lens objective always suffers from geometric aberrations that decrease optical performance (image resolution). In practice, it is difficult to make aberration corrected miniature objective from a single lens.

Discussed before theta confocal system allows the use of lower NA objective or objective of low quality to achieve a good optical resolution in 3D. Ra and coworkers [116, 117] constructed

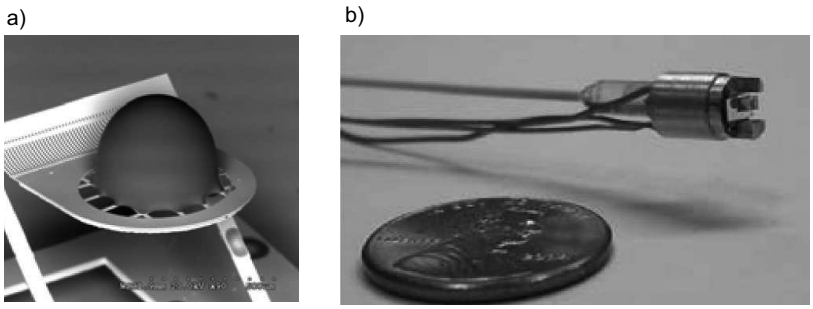


Figure 1.32: Confocal system based on micro-optical components - In this system the scanning is performed by movable microlens that is assembled on the micro-actuator a). The system is composed of only two optical components: collimation lens (pig-tailed to the fiber) and actuated objective lens. [115]

miniature theta confocal microscope. In their system the illumination and collection beams are separated and coincide only in the focal volume of the system (figure 1.33). The both beams use same objective (Single lens theta configuration) made of a single lens in the form of hemisphere. This configuration allowed to obtain high resolution $2 \times 3 \times 6\mu m^3$ ($\delta_x \times \delta_y \times \delta_z$) with relatively large field of view ($400 \times 260\mu m^2$) and working distance ($300\mu m$).

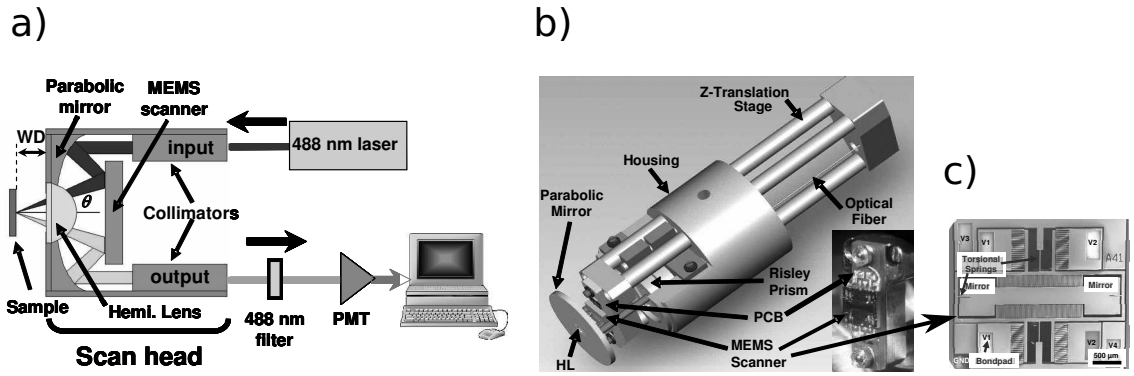


Figure 1.33: Miniature theta confocal microscope - Theta configuration applied in miniature confocal microscope, (a) scheme of the device, (b) model of the package, and (c) micromachined mirror used for implementation of 2D beam scanning. Axial scanning is performed by additional actuator - piezoelectric z-stage. [116]

1.5.3.2 MOEMS approach to miniature confocal microscopes

In the opposite to assembly-based construction principle of systems presented in previous section, the MOEMS approach used for construction of confocal microscope presents higher degree of integration of micro-mechanics and micro-optics. The principal aim of the MOEMS is to integrate the optical components into MEMS. To achieve this, the use of optics that can be fabricated on the wafer is essential [118]. The microlenses and micromirrors have been successfully generated by means of MEMS technologies. The most popular methods to generate microlenses are resist reflow [71, 119, 120], UV-polymer injection [121, 122] or combination of etching and molding techniques [123, 124]. The combination of micromechanical structures with wafer-level micro-optics have lead to creation of the dynamic opto-mechanical systems. In the MOEMS the micromechanical as well as micro-optical elements are fabricated within compatible processes using wafer-level approach. In the context of miniature confocal microscopy the combination of micro-actuators with wafer level micro-optics (microlenses, micro-beam-spliters) allows to avoid difficult assembly procedure increase the possible alignment precision and provide reliable system packaging withing system fabrication work-flow. The first example of a complete miniature confocal microscope made within MEMS

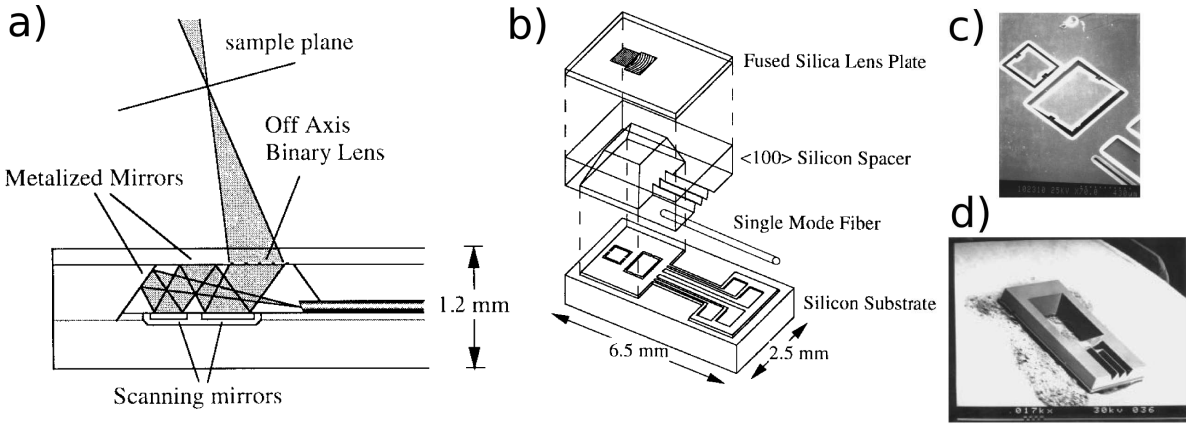


Figure 1.34: Mirror-based MOEMS confocal system - miniature system made by Dickensheets and Kino [125] high degree of miniaturization is achieved by simplification of optical system and specific zig-zag optical path.

only technologies was presented by Dickensheets and Kino [54, 125]. In their construction two electrostatically actuated mirrors realize beam scanning (fig. 1.34). The employed zig-zag beam path following the substrate plane reduces the size of the system. As an objective a diffractive microlens fabricated within fused silica by electron lithography and plasma etching. The microlens

substrate used also as a top lid for the microsystem providing its encapsulation. The single mode optical fiber is used as illumination/collection subsystem wheres fiber coupler located outside the system serve as a beam-splitter and redirect signal from specimen to the detector. The 2D scanning that employs electrostatically actuated mirrors fast axis can reach speed of 4.3kHz (resonance of fast axis) and 1.07kHz (resonance of slow axis) of the device allows field of view of $100 \times 100\mu m^2$. This miniature system achieve $1\mu m$ lateral and $11\mu m$ axial resolution while the size of the device is $6.5 \times 2.5 \times 1.2mm^3$.

Different architecture of a MOEMS confocal microscope was proposed by Kwon at al. [126, 127]. This system is characterized by vertical architecture 1.35 and non-conventional scanning system that base on actuated micro-lenses. The scanning system utilizing lenses displacement is more challenging because the in contrary to flat-mirrors lenses can introduce undesired optical aberrations to the optical system. For this reason authors reported relatively low resolution of their system as $3 \times 3 \times 37\mu m$ $(\delta_x \times \delta_y \times \delta_z)$ while used numerical aperture in their system was relatively high $NA \approx 0.3$.

However, this architecture assure linear beam paths and allow strictly vertical assembly of the system components. For this reason the vertical configuration is well adapted for wafer-level fabrication of complete microscope.

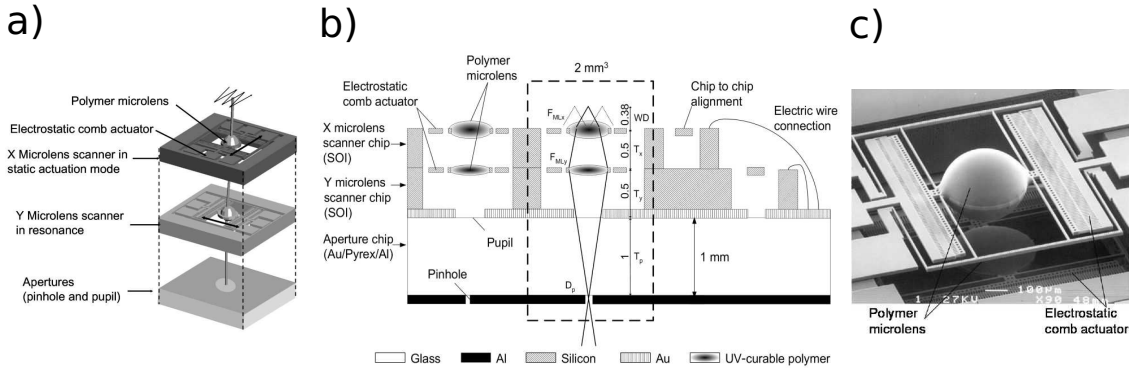


Figure 1.35: Microlens-based MOEMS confocal system - Alternative configuration of miniaturized confocal system utilizing stacked movable microlenses for beam scanning and focusing [127]

.

1.5.4 Review of performances of miniature confocal systems

Miniature imaging devices because of simplified optical construction and often lower quality optical elements used are less performant than classical systems. However, different architectures and different technologies used construction of different systems impact largely the performance of miniature confocal systems. In table 1.1 summary of optical performance of selected miniaturized confocal microscopes is presented. It is visible that low NA possible in micro-optical system leads to relatively low axial resolution in all presented system. Another effect of miniaturization is decreased field of view that is in most cases defined by the size to the objective lens.

SRC Reference	**Type**	**Technology**	**Resolution** XxY(xZ) [μm^3]	**FOV** XxYxZ [μm^3]	**WD** [μm]	**Objective size [mm]**	Comments
[128]	RL	MEMS mirrors	$0.82 \times 0.82 \times 13$	140×100	500	3.3	Classical optics used
[129]	RL	fiber bundle	$3.1 \times 3.1 \times 16.6$	340×340	74	1	GRIN Lens as the objective
[7]	FL	fiber bundle	$3 \times 3 \times 25$	$450 \times 450 \times 200$	0-200	3	*In vivo* ovary cancer diagnosis, GRIN lens as objective(fig. 1.29)
[97]	FL	fiber bundle	$0.7 \times 0.7 \times 7.0$	$475 \times 475 \times 250$	0-250	5*	Commercial product (Optiscan Five 1) for in-vivo animal imaging (fig.1.25a)
[98]	RL	miniature galvo	$1.25 \times 1.25 \times 5.0$	$1000 \times 1000 \times 200$	0-200	5	Commercial product (Vivascope3000) for dermatological application (fig. 1.25b)
[116]	FL,θ	MEMS	$1.7 \times 3.2 \times 5.8$	$400 \times 260 \times 90$	300	1*	MEMS mirror for in-plane scan, piezo for z-scan (fig. 1.33)
[130]	FL	Oscillating SMF	$0.87 \times 0.87 \times 11.5$	70×70	65	0.35	GRIN lens as the objective
[131]	RL	Magnetic MEMS	$3.8 \times 3.9 \times 10.7$	$0 \times 145 \times 190$	1400*	2.4	Aspheric lenses oscillating fiber for lateral scan, magnetic MEMS for axial scan
[125]	RL	MOEMS/SMF	$1 \times 1 \times 11$	100×100	600*	1	Binary off-axis μlens (figure 1.34)
[127]	RL	MOEMS	$3 \times 3 \times 37$	100×50	380	0.3*	Vertical μLens scanner (fig. 1.35)

Table 1.1: Optical performances of selected miniature confocal microscopes - RL-Reflectance, FL-Fluorescence confocal microscopes, θ configuration; * value estimated not specified by the authors.

1.6 Motivations

The aim of this work is to introduce a new conception and to demonstrate the different required technologies in order to develop a MOEMS confocal microscope. The main idea lies in the joining of classical MEMS technologies along with wafer level microoptics to produce complete optical imaging microsystem. The wafer-level processing scheme does not allows only potentially cheap mass production of such devices but also generation of dense arrays of microscopes allowing enlarging field of view or perform parallel measurements. Our approach is based on the need of integration of the fabrication, assembly and packaging steps on the wafer-level processing scheme. Joining all production steps within classical MEMS work-flow requires a specific design of the considered system. In here we propose specific optical design that takes into consideration the system encapsulation, the vertical integration, the electrical connections; and at the same time, allows a high degree of miniaturization and array-ability of the device.

The presented work was performed in the frame of DWST-DIS project. DWST-DIS - Development of multi-Stacking Technologies for Display and Imaging micro-Systems. The aim of the project is the development of MOEMS technologies specific to micro-optical systems. The stress was made onto wafer-level vertical integration and packaging. The project is realized by two institutes FEMTO-ST responsible for building blocks of the system (optical elements, actuators) and Franhoufer-ENAS that was working on integration of the system. The design of the system was largely defined by technological constraints mainly the integration feasibility and actuators interfacing.

2

Optical Design

The ultimate aim of the project is the construction of a compact, miniaturized, beam-scanning, reflectance (or fluorescence-based), confocal microscope. The miniaturization of such system imposes not only scaling down of the elements composing the system, but also minimization of the number of components and simplification of their arrangement. In the scope of MEMS-based devices, the architecture of the device largely determines the fabrication flow that defines the price and thus the accessibility of the system. In this work, we are focused on a system that allows as much as possible the use of the advantages of parallel (wafer-level) processing. This is a step forward in respect to most of the miniaturized imaging systems existing today, where MEMS-devices are fabricated using different technology than the rest of the system. Indeed, as reviewed in previous chapter, many different miniature confocal systems were proposed in the literature but most of them are based only partially onto MEMS technologies and require assembly and packaging realized during different fabrication processes. In here, we describe the design of a complete[1] system that can be constructed within silicon MOEMS technologies. Moreover, the architecture of the system is conceived in a way that allows the vertical wafer-level system fabrication. The main advantages of this approach for system construction are high level of miniaturization, array-ability and batch fabrication that result in low-cost of fabricated system in case of high volume production.

The main constraint of the vertical architecture of the system is the transmissive scanning design that requires adequate design of the optical train. The most common beam scanning method, based on beam deflection using a mirror scanner, cannot be easily adapted to the vertical architecture. Consequently, the discussed system is based on the 3D-beam scanning where the beam steering is achieved by transversal and axial microlenses actuation.

[1] excluding electronics and source

2.1 Design Specifications

In addition to the vertical architecture that is defined by the system fabrication philosophy, the main points of interest in the construction of the confocal microscope are: scanning volume (3D field of view), resolution (also in 3D space) and working distance (WD), thus, for this specific system, we need to target the following specifications: maximize scanning zone, maximize resolution, and consider reasonably large working distance (for easier encapsulation).

Another important constraint resulting from the wafer-based fabrication principle is the alignment accuracy. On the one hand, lateral alignment is achieved at the wafer-scale by the precise (in the order of one micron[1]) pattern transfer by photolithography and wafer to wafer bonding [74]. On the other hand, the axial positioning of the system components is set by the substrates (wafers) thicknesses. The latter are more difficult to adjust and control, since, for example, wafer to wafer thickness dispersion can reach $20\mu m$, standard wafer TTV: 5-10μm, and wafer bow can be as high as $40\mu m$. Thus, it is important to release the tolerances on the axial positioning of the optical elements wherever it is possible.

2.1.1 MEMS-based system

The scale of the MEMS devices specifies the dimensions of used components as well as the possible distances between them. From the point of view of optical design (OD), the possible sizes and accessible space for the positions of the optical elements are very important. The considered system uses MEMS actuators (figure 2.1) as the active parts of the scanning system. The actuators are usually limited in size so that the payload to be displaced remains as small as possible, especially because the speed of the system is highly dependent on the mass of the elements placed on the micro-device. In practice, these elements can be efficiently actuated with MEMS actuators on ranges up to several mm [134], however, when waver-level packaging is considered, mm-range displacement is often too large to package the system made within standard (relatively thin) wafers technology. In consequence, the optical system that need to be designed for wafer-level processing (from components to packaging) requires sub-millimeter optical elements.

[1] In practice the accuracy of elements alignment strongly depends on the architecture and technology sequence. In the case of structures generated on a single-side wafer reaches $1\mu m$, in case of double side wafer processing decreases to 2-3μm and for structure produced in the multiwafer approach further decrease to around of $5\mu m$.

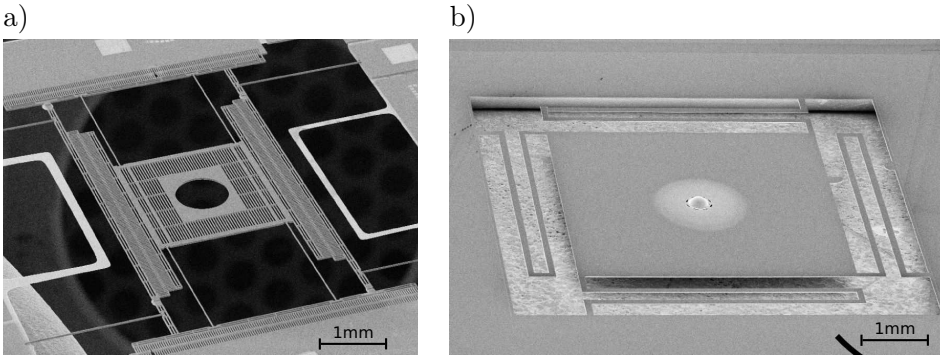


Figure 2.1: MEMS elements for μconfocal microscope - (a) comb-drive based actuator realizing in-plane (XY) displacement [132] (b) parallel-plate based actuator for out-of plane (Z) motion with integrated microlens [133].

2.1.2 Micro-Optics

This work is then focused on micro-optical devices. The fact of working with micro-optical components affect performances and tolerances of the optical systems, that are in some cases very different compared to the ones encountered in macro-devices. The different optical phenomena have different scale dependencies and it is then important to be aware of theoretical and practical differences between micro- and macro-optical systems [135].

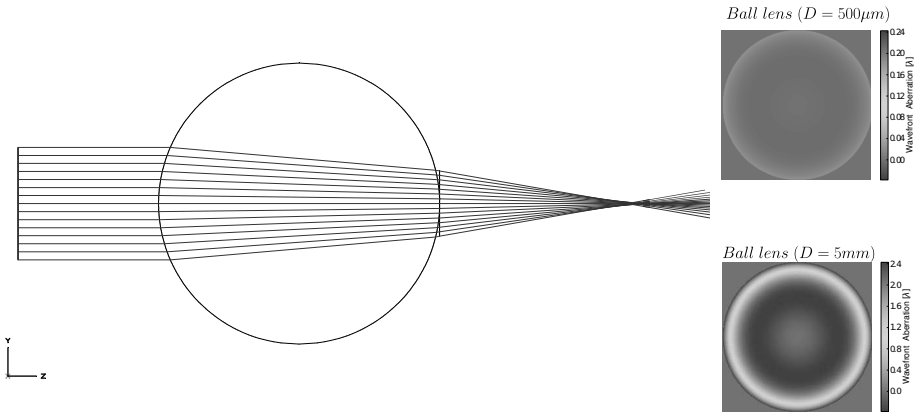


Figure 2.2: Ball lens as a focusing element: scale effect - The wavefront transformed by a ball-lens depends on the scale of the element. Two cases are compared in the two insets: $500\mu m$ diameter lens and $5mm$ lens. It is visible that wavefront is much more deviated in case of larger lens than in the case of a microlens. In both cases, NA of the system is fixed and is equal to 0.16.

The basic geometrical properties of optical systems (focal length, aperture size) are linearly dependent with scale. One consequence of linear scaling of metric parameters is that angles do not scale with the change of the system size. Consequently, NA is invariant regarding the scale of the system. As it was discussed in the previous chapter, limit of the optical resolution is defined only by NA and λ. Then, the resolution is not scaled together with the system size neither. However, an important scaling behavior appears when optical aberrations impact the system resolution. Wavefront aberration is a deviation of the wavefront generated by the optical system from a perfect spherical shape. Since the wavefront accuracy has to be compared to the wavelength rather than to the optical system scale, this leads to optical performances dependence with the scale of the system. One of examples of this scaling behavior can be seen with microlenses having the form of glass spheres and so-called "ball lenses" that are often used in micro-optical systems. Their size determines the optical performance of the optical system where they are employed. Figure 2.2 shows the behavior of two ball-lenses used as focusing elements. The two cases differ only by the ball-lens diameters that are equal to $500\mu m$ and $5mm$. It is clear that the aberrations are scaled together with the size, leading to much better performance of the smaller lens (figure 2.3)

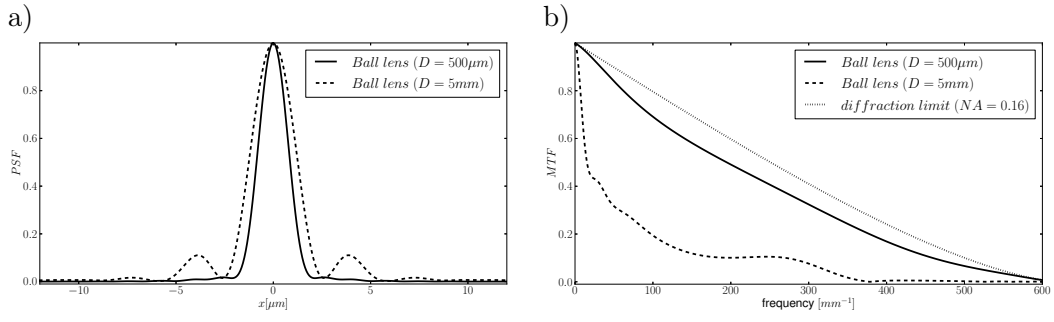


Figure 2.3: Performance comparison of two ball lenses of different scales - The intensity PSF of two ball lenses of different sizes a) and MTF b). Smaller lens has much better performance compared to the larger one and is close to the diffraction limit.

Another scale dependent important phenomena that needs to be considered in the design of micro-optical system is the diffraction. As it was discussed before, diffraction is responsible for the limitation of the optical systems resolution. In addition, another important aspect of the diffraction appears when small light beams are used. The effect of divergence caused by diffraction of geometrically-limited light beams limits the geometrical treatment of optical rays. In particular, collimated light beam spreads by itself with a divergence rate that depends on the size of the beam.

In general, smaller beams spread much faster than larger ones. The quantification of the diffraction effects is usually made with the use of the Fresnel number F:

$$F = \frac{a^2}{L\lambda} \tag{2.1}$$

where a is the beam size, L is the distance of propagation and λ is the wavelength. It is then possible to set limits between geometrical and wave optics in terms of Fresnel number[1]. Usually, it is claimed that geometrical optics are valid when $F >> 1$, which means that diffraction effects can be neglected and ray optics formalism is sufficient when the propagation length is much smaller than the ratio a^2/λ. When this condition is not valid, the diffraction-related divergence has an important contribution to the propagation of the beam. For example, beam of size $a = 100\mu m$ can be treated as a ray bundle on the propagation distance $L << 16mm$ for $\lambda = 633nm$, and for a beam size $a = 200\mu m$, the diffraction free propagation is $L << 63mm$. This simple example shows that the ratio between the beam size and the optical system length is an important parameter in the micro-optical system design.

2.2 Beam scanning by lens displacement

The scanning beam confocal microscope is based on the three-dimensional controllable displacement of focused light spot in the volume of the investigated specimen. The principle of the confocal microscope relies on the point-by-point image formation, where each point of the sampled volume is interrogated at a different time moment. Figure 2.4 schematically illustrates the aim of the investigated system. As it was discussed before, real beam scanning is actually performed in the XY plane in most of typical 3D imaging systems. The third dimension (Z) is then performed either by the sample displacement (object placed on a piezoelectric stage), or by the objective movement (changing effective distance objective-sample). In our system, axial scanning is also implemented optically.

2.2.1 Single Lens Scanning Relations

Beam steering investigated in this work employs lens displacement as the only means to displace the focused spot inside the sample. This approach was chosen because of its natural straight (linear)

[1]The Fresnel number is not the only parameter used to quantify the diffraction divergence. The Rayleigh range is often used as a quantification of the diffraction-less propagation length. Rayleigh range was defined for Gaussian beams as $z_R = \frac{\pi w_0^2}{\lambda}$ where w_0 is the beam-waist. Despite, slightly different definitions and a specific geometrical case (laser Gaussian beams), the main dependence is the same (a^2/λ) so that both formalisms are consistent.

geometry which is well suited for wafer-level fabrication work-flow. When considering a single lens, the focus position can be calculated using the lens equation 2.2:

$$\frac{1}{f} = \frac{1}{z_0} + \frac{1}{z_1} \tag{2.2}$$

where f is lens focal length, z_0 and z_1 are the distances (relatively to the lens) of the beam focus before and after the lens, respectively (fig. 2.5). In the single lens case, the axial (z coordinate

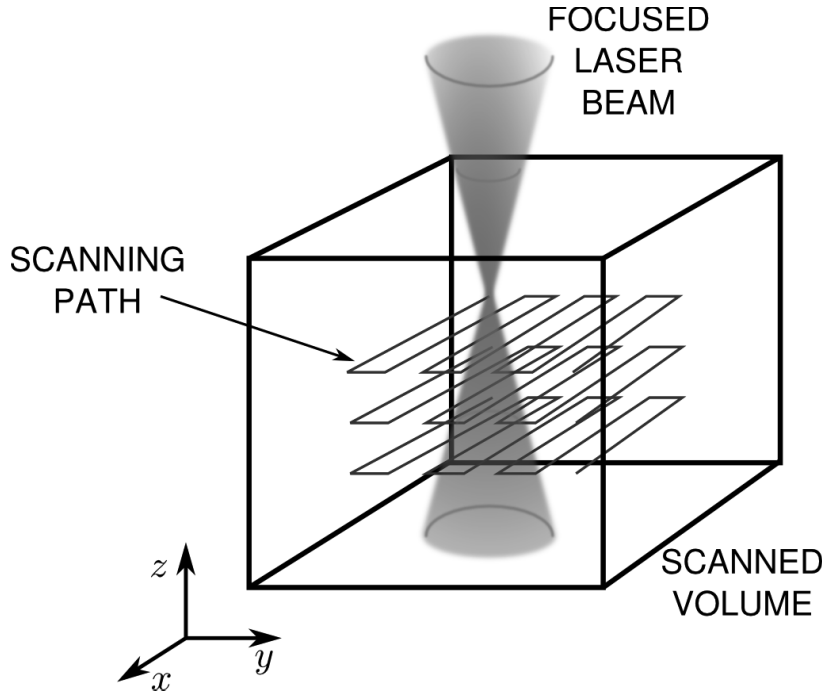


Figure 2.4: 3D scanning - Focused light spot moved inside a defined scanned volume.

- along optical axis of the system) displacement of the focused spot can be achieved with an axial lens displacement. Figure 2.5 presents two scenarios for axial focus point scanning by simple lens longitudinal displacement. In the first option (figure 2.5a), a collimated beam is incident upon the lens, so that the focused spot is located at the focal point of the lens. Thus, the lens displacement Δz results in the same focus displacement $\Delta_z = \Delta z$. This is the most common configuration when axial scanning is made with the system objective, however, one disadvantage is that objective lens (the last lens of the system) has to be movable. If non-collimated (divergent or convergent) beam enters the lens, the position of the focused spot strongly depends on the location of the divergence (or convergence) point of the input beam. The relations between lens displacement and position of the beam focus are plotted in figure 2.7a).

The lateral (direction laying in the xy plane perpendicular to the optical axis) beam steering can also be achieved by lateral displacement of a lens 2.6. As for axial displacement, collimated beam entering a lens that can move laterally produces the same lateral displacement of the beam focus $\Delta_y = \Delta y$. Similarly, the divergent/convergent incoming beam can produce an amplification of the spot displacement, depending on the position of the source origin position. An important case for lateral scan is the collimation configuration (fig. 2.6c). In this case, a focalized spot is not generated, instead, a collimated beam with lens-displacement dependent tilt is produced.

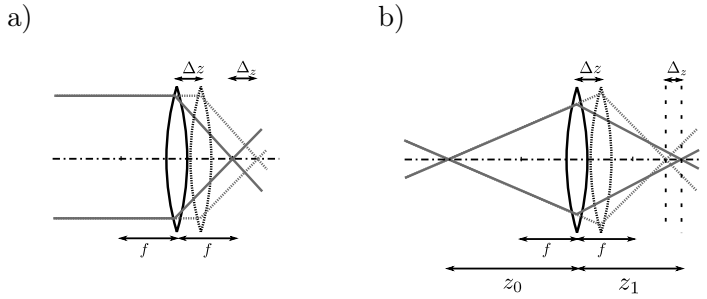


Figure 2.5: Axial scanning by single lens displacement - Single lens used for beam focus displacement in the case of (a) collimated and (b) divergent beam entering the lens. .

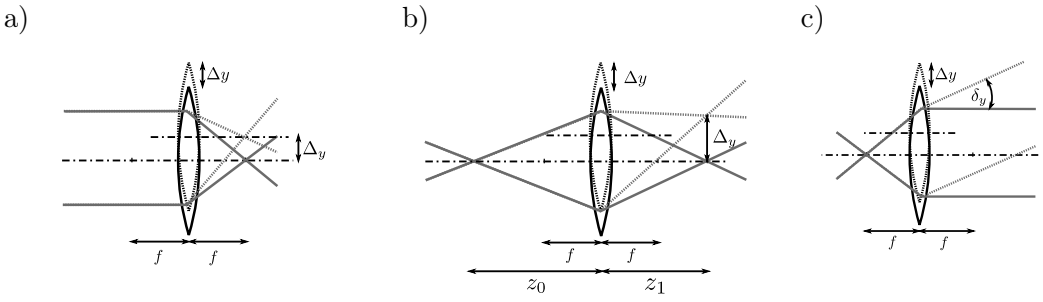


Figure 2.6: Lateral beam scanning by lens displacement - Single lens used for lateral focus displacement in the case of (a) collimated, (b) divergent beam entering the lens. (c) Special case when beam divergence is located in the focal point of the lens.

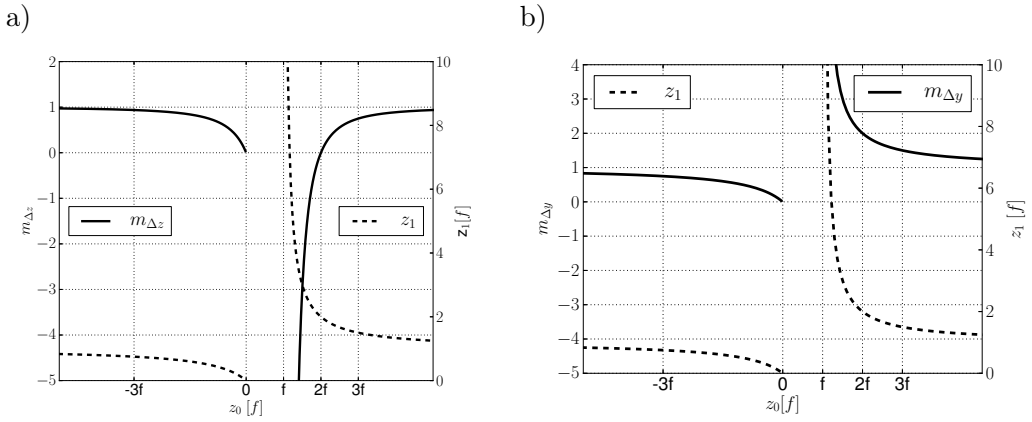


Figure 2.7: Single lens scanning relations - (a) magnification of lens axial displacement ($m_{\Delta z} = \frac{\partial \Delta_z}{\partial \Delta z}_{\Delta z \to 0}$) and (b) magnification of lens lateral displacement ($m_{\Delta y} = \frac{\Delta_y}{\Delta y}$) both in function of beam divergence (convergence) position (z_0), Resulting focus position is also indicated in both plots (dashed curve with scale on the right).

2.2.2 Afocal doublet for 3D beam scan

In order to achieve the 3D beam-scanning, 3D movement of the lens would be the simplest configuration, however, it is not the most suitable if system encapsulation is considered. Moreover, realization of 3D-motion of micro-optical elements is not an easy task. Only very limited types of micro-actuators are able to provide simultaneous 3D Cartesian movements [42].

In this work, we consider only one of many possibilities of implementation of 3D scanning by lens displacement. The base of the considered system is two separate movements of microlenses. An "in-plane" displacement (XY plane perpendicular to the optical axis of the lens), and a movement along the optical axis ("out-of plane", i.e. along the z-axis or the optical axis of the lens). Since those two movements cannot be applied to a single element only, two-elements scanning-system is considered for the generation of the 3D scanner.

Hence, the coupling of the two microlens/movements to obtain 3D scanning can be achieved in many different configurations. In here, we have chosen an afocal system composed of two lenses as a base for the 3D scanner . In such a system, a collimated beam enters the scanner, and axial or lateral misalignments in the system (provided by controllable lens displacements) result in decollimation or tilting of the output beam. This afocal doublet itself does not provide the focusing power if the incident beam is collimated and an additional focusing element is needed

to obtain real 3D beam-scanning: the focusing block (the objective). Moreover, a collimation block is also required if single element source is to be used. The scheme of two possible setups of the scanner working in the afocal configuration are presented on figure 2.8. The two systems differ by the scanners order. The first setup (fig. 2.8a), so-called Z-XY configuration, is made of the axial scanner (Z-scanner) located before the in-plane scanner. In the second system (XY-Z configuration), the scanners order is inverted (fig. 2.8b). The important advantage of such system is the incident/output nearly collimated beams that release axial positioning tolerances between the scanner and preceding/succeeding elements of the system. This is especially important in the wafer-based fabrication where axial positioning are usually set by the construction wafers of the building blocks. Moreover, if 3D scanner is used for, e.g. confocal microscopy, addition of optical elements to the system, such as beam-splitters or dichroic filters, can be simplified by the use of collimated beams.

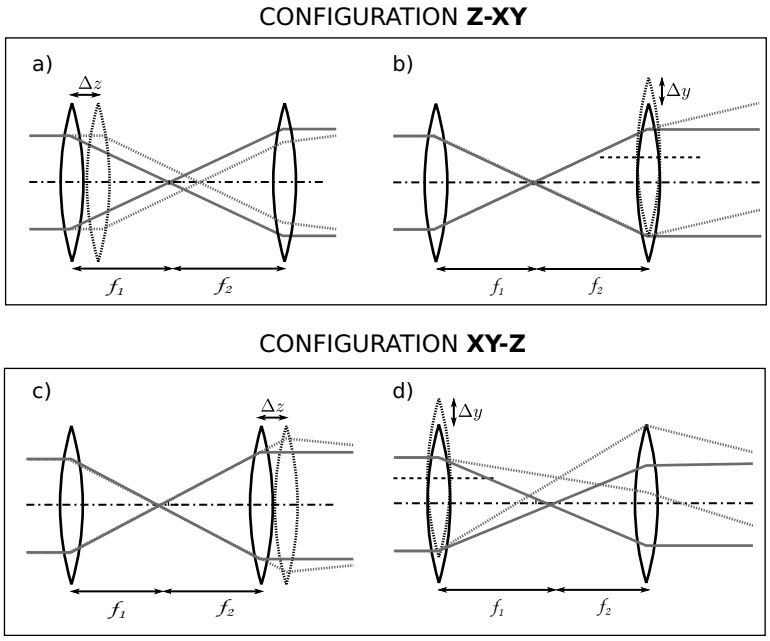


Figure 2.8: Afocal systems for 3D beam scanning - Two lenses separated by a distance equal to the sum of their focal lengths is used as a scanning system. The displacement of a lens along the optical axis a) and c) adds curvature to the output beam whereas lens lateral displacement b), d) produces a tilt of the output collimated beam. The two configurations are possible with different lens movement order. However, the latter influences the ray paths in the system, which means that the optical properties of the two setups are not equivalent on the level of scanning behavior and aberrations present in the system.

2.3 Four lens system for scanning and focusing

Consequently, the 3D scanning system, built around the afocal scanning-doublet, is composed of three parts: a collimation block used to collimate the light from point-like source, a scanning block, composed of the actuated lenses, and responsible for the beam-steering, and finally a focusing block, responsible for the generation of focused spot at the output of the system. Schematic design of the system is presented in figure 2.9.

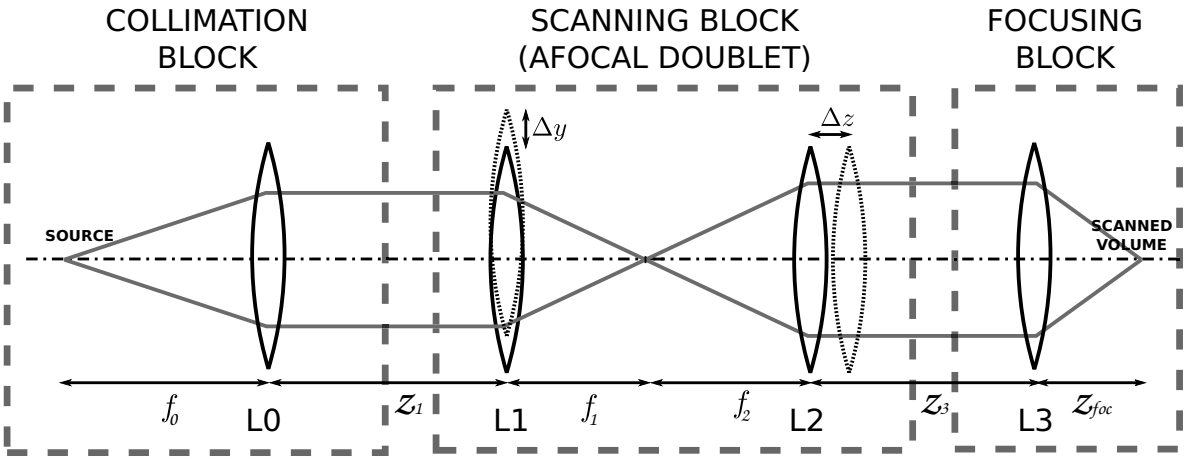


Figure 2.9: Layout of the 4-lens system - Collimation and focusing lenses added to afocal scanning doublet for 3D beam scanning. Two lenses located in the center of the system (i.e. L1 and L2) are movable so that L1 can be displaced in-plane (XY), and L2 can be moved along the optical axis.

The view of the complete system reveals the advantages of using an afocal system for the scanning function. The active part of the system (actuated microlenses) are located in the center of the system and can be easily protected from the environment. The light-path is relatively simple and since collimated beams are employed, tolerances on the distances are loosen. Moreover, collimated light allows also the presence of additional elements in the light-path without issues related to their angle dependence. This is especially important since we consider this scanner to be a part of the confocal microscope for which a beam splitter (difficult to design in case of divergent beams) has to be added to the system.

The scanner is thus based on two microlenses assembled onto MEMS actuators that can be independently moved for realization of the scanning block. The fragile micromechanical systems can be sealed in an hermetic package made of the other optical elements (L0 and L3) at each end.

In other terms, the collimation lens (L0) and the objective lens (L3) separate the fragile MEMS actuators used for microlenses displacements from the environment.

2.3.1 Paraxial Description - ABCD-EF formalism

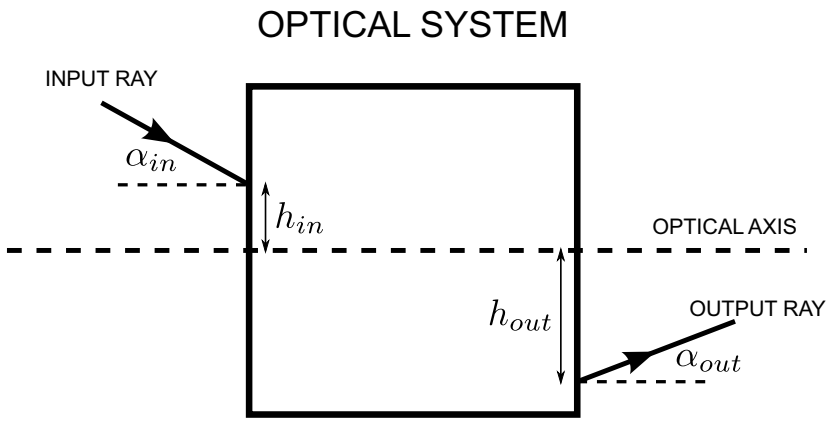


Figure 2.10: Illustration of ray transfer matrix - Input ray of coordinates α_{in}, h_{in} is transformed by the system described by transformation matrix M into output ray α_{out},h_{out}

The scanning performance of the proposed system has been analyzed with the ABCD-EF matrix formalism [136]. The method is a standard ABCD ray transfer matrix method extended to handle shift-tilt transformations of the optical components in the optical train. The standard ABCD ray transfer matrix that handles centered symmetric systems transforms the paraxial ray described by height h_{in}, and angle α_{in}. The output ray coordinates h_{in}, and α_{in} are expressed by equation 2.3.

$$\begin{bmatrix} y_{out} \\ \alpha_{out} \end{bmatrix} = \underbrace{\begin{bmatrix} A & B \\ C & D \end{bmatrix}}_{\mathbf{M}} \cdot \begin{bmatrix} y_{in} \\ \alpha_{in} \end{bmatrix} \tag{2.3}$$

where the coefficients in the transformation matrix $\mathbf{M}$: A, B, C, D are defined by the optical system under consideration. However, equation 2.3 can be used only in centered systems where ray coordinates are measured from the optical axis of the system. In the case of optical setups consisting in decentered or tilted elements, extended matrix formalism is used. The Equation 2.4

describes ray transformation in such system.

$$\begin{bmatrix} y_{out} \\ \alpha_{out} \\ 1 \end{bmatrix} = \underbrace{\begin{bmatrix} A & B & E \\ C & D & F \\ 0 & 0 & 1 \end{bmatrix}}_{\mathbf{M}} \cdot \begin{bmatrix} y_{in} \\ \alpha_{in} \\ 1 \end{bmatrix} \tag{2.4}$$

where additional matrix elements E and F originate from misalignments present in the optical system.

The matrix for the whole system $\mathbf{M_{sys}}$ is constructed from matrices describing each elements composing the system. As mentioned before, the system can be naturally divided into three parts: collimation block, scanning block and focusing block. Then $\mathbf{M}_{sys} = \mathbf{M}_{foc} \cdot \mathbf{M}_{scan} \cdot \mathbf{M}_{col}$. The matrix representing the scanning block, i.e. M_{scan}, can be expressed as a multiplication of matrices representing components of the block. As it was mentioned before, two scanner configurations are possible (figure 2.8). The ray transformation matrices for two scanning configurations are different and expressed by equation 2.5 for "XY-Z" scanning order, and by equation 2.6 for scanner with inverted scanner configuration ("Z-XY").

$$\mathbf{M}_{scan}^{(xy-z)} = \underbrace{\mathbf{M}_{\Delta z}\mathbf{M}_{L2} \cdot \mathbf{M}_{-\Delta z}}_{axially\ displaced\ L2} \cdot \mathbf{M}_{z_2} \cdot \underbrace{\mathbf{M}_{\Delta y} \cdot \mathbf{M}_{L1} \cdot \mathbf{M}_{-\Delta y}}_{laterally\ displaced\ L1} \tag{2.5}$$

$$\mathbf{M}_{scan}^{(z-xy)} = \underbrace{\mathbf{M}_{\Delta y}\mathbf{M}_{L2} \cdot \mathbf{M}_{-\Delta y}}_{laterally\ displaced\ L2} \cdot \mathbf{M}_{z_2} \cdot \underbrace{\mathbf{M}_{\Delta z} \cdot \mathbf{M}_{L1} \cdot \mathbf{M}_{-\Delta z}}_{axially\ displaced\ \ L1} \tag{2.6}$$

For sake of simplicity and to investigate the general behavior of proposed optical system, all lenses are modeled with thin lens approximation: $\mathbf{M_{lens}} = \left[\begin{smallmatrix} 1 & 0 \\ -f^{-1} & 1 \end{smallmatrix}\right]$, where f is the lens focal length. The free space propagation is described by $\mathbf{M_{z_i}} = \left[\begin{smallmatrix} 1 & z_i \\ 0 & 1 \end{smallmatrix}\right]$, where z_i is the propagation distance. The coordinates shift is $\mathbf{M_{\Delta y}} = \left[\begin{smallmatrix} 1 & 0 & \Delta y \\ 0 & 1 & 0 \\ 0 & 0 & 1 \end{smallmatrix}\right]$ ($\mathbf{M}_{\Delta z}$), where Δy (Δz) defines the element's shift perpendicular to (along) the propagation axis.

$$\mathbf{M}_{scan}^{(xy-z)} = \begin{bmatrix} \frac{\left(-\Delta z^2+\Delta z f_2-f_2^2\right)}{f_1 f_2} & \frac{\Delta z^2-\Delta z f_1+(f_1+f_2-\Delta z)f_2}{f_2} & \frac{\left(\Delta z^2-\Delta z f_1-\Delta z f_2+f_1 f_2+f_2^2\right)}{f_1 f_2}\Delta y \\ -\frac{\Delta z}{f_1 f_2} & \frac{(\Delta z-f_1)}{f_2} & \Delta y\frac{(\Delta z-f_1)}{f_1 f_2} \\ 0 & 0 & 1 \end{bmatrix} \tag{2.7}$$

$$\mathbf{M}_{scan}^{(z-xy)} = \begin{bmatrix} -\frac{(\Delta z+f_2)}{f_1} & \frac{\Delta z(\Delta z+f_2)+f_1(\Delta z+f_1+f_2)}{f_1} & 0 \\ \frac{\Delta z}{f_1 f_2} & \frac{\left(-\Delta z^2+f_1 f_2-f_1(\Delta z+f_1+f_2)\right)}{f_1 f_2} & \frac{dy}{f_2} \\ 0 & 0 & 1 \end{bmatrix} \tag{2.8}$$

From equation 2.7 and 2.7, we can extract the most important scanner properties. Firstly, the axial displacement of lens L2 leads to decollimation of the scanning block output beam. The focal length of the scanner $f_{scanner}$ is proportional to the inverse of axial lens displacement (eq. 2.9).

$$f_{scanner} = \frac{f_1 f_2}{\Delta z} \tag{2.9}$$

Secondly, the lateral displacement of the lens L1 provokes the tilting of the output beam such as:

$$\delta_y^{xy-z} = \Delta y \frac{\Delta z - f_1}{f_1 f_2} \tag{2.10}$$

$$\delta_y^{z-xy} = \frac{\Delta y}{f_2} \tag{2.11}$$

2.3.2 The scanning performance

The scanning performance is defined as the scanning range in all three dimensions and depends only on the scanning doublet and the objective lens (L3). From the total system matrix M_{sys}, we can get the "scanning equations", i.e. equations that define the displacement of focal spot as a function of the lenses displacement Δy, Δz and the system configuration f_i and z_i. The scanning performance are according to equations 2.12 and 2.13:

$$\Delta_z^{(xy-z)} = \Delta z \frac{f_3^2}{\Delta z^2 + f_2^2 + \Delta z(z_3 - f_2 - f_3)} \tag{2.12}$$

$$\Delta_y^{(xy-z)} = -\Delta y \frac{f_2 f_3}{\Delta z^2 + f_2^2 + \Delta z(z_3 - f_2 - f_3)} \tag{2.13}$$

The focused spot moves around the focus point of the objective lens (L3). Thus, the focus position is defined by $L3$ focal length and the displacement due to the scanner so that: $z_{foc} = f_3 + \Delta_z$. In the case of the inverse scanner configuration, scanning relations are slightly different (equations 2.14 and 2.15):

$$\Delta_z^{z-xy} = -\Delta z \frac{f_3^2}{\Delta z\,(z_3 - f_2 - f_3) - f_2^2} \tag{2.14}$$

$$\Delta_y^{z-xy} = \Delta y \frac{f_3\,(\Delta z + f_2)}{\Delta z\,(f_2 + f_3 - z_3) + f_2^2} \tag{2.15}$$

An important characteristic of the scanner is the non-linearity of the axial scanning (equations 2.12 and 2.15). The lateral scanning, according to the equations 2.13, is linear in Δy, however, it is

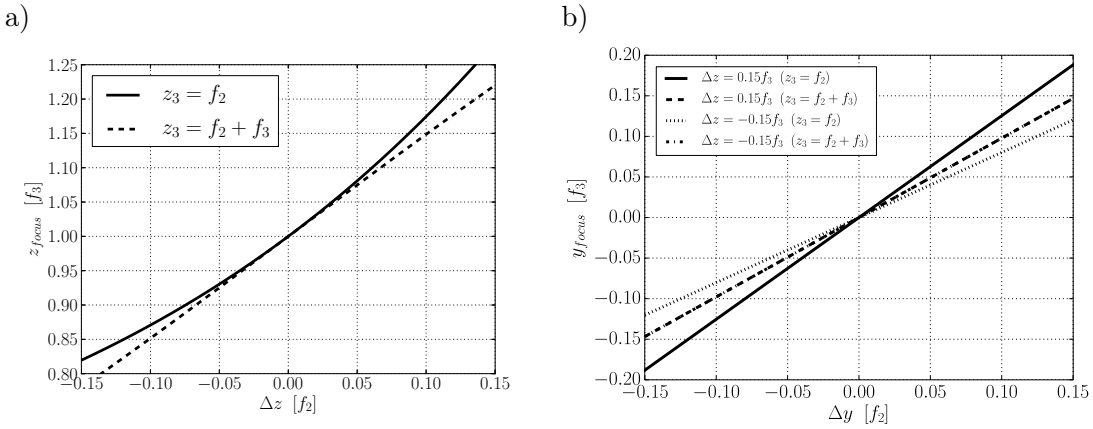


Figure 2.11: Afocal scanner paraxial scanning behavior - (a) nonlinear dependence of scanning in axial direction and (b) coupling effect in the case of simultaneous axial and lateral scanning (solid line). In the *Z-XY* setup, nonlinearity can be cancelled and coupling minimized when z_3 is chosen as $(z_3 = f_2 + f_3)$ (dashed line). (plot for system with $f_3 = \frac{3}{2} f_2$) .

also coupled to the axial scanning ($\Delta_y = y_{foc}(\Delta z)$). This effect defines the shape of the scanning volume. Then, in the perfect case, i.e. linear and not coupled, scanning would generate a scanning volume in the form of a cuboid. But, the nonlinearity and coupling effect leads to a scanned volume having a more complicated form (fig. 2.12). Then, it can be noted that it is preferable to set $z_3 = f_2 + f_3$ in order to minimize these effects (equations 2.12 and 2.15 and fig. 2.12), although complete linearization can be achieved only with the "Z-XY" configuration. Nevertheless, the scanning coupling and nonlinearity are of the second order, and then, simpler linear scanning relations can be written in the approximation of small lenses displacements (Equations 2.16-2.17) that holds for both configurations of the scanner system:

$$\Delta_z \approx \Delta z \left(\frac{f_3}{f_2}\right)^2 \tag{2.16}$$

$$\Delta_y \approx \Delta y \frac{f_3}{f_2} \tag{2.17}$$

It is visible that the scanning performance depends mostly on the ratio $\frac{f_3}{f_2}$ for both considered cases. Consequently, in order to amplify the scanning amplitude, f_3 should be chosen higher than f_2.

$$NA \approx \frac{h_3}{f_3} = \frac{h_1}{f_1}\left(\frac{f_2}{f_3}\right) \tag{2.18}$$

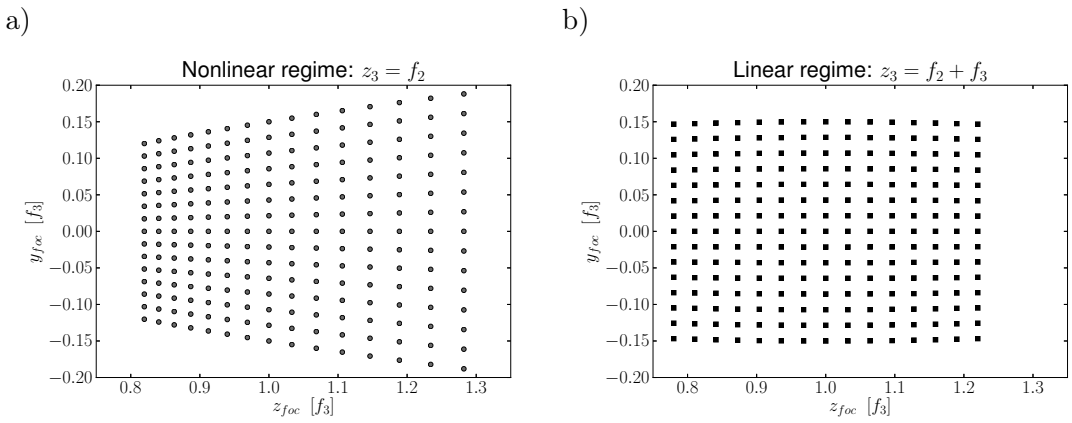


Figure 2.12: Paraxial prediction of the shape of scanning volume - Scanning zone (yz cross section) for the two discussed cases: (a) nonlinear regime ($z_3 = f_2$) and linear case ($z_3 = f_1 + f_2$).

However, resolution is defined by the system NA (eq. 2.18) which is proportional to $\frac{f_2}{f_3}$,i.e. inverse of the dependence of the scanning performance. This implies that is not possible to maximize the scanning volume and resolution at the same time[1] using only f_2/f_3 as parameters. Thus, the optimization of the system parameters have to be a tradeoff between the desired scanning zone and the resolution. In consequence, according to (eq. 2.18), the NA maximization with no decreasing of the scanning performance can be done by increasing the scanner input beam (h_1) and/or minimizing f_1 of the scanner. This, in practice, leads to maximization of the NA within the scanner doublet.

2.3.3 Conclusions of paraxial analysis

In the paraxial analysis aimed at analyzing the scanning performance, two possible configurations have been considered based on different scanners arrangements. From the optical point of view, the scanning properties of both systems are very similar. However, an important difference appears when the scanning doublet is coupled to the focusing block (figure 2.8). In the Z-XY configuration, the position of the beam center leaving the scanner follows the position of the XY scanning lens, whereas in the case of XY-Z system, the beam center does not change in the focal plane of $L2$ where only a tilt of the optical axis is generated. This effect is expected to lead to a more efficient, and optically optimal, use of the focusing block in the complete system. This is because, when the

[1] we can notice that this a common rule also in classical microscopy where improvement of the resolution usually leads to a decreased field of view.

$L3$ lens is placed near the focal plane, scanning leads to only a change of the incident tilt without any lateral shift of the illuminated area onto the scanning block.

Moreover, from the perspective of micro-fabrication, system construction and integration depends strongly on the scanners order. In the considered system, micro-actuators are enclosed between collimation and focusing blocks, then the electrical connections required for actuators control have to be implemented through the wafers of both micro-mechanical systems. Since the XY-scanner is more complicated and require more electrical connections than the Z-scanner, the XY-Z order allows minimization of the number of electrical through wafer connections. As it was discussed before, one advantage of Z-XY configuration is the possibility of linearization of the scanning zone, that is not entirely possible within XY-Z setup. However, although complex shape of the scanning zone seems inconvenient, it can be acceptable if appropriate data post-processing (or scanners control) is applied to remap the scanning zone to the Cartesian coordinate system. In consequence, the following optical implementations are focused on the XY-Z configuration only.

The paraxial analysis provided analytic formulas for the scanning performance as a function of optical elements parameters. A general rule to obtain good scanning behavior (i.e. small lens displacement leading to large focus one) is the seek of a high numerical aperture within scanning lenses (in the afocal scanning doublet). This conclusion corresponds to the observations of Schwertz *et al.* [137]. Moreover, the system NA should be maximized to obtain a good optical resolution (spot size) on the output of the system (including also the focusing block).

2.4 Scanner implementations

The system performance is defined by the amount of aberrations present in the system. Thus, a high NA with minimum of aberrations is required to reach high resolution. In general, the on-axis aberrations (mainly spherical aberrations) will limit the accessible NA of the system, and off-axial aberrations (coma, astigmatism) will limit the scanning (lateral) range of the system. In the following, the aberrations analysis and design optimization is performed within ZEMAX package.

2.4.1 First demonstrator: ball-lens based scanner

The first investigated system is based on discrete micro-optical components that are assembled onto the micro-actuators by means of pick-and-place principle.

This hybrid approach (wafer level fabrication and discrete microlenses) was aimed at testing the system integration technologies in parallel to the development of, on the one hand, an optical

design better adapted to batch fabrication principle, and on the other hand, dedicated components required for the optically optimized system. In consequence, the first considered system is based on commercially available ball-microlenses, assembled and bonded into the MEMS by means of local adhesive or thermal bonding [138].

Indeed, the available elements that can be used in our system only exist in limited geometrical forms. The most common microlenses that are commercially available are then so-called ball-lenses and takes the form of spheres. This type of elements are mostly used in fiber optics systems to couple the light into fibers or for fiber to fiber interconnections [78]. Because of their well-defined geometry and their good optical quality, they were already employed in optical MEMS in embedded fiber switches [139, 140] or as a simple high NA objective [141].

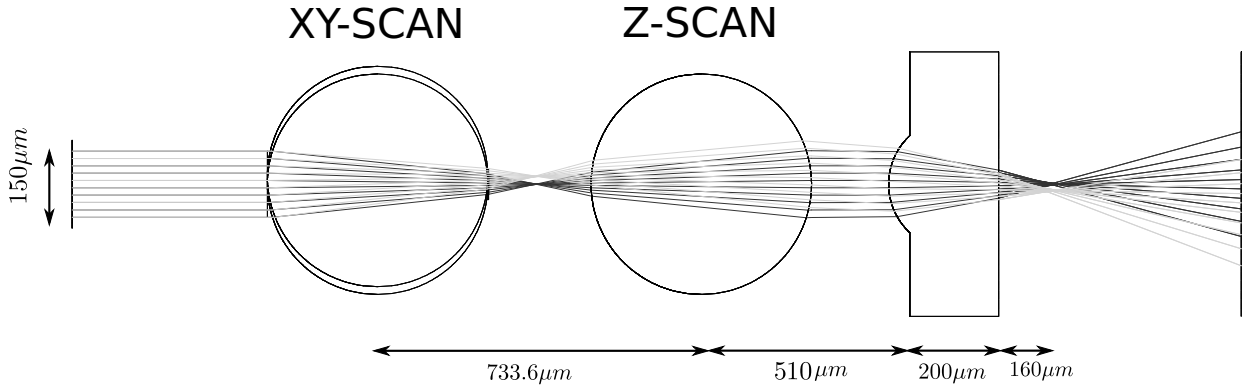


Figure 2.13: Ray-tracing through ball-lens based scanner - The scanner is composed from two identical ball lenses $f_{BL} = 366.8\mu m$, and a focusing lens ($ROC = 150\mu m$, diameter $220\mu m$). Ray-tracing is shown for two cases: no lens-displacement (blue rays) and $17.5\mu m$ displaced XY scanning lens (green rays).

The optical design of the scanner is presented on figure 2.13. Two movable ball-lenses ($500\mu m$ diameter, made from NBK7 glass, from Edmunds) compose the discussed scanning doublet that is set-up in the XY-Z configuration. The collimated input beam ($150\mu m$ diameter) impinges the first lens placed on a laterally movable stage, and the second lens that can be displaced along the system optical axis re-collimates the beam finally focused by the last lens. The focusing lens is made within wafer-level approach by means of silicon-glass molding techniques. The glass holding wafer of the focusing lens provides the encapsulating wafer that allows to isolate the system from the environment.

The presented system in figure 2.13 is characterized by a working distance $WD \approx 160\mu m$, a numerical aperture $NA = 0.25$ that provides in diffraction-limited case a focal spot in the order

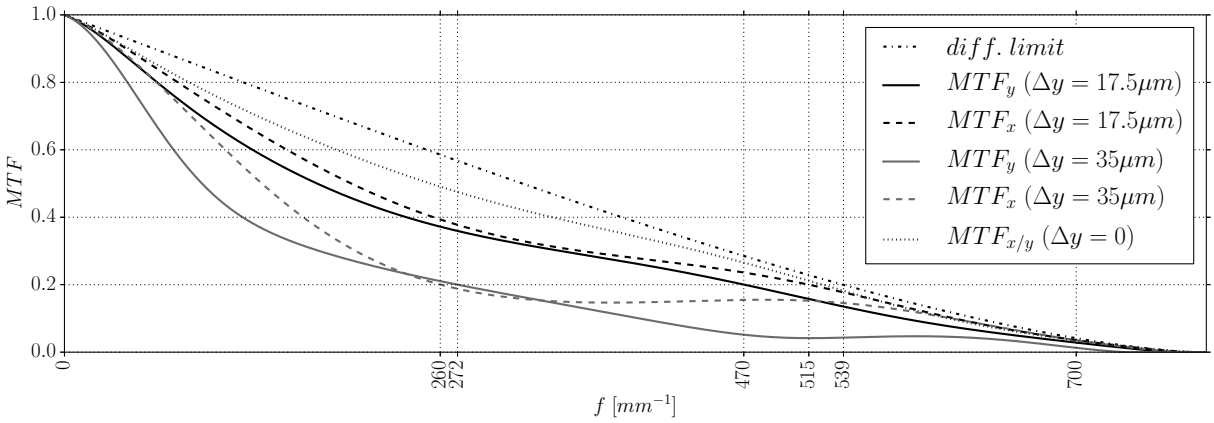


Figure 2.14: Ball-lens-based scanner: MTF - Modulation transfer function plotted for three cases: axial state (dotted blue curve), lateral scanning lens displaced by $\Delta y = 17.5\mu m$ (solid and dashed black), $\Delta y = 35\mu m$ (solid and dashed red), diffraction limit marked as black dash-dotted curve.

of $\delta_{x_{airy}} = 1.5\mu m$ and $\delta_z = 15\mu m$. However, the aberrations present in the system are responsible for optical performance degradation. The used components and limited positioning freedom do not provide much space for optimization of the optical setup. Consequently, the described system exhibits deterioration of optical resolution due to the aberrations.

The axial behavior of the system is determined mostly by the spherical aberrations generated by spherical lenses. All optical elements in the system contribute to the spherical aberration, with the principal contribution brought by the focusing lens. However, the main limitation of the system performance appears when the lateral scanning is considered. In figure 2.14, the contrast transfer function is presented for the system in three cases: axial case (all lenses aligned on-axis - no displacements) and two lateral scanning positions. Resolution in the on-axis case is reasonably close to aberration free system (i.e. diffraction limited) in the region of high frequencies, however, the scanning visibly deteriorates the system performance. In particular, for large lateral lens displacements, off-axial aberrations (coma, astigmatism) deform the focal spot, resulting in a different resolution along the two perpendicular directions. This resolution is always worse along the scanning direction.

Another common method to visualize (qualify) the effects of aberrations onto the systems resolution (lateral spot size) is the so-called “spot diagram”. The latter is obtained by geometrical tracing of rays through the optical system by means of geometrical optics. Then, intersection of rays within the focal plane defines the geometrical spot shape.

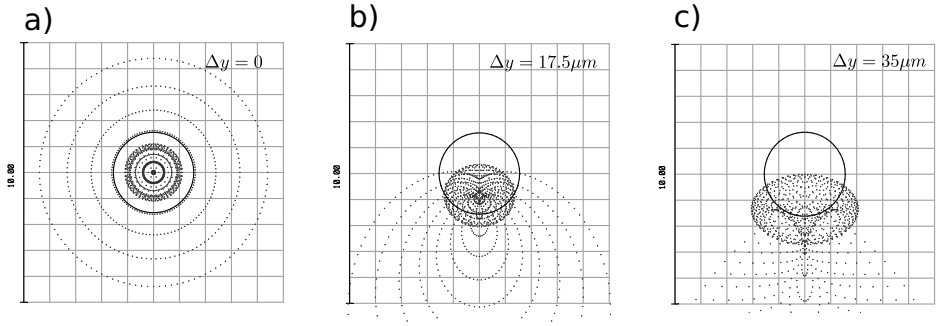


Figure 2.15: Spot diagrams of ball-lens scanning system - Impact of aberrations on the geometrical (ray-traced) focus spot in the case of (a) $\Delta y = 0$, (b) $\Delta y = 17.5\mu m$ and (c) $\Delta y = 35\mu m$ of the lateral displacement of first scanning lens. The circle drown in each spot diagram represents the airy disk of radius defined by the NA of the system ($1.5\mu m$).

The spot diagram is presented in figure 2.15. Off-axis aberrations are visible when lateral scanning is considered. Its effect (figure 2.15b,c) is to enlarge and deform the focus spot. The wavefront analysis for the three considered cases (table 2.3) also shows that σ_{rms} changes drastically with lateral scan and that astigmatism and coma are the main aberration terms involved.

As it was discussed before, displacement of lenses in the scanning doublet is in general nonlinear ($\Delta_z(\Delta z)$) and coupled ($\Delta_y(\Delta y; \Delta z)$). In addition, image plane tends to be curved due to the optical aberrations. Thus, the knowledge of the exact shape of the scanned volume is important since its allows to relate the positions of lenses (defined directly by the scanners positions) to the location of the focused spot generated by the system. The X-Z cross section of the scanned volume is schematically presented on figure 2.16. In the considered case, the scanned volume is highly curved with a shape having a parabolic form ($z(x) = \frac{x^2}{2R_{img}}$) with curvature at center $R_{img} = 33\mu m$. The not spherical but parabolic image plane is an effect of the combination of classical image curvature (Petzval curvature [6]) and specific dependence of astigmatism on the lateral scanning.

This first design, based on two $500\mu m$ diameter $NBK7$ ball-lenses and a plano-convex glass lens was used to perform the first demonstration of the vertically integrated multi-wafer MOEMS optical scanner for the DWST-DIS project (more details can be found in the chapter 5 of this manuscript). Considering optical performances, this system is not efficient enough, especially for an application such as confocal microscopy. In particular, the ratio between axial scanning range and axial resolution is too weak to achieve a true optical sectioning. However, systems such as differential confocal ones that perform uniform surface topography, could be already realized based on this micro-system configuration. Obviously, the complete system integration requires source and

Δy $[\mu m]$	0	17.5	35
σ_{RMS} $[\lambda]$	0.06	0.09	0.18
Z_6 $[\lambda]$	-	-0.035	-0.13
Z_7 $[\lambda]$	-	-0.069	-0.11
Z_{11} $[\lambda]$	0.06	0.05	0.033
SR	0.87	0.71	0.27
δ_x $[\mu m]$	1.9	1.9	3.7
δ_y $[\mu m]$	1.9	2.2	3.8

Table 2.1: System performance statistics for ball-lens scanner - The aberration analysis made within Zernike wavefront expansion quantify the effect of lateral scanning (Δy dependence) on optical performance of the system. The principal Zernike terms that contribute to the total wavefront error (σ_{RMS}) were considered, i.e., Z_6 - astigmatism, Z_7 - coma, and Z_{11} - spherical aberration (in all calculations $\lambda = 670nm$), Strehl ratio SR is also indicated. The resolutions $\delta_{x/y}$ derived from the system MTF with 0.2 contrast criteria.

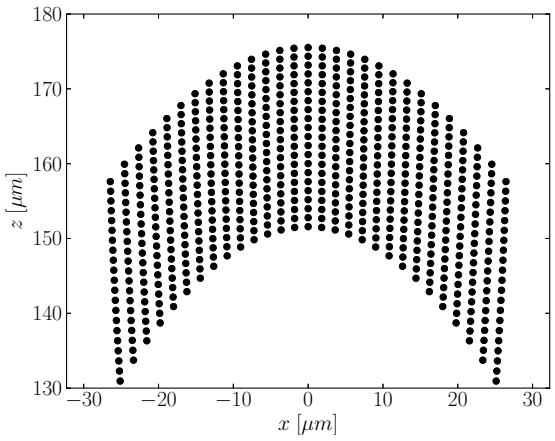


Figure 2.16: Shape of scanning volume of ball-lens based system - Curved scanning volume resulting from off-axis aberrations present in the system calculated by ray-tracing within ZEMAX. Neighborhood points correspond to scanning lenses displaced by $2\mu m$ for two considered (x, z) directions.

detection units. It will be shown later (Chapter 5), that fiber optics components are an easy solution for this aim. In particular, when fiber-coupled laser source and photodiode, connected to a fiber coupler serving as a beam splitter are employed.

2.4.2 Advanced system I: plano-convex scanning lenses

The ball-lenses for scanning doublet are clearly not an optimal solution. Aberrations generated by the scanner, in particular, astigmatism and coma appearing during lateral scanning, seriously deteriorate the resolution of the system in the edges of the scanning zones. Moreover, spherical aberration and astigmatism are responsible for a low axial resolution. Scaling of this system, to reach higher numerical apertures required to obtain real confocal imaging, is then not possible. Finally, ball lenses cannot be integrated onto the MEMS scanner with batch-fabrication processes and inconvenient pick-and-place scheme has to be employed for the system construction.

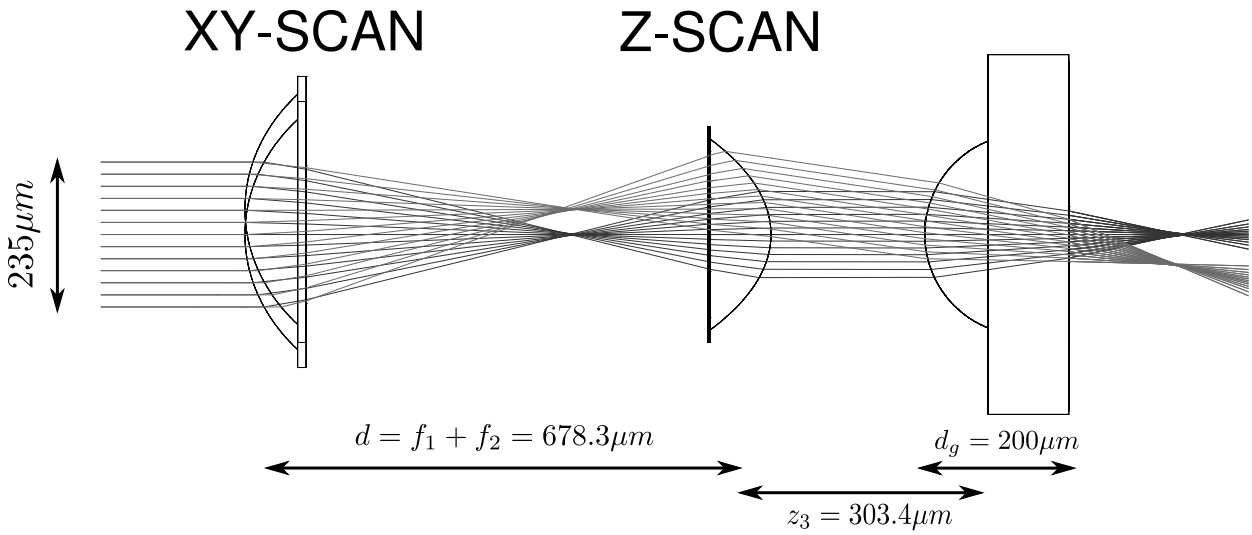


Figure 2.17: Ray-tracing through plano-convex lens-based scanner - Scanner is composed from two plano-convex aspherical lenses placed in the afocal configuration, in the figure lateral scanning is visualized: blue rays correspond to aligned system while the red rays correspond to system where first lens in laterally displaced by $35\mu m$.

For all these reasons, it is necessary to design a more optimal scanner. The latter could be constructed with plano-convex lenses that are expected to generate less optical aberrations. In addition to the improvement of the overall optical performance of the system, it would also allow their wafer-level (batch mode) integration with actuators, provided that compatible microlens fabrication is used.

However, similarly to ball lenses, the use of plano-convex lenses having spherical shape always leads to poor off-axis performances of such scanning system. One of the solution to improve the scanner optical performance is thus to rely on aspherical lenses.

The scanning system built around two aspheric conic microlenses is presented in figure 2.17. The lenses are arranged in the same architecture, however, ball-lenses of the scanning block are replaced by plano-convex microlenses whose geometry is optimized for the considered scanning system. As previously, the focusing objective is a standard spherical microlens.

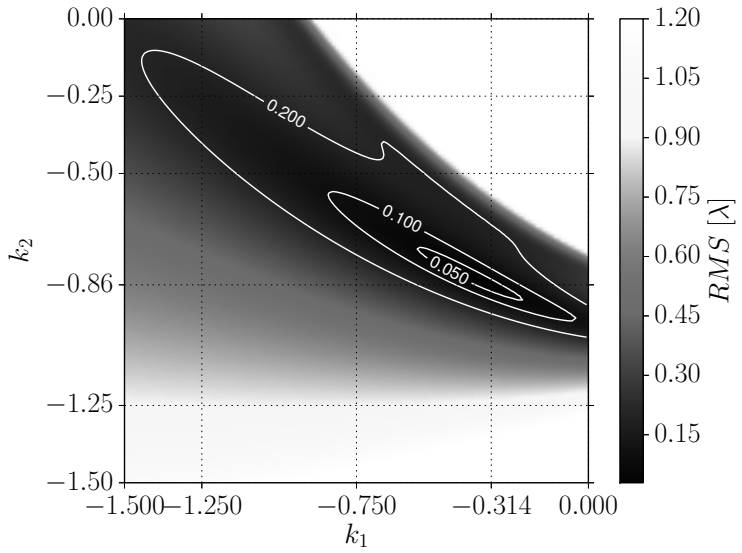


Figure 2.18: Aspherical scanning doublet: conic constants tolerances - Impact of conic constant on the optical performance (via σ_{RMS}) of the scanning block.

The afocal scanning doublet was optimized as a separate block. Its magnification was chosen to be less than 1.0 to allow the use of larger input beam than in the case of the ball-lens setup ($150\mu m$ only). Based on ZEMAX optimization, the best conic constants of the doublet were found to be $k_1 = -0.314$ and $k_2 = -0.859$ for lenses fixed in the afocal configuration. Their radii of curvature should then be $R_1 = 200\mu m$ and $R_2 = 110\mu m$, their thickness $d_l = 85\mu m$, and their diameters $D_1 = 370\mu m$ and $D_2 = 275\mu m$. The considered lenses are made of glass (n=1.457).

Although, microlenses with negative conic constant have been already fabricated [142] within combination of resist reflow and reactive ion etching techniques, precise control of their shape is a challenging task and the possibility of aspherizing the geometry of usual spherical microlenses highly depends on the employed technology. The tolerances concerning these conic constants for lenses of the afocal doublet are presented on figure 2.18 where the wavefront error is drown as a function of the conic constants of the two microlenses. It can be noted that wavefront deviation

Δy [μm]	0	17.5	35
σ_{RMS} [λ]	0.046	0.053	0.070
Z_6 [λ]	-	-0.005	-0.012
Z_7 [λ]	-	-0.002	-0.010
Z_{11} [λ]	0.05	0.05	0.05
SR	0.92	0.89	0.85
δ_x	2.34	2.38	2.53
δ_y	2.34	2.45	2.94

Table 2.2: Plano convex lenses based scanning system: performance summary - as in table 2.3

should remain lower than 0.050λ. According to figure 2.18, tolerances are larger on the first lens of the doublet than on the second one.

Resolution obtained with such scanning system and a focusing block based on a spherical microlens ($R_3 = 140\mu m$, $d_{glass} = 200\mu m$, $D_3 = 260\mu m$) is presented on figure 2.19 by use of the spot diagrams, and in figure 2.20 by means of a modulation transfer function. It is visible that this system is characterized by much better off-axis performance than the one based on ball-lenses, i.e. the lateral resolution is not degraded on the edges of the scanning zone. Table 2.2 summarizes the optical performance of the system where it can be seen that comas and astigmatism terms are divided by a factor 10 compared to ball-lens system. Also, Strehl-ratio remains high while lenses are displaced.

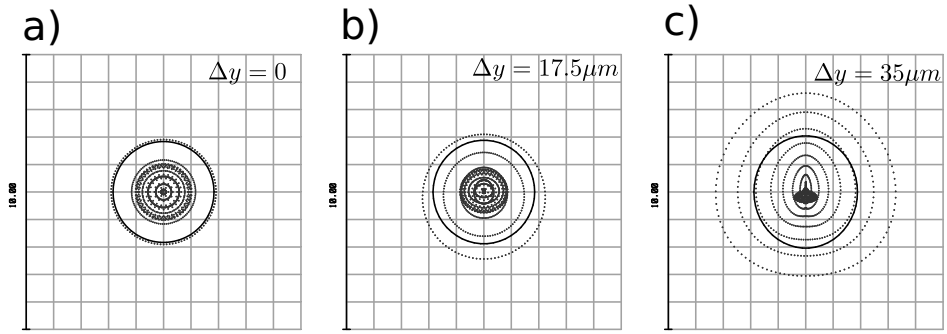


Figure 2.19: Plano convex lenses based scanning system: spot diagram - Ray-traced form of focal spot generated by scanning system, the circle in the center represents the Airy-disk of size $r_{Airy} = 1.99\mu m$. The three spots correspond to three lateral positions of the scanner: (a) $\Delta y = 0$, (b) $\Delta y = 17.5\mu m$, (c) $\Delta y = 35\mu m$.

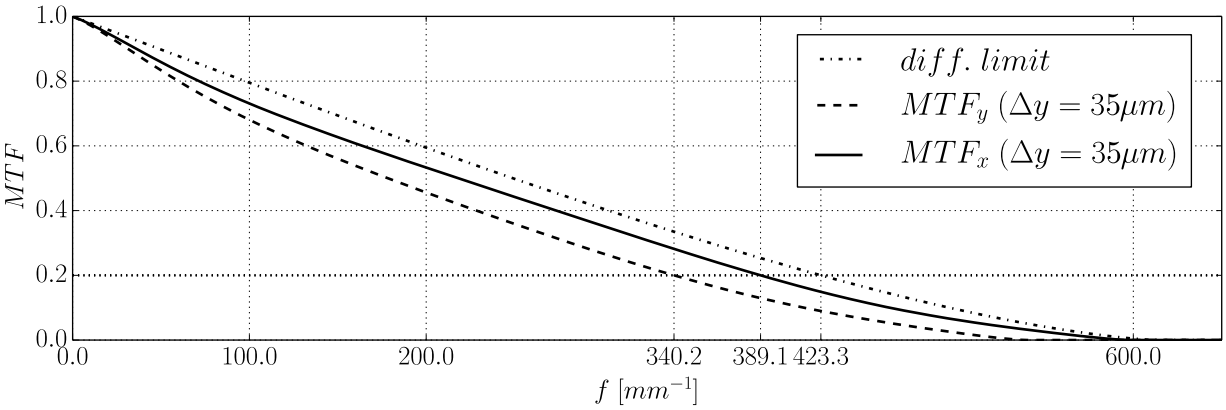


Figure 2.20: Plano convex lenses based scanning system: MTF - Contrast transfer function for the case of maximal considered lens displacement in the scanner. The difference between the diffraction limit and obtained MTF within the system is significantly improved compared to the ball-lens system.

Finally, lower aberrations generated by the scanning doublet (because of aspheric lenses) as well as the magnification that can be chosen lower than 1 (more freedom on the choice of plano-convex lens geometries) allow to achieve a higher NA within the scanning block. This higher NA within the scanning block allows in turn to reduce the NA of the focusing block without changing the resolution of the entire system. Consequently, longer focal length of the focusing block $f_3 = \frac{R_3}{n-1}$ can be used to provide better scanning magnification (equations 2.17 and 2.16). The scanning zone obtained with lenses scanning range $\Delta y = \Delta x = \pm 35\mu m$ and $\Delta z = \pm 20\mu m$ is then: $84x84x60\mu m^3$ outperforming the one of the ball-lens based system. Moreover, it can be noted that the scanning zone is less curved (figure 2.21).

2.4.3 Advanced system II: Anastigmatic focusing block

According to the table 2.2, the biggest contribution to the wavefront deviation comes from the spherical aberration term, that can be attributed to the focusing block lens. Then, the use of single plano-convex lens within the focusing block is the limiting factor to improve the system resolution. This is particularly the case if the scanner is aimed to be used in confocal microscopy where single lens objective is not capable to provide high enough NA without introducing aberrations. Consequently, as the third considered optical configuration, we discuss the implementation of a mirror objective instead of the lens, that is expected to provide higher NA with lower aberrations. In particular, our proposition is to rely on a reflective micro-objective architecture, based

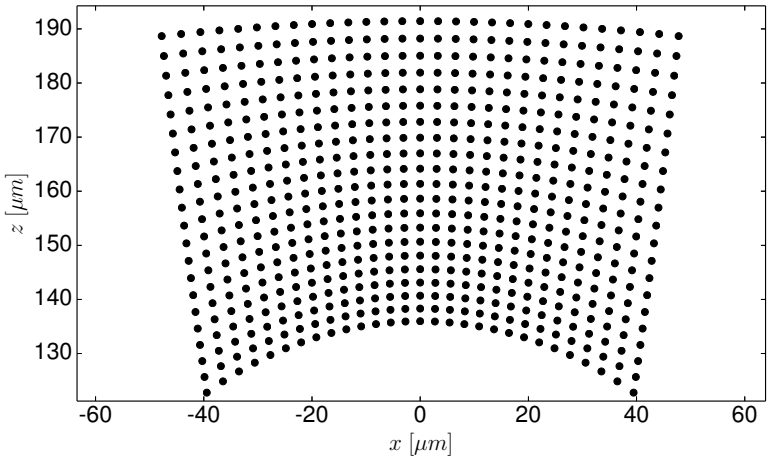


Figure 2.21: Plano convex lenses based scanning system: scanned volume shape - XZ cross section of the scanning volume obtained with aspheric lenses based system.

on the Schwarzschild and Burch [143] designs. This component is often referred in the literature as "Schwarzschild objective" or "Schwarzschild anastigmat" to underline its aberration compensation property. The details of the architecture and the first attempt of fabrication of such device by means of micro-fabrication techniques are described in the section 4.2 of this thesis. In here, we present the important advantages of this specific component for the considered scanning micro-system.

The Schwarzschild objective is composed of two mirrors, i.e. one concave (primary) and one convex (secondary). The appropriate choice of their radius of curvatures and the separation between them allow the elimination of the three primary aberrations, i.e. spherical, astigmatism and coma.

The system layout equipped with a Schwarzschild objective as the focusing block is presented in the figure 2.22. In this system, the scanning doublet is exactly the same as in previously described system and only the focusing block differs.

The optical performance presented by means of the spot diagrams (figure 2.23) shows very efficient focusing. Indeed, all traced rays through the system are well embedded within a circle defined by the airy radius of $1.1\mu m$. However, MTF plots (figure 2.23) show that the resolution is not as good as the one indicated by the simple geometrical analysis. This effect is due to the obstruction generated by the specific reflective architecture. As wave-optics show [5], an optical system, possessing circular shadow in the light path, yields to a different point spread function (PSF) and hence to a different MTF than clear (unobstructed) system. In consequence, systems having different pupils (obscured or not) are not directly comparable simply by use of NA or of

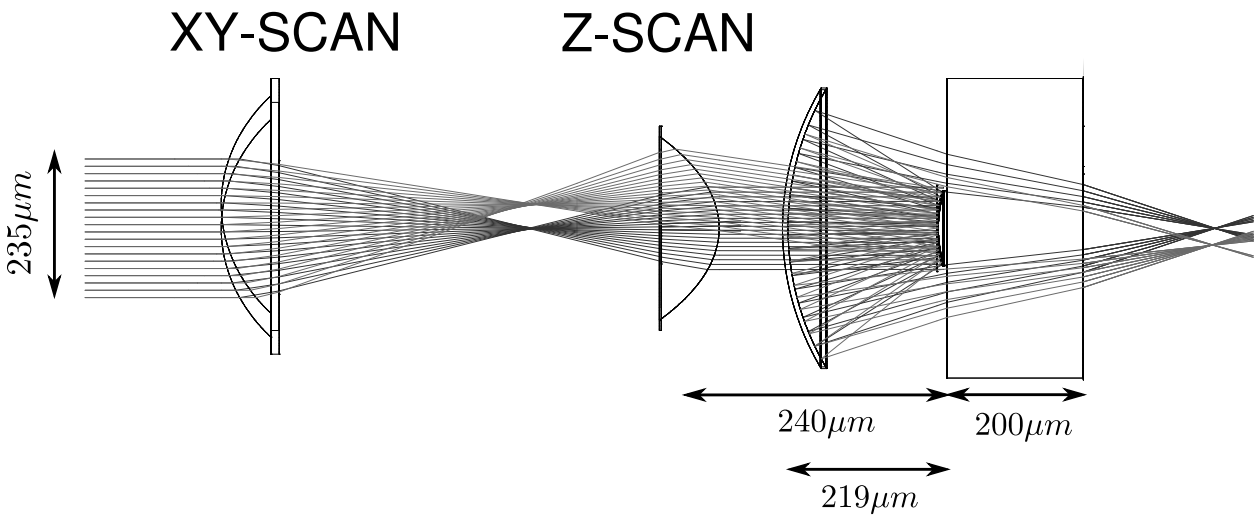


Figure 2.22: Scanning system with Schwarzschild objective as the focusing block - Mirror-based objective, replacing the lens in the focusing block, allows increasing the NA of the system and enlarging the working distance of the device. The specific construction of the mirror objective requires a port in the primary mirror to allow the scanned beam to reach the secondary mirror, this port together with secondary mirror creates shadow in the output beam.

derived airy radius. Instead, it is preferable, for general analysis of the system resolution, to use the MTF formalism. The latter indicates that this system, in addition to its slightly higher resolution than the one estimated from its NA ($NA = 0.35$), owns very good off-axis performance, with MTF values slightly affected by the lens displacements. Another important advantage of this system is the longer working distance of the Schwarzschild objective comparing to a simple lens. This feature allows larger degree of system miniaturization while preserving the encapsulation possibility, which in case of microlenses is limited by the focal length of the lens that needs to be longer than the construction wafer thickness (figure 2.17).

The Schwarzschild objective is composed from two mirrors $R_s = 190\mu m$, $R_p = 400\mu m$, with diameters $D_p = 410\mu m$ and $D_s = 130\mu m$, separated by $d = 219\mu m$ (vertex to vertex) where glass support (n=1.457, thickness $d_{glass} = 200\mu m$) serves as the secondary mirror support and system encapsulation lid. The position of the objective in respect to the scanning doublet is chosen to minimize the obstruction within the system, i. e., the secondary mirror is placed in the focal plane of the second lens ($f_2 = 240\mu m$) of the scanner. In this way, the secondary mirror is uniformly illuminated, independently on the angle of the illuminated beam. Both subsystems (scanning doublet and the objective) have been optimized separately so that the wavefront after the scanning doublet is faintly aberrated. Hence, the separation distance between the two blocks do not affect

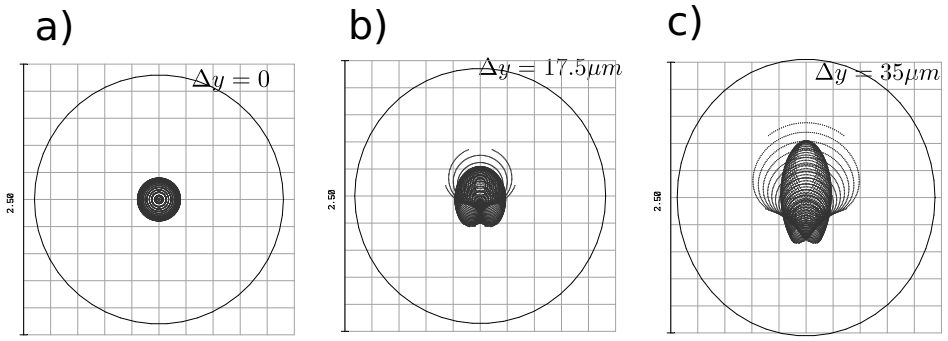


Figure 2.23: Scanning system with Schwarzschild objective: spots diagrams - Ray-traced form of focal spot generated by scanning system, the circle in the center represents the Airy disk size of $r_{Airy} = 1.11\mu m$. Three spots correspond to three lateral positions of the scanner: (a) $\Delta y = 0$, (b) $\Delta y = 17.5\mu m$, (c) $\Delta y = 35\mu m$.

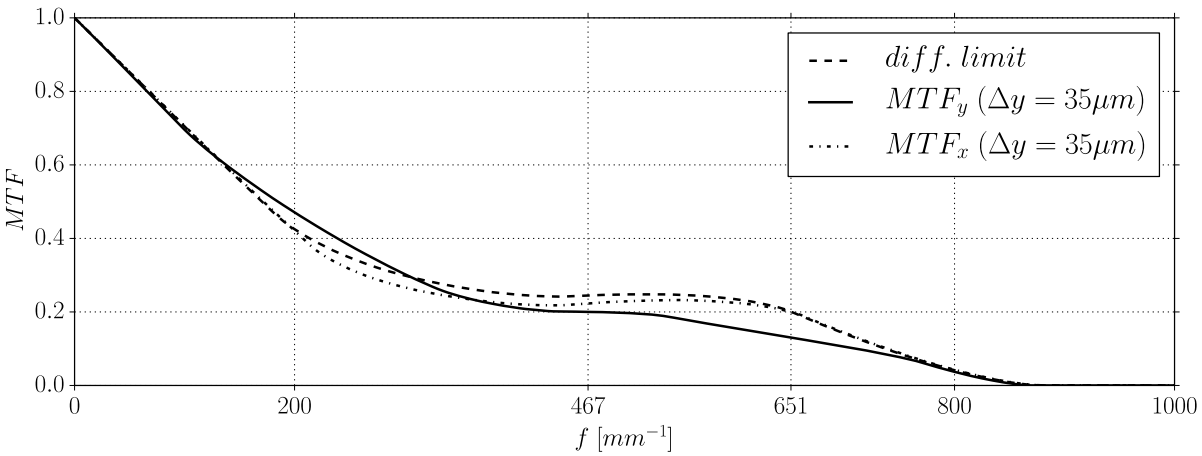


Figure 2.24: Scanning system with Schwarzschild objective: MTF - Contrast transfer function even in case of diffraction-free (dash-dotted curve) is visibly different than in the lens based case (fig. 2.20), the scanning weakly decrease the contrast transferred by the system.

the performance of the system[1].

[1] in this case, only field distortion is dependent on the separation distance between the blocks, however as distortion does not directly deteriorates the system resolution, we do not consider its minimization here.

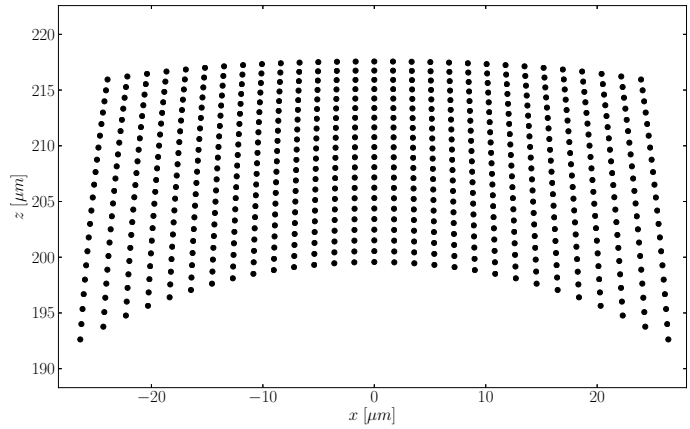


Figure 2.25: Scanning system with Schwarzschild objective: scanning volume shape - XZ cross section of the scanning volume obtained within system.

Δy $[\mu m]$	0	17.5	35
σ_{RMS} $[\lambda]$	0.01	0.018	0.03
Z_6 $[\lambda]$	-	0	-0.0075
Z_7 $[\lambda]$	-	0.033	0.034
Z_{11} $[\lambda]$	-0.01	-0.01	-0.01
SR	0.997	0.99	0.96
δ_x	1.53	1.53	1.53
δ_y	1.53	1.63	2.15

Table 2.3: System statistics for plano-convex scanner with Schwarzschild objective - as in table 2.3

2.5 Summary

In this chapter, optical design for 3D scanner constructed within MOEMS technologies was considered. The technological constraints related to the micro-construction of the considered device, i.e. a simple 3-elements optical system, was considered. As a result, 3 optical configurations were proposed that differ in difficulties of technological realizations as well as in optical performances. The first design, based on ball-lenses, does not perform well in the off-axis configuration However, it allows to test the other (non-optical) challenges related to the project such as vertical integration and connections. The second configuration is optimized in terms of optical performance, and relies

on plano-convex microlenses with aspherical geometries. These lenses can be integrated into the device by means of wafer-level approach, which is not possible in the case of ball lenses. Finally, the third design pushed forward the optimization of the optical performance by adding a reflective micro-objective as the focusing block. This system, weakly affected by optical aberrations, shows much better off-axis performances and can be used to achieve higher optical resolutions than with the two first systems. However, technological realization is also more challenging as it will be discussed in the chapter 4.

3

Characterization of focusing components

To provide high resolution imaging the MOEMS confocal microscopes described in the second chapter needs high quality optical components. For this purpose, wafer-level microoptics that rely on specific methods of micromachining are adapted for generation of optical components. As it was demonstrated [142, 144] such technologies allow to fabricate high quality microlenses within wafer-level processes. Considered here MOEMS confocal microscope project focuses on micro-optical elements that are fabricated in materials compatible with integration technologies, i.e., mainly anodic bonding. Thus, using silicon and glass requires also specific technologies for optical-elements generation. In particular, micromirrors and microlenses to be used in the conceived system are fabricated within silicon etching technology and glass molding technique, respectively. Then, such relatively new [123, 124, 145] technology requires fabrication processes optimization which, in turn, has to be based on reliable and pertinent characterization methods of generated structures. Consequently, we present in the following different characterization techniques that will be employed during the fabrication of micro-optical components. In particular, we present a setup developed specifically for characterization of high NA transmissive and reflective micro-optical components.

3.1 Topography measurements

The optical properties of lenses or mirrors are largely defined by their geometry. Consequently the basic evaluation of their quality starts with the measurement of their geometry. Topography metrology can be realized by many ways among which the most popular methods are scanning profilometery and various types of interferometric systems. However, it is important to underline

that geometry measurements of micro-components made of highly curved and optically smooth surfaces are not easy with standard equipments[1].

3.1.1 Dicing and SEM imaging

One common method for micro-structure characterization is based on precise dicing and subsequent imaging of sliced samples under a microscope. When high precision is needed or small structures are investigated, cross sections are imaged with scanning electron microscope (SEM).

Figure 3.1 shows an example of cross section of a diced matrix of microlens molds. The image itself does not provide information about the quality of the fabricated structure, however its profile can be retrieved and analyzed to quantify its optical performance. For this purpose, we developed a simple algorithms for profile retrieval and analysis obtained from digital images is described in appendix A.

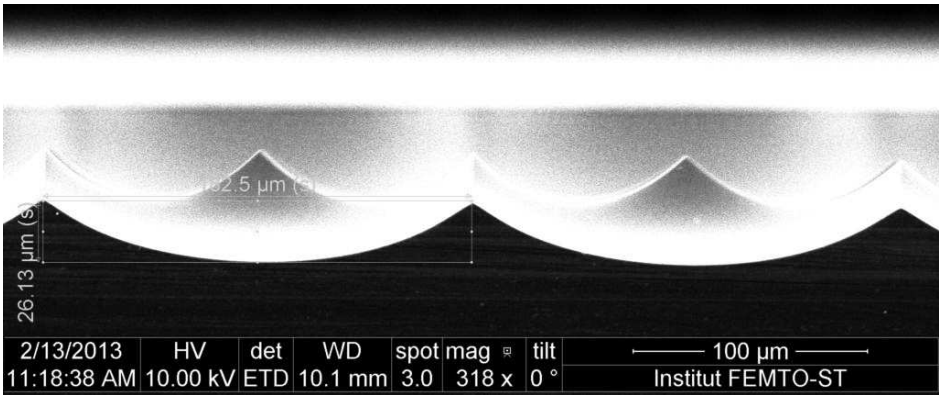


Figure 3.1: Dicing as a method for geometry characterization - SEM image of diced silicon mold visualizing the profile of the structure

The dicing-based geometry analysis is straight-forward, however by definition, it provides only information about a specific section of the structure. In consequence, it is not possible to get complete information about the 3D shape of investigated structure. In particular, for microlenses/micromirrors, the dicing approach is not adequate for characterization of the structure symmetry. Another drawback of this method is the fact that this method is destructive.

[1] in the sens of typical instruments accessible in MEMS-focused cleanrooms

3.1.2 Scanning profilometry

In order to obtain full information of the geometry of fabricated structures 3D topography measurement is needed. The simplest system that can provide this kind of information is the scanning profilometer. Scanning profilometer is a mechanical device that measures relative altitudes of the sample by probing point by point its surface. It can be used to measure 2D surface topography and quantify the surface roughness. Scanning profilometry systems are divided in two categories: contact profilometry, where the small tip (diamond stylus) touches the measured surface. In this method variations in the vertical movement of the stylus are measured and simultaneously recorded during the sample (or tip) lateral scanning. The second category is a so-called non-contact profilometry the surface to be measured is probed by an optical signal [146]. In this case the sample altitude is derived from the optical signal reflected from the sample.

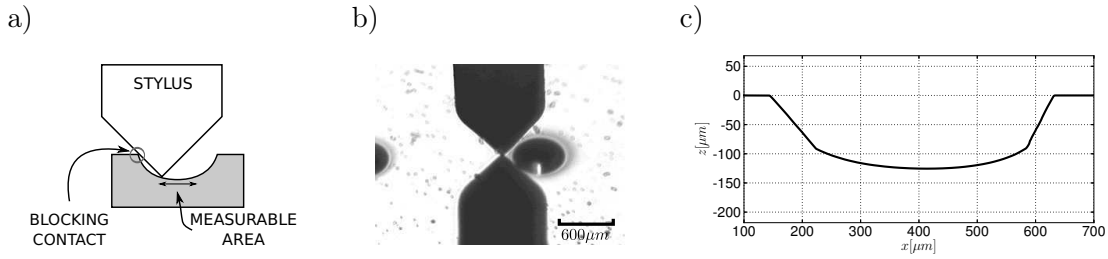


Figure 3.2: Profilometry for mold topography measurements - (a) Principle of contact profilometry, (b) image of profilometer during a measurement, (c) example of a profile obtained from contact scanning 1D profilometer - visible measure artifacts on the edges of the structure (linear slope) originate from finite size of the profilometer tip.

However, the important limitation of the scanning profilometry is related to geometrical limits with which samples can be measured. Concerning contact profilometry the main constraint originates from the finite size of the scanning stylus. Firstly, the lateral resolution is limited by the radius of curvature of the scanning stylus. Secondly, in the case of small and deep structures limited area of structure can be investigated. In particular, according to the geometrical shape of the tip areas with high slope cannot be measured (figure 3.2).

In the case of optical systems, similar problem arises when optically smooth surfaces are investigated. The limit of observation area is connected to the numerical aperture of the probe objective. The optical signal reflected from surface cannot be collected by the probe objective if the local slope of the sample is higher then the collection angle of the objective ($\alpha_{slope} > \alpha_{obj}$). In this case, the

reflected signal does not reach the detector and some regions of the sample are not visible by the system (figure 3.3). The lateral resolution of optical profilometry follow classical relation as for all optical systems and is defined by the numerical aperture of the objective used in the probe.

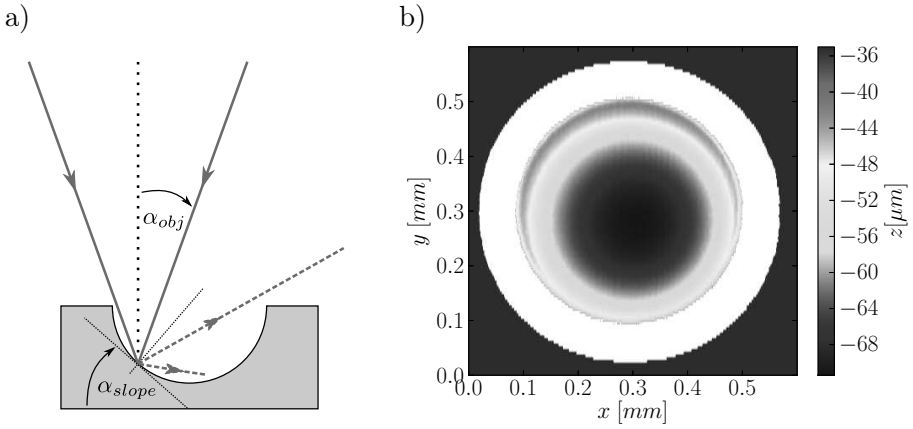


Figure 3.3: Limits of optical measurements of curved surfaces - When Smooth reflecting structures are under optical characterization, (a) depending on the angle of the slope the reflected light can be redirected outside the collection cone of the objective leading to unmeasurable regions of the sample, the higher slopes can be observable only when higher NA in the optical system are used, (b) example of measurement by scanning optical profilometer visible unmeasured zone (edges of the structure) are due to limited NA of the measuring objective.

3.1.3 Interferometric methods

Various metrology techniques based on interferometry were developed for characterization of M(0)EMS and their components [147]. The dynamic behavior of mechanical micro-systems can be investigated by white-light stroboscopic interferometry [148, 149], while topography characterization is usually investigated by different types of interferometers like phase-shifting [150], white-light [151, 152], speckle [153, 154], or holography-based systems [155, 156, 157].

Interferometric systems, as the name suggests, are based on the interference of monochromatic or wide-band light. The light source (usually laser) is divided into two beams: one is used as a reference whereas the second one is a probe. Probing beam is directed to the sample so that its reflection is mixed with the reference beam. Interference between the beam that interacted with the sample and the reference beam generates an interference pattern defined by the geometry of the object. Thus topography of the measured object can be recalculated from the interference pattern. The usual

method for geometry extraction employs phase-shifting method, in which several interferograms are recorded for different positions of the measured object.

Various architectures of interferometers employs different configurations of beam splitting and sample illumination. In the case of micro-structures characterization, interferometric systems are built on the base of a microscope objective that allow high magnification of investigated objects. The different architectures of illumination and beam splitting allows different types of measurements. For example, Twyman-Green interferometer is well adapted for topography measurements of curved objects (reflection mode)[158, 159], whereas Mach-Zehnder architecture is well suited for wavefront aberrations measurement in the transmission mode (in case of microlenses) [158, 159]

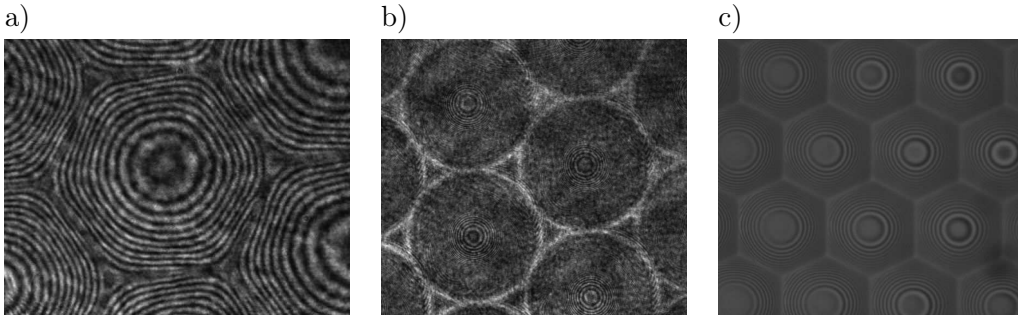


Figure 3.4: Interferograms examples of Silicon micromolds - (a) interferogram obtained within Michelson system of micromolds with hexagonal footprint - the fringe pattern clearly indicates deviation from axial symmetry of this structure; (b) interferogram of Si mold of high NA - small part of the structure can be analyzed within used system (to small used NA in the interferometer); (c) interferogram obtained within Mirau architecture with wide-band light source structure similar to (a).

In case of characterization of spherical surfaces, the resulting interference pattern takes the form of circular fringes (figure 3.4). When the object is not axially symmetric, the fringes deviate from the circular form. This observation allows to qualify the symmetry of the structures by analyzing single interferogram. As an example, figure 3.4a shows an interferogram of microlens molds matrix. In the observed structure, neighborhood effects (etching nonuniformity due to neighboring structures) cause large asymmetry (deviation from axial symmetry) that is well visible by the deformation of the fringes. The neighborhood effect is very scale dependent, so that it becomes negligible with smaller structures as confirmed in the inteferogram shown at figure 3.4c.

The limitation of interferometry is similar to the one of optical profilometry. The numerical aperture of the objective has to be high enough to capture the light from the whole structures.

Moreover, with increasing slope, the fringes become denser and are more difficult to distinguish [160]. In consequence, when measuring highly curved structures, only a small part of the structure can be analyzed (figure 3.4b).

3.2 Direct Optical Characterization

As described above, topography measurements provide information about the shape of the element. Indeed, the optical performance of the optical elements is strongly defined by their geometry. However, relation between the geometry and optical characteristics has then to be calculated using optical propagation algorithms (by ray-tracing or diffraction theory). An alternative characterization method used for optical components metrology is the direct measurement of their optical properties. The advantage of this approach is that complicated data reinterpretation is not required. Moreover, it is a more general methodology in the sense that it can be applied not only to single elements like microlenses, but also to more complex optical systems composed of several elements or even to complete confocal microscopes.

The most popular method of direct optical measurement is the measurement of the wavefront generated by optical systems [161]. Several setups proposed for this aim can be divided in two distinct families: the first one is the interferometric systems [162] whereas the second one gathers the wavefront sensing by discrete wavefront sampling, usually achieved with Shack-Hartmann sensors [163].

Nevertheless, wavefront detection in case of micro-optical elements is not a trivial task since complicated optical systems are necessary to provide high quality probing wavefront. Moreover, they have to be scaled down to the size of the measured element and later rescaled to the size of the detector. This "multi-scale" optical measuring system has to maintain high optical quality (because of the need of well defined reference beam) and needs accurate alignment of measured micro-elements [162].

In this work, we propose a simpler setup based on the measurement of 3D IPSF generated by the optical elements [164]. As the IPSF is often used to define the imaging quality of optical systems, measurement of system IPSF has been employed as characterization tool for complex optical systems like confocal microscopes [165, 166] or lithographic objectives [167].

Considered method is easier to realize because it is less affected by probing beam quality and much less demanding in terms of alignment accuracy than wavefront metrology systems. IPSF, that is the point of interest in the characterization system, is simply defined as the 3D shape of the

focal spot generated by the focusing micro-element. As it was discussed before, optical resolution is directly defined by the shape of the PSF, but it is important to underline that PSF also depends on the optical configuration in which the element is tested. In consequence, with this measurement system special attention has to be made during data interpretation.

In particular, our system can be adapted to two different imaging cases: the first one is based on the investigation of focusing of a collimated probing beam which corresponds to imaging a point located at infinity, whereas the second one, adapted to the characterization of reflective elements, relies on imaging a point (focused probing beam) located at the center of curvature of the investigated element. Nevertheless, the fixed imaging configuration allows rapid estimation of the quality and repeatability of fabricated focusing optical component. Moreover, if additional data analysis is performed, then wavefront or in certain cases the 3D topography can be calculated from the IPSF data [164].

3.2.1 Characterization setup for transmisive elements

The characterization of beam transformation generated by the optical elements depends on the type of considered transformation. The first proposed architecture aims to characterize the transmisive focusing elements. The "transmisive" configuration means that focus is generated along the optical axis of the system, without changing the propagation direction.

3.2.1.1 Theory

System architecture for measuring 3D IPSF of a transmisive micro-elements is presented in figure 3.5. The collimated beam from laser source (probing beam) impinges a microlens that focuses the light. Then, a collection system made of an objective lens, a tube lens and a CMOS camera is used to analyze such focus. The collection system aims to project magnified images of the slices of the 3D focus spot to the camera located in the image plane where the camera is located. The 3D intensity distribution generated by the system can be described by the classical diffraction analysis [6].

$$I_t(u,v,\Phi) \propto \left| \int_0^1 \int_0^{2\pi} P_{obj}(\rho,\theta) P_m(\rho,\theta) \underbrace{e^{ik\Phi(\rho,\theta)}}_{\substack{\text{aberration}\\ \text{term}}} \underbrace{e^{-i\frac{1}{2}u\ \rho^2}}_{\substack{\text{defocus}\\ \text{term}}} e^{-iv\rho\ cos(\theta-\phi)} \rho d\rho d\theta \right|^2 \tag{3.1}$$

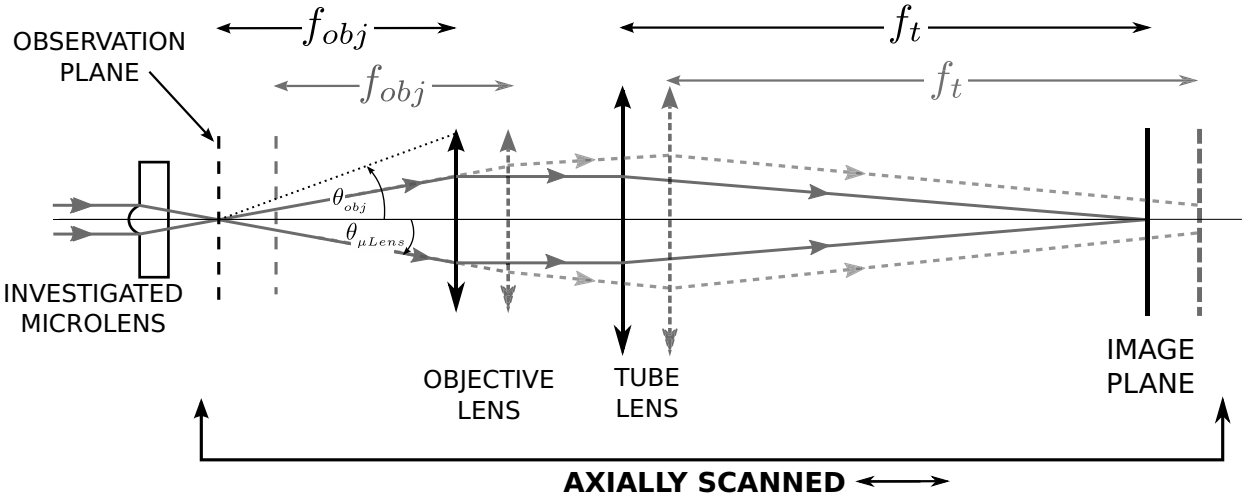


Figure 3.5: Scheme of characterization system "in transmission" - A microlens illuminated with collimated laser beam (HeNe $\lambda = 633nm$) generates the focus whose volume is observed by the collection system that can be axially displaced in order to change distance from lens to collection objective. The sequential scanning allows reconstruction of 3D shape of the focus spot generated by the microlens.

where $u = \frac{2\pi}{\lambda} zNA^2$ and $v = \frac{2\pi}{\lambda} rNA$ are normalized axial and lateral coordinates, Φ is wave aberration function, θ and ρ are normalized pupil coordinates, $P_{obj}(\rho, \theta)$, is a pupil function of the objective lens, $P_m\rho, \theta$ is the pupil function of measured microlens, and z is axial coordinate of the system in respect to the focus position of the investigated microlens. In a perfect system (clear, aberration-free, circular lenses), the pupil functions take the form of unit values over the pupil $P(\rho, \theta) = 1$. An important condition on the collection system has to be imposed to be able to obtain data about the whole investigated structure: The collection system has to have larger numerical aperture (NA_{obj}) than the investigated microlens ($NA_{\mu Lens}$): $NA_{obj} > NA_{\mu Lens}$, so that all light passing through the microlens contributes to the image formed on the image plane. From the point of view of equation 3.1, it signifies that the product $P_m(\rho, \theta)P_m(\rho, \theta)$ is equal to $P_m(\rho, \theta)$, where $P_m(\rho, \theta) = \begin{cases} 1 & \text{if } \rho < NA_m/NA_{obj} \\ 0 & \text{otherwise} \end{cases}$. If this condition is not fulfilled, only a part of the object can be characterized. However, in some cases, it is convenient to probe the object under *a priori* known NA that can be defined via the collection system NA_{obj}.

3.2.1.2 Implementation

Realization of the characterization system is presented in figure 3.6. The laser beam from HeNe source is expanded by a two-lens telescope and directed onto the microlens to be measured. The

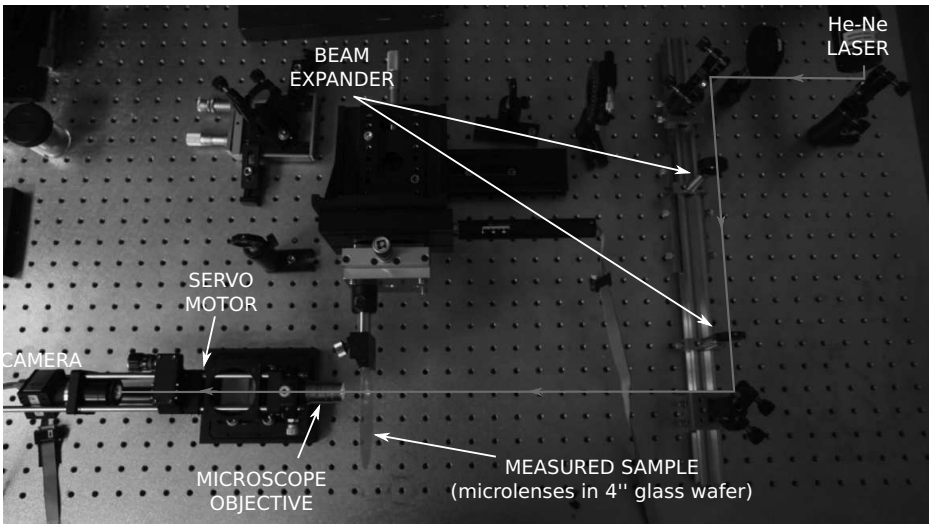


Figure 3.6: Optical system for focal spot measurement - The light from HeNe laser source expanded by a telescope system composed of two lenses impinges the investigated microlens, the focused beam after the lens is collected by the microscope objective and projected to the camera by the tube lens. The objective-tube lens-camera system is placed on the movable stage that can be precisely displaced along the beam propagation axis by precise servo motor.

focused spot generated by the microlens is collected by the microscope objective and consequently projected onto the camera. The microscope objective used as a collection lens assures high numerical aperture of the imaging system and provides large magnification. This is necessary since observed features in the focal spot generated by microlens have usually sub-micron sizes. The use of high quality microscope objective is necessary to avoid disturbance of the image by aberrations present in the imaging system. Consequently, such system allows imaging of one slice of the focus generated by the element under analysis. Thus, the distance between the collection system and the microlens can be controlled by precise servo motor in order to displace the whole imaging system (objective - tube lens - camera). Such axial scanning of the system allows a sequential registration of images (slices) from the focal volume. Scanning of the imaging system was chosen over the scanning of the microlens to fix the illumination conditions. In practice, when using a coherent source, completely uniform illumination is difficult to generate when using relatively large (few mm diameter) collimated beam because of some imperfections of optical elements. In our system, where the microlens is fixed, small non-uniformity's of illumination block are easier to handle.

It has to be noted that the image of each focus slice is recorded by a CMOS camera (ueye from IDS). Low dynamic range of CMOS sensor employed in the system (8bits) is insufficient to register

the rapidly changing structure of the observed focal spot. In order to improve the dynamic range of the obtained data, multiple frames of each focus slices are then recorded with different exposure times. The consecutive 6 frames (with exposures from 0.05ms to 100ms) are recorded and final image is reconstructed from multi-exposure data. The reconstruction involves images normalization (according to exposure time) of the different frames followed by frames averaging with exclusion of saturated or under-threshold pixels. Then the axial scanning is performed by use of the linear servo-motor that displaces a stage holding the optical module (figure 3.7). The camera and the motor are controlled by a PC, for which system control and data post-processing have been programmed in Python [168].

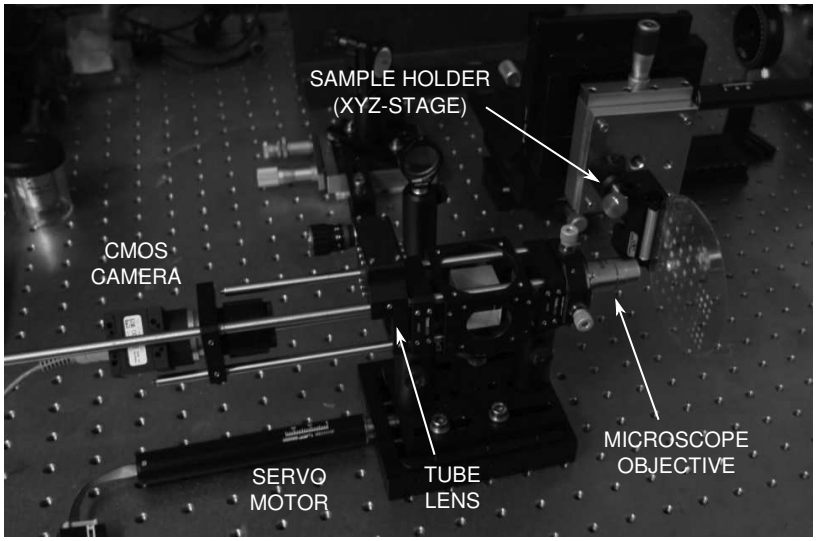


Figure 3.7: Collection system for through focus imaging - The system was built on an axially movable stage. The exchangeable microscope objectives allow simple adaptation of system magnification and numerical aperture to the characterized object. The measured sample, usually in the form of a 4inch wafer, is fixed to the XYZ stage that allows its accurate alignment.

3.2.1.3 Data analysis and example measurements

The data obtained from measurements represent the 3D intensity variation near the focus of the investigated element. The simplest data analysis is a qualitative comparison of measured data with an ideal case, for example a perfect (aberration free) microlens. However, the intensity distribution function defined in 3D volume is difficult to interpret, instead, 2D slices (XY and ZX) can be easier analyzed (figure 3.8).

The aberrations generated by non-ideal optical element typically deform the IPSF. In particular, when comparing to ideal aberration-free response, the focal spot of aberrated system is always wider along all three directions. Thus, this focus stretching can be used as a measure of aberration generated by the microlens.

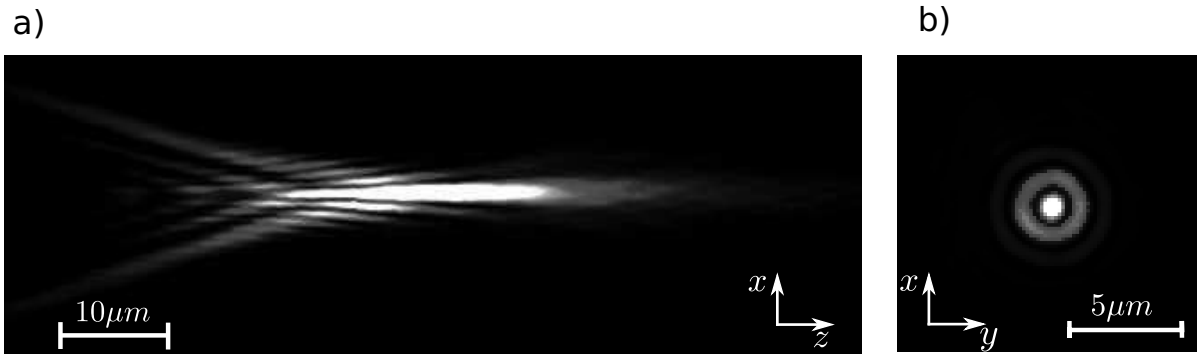


Figure 3.8: Measurements of $500\mu m$ diameter ball lens - (a) XZ-slice of focus spot generated by the microlens and (b) the focal plane (XY-slice), measurement performed with $NA_{obj} = 0.45$.

As an example measurement and in purpose to test the system, the first object under consideration is a microlens which has the form of a sphere, i.e., a so-called ball-lens. The investigated ball-lens (Edmunds Optics) is made of N-BK7 glass ($n_d = 1.517$) and is characterized by a diameter $D = (500 \pm 3)\mu m$, and a focal length $f = (367 \pm 2)\mu m$. The sphericity precision is specified by the manufacturer[1] as $1\mu m$. Although, the ball-lens has very well defined spherical geometry, the optical performances in the used configuration (collimated light, relatively high NA) are not very high.

When completely illuminated, the ball-lens has a numerical aperture $NA_{BL:100\%} = 0.56$. However, complete illumination is almost never used with ball lenses. Then, in order to characterize lower-NA configuration, the objective used in the imaging system has a lower NA than the one of the microlens. This configuration $NA_{obj} < NA_{\mu Lens}$ limits the observation zone of the beam generated by microlens to the defined NA_{obj}. As it was discussed before, although it is usually the case to characterize the whole fabricated structure, performing measurements under *a priori* known NA (defined precisely by NA_{obj}) can simplify the analysis of the obtained data. Consequently, the ball lens was investigated under NA=0.45. The processed data visualized as two perpendicular slices of the focal spot generated by the ball lens are presented in figure 3.8. The image of focal plane (figure3.8b) shows the well defined spot similar to an Airy disk, however, with stronger outer rings than in the case of aberration free imaging systems. On the one hand, the geometrical deviation

[1] sphericity is defined here (Edmunds) as maximum difference across the different cross section of a lens diameters

from the ideal case is difficult to notice simply by investigating the image of the focal plane. On the other hand, the XZ slice of the focal volume (figure 3.8a) is very different from the ideal case. The visible lack of symmetry in respect to the focal plane is attributed to the wavefront aberrations introduced by the microlens. The level of asymmetry in the XZ focus slice is then an easy qualitative indication of aberrations generated by characterized element.

The focus lateral and axial size directly measured from the 3D spot distribution are $\delta x_{fwhm} = 1.8\mu m$ and $\delta z_{fwhm} = 25\mu m$ (for comparison, aberration free system ($\Phi = 0$) is characterized by $\delta x^{\Phi=0}_{fwhm} = 0.7\mu m$ and $\delta z^{\Phi=0}_{fwhm} = 4.7\mu m$). However, it has to be noted that FWHM measure of PSF does not well represent the resolution of aberrated system, in particular in the case of spherical aberrations whose main effect is the generation of strong side-lobes (rings) around the principal focal spot. In consequence, the effective resolution of the system is not defined only by the width of the intensity peak, but also by the amplitude and size of the outer rings.

The spatial spread in the focus is often analyzed by means of an encircled energy plot, i.e. a plot illustrating the power distribution in the focal plane. Figure 3.9 presents the power analysis for the considered ball-lens. The numerical analysis performed with ZEMAX software, is compared with data calculated from the measurement. The curve for diffraction limited system is also plotted to illustrate the large difference between aberration free and aberrated cases. The shape of curves obtained from numerical analysis and measurement data are not exactly the same, however, the limits behave similarly (75% of energy is contained in a circle of radius $\approx 8\mu m$ for both cases). The difference can originate from not accurate location of focus center, or can be caused by data sampling (in the considered case pixelation $\Delta x = 0.168\mu m$). Those two limitations makes difficult very precise analysis of focal plane images.

The simulations [1] of the focusing performance of the ball-lens shows that, in this configuration (NA=0.45) the wavefront aberrations are severe $\sigma_{RMS} = 0.7\lambda$ and can be described by primary and secondary spherical aberrations ($Z_{11} = 0.68\lambda$ and $Z_{22} = 0.11\lambda$).

3.2.2 Characterization setup for reflective elements

The second considered system is similar to the one described in the previous section. The difference consist on adaptation for measurements of the reflective structures (e.g. mirrors, silicon molds of microlenses or curved faces of microlenses). The measurement of reflective optical micro-components tends to be problematic as it was discussed before. This system is similar to the transmissive one

[1] performed within ZEMAX

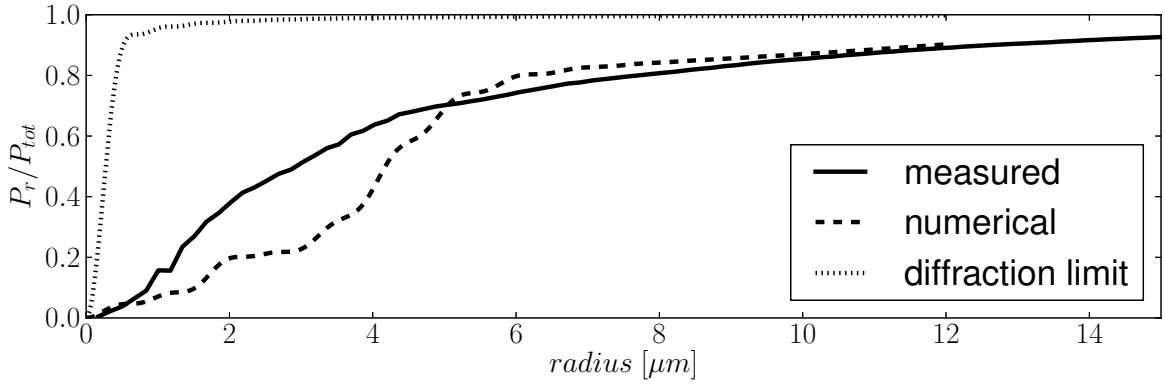


Figure 3.9: Encircled energy plot for focal plane of a ball lens - Energy distribution visualized by the plot of fraction of total power encircled in a circle of certain radius. Plot compares measured dependence with numerical calculated relation and the diffraction limited case.

and helps to quantify the quality of curved reflective surfaces without the problem of light vignetting encountered in the classical systems (figure 3.3).

3.2.2.1 Theory

The basic aim is to obtain similar data from a measured object as in the transmission system. In particular, estimation of aberrations generated by the investigated structure is targeted.

In the reflection mode, the use of collimated beam as the probing beam is not an applicable. In here, we use the optical configuration that is commonly employed for optical measurement of radii of curvature (ROC) of reflective surfaces [161, 169, 170]. This system (figure 3.10) relies on specific reflection from a spherical surface. When a convergent beam impinges on a spherical mirror, the reflected beam is perfectly inverted if its focus is located at the center of curvature (COC) of the mirror. This arrangement is usually referred as "confocal configuration". The measuring system then relies on measuring the IPSF of the measured object in this specific imaging configuration. This measurement configuration corresponds to imaging a point located in COC. And IPSF of this specific configuration (aplanatic point of spherical mirror) is analyzed. The optical implementation of the imaged point-object located at COC is achieved by a focused beam used as a virtual source (point object). The beam focusing is performed by the objective already used in the collection system.

In here, we perform sequential axial scanning of the investigated object in order to image different slices of the focal spot generated by a measured surface. Similarly, to the transmission system, the

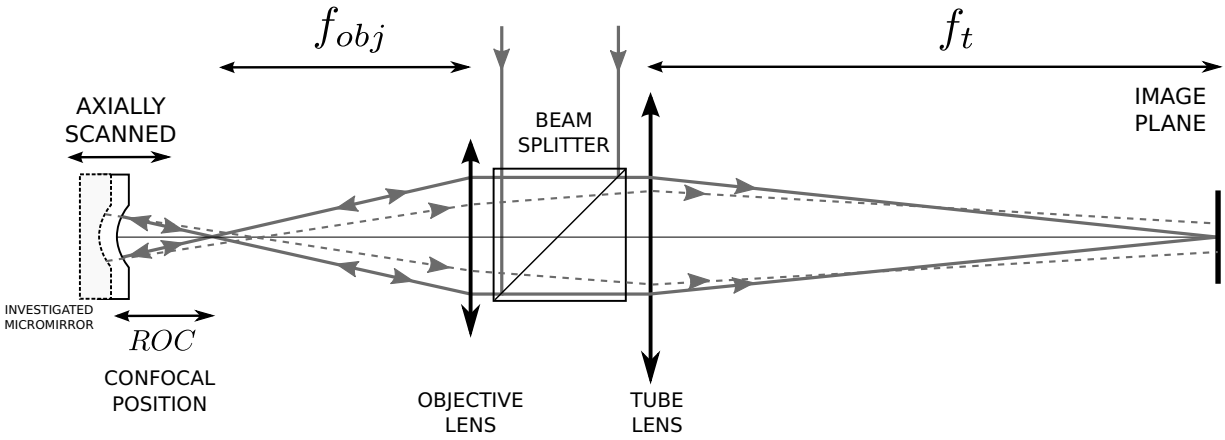


Figure 3.10: Measuring system for reflective elements - Collimated beam enters the system from the side and is redirected by a beam splitter to the objective that focuses the beam in front of the measured sample. The confocal position is a specific arrangement of (objective)-(curved measured object) where divergent beam impinging the curved object is retro-reflected to the imaging system along the same trajectories. The probing beam is generated by the same objective that is used in collection block, the beam input to the system is achieved by placing a beam-splitter between the objective and the tube lens.

imaging of the system can be described by the diffraction integral (equation 3.2) [170]:

$$I_r(u,v;\Phi) \propto \left| \int_0^1 \int_0^{2\pi} P_{obj}(\rho,\theta) P_m(\rho,\theta) P_{obj}(\rho,\theta-\pi) e^{ik\ 2\Phi(\rho,\theta)} e^{-iu\rho^2} e^{-iv\rho cos(\theta-\phi)} \rho d\rho d\theta \right|^2 \quad (3.2)$$

The response consecutive to the scanning is slightly different than in the transmission mode (equation 3.1). This is a natural consequence of working in reflection for which light encounters a round-trip. This round-trip leads, on the one hand, to a factor 2 multiplying the aberration term. It is important to note that, in here, the aberration function $\Phi(\theta,\rho)$ is directly defined by the geometry of the measured object, literally how it geometrically deviates from a sphere. This is not true for measurements of microlenses in the transmission mode for which basic geometrical analysis demonstrates that perfectly spherical lenses do not generate spherical wavefronts [6]. The second consequence of the round-trip, visible when comparing diffraction formulas describing the two systems, lies in the defocus parameter, which is also multiplied by two. In consequence, measured 3D intensity does not correspond directly to the object IPSF but is axially compressed. Another difference with the transmisive system is the double use of the objective of imaging system (focusing and collection). Thus, the quality of objective is literally twice more important than in the transmisive system, since any aberrations present in the objective are also doubled within the round-trip of the beam.

As it was mentioned before, this optical configuration is based on the systems for radius of curvature (ROC) measurement [170]. Consequently, although the primary target of our system is the measurement of micro-components quality via the IPSF analysis, this system can also be used (without any modification) to precisely measure the radius of curvature of the investigated micro-components. The ROC measurement principle is sketched on figure 3.11, it is based on axial scanning of sample between two characteristic points of a spherical surface. In addition, to the confocal position, the second particular position of the measured object corresponds to the generation of a focalized spot in the image plane of the collection system. This point, so-called "cat's eye position", corresponds to the location of the object in the focus of the probing beam. The difference between confocal and cat's eye positions is equal to the radius of curvature of the object.

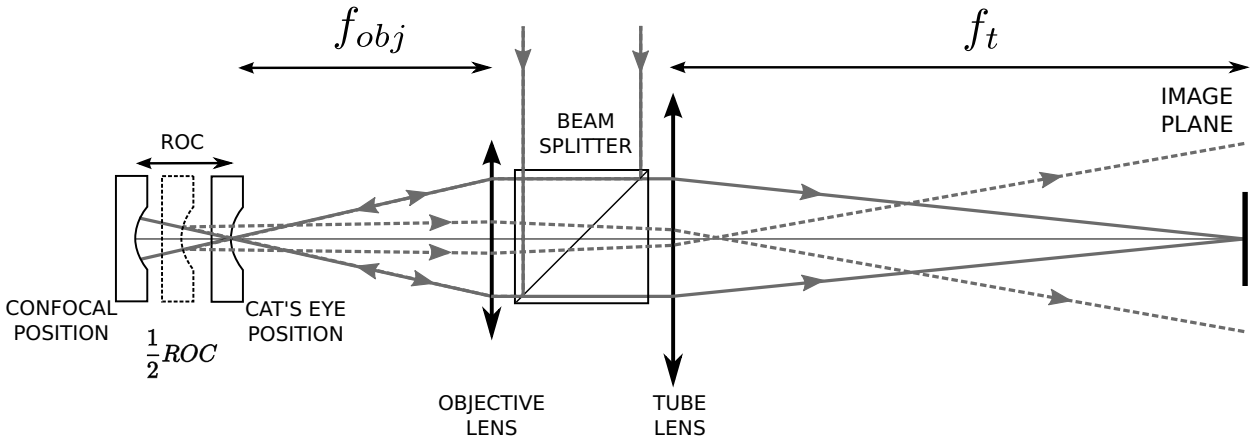


Figure 3.11: In reflection measuring system for ROC measurements - Cat's eye and confocal positions are the two positions that "refocus" the beam at exactly the same location than when the incoming beam is focused by the objective. The detector located in the conjugate plane to the focal plane of objective records the form of reflected beam.

The ROC measurement within this system can be simply understood when considering the ideal case of a perfect spherical reflector as a measured object. In such case, the object axial scanning generates a spot in the image plane whose size depends on the object position. When the sample is located in the cat's eye or confocal position, the image on the camera takes the form of the focused spot (solid rays in the figure 3.10). In the other cases, the spot projected onto the camera has larger size (dashed rays in the figure 3.10). Then, the on-axis intensity is recorded as a function of the object displacement and the two intensity peaks correspond to the cat's eye and confocal positions of the investigated object and their separation to its ROC (figure 3.15). The axial response of the

system near the cat's eye is described by equation 3.3.

$$I_r(u, v = 0; \Phi = 0) \quad = \quad \left| \frac{sin(u/4)}{u/4} \right|^2 \tag{3.3}$$

where $I_r(u, v = 0, \Phi = 0)$ is the on-axis intensity in the vicinity of the cat's eye position. In the case of a perfectly spherical mirror, the intensity responses at the two positions are supposed to be the same. However, the intensity response near the confocal position is highly dependent on the geometry of the reflecting surface and thus, any deformation of the geometry of measured surface leads a different axial response at the cat's eye position. In consequence, the ROC measurement of not-ideally spherical objects results in ROC averaged over the area of the object [170].

Additional, advantage of the cat's eye position is that it can be used as a reference measurement for testing the imaging system quality. In fact, the 3D response function of reflection from cat's eye mirror location does not depend on geometry of the mirror but only from the quality of the optical system used for illumination and collection (figure 3.14a).

3.2.2.2 Implementation.

Both measurements systems (transmissive and reflective) are assembled as a single measurement station (figure 3.12). The illumination beam in the reflection mode is redirected to the objective by a beam-splitter cube placed between the objective and the tube lens of the imaging system. The measured object reflects the incident focused beam to the imaging system. The latter images the focal plane of the objective onto the CMOS camera.

The imaging setup works in the infinite conjugate configuration[1], so that the beam-splitter can be placed between the tube lens and the objective without deterioration of optical quality of imaging system. Since polarizing beam-splitter is used, a quarter-waveplate is required to rotate polarization before re-entering the beam-splitter (figure 3.13). To investigate the volume of the focus generated by the measured object, axial scanning is performed by displacing the object by a servo motor along the optical axis. From the point of view of system control and data analysis, the system is not different from the transmission mode, i.e., same image acquisition and post-processing is used.

3.2.2.3 Data analysis and example measurement.

The reflection mode system allows two types of measurements. The first one corresponds to the same analysis than the one performed by the transmissive system.

[1] imaged plane corresponds to focal plane of the system objective

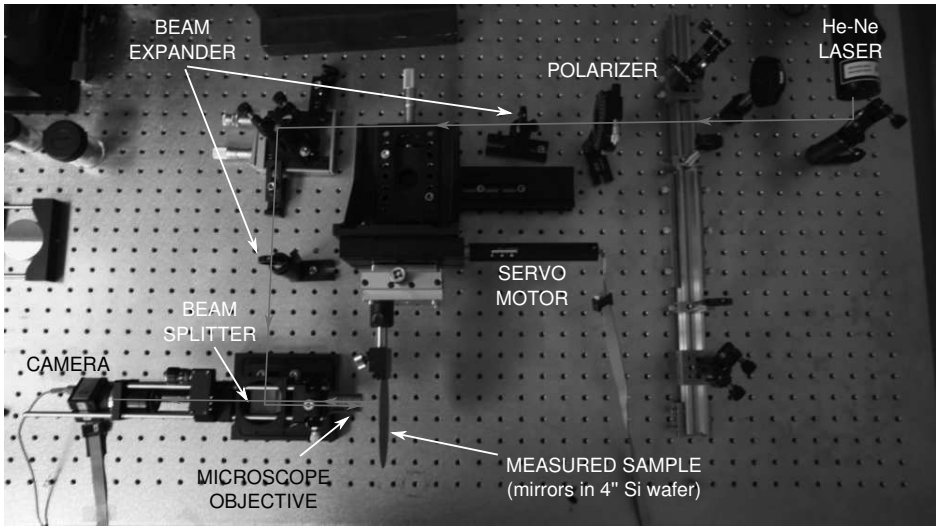


Figure 3.12: Realization of characterization system in "reflection mode" - Optical setup is the same as used in transmission mode, the main difference is different path of illumination beam, that is introduced to the measuring system from the side by the use of a beam splitter cube. The reconfiguration of the setup between transmission and reflection modes is made by sliding-in or out the rail with mirrors and beam expander of transmission configuration.

The second analysis is a classical measurement of ROC. As it was discussed before, the accurate determination of ROC can be done by investigating the axial intensity variation $I_r(u, v = 0)$. In practice, since used detector is a pixelized camera, the real intensity information are not accessible. Moreover, since perfect alignment of the optical system is never possible (measurement setup - sample), the optical axis of the system is not well defined. To address this problem, the axial dependence of power encircled in the small pinhole located in the center of the beam instead of axial intensity is investigated. The beam center is found for each z-frame separately, that makes the method insensitive on possible beam misalignment. The power in the pinhole is calculated by numerically integrating the intensity located in the circular pinhole of a given size (usually pinhole size is in order of the lateral size of the focal spot).

In order to validate the characterization system, test measurements were performed with an object of known and well-defined geometry, i.e., the previously used micro ball-lens. The measurement data used for ROC determination are presented on figure 3.15. The resulted $ROC_{meas} = (247.5 \pm 0.7)\mu m$ is consistent with specifications given by producer (deduced from the diameter precision: $ROC_{spec} = (250 \pm 1.5)\mu m$). It can be noted that the lens was measured without any additional reflective coatings. Indeed, all reflections observed by the system originate from the

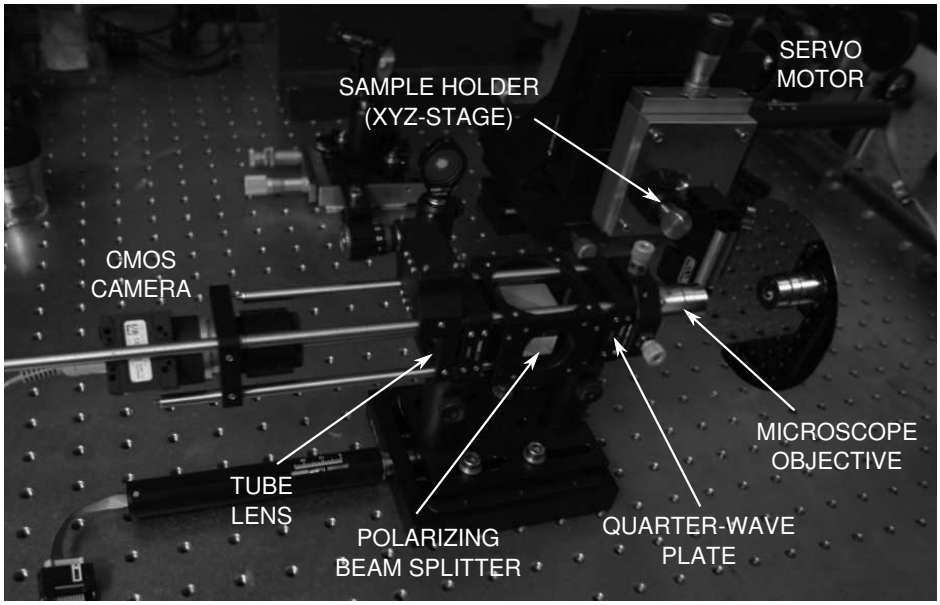


Figure 3.13: Reflection mode - imaging system - Same system as used in transmission configuration, additional elements needed to work in reflection - the beam-splitter cube and quarter wave plate does not influence the measurement in transmission mode.

Fresnel reflections on the dielectric boundary[1]. From the same data set, the geometrical extension of focal spot can be extracted and reads as: $\delta z^{fwhm}_{cat'seye} = (6 \pm 1)\mu m$, $\delta x^{fwhm}_{cat'seye} = (1.0 \pm 0.2)\mu m$, $\delta z^{fwhm}_{confocal} = (9 \pm 1)\mu m$ and $\delta x^{fwhm}_{confocal} = (1.0 \pm 0.2)\mu m$. From the sizes of the focal spots and their geometry (figure 3.14), we can deduce that aberrations are small (the diffraction limited spot would have sizes: $\delta z^{fwhm} = 4.5\mu m$ and $\delta x^{fwhm} = 0.7\mu m$).

Another, often used measure of aberration is the Strehl ratio (SR) which compare the maximal values of IPSF of aberrated system with the ideal one.

$$SR = \frac{max(IPSF(\vec{x}, \phi))}{max(IPSF(\vec{x}, \phi = 0))} \tag{3.4}$$

where ϕ is a wavefront aberration function. Since it is a single scalar value, Strehl ratio gives a simple but pertinent quantification of the lens quality [167, 171]. In the low aberration systems, the SR is defined by statistical measure of aberration function, literally the wavefront RMS (root mean square) related by Maréchal approximation:

$$SR \approx e^{-(\sigma_\phi)^2} \approx 1 - \sigma^2_\phi \tag{3.5}$$

[1] this can pose a question if in this configuration cat's eye and confocal position are complementary, the answer is yes since focused beam reflected in object vertex has flat wavefront whereas in confocal position, reflection for all rays are normal to the lens surface

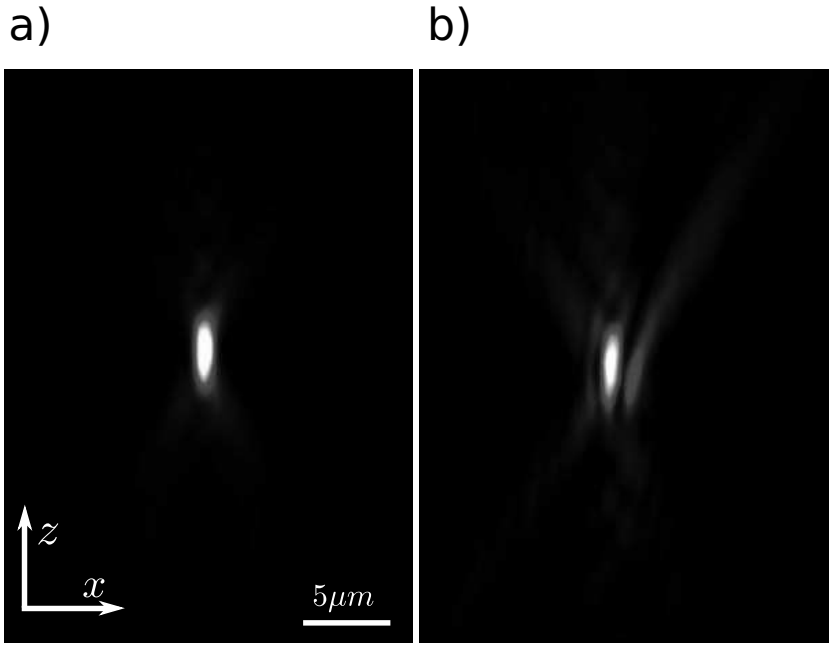


Figure 3.14: Focus spot response in reflection mode of $500\mu m$ diameter ball lens - Measured focal spot (xz slice) in two cases (a) reference reflection, i.e. cat's eye position and (b) confocal position.

From the equation 3.5, it can be noted that determination of Strehl ratio allows the estimation of wavefront σ_ϕ that is the most common aberration quantification. Moreover, SR is a decreasing function of σ_ϕ. The strong relation $SR(\sigma_\phi)$ allows precise estimation of the optical quality of analyzed optical system through the experimental measurement of SR. However, this approximation is only valid for system having low aberrations ($\sigma_\phi < 0.15\lambda$). For systems characterized by higher aberrations, the peak intensity value is not directly related to σ_ϕ but depends on specific form of the system aberrations [172, 173]. In consequence, the SR is meaningful only for the elements of relatively high optical quality[1]. The through focus images (sometimes called aerial images) of the focus spot can be directly used to obtain SR [167].

$$SR = \frac{max(IPSF(\vec{x}, \phi))}{P_{tot}\pi\frac{NA^2_{\mu Lens}}{\lambda^2}} \tag{3.6}$$

where, $max(IPSF(\vec{x}, \phi))$ is the peak intensity in the 3D focus pattern and P_{tot} is the total power

[1] in some cases, highly aberrated system can exhibit larger SR than less aberrated system [172]. However, in such pathological cases, SR cannot be correlated with optical quality (resolution) of the optical system.

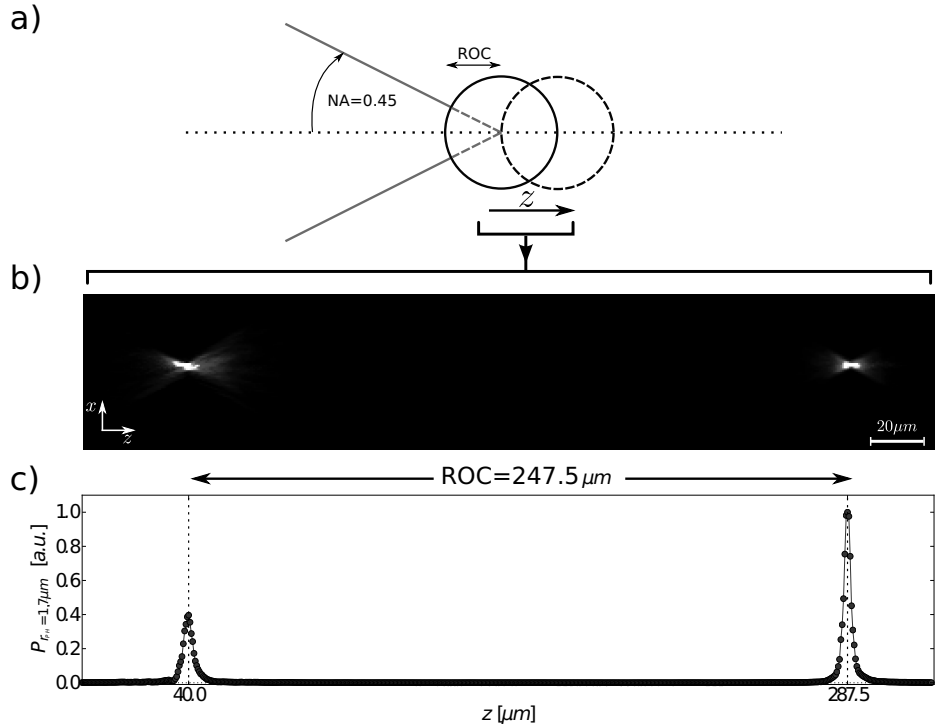


Figure 3.15: ROC measurement of $500\mu m$ **diameter ball lens** - a) scheme of measuring configuration, b) slice (XZ) of measured intensity along all scanned distance ($320\mu m$) visible two focal spots correspond to confocal (left) and cat's eye (right) positions, c) plot of power passing through virtual pinhole ($r = 1.7\mu m$) located on the center of the beam, clearly visible two peaks allows accurate location of confocal and cat's eye position and determine the ROC value.

carried by the beam. Both $max(IPSF(\vec{x}, \phi))$ and P_{tot} can be obtained from measured 3D IPSF data. Although the $NA_{\mu Lens}$ has to be known *a priori*, it can be, in some cases, also calculated from the data (for SR measurements, it is preferable to set $NA_{obj} < NA_{\mu Lens}$ to set a well-defined NA). The estimation of numerical aperture could be made by measuring lateral or/and axial extension of the focal spot, i.e. recalling that $\delta_x^{fwhm} = 0.5\lambda/NA$ and $\delta_z^{fwhm} = 1.4\lambda/NA^2$. Nevertheless, in the presence of aberrations, these relations do not hold and estimation of NA based on focus extensions is not precise. However, it can be mentioned that if the measured microlens tends to be used in the same configuration than in the measuring system, the values δx, δz represent a good estimation of the optical resolution of the element.

With the ball lens, since aberrations are relatively low, the Strehl ratio is well-defined and directly related to wavefront aberrations by equation 3.5. The calculation of Strehl ratio requires calculating P_{tot} and $max(IPSF(\vec{x}))$. For this purpose, the first step consists in the determination

of the focal plane localization from the 3D IPSF data. The focal plane location can be defined in different ways (for instance by minimal spot radius or wavefront deviation [174]), however, since we do not have information about wavefront and since calculation of the spot radius for every collected plane is cumbersome, we look for the maximum intensity peak value of 3D IPSF. This approach is equivalent to the definition of the focal plane by maximal Strehl ratio, that, in the limit of small aberrations, is equivalent to minimal wavefront deviation at focus plane.

Total power is calculated by integrating the intensity over the whole focal plane. In the context of available numerical data, the simplest approximation of total power can be made by summing the intensity values recorded by the camera, i.e., $P_{tot} = \sum_{i,j} I(i,j)\delta x^2$, where $I(i,j)$ is the intensity level in the focal plane at the grid coordinate system defined by pixel indexes i, j, and where δx^2 represents the surface of the pixel (in $\delta x = 0.168\mu m$ at object space coordinates). Peak intensity is approximated as the maximal value in the measured data. The estimated Strehl ratio is for cat's eye position $SR_{CE} = 0.85$ and is, in the case of confocal position, $SR_{CF} = 0.5$. The < 1 value of Strehl ratio in the cat's eye position can be attributed to the aberrations present in the imaging system (optical system characterized by $SR > 0.8$ can be considered as diffraction limited) which limits the precision of our measuring system. Wavefront aberration of the imaging system can then be estimated using the approximation (3.5) as $\sigma_{obj}^{ref} \approx \frac{\lambda}{16}$. Moreover, since this value corresponds to a round-trip, the estimation[1] for a single pass about the performance of the imaging system in the transmission mode is $\sigma_{obj}^{tr} \approx \frac{\lambda}{32}$, that corresponds to $SR = 0.96$. This value demonstrates the high quality of the imaging system used in our setup based on a high quality microscope objective (Nikon CF Plan, 50x/0.45 SLWD). In the confocal position, wavefront deviation reads as $\sigma_{\mu Lens}^{r} \approx \frac{\lambda}{8}$ that once transformed to geometry RMS deviation is equal to $\sigma_{\mu Lens}^{geom} \approx \frac{\lambda}{16}$. For used $\lambda = 633nm$, it gives a surface deviation as $\sigma_{\mu Lens}^{geom} = 40 \pm 10nm$. The manufacturer specifications on the lens geometry accuracy mention only the sphericity precision defined as maximal expected diameter difference of lens sections. In consequence, it can be expected that used ball lens exhibits some level of spheroidal form. From maximal diameter difference (specified as $1\mu m$), the RMS geometrical deviation on an observed zone (45% of lens diameter defined by $NA_{obj} = 0.45$), is calculated as 27nm. This value is in good agreement with the experimental results showing the high performance of the direct characterization despite its rather simple implementation.

[1] used estimation assumes doubling of aberration in the round-trip case, that is not strictly valid: firstly the beam formation (beam expander) is different in two modes, secondly objective aberrations should according to eq. 3.2 be added as $\Phi(\rho,\theta) + \Phi(\rho,\theta-\pi)$ not simply doubled. However only objective is working in the high NA configuration and since aberration doubling, instead adding, is the worst case scenario, this approximation can be safely used.

3.3 Conclusion and perspectives

Characterization of focusing micro-optical components fabricated by wafer-level methods is important for optimization of fabrication processes. Nevertheless, standard methods are usually limited to low numerical aperture components. Thus, in this chapter, different techniques that will be employed in the next chapters are presented, namely topography measurements based on dicing and SEM imaging as well as scanning profilometry and interferometry. In addition, a direct optical characterization based on a rather simple setup has been proposed. The direct characterization of optical response of focusing micro-elements allow simple, but very precise estimation of micro-structures quality. As the geometry of optical surfaces largely defines the optical transformation of the beam, the measurement of point spread function is adapted for precise characterization of micro-elements. Moreover, the measurement corresponds to the typical use of optical components, then optical performance in terms of achievable resolutions can be directly obtained. In this preliminary work, we use only a simple data analysis to derive basic parameters of the measured focal spots. However, much more information about the micro-optical elements can be obtained from such data (3D IPSF). More sophisticated analysis, for example Njober-Zernike wavefront retrieval algorithm developed by Braat et al. [164], allows to calculate the wavefront shape from the through focus images. This method would give full information about the investigated object including the additional possibility of calculating the object geometry in the case of measurements in reflection.

4

Realization of microoptical components for on-chip confocal microscopy

Introduction and Objectives

This chapter is dedicated to the development of all the different optical sub-components required for the MOEMS-based confocal microscopes. It concerns, namely the investigation of silicon etching processes aimed at fabricating mirrors (i.e. for Schwarzschild micro-objective) or molds for microlenses that are supposed to be integrated onto actuators (scanning block) or to be integrated onto the last substrate (focusing block in 1^{st} demonstrator). This part, gathering different types of wet and dry etching of silicon is addressed in the first section of the chapter.

Then, the second section deals with the generation of a micro-beam-splitter, that can be fabricated at wafer level and allows once added to the 3D-scanner, to build a complete, miniature, vertically integrated confocal microscope.

Finally, in the third section, the design and fabrication of the Schwarzschild objective is addressed. As it was discussed in the second chapter, this anastigmatic component allows increasing the performance of the system, especially in the edges of the scanning volume. For this purpose, theoretical study of the objective is first given, to set the required dimensions and fabrication tolerances.

4.1 Technology of micro-mirrors and micro-lenses

In this section, we investigate the process for micro-optical components (lenses/mirrors) that are based on silicon etching. Three different techniques are investigated: anisotropic wet etching in aqueous KOH solution, isotropic wet etching in mixture of HF and HNO_3 acids, and silicon dry etching in SF_6 plasma.

The micro-optics fabrication based on silicon as the building material, allows using established bonding technologies for the integration of optical elements with MEMS structures. The use of monocrystalline silicon as building material for curved optical structures can be challenging. Indeed, The well-defined crystallography of used silicon substrates is responsible for anisotropic properties of the material. In the context of fabrication of smooth, curved structures, these effects can lead to undesired effects such as direction dependent etching resulting in asymmetry of generated structures.

Silicon as non transmissive material in visible spectrum can be directly used as a substrate for mirrors. In the context of microlenses generation same techniques can be employed, however, etched structures are used as molds, that in the process of replication are transformed into refractive microlenses.

The aim of this section is to investigate and to compare different etching techniques for fabrication of microlenses and micromirrors that can be part of miniaturized confocal microscope.

4.1.1 Wet etching of silicon with KOH solution

Aqueous solution of KOH is widely used in MEMS fabrication as a simple method of anisotropic etching of monocrystalline silicon [175]. The usual geometries generated by KOH mixture takes the form of sharp structures limited by planes bounded by corners. This property of KOH etching solution is frequently use for generation of membranes and tilted or vertical planes. The specific topography of generated structures originates from chemical anisotropy, i.e., the chemical etchrate (silicon removal rate) of monocrystalline silicon is highly dependent on the crystallography of the exposed surface. However, if anisotropic structures are mostly generated, KOH etching can also in some cases be employed for fabrication of smooth, curved structures.

4.1.1.1 Theory

The process proposed by Kendall [176, 177] allows generation of mirror-like structures by use of a two step KOH anisotropic silicon etching process. The scheme of the process is presented in figure 4.1. The first step consist in anisotropic etching through a mask. In case of (100) oriented wafers this

process eventually leads to the creation of an inverted pyramid (figure 4.1b). The pyramid is formed by {111} planes that are not etched in KOH solution[1]. Subsequently, the second etching process is performed without the mask. This so-called maskless etch is responsible for the transformation of pyramidal depression into a smooth spherical-like structure. During this step, sharp corners between {100} and {111} planes are rapidly etched. Actually, etching of the convex corners leads to exposition of {411} planes (figure 4.1d) that are locally (between {100} and {111}) the fastest etched planes (figure 4.2). Then, when etching progresses four {411} meet at the vertex of the original {111} pyramid forming at this moment an inverted pyramid made by {411} planes (figure 4.1e). From this point the bottom of the structure starts etch with different (slower) speed than other regions of the structure. This etchrate gradient is responsible for the curved bottom of the pyramid (figure 4.1f). The prolonged process leads to evolution of the size and the curvature of the bottom part and eventually suppresses pyramid forming facets and create a smooth cavity.

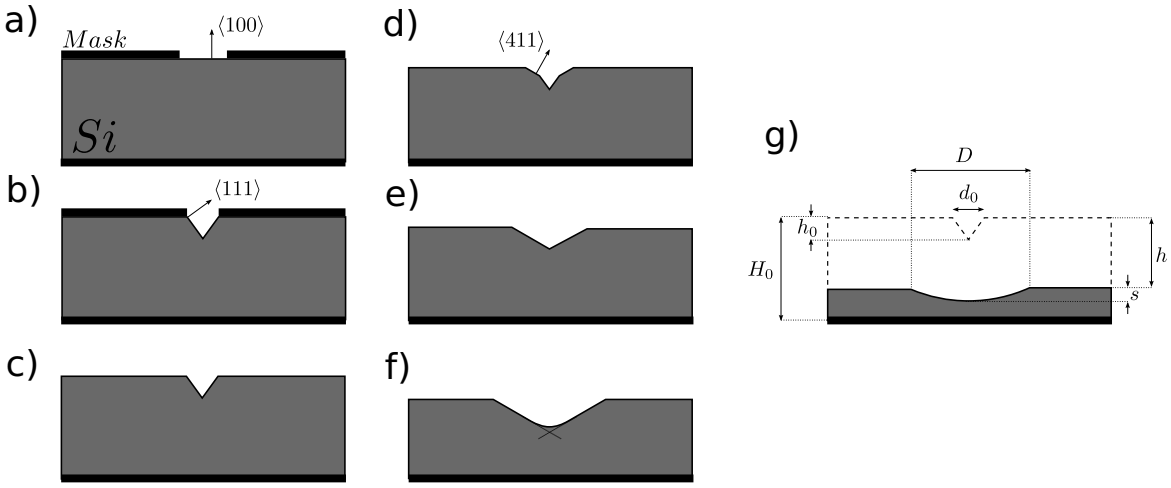


Figure 4.1: KOH etching for spherical cavities generation - Two-step etching process proposed by Kendall: (a) the first step, the etching is performed through a mask. This results in a pyramid structure limited by four {111} planes (b). After removing the mask (c), the maskless etching is performed (d)-(g). During this step, the {111}-limited pyramid is transformed into a pyramid bounded by {411} planes (e). Continued etching produces the rounded part at the bottom of the pyramid that grows and eventually replaces all {411} planes, leading to smooth spherical-like depression.

The evolution of depth and diameter of the curved cavity is given by [177] relation derived by

[1] {111} Si planes have non-zero etchrate but etching speed is much slower than for other planes

geometrical reasoning (equation 4.1) or by empirical approach (diameter) (equation 4.3)

$$s = \frac{d_0}{\sqrt{2}} + \frac{d_0}{m}\left(\frac{1}{2}sin(\theta) - \frac{1}{\sqrt{2}}cos(\theta)\right) \tag{4.1}$$

where m is a ratio of etchrate of the locally fastest etched planes ($\{411\}$) to the etchrate of $\{100\}$ plane: $m = v_{411}/v_{100}$ (in solution used in this work $m = 1.71$), and θ is the angle between two mentioned planes $\theta = 19.24^o$.

$$D = 7.8h^{0.58}d_0^{0.42} \tag{4.2}$$

where h is the etch depth along the wafer thickness. The curvature of generated structure is usually obtained from equations 4.1 and 4.3 **assuming** the spherical geometry [145, 177] of the curved area.

$$R = \frac{D^2}{8s} + \frac{s}{2} \tag{4.3}$$

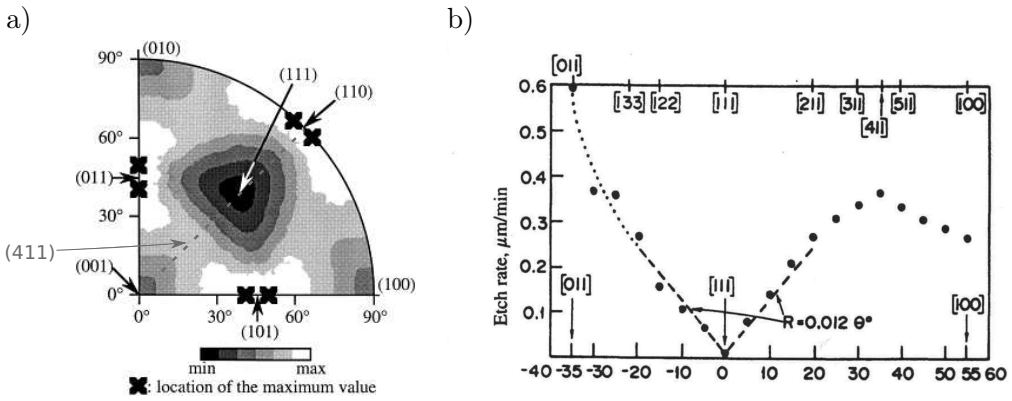


Figure 4.2: Anisotropic etchrate in KOH solution - (a) Experimental etchrates map obtained by Sato *et al.* [178] from hemisphere etching experiment and (b) etchrate dependence along different crystallographic directions (investigated directions indicated by the dashed red line on (a)) showing smooth local etchrate maximum around (411) direction [179].

4.1.1.2 Fabrication

The realization of curved microstructures by KOH etching of silicon is based on standard MEMS fabrication processes. Silicon (100) wafers are employed. The first KOH etching (figure 4.1) requires protective mask on the silicon substrate. Depending on the etching conditions (temperature, etching time) different masking materials can be used. The common masking material used for wet-anisotropic silicon etching is thermally grown SiO_2. However, silicon oxide is also slowly etched

by KOH solution ($v_{SiO_2} \approx 7nm/min$). The oxide mask can be used only for relatively short etching processes since thermal oxidation can provide only limited thickness of masking layer ($d_{SiO_2} < 2\mu m$).

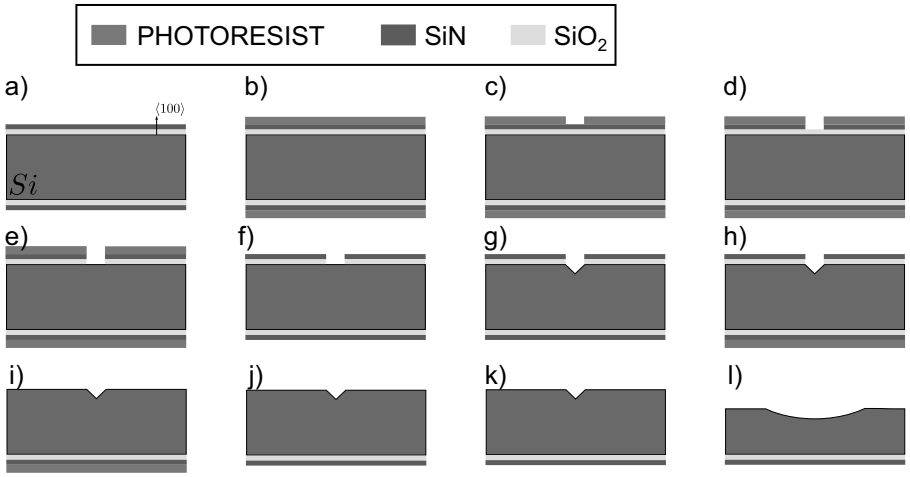


Figure 4.3: Fabrication process steps for mold generation by KOH - initial silicon wafer with SiO_2 (500nm) and SiN (150nm) (a) is covered with photoresist by spincoating, desired pattern is transferred into resist by UV lithography (c), patterned resist is used as masking layer for etching SiN and SiO_2 layers (d) and (e), that is performed by RIE processes (SF_6 based for SiN etching and fluorocarbon based for SiO_2 etching), After SiO_2/SiN opening resist is removed and wafer is cleaned (f), the next step is first KOH etching process that form inverted pyramids in the silicon (g). The consequent steps concerns mask removing from the wafer frontside of the wafer by use of a fluorocarbon RIE process (i). Next step is a backside resist protection removal (j) and wafer cleaning with Ar/O_2 plasma (k), the last step is the KOH etching that generates the final structure (l).

Alternative mask materials are gold (Au) or silicon nitride (SiN). Gold mask is characterized by high chemical resistance, however, it has low mechanical strength, and poor adhesion to silicon surface. The adhesion problem is usually solved by an adhesive layer, i.e., thin layer ($d_{ad} = 10 - 50nm$) of chromium (Cr) or titanium (Ti) deposited between silicon surface and the gold layer. Poor mechanical robustness of gold mask can results in mask cracks and solution contamination that can in turn cause increased roughness of the etched structures.

Mask from silicon nitride is chemically and mechanically very stable and is often considered as the best mask for deep KOH etching. It is important to notice that properties of thin layer of silicon nitride is very dependent on the method of deposition. The silicon nitride layers deposited by means of PECVD process usually have much lower chemical resistance than the one deposited by LPCVD process. Moreover, within those two families of deposition processes various parameters

can change the behavior of the final layer. In this work, KOH etch has been performed with mask made of LPCVD SiN layer deposited on thermally grown oxide layer that provides buffer layer between Silicon and rigid SiN layer, moreover tensil stress generated during LPCVD SiN deposition can be compensated by compresive stress present in the thermal oxide.

The fabrication scheme is presented on figure 4.3, as the starting point silicon wafer (100mm diameter) with double layer of SiN/SiO_2 (bought already prepared from the supplier) is employed. The pattern generation in SiN/SiO_2 layer is performed by contact UV photolithography technique. For this purpose the photosensitive resist (SPR220, thickness $2.7\mu m$) is spincoated on the wafer and the desired pattern is transferred to the resist thought the chromium mask prepared by laser writing system[1]. The initial mask openings are circular and inverted pyramid created in the first KOH process are self-aligned to the crystallography of silicon substrate. The etching of SiN with mask formed from photoresist is performed by RIE in SF_6 plasma ($p = 60\mu bar$, $flow_{SF_6} = 15sccm$, $U_{bias} = 260V$). Oxide etching is also performed by RIE but witch a mixture of fluorocarbon gases ($p = 60\mu bar$, $flow_{CHF3} = 10sccm$ $flow_{C2F6} = 15sccm$,$U_{bias} = 380V$). One the mask opened KOH etching is performed in 10M aqueous solution at a temperature 80^oC. For this purpose, the glass etching baker containing the KOH solution (1.5L) is placed into a heated water bath in order to achieve good control of the etchant temperature. The etching is performed without the agitation, where wafer in the etching baker is placed horizontally, etched side up, this assures uniform temperature during the process and facilitates releasing gas generated during etching process. The process time (t_1) of the first etching aiming at generation inverted pyramids (figure 4.3) is defined by the size of the larger openings patterned on the wafer.

$$t_1 > \frac{d_0}{v_{100}\sqrt{2}} \tag{4.4}$$

The inverted pyramid generation by KOH is a self stopping process ($\frac{v_{100}}{v_{111}} \approx 300$), and prolonging the time does not influence the final structure. This effect will allow the generation of mirrors of different parameters on the same wafer simply varying opening of the initial mask (d_0) within the substrate. The mask removing (stripping) necessary for second anisotropic etch is performed in RIE system by means of fluorocarbon plasma process used to dissolve both masking layers. After mask stripping, wafer is cleaned in reactive plasma (flow$_{O_2}$ = $18sccm$, flow$_{Ar}$ = $3sccm$,p=0.21Torr,P=550Watt,T=170°C, in Nanoplas) to remove fluorocarbon film deposited on Si during mask removing process. This step is important since any residual fluorocarbon that rests

[1] mask design is prepared in the KLayout - an open source CAD software [180]

on the silicon surface can act as a mask during KOH process and can lead to increased roughness of resulting structures. The final KOH maskless etching is performed in the same conditions than inverted pyramid generation. Front side of the wafer is etched on the whole surface, while the backside is protected by original mask material.

4.1.1.3 Experimental results and discussion

Realized structures appears to be circular (footprint) and spherical-like (profile) when they are observed by an optical microscope or a 1D-scanning profilometer. However, the more precise characterization of their geometry reveals that structures poses residual 4-fold rotational symmetry originated from the Si substrate crystallography. In figure 4.4 the 3D-topography measurement obtained by scanning optical profilometer[1] is presented. It can be noticed that the raw data

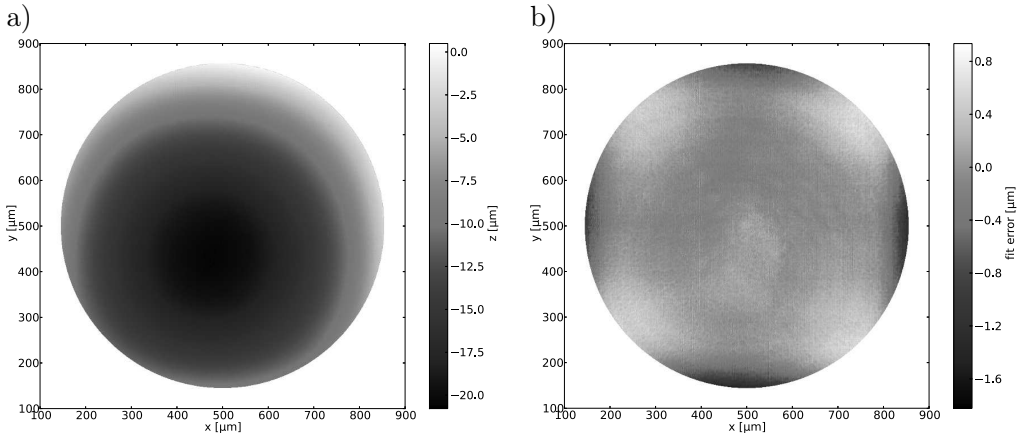


Figure 4.4: Scanning profilometer topography measurement of KOH structure - (a) topography of KOH structure obtained by scanning optical profilometer (NanoJura) and (b) difference between fit and measured data. Deviation from axial symmetry is well visible, large deviation from symmetry assumption of the model results in a poor fit quality: $RMS = 0.3\mu m$, The structure generated by relatively short maskless etch ($h_0 = 3.5d_0$).

obtained from the measurement (figure 4.4a) does not allow distinguish an asymmetry. However, when data are fitted to an axially symmetrical model[2], the 4-fold symmetrical pattern be noticed by observation of fitting error distribution. The level of asymmetry is directly related to the depth (duration) of the maskless etching, i.e., the deeper maskless etch, the lower amplitude of deviation

[1] Acknowledgments to Florian Maury from Institute Pierre Vernier for performing the measurements.
[2] in this case, axially symmetric parabola was used as a model

from axial symmetry. Figure 4.5 shows the topography measurement of the structure fabricated with a deeper maskless etch. Although, the same specific symmetry is still visible the amplitude is visibly smaller.

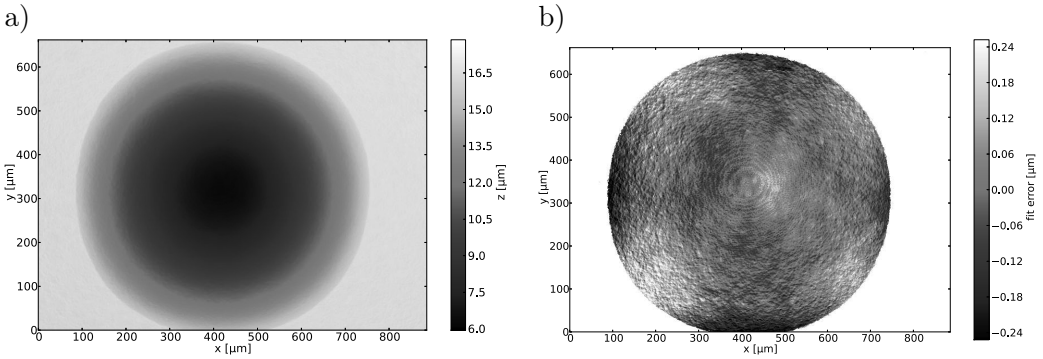


Figure 4.5: Optical measurement of KOH structure topography - (a) topography of the structure obtained by white light interferometer (Polytec) and (b) difference between the data and fitted axially symmetric parabola. The considered structure was fabricated within a longer etching ratio ($h_0 > 7d_0$). In this case asymmetry is less pronounced than in the previous case (fig. 4.4) but still visible. The fit error is $RMS = 0.08\mu m$.

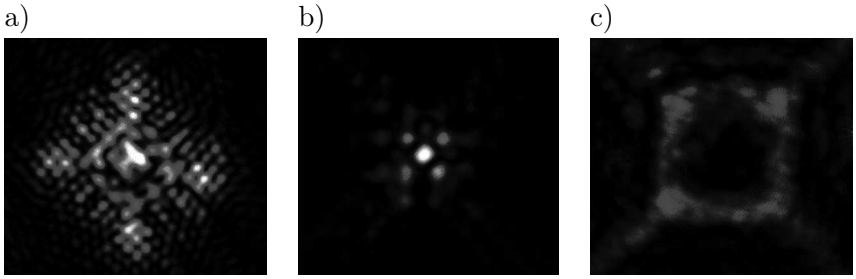


Figure 4.6: Lateral cross section of measured focus spot generated by KOH etched mirror - Optical measurements of beam reflected by the structure, reflected beam is not axially symmetric. The three images represent sections of a beam focused by the Si mirror: (a) before (b) at and (c) after the focal plane. It can be mentioned that three images are have not the same scale.

The optical consequences of particular non-axial symmetry of fabricated micro-structures was investigated by use of the 3D-IPSF characterization setup (described in chapter 3). The figure 4.6b shows sections of focal volume generated by the mirror generated by KOH based process (similar structure to the one analyzed in fig. 4.5). It is clearly visible that the focus is highly

influenced by the symmetry of the mirror (similar 4-fold symmetrical pattern in focal plane as seen in topography measurement). When observing IPSF section along propagation direction the effect of mirror asymmetry can also be noticed in the form of axial elongation of focal spot that is significantly different along two considered sections.

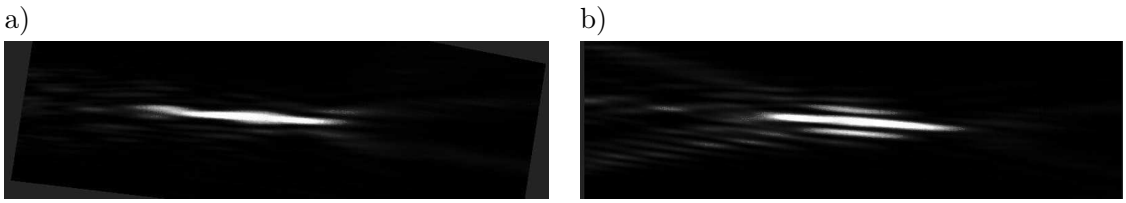


Figure 4.7: Axial cross sections of measured focus spot generated by KOH etched mirror - (a) focus section along XZ plane and (b) and along the diagonal $(X/Y)Z$ plane (in respect to fig. 4.6.

According, to these characterization, KOH etching in order to fabricate spherical structures can be employed only when long etching is applied. However, it also signifies that only low NA structures can be fabricated. The impact of slightly asymmetrical geometries depends largely on the specific application. In case of using as a mirrors the impact of asymmetry will be much more pronounced than in the case of microlenses replicated from KOH-generated molds.

4.1.2 Isotropic wet etching of silicon

The term "isotropic" in the context of etching of crystalline silicon has two interpretations. The first one is the independence of the etching regarding the crystallography of the substrate, whereas the second interpretation originates from the geometry of structures generated by masked etching. In the latter case isotropy means that etching is the same in all directions in respect to the wafer surface, i.e., vertical and lateral etch rate are the same. To distinguish this two often confused interpretations, we use in this work the term isotropic to describe the independence of etching versus crystallography, while we refer to the local uniformity of the process to define the directionality in respect to the wafer surface. This distinction is necessary when geometry of the rounded structures is considered. In case of fabrication of microlenses or micromirrors, any crystallographic dependence is undesired, however, the local non-uniformity of the etch rate can be used to control geometry of fabricated structures.

4.1.2.1 Wet etching models

In the framework of fabrication of optical components, for which the precise control of their geometry is required, model of process kinetics is needed. The kinetics of chemical etching is usually divided into two categories: reaction limited and mass-transfer limited.

In the reaction limited system the etching speed is defined by the chemical reaction rate of the dissolution reaction. This type of process, from the one hand is highly dependent on crystallography and temperature. From the other hand it is less dependent on etchant concentration and dynamic properties (viscosity, density, diffusion coefficient, agitation). Silicon etching in discussed in previous section aqueous KOH is an example of reaction limited process[1]. Anther reaction limited etching system often used in microfabrication that is etching of SiO_2 by aqueous solution of HF/NH_4F. This system in the case of crystalline material (quartz) exhibit high anisotropy [181], but produce uniformly etched smooth structures when applied to amorphous material etching [182].

The second family of processes is so-called mass-transfer limited. These etching processes are then defined by the concentration of etching species in the vicinity of the dissolved material. The particular case of mass-transfer limited etching appears when chemical reaction rate is faster than the delivery rate of reactive species to the etched surface.

[1] KOH silicon etching is usually considered as reaction-limited but it has some particular properties such as specific dependence of etch rate on the solution concentration, for some concentrations mass transport effects are also important.

In the case of wet-etching processes where the process takes place in a liquid (usually water based solution) the mass-transfer in the direct neighborhood of the surface is due to the diffusion phenomena. The diffusion originates from atomistic, random movement of the molecules composing the solution and it always tends to uniformization of concentration in the mixture.

An additional mass-transfer factors can also be important in etching processes related to large scale movements of the liquid (advection, agitation). However, in real systems where solution has non-zero viscosity in the vicinity[1] of the surface the diffusion is dominant mass transfer phenomena.

One important consequence of the mass-transfer governed processes is the particular tendency to form smooth and rounded structures in the case of masked etching. Moreover, even if the chemical reaction has some crystallography dependence the anisotropy is suppressed when the process is mass-transfer limited.

When of processing crystalline silicon, the mass-transfer processes are necessary to obtain isotropic etching unlike amorphous material (for example glass) where both type of processes can generate curved surfaces. However, the different process kinetics lead to different geometries of the etched structures. In particular, the isotropic etching of glass (reaction limited process) the bottom of generated structure remains flat [183, 184] while only underetched areas became rounded (figure 4.8b). Nevertheless, in the case of the mass transfer-limited process, nonuniform (geometry-dependent) etching leads to curved profile of the etched cavity (figure 4.8a). The shape evolution is then more complicated and more difficult to control than in the case of reaction-controlled case (figure 4.8b).

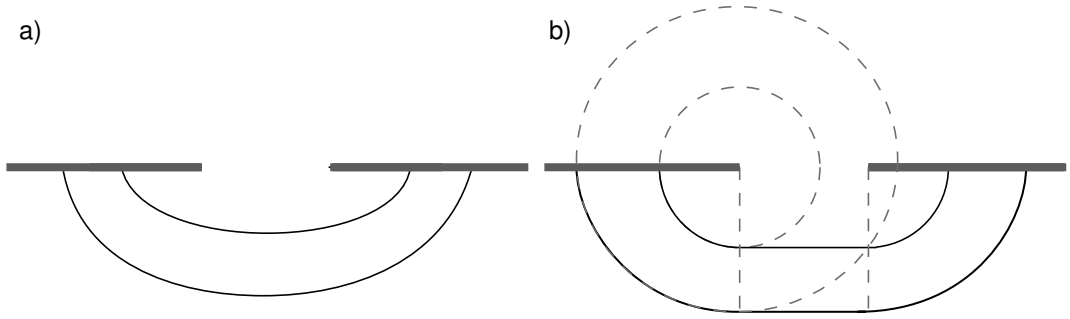


Figure 4.8: Isotropic etching geometries - a) mass transfer-limited and b) reaction-limited processes produce different geometrical structures

[1] In practice viscosity is responsible for stopping the macroscopic flow of a fluid at the stationary surface, it is responsible for creation of so-called diffusion layer - the area close to solid-liquid interface where diffusion dominates.

Chemistry of HF/HNO_3 silicon etching process: Isotropic wet-etching can be achieved in the mixture of concentrated water solution of HF and HNO_3 acids. The first chemical investigation of etching in HF/HNO_3 mixtures was done by Robbins and Schwartz [185, 186, 187, 188]. The etching process, achieved by multi-component mixture and being a multi-step reaction is difficult to describe by simple chemical formula. The overall reaction is often written as equation 4.5 [185]:

$$3Si + 4HNO_3 + 18HF \rightarrow 3H_2SiF_6 + 4NO + 18H_2O \tag{4.5}$$

where the resulting H_2SiF_6 is dissolved in the solution. This reaction, although commonly recognized, is a rough simplification and do not explain the chemistry of the etching process.

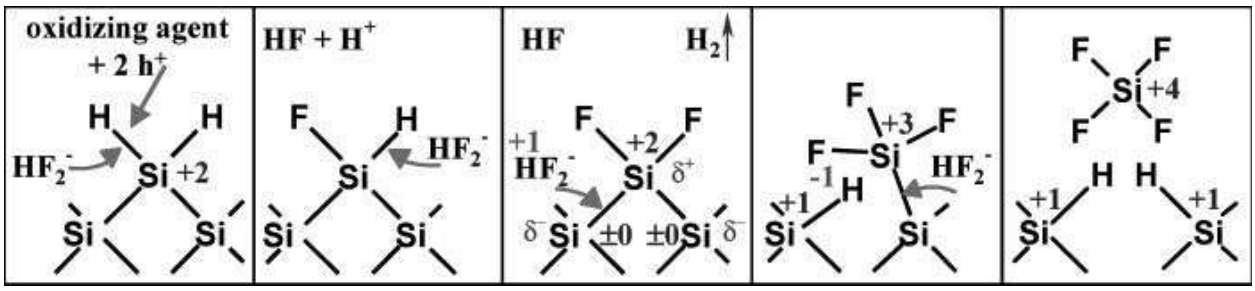


Figure 4.9: Scheme of silicon dissolution in HF/HNO_3 mixture - Reaction scheme proposed by Steinert [189] to explain silicon etching without intermediate SiO_2 formation. The form generated hydrogen (gaseous H_2 or H^+ ion) depends on HF/HNO_3 ratio of the etching mixture.

The complex electrochemical reactions that lead to dissolution of silicon are still under discussion [189, 190, 191]. The first model, relying on silicon oxidation by derivatives of HNO_3 forming SiO_2, that are subsequently dissolved by HF, was recently [189, 191] replaced by a model in which SiO_2 is not created (figure 4.9). The oxidation step occurring in the etching process relies on the N(III) species (N_2O_3,NO^+) created by decomposition of HNO_3 in the etching solution. The efficiency of this step determines the etching characteristics in the mixture. Moreover, since NO^+ is generated in the etching process (equation 4.5), the etching reaction is in some level autocatalytic [186, 192]. The effects of auto-catalysis is more pronounced in HF-rich regions where etch rate can be much lower in the beginning of the etching process than after a certain amount of Si is already dissolved [189]. Another important effect of non-direct species (created in the etching mixture) participating to the etching reaction is the fact that they are not stable when exposed to the ambient atmosphere. The decomposition ratio depends on solution composition, and according to [189] the better stability is achieved in HNO_3-rich mixtures.

The precise study of etching mechanism in HF/HNO_3 mixtures divides the process in two regions, differing in principal chemical mechanism that determines the etching kinetics. The two regimes are defined by the composition of the etching solution: the first one, so-called HF-rich regime produces rough (sometimes even porous structure) silicon surfaces because oxidation process is the rate limiting step. The second one, the so-called HNO_3-rich regime, leads to very smooth, rounded surfaces of etched sample. This system is also called the "polishing regime" since it is often use as a chemical polishing method in silicon wafer processing [193]. The obtained smoothing character and low-roughness surfaces with those mixtures allows using it for generation of spherical cavities in silicon that can be used as micromirrors [194] or microlenses molds [123]. Consequently, we focus in the following on HNO_3-rich etching solution, for which the etching kinetics is governed by mass transfer of HF (minority reactive species) to the etched surface [185].

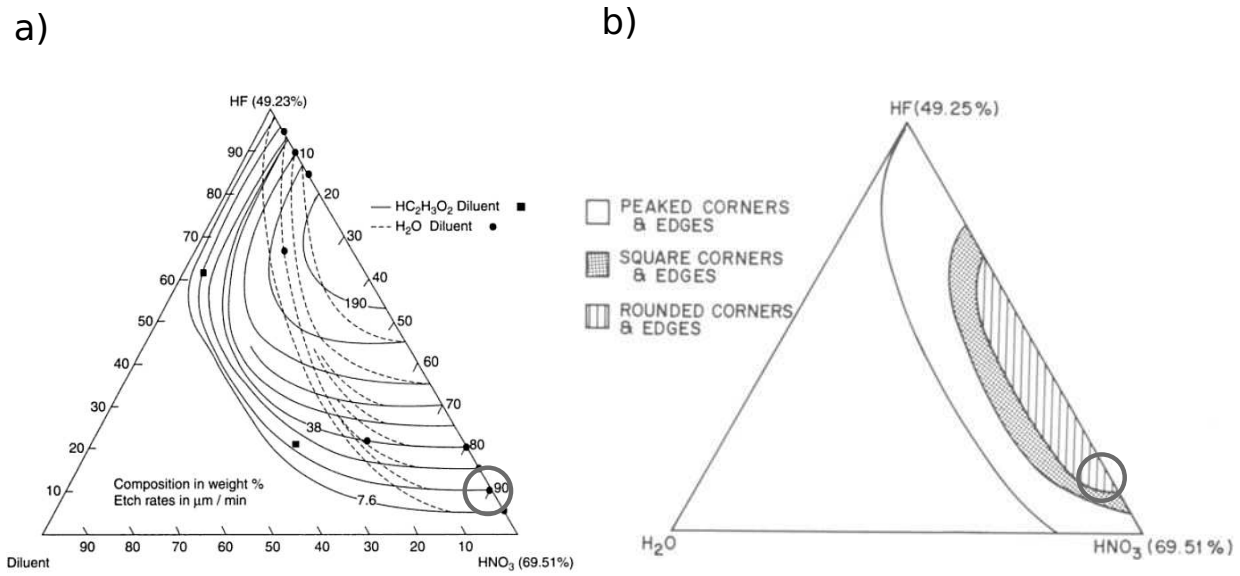


Figure 4.10: Etch Rate tri-plot of isotropic etching mixtures - (a) Iso-curves of etch rate and (b) surface topology in function of etching mixture composition [188] (diluent - bottom, horizontal axis; HF - left axis and HNO_3 right axis), the mixture we use in this work is indicated by red circles and corresponds to mixture HF/HNO_3 in proportion 1:9 with no diluent added.

The mass-transfer regime in considered mixtures is relatively wide, i.e., different composition of etching mixtures can be used. In particular the solutions that can be used to etch rounded, smooth structures are schematically indicated on the figure 4.10b. Our mixture is composed of HF (48% wt. water solution) and HNO_3 (65% wt. solution) mixed in a ratio 1:9 without any diluent added to the mixture. For this concentration ratio etched structures are characterized by very good surface

roughness (in the order of several nanometers), and can be well described as mass-transfer governed process. From etch rate vs composition plot (figure 4.10a), it is visible that etch rate does not depend on concentration of HNO_3 if the mixture ratio is about 1:9 (etch rate isolines are parallel to constant value of HF concentration). This is characteristic of mass-transfer regime in which process kinetics depend only on transfer HF (the minority reaction species) to the etched silicon surface.

Kinetics and geometry of masked etch. The geometry of the etched structure is defined by the transport phenomena. The evolution of the shape is then not trivial. Kuiken presented so-called asymptotic solutions of the masked etching process for two basic geometrical cases: etching through a slit (mask opening in the form of long rectangle) [195] and in the case of circular mask opening [196]. According to [196], long etching[1] through circular mask produces a shape described by equations 4.6-4.8[2]:

$$x = \frac{a}{2}\left(\zeta + \frac{1}{\zeta}\right) Cos(\theta)Cos(\phi) \tag{4.6}$$

$$y = \frac{a}{2}\left(\zeta + \frac{1}{\zeta}\right) Cos(\theta)Sin(\phi) \tag{4.7}$$

$$z = \frac{a}{2}\left(\zeta - \frac{1}{\zeta}\right) Sin(\theta) \tag{4.8}$$

$$\zeta = \left(\frac{24DM_{Si}C_0}{\pi n\rho_{Si}} \frac{t}{a^2}\right)^{\frac{1}{3}} \tag{4.9}$$

where ϕ and θ are angular coordinates and t is the etching time. The physical parameters of the model are summarized in table 4.1. Kuiken formula is an asymptotic solution of diffusion-limited etching problem, i.e., under the assumption that diffusion is the only mass transfer mechanism present in the system. The asymptotic solution is based on the fact that diffusion process weakly depends on initial conditions i.e., for relatively deep etching the shape and location of the mask does not defines the etching kinetics. Only the average diffusive flux through the mask window defines the etching characteristics (figure 4.11). In practice, asymptotic solution signifies that the formula is valid for a limited range of process parameters - equation 4.10 defines validity range of equations 4.9:

$$a \ll \sqrt{\frac{DC_0M_{Si}}{n\rho_{Si}}\, t} \tag{4.10}$$

[1] Kuiken presents two separate solutions: one for shallow and one for deep etchings. In here we discuss only the deep one since it corresponds to our targeted geometry.

[2] [196] utilizes spheroidal coordinate system. In here, equations are expressed in classical spherical coordinates system.

In practice this condition means that Kuiken solution in context of HF/HNO_3 etching is valid only for long etching times and/or small mask window openings (for t=30min, $a \ll 100\mu m$). Kuiken solution properly describes evolution characteristics (week time and strong aperture size dependencies) of etched structures even outside the formal validity condition. Important relation obtained from the Kuiken's analytic solution is the particular dependence of geometry with etching time and mask opening radius. Actually, the geometry is parametrized by ratio $\frac{t}{a^2}$ which signifies that exactly the same geometry (of different scale) can be produced from different mask opening only adjusting the process duration. This important correspondence was confirmed experimentally for HF/HNO_3 etching mixture by Svetovoy et al. [197].

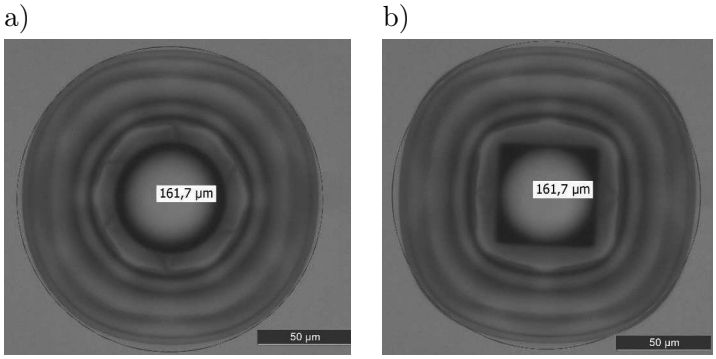


Figure 4.11: Impact of mask window shape in isotropic etching - Resulting structure of wet-etching in case of (a) circular and (b) square mask window respectively. The mask opening area was set to be the same in both cases. As the result, very similar structures are generated. The optically measured ROC for both cases was $123.5\mu m$ and $125.7\mu m$, etching time: 35min. Image by optical microscope (DIC), structures after etching SiN/SiO_2 mask was not stripped - mask pattern is visible together with the structures.

Equations 4.6-4.8 describe oblate spheroid that can be also seen as conic section with positive conic constant k given by equation 4.11:

$$k \approx \frac{4}{\zeta^2} \propto \left(\frac{a^2}{t}\right)^{\frac{2}{3}} \tag{4.11}$$

prolongation of the etching time leads to vanishing conic constant meaning a hemispherical shape of the etched cavity. From the perspective of application of the etching process for fabrication of microlenses and micromirrors positive conic constant is hardly ever desired, for this reason long etching time and/or small mask opening are needed under Kuiken conditions (diffusion only system).

variable	description	value range	unit
a	mask opening radius	2-250	μm
D	Diffusion coefficient	$6 \cdot 10^4$	$\frac{\mu m^2}{min}$
M_{Si}	Silicon molar mass	28	$\frac{g}{mole}$
ρ_{Si}	Silicon density	2.33	$\frac{g}{cm^3}$
n	reaction stechiometric ratio	6	1
C_0	HF etchant initial concentration	$\approx 2.7 \cdot 10^{-3}$	$\frac{mol}{cm^3}$
k	surface reaction rate	$\approx 6 \cdot 10^3$	$\frac{\mu m}{min}$

Table 4.1: Etching modeling data - Variables and constants used in mathematical formulation of the etching problem.

We performed simulations based on finite element method [198] that allowed to cover a wider range of geometrical cases than Kuiken model (limited to small structures). It also allowed simulation of etching evolution in whole range of process time. Figure 4.12 presents the simulation of etching process, where diffusion-governed etching leads first to developing an ellipsoidal cavity that with time is transformed into a spherical shape.

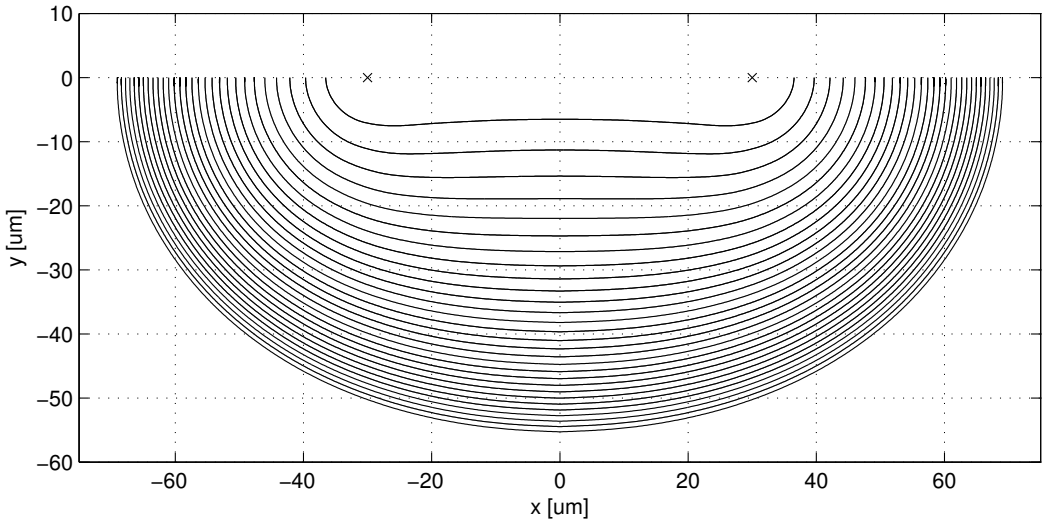


Figure 4.12: Etching evolution calculation by FEM simulation - Profile evolution of etched cavity starts from flat unprotected silicon surface limited by circular mask window opening (diameter $60\mu m$), in the beginning become concave and with progression of the etching become more ellipsoidal that with progressing etching transforms into hemi-spherical shape (simulated etching time t=30min).

Limits of mass-transfer regime approximation. The mass transfer regime is defined as system in which kinetics of the process depends only on transfer of reactive species to the reacting surface. The etching reaction in this case can be considered as infinitely fast. This regime is characterized by high dependence on agitation (stirring the solution during the process), concentration of minority species and week temperature dependence[1]. The intermediate case where reaction-rate do not dominate however has non-zero impact on the etching kinetics is referred as reaction-influenced regime. In the HF/HNO_3 system in the high HNO_3 regime effects of chemical rate in some cases can be observed. As was noticed by Svetovoy [197] the masked etch of silicon in $HF/HNO_3/H_2O$ (ratio 1:6:2) mixture exhibits some degree of anisotropy correlated with crystallographic directions of etched silicon substrate. Also, investigations made by Schwartz and Robbins [187] on maskless etching revealed a small correlation between etch rate and crystallography of etched samples (figure 4.13). This observations indicate that even the HNO_3-rich etching mixtures are not perfectly mass-transfer governed but also reaction-influenced. It is important to underline that character of the etching system is not defined only by the chemistry (composition) of etched mixture. In general, the etching is governed by the slowest of two processes (mass transfer or reaction) at the etched surface. Consequently, if aggressive agitation is applied accelerating the mass-transfer, the chemical character of the process can be amplified. Similarly, if the process is performed at lower temperature, the decreased reaction rate can cause a increased degree of the chemical behavior (figure 4.13a).

The formal condition defining when mass-transfer dominates the chemical kinetics can be derived by comparing reactive flux (flux of reactive particles that can react due to finite reaction rate) with diffusive flux (mass-transfer flux due to diffusion). The diffusion governed process takes place when reactive flow is much higher than the diffusive flux. This can be written as condition 4.12:

$$k \gg \frac{D}{L} \tag{4.12}$$

where k is reaction constant, D diffusion coefficient, and L is the length scale of the system. The dependence of eq. 4.12 on the system scale indicate that small structures are more affected by chemistry of the process than the large ones [198]. This effect is clearly visible in the case of etching through small mask apertures. Figure 4.13b presents structures etched by our isotropic solution through very small mask openings (mask-defects) where clearly anisotropic pyramid-like forms can be observed.

[1] there is always some level of temperature dependence however it is more connected to kinetics of mass transfer processes (diffusion coefficient, viscosity) than the reaction itself

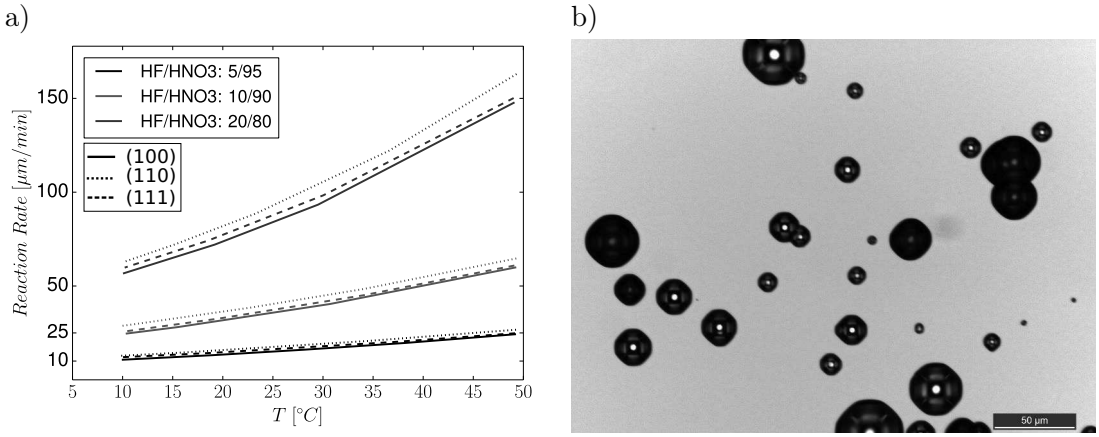


Figure 4.13: Anisotropy in HF/HNO_3 solution - a) effects of temperature, crystallographic orientation ((110) dotted; (111) dashed; (100) solid) on reaction rate, for three different mixtures (ratio: HF/HNO_3 5/95; 10/90; 20/80), the reaction rate obtained from maskless etching experiment (plotted data from [187]). b) anisotropic effects in the case of masked etching are clearly visible when very small structures are etched. In here, etching through sub-micron openings (mask defects) cause formation of pyramid-like structures correlated with crystallography of etched (100) Si wafer.

Effects of agitation. The principal assumption leading to asymptotic solution is diffusion-only mass-transfer. In practice, structures generated with a properly agitated mixtures are better in terms of geometry (for considered application). Agitation i.e. stirring or introducing movement in the etching solution, can accelerate and locally change the uniformity of the etching. In practice, when masked etching is performed, agitation accelerates the etching more vertically (in depth) than in the lateral direction. It is than easier to obtain spherical shape than based on diffusion-only governed process [199]. In figure 4.14a, comparison of vertical and lateral etching extents for processes with and without agitation is presented. The numerical simulations (figure 4.14b) shows the change of structure shape when agitation is used.

4.1.2.2 Fabrication

The fabrication process relies on standard MEMS tools, i.e. photolithography, RIE etching, wet etching and thin layer deposition. The wet silicon etching process as the one requiring special attention is made in a dedicated system in which agitation is optimized for generation of the desired structures. Only single etching composition is used made of HF (48% wt.) and HNO_3 (65%wt.) in proportions 1:9.

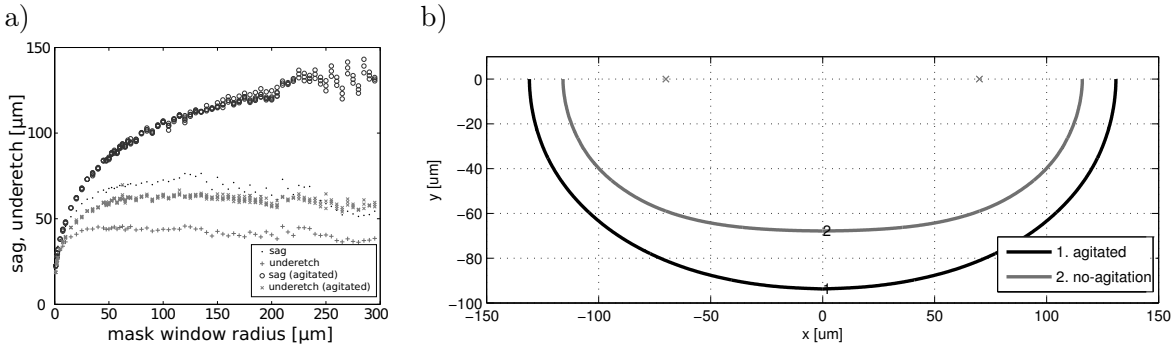


Figure 4.14: Agitation effect on underetch and sag - (a) experimentally measured effect of agitation demonstrated by measuring lateral and vertical etching extents (underetch and sag) of structures etched with and without agitation [200]. (b) FEM simulation of etching with and without agitation applied.

Mask material choice. HF/HNO_3 etching mixtures are very demanding with respect to masking material. Photoresist-like mask do not withstand this type of solution and only so called hard masks can be used. Moreover, in high concentration HF/HNO_3 mixtures only few materials are possible. For short processes, SiO_2 mask can be employed [201]. However, for long etching processes, Cr/Au and LPCVD nitride masks are preferable [123, 197, 202]. The metal mask as Cr/Au are chemically resistant to the etching solution. However, it is also more fragile which in case of large underetching can lead to mask breaking during the process. LPCVD silicon nitride is mechanically more stable than standard metal layers, but chemically less resistant (etch rate $\approx 3nm/min$). Silicon nitride layer is often used in the form of double layer where first layer is thermally grown SiO_2. In this work such nitride-based mask has been used made of SiO_2(500nm) / SiN(150nm). Mechanical characteristics of oxide/nitride masking layers[1] are uncertain: from one side the double layer is robust in terms of adhesion and mechanical strength (no cracks was ever observed). From the other side, deformation of mask is observed in the underetched regions (figures 4.16a and 4.16c). The silicon nitride layer is specified by the producer as "super-low-stress" which means that mechanical stress of the layer is minimized.

Nevertheless, residual compressive stress in the masking double layer can result in the deformation of the mask during the process and thus, can impact the geometry of the etched structures. For example an asymmetrically deformed mask can provoke asymmetry in the etching. The particular case where mechanical properties of the mask are important is the case of generation of dense

[1]Silicon wafers are purchased (SI-MAT) with masking double layer.

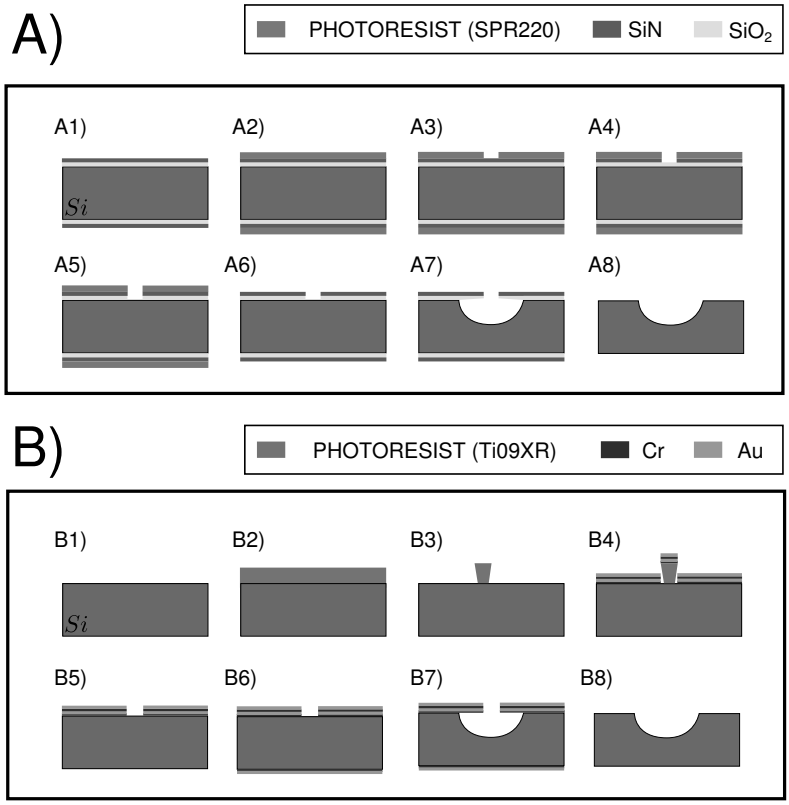


Figure 4.15: Process flow of wet isotropic Si etching - Two schemes for two used mask materials used with (A) SiN-based and (B) Cr-Au masking layers. Patterning method for two masks are different: the SiN mask is patterned via positive photo-resist (A2-A3) and RIE process for window mask opening for (A4),

matrices of etched structures. This effect is strongly pronounced in the case of generation closely packed structures. In figure 4.17, the structure fabricated with SiO_2/SiN mask is characterized by surprising "double" periodicity that does not correspond to the pattern of the mask openings. This effect was observed for all investigated wafers with SiO_2/SiN mask, although, different degree of deviation from desired pattern are observed within different batches of silicon wafers[1]. It is important to notice that this effect is highly pronounced in the case of fabrication of dense matrices. However, in the case of generation of singular structures mask deformation also visible has smaller impact on

[1] Since wafers was ordered with the SiO_2/SiN layers wafer batch usually means that all layers are created in the same fabrication run, the difference between batches can be attributed to slightly different SiN deposition conditions. That can leads to different stress values, stress is specified as $\sigma_{res} < 50MPa$, the exact value of stress is not known to the author.

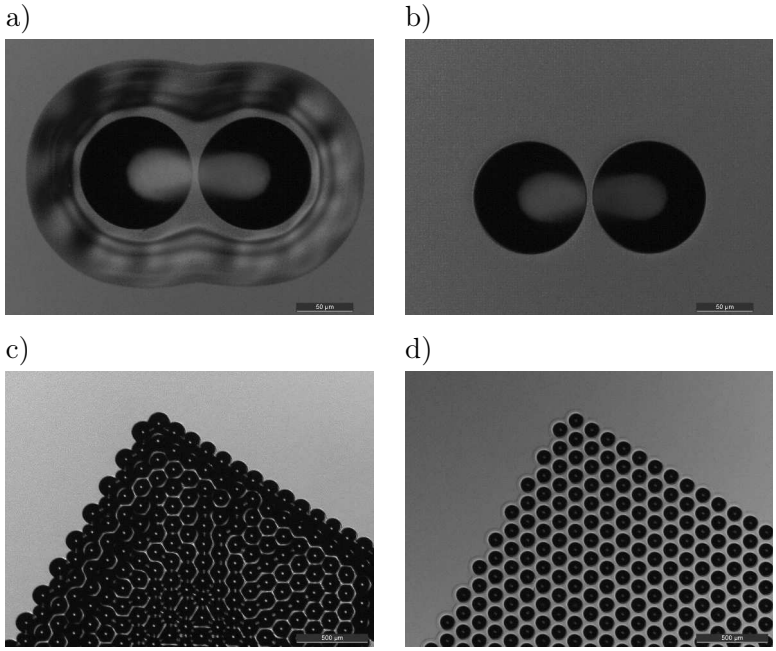


Figure 4.16: Mask state after HF/HNO_3 etching - a) and c) LPCVD SiN mask is visibly deformed; b) and d) same structure when multilayer metal mask was used (Cr/Au/Cr/Au) this type of mask has no visible deformations.

the final shape of the etched cavities.

The standard Cr/Au mask used for deep HF/HNO_3 etching often breaks during the etching process (especially when agitation is applied). In order, to improve the mechanical stability of the metal mask, we used multilayer in the form of Cr/Au/Cr/Au (10nm/100nm/100nm/100nm). This configuration allows to combine high chemical resistivity of gold and good mechanical properties of chromium. The first layer of chromium (10nm) assures good adhesion of consequent layer to the silicon surface. Then, first gold layer (100nm) creates chemical protection of mask for the underetched zone. The middle chrome layer (100nm) provides mechanical support for the mask, and the last layer of gold (100nm) is employed for front-side chemical protection of the multilayer.

This composed mask allows to suppress mask deformation effects that were observed with SiO_2/SiN masked samples. In figure 4.16, comparison of mask state after etching with two types of masks is presented for two close structures and for a large matrix ($3x3mm^2$). The matrix is etched until the connection between all structures is achieved, so that the mask forms a membrane suspended over the structures. The SiO_2/SiN mask is highly deformed, in the case of metal mul-

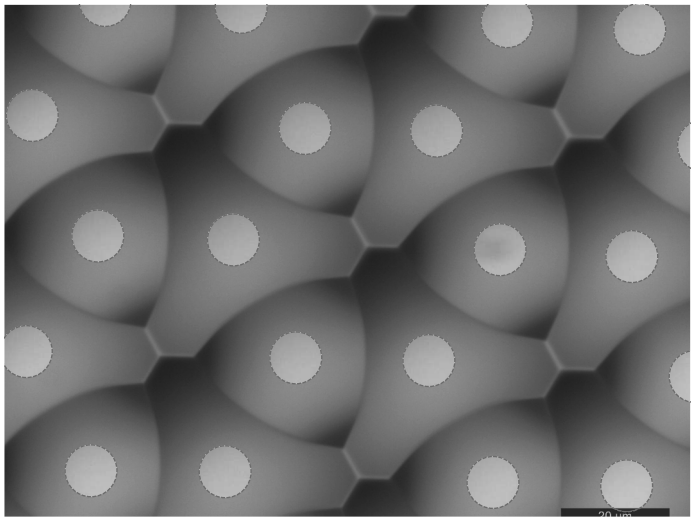


Figure 4.17: Mask deformation effects on the geometry of the etched structure - SEM image of structure etched from periodic mask aiming at generation of the spherical depressions with triangular footprint Resulting final "double periodic" structure is attributed to mask deformation during the etching. The mask pattern is superimposed with the image where mask openings marked as red dashed circles.

tilayer mask, there is no sign of mask deformation nor bending of the membrane. In consequence generated structures are strictly dependent on mask pattern not on dynamic evolution of the mask shape during the process.

The multilayer metal mask was fabricated by sputtering processes where the mask pattern was created by a lift-off procedure (figure 4.15b). In this particular case, the motivation of using lift-off avoids the metal etching process that can leave residues of metal particles on the silicon surface to be etched. Indeed, metallic contaminants on the surface etched in acid solutions can cause increased surface roughness.

To avoid stress induced mask deformation, deposition of metal multilayer are made in the conditions that minimize stress in metal layers. Metal deposition of all 4 layers are performed in a single run (sample was not removed from the vacuum chamber). The parameters of the deposition, that largely define the mechanical properties of the layers, are as follows[1]: Cr deposition: 0.5A (deposition rate: 0.870nm/s), Au deposition: 0.3A (deposition rate: 1.75nm/s). All processes are performed at Argon atmosphere under a pressure of $p = 5\mu bar$. Stress in metal layers deposited by sputtering depends on the distance the sputtering target - the substrate and the gas pressure in

[1]Acknowledgments to Jean-Yves Rauch for finding optimal parameters for the deposition

the chamber[1]. In consequence controlling the pressure it is possible to optimize the stress in the layer [182]. In our work, we did not performed precise stress measurement of deposited metallic multi-layer however, since no deformation was observed after etching experiment, we claim that fabricated multilayer is of low tensile residual stress.

An important parameter related to the multilayer mask concerns the proper choice of the adhesion layer. The adhesion layer is necessary to ensure good mechanical connection between the Au layer and the silicon substrate (generally gold has very poor adhesion to Si). Different metals can be used as adhesion layers. The most popular are Cr, Ti and Ni. However, in considered case where etching process is performed in HNO_3-based solution. Ti and Ni cannot be used since they are rapidly etched out by etching solution[203]. Chromium is characterized by good chemical resistivity to the employed etching solution and can provide good adhesion between Au and Si interface. The performance of adhesion layer depends also on its thickness and the cleanness of the host (Si) surface. Thus, RF argon plasma is used to clean the surface directly before the deposition ($t = 20s$ [2], $P_{RF} = 150W$, $p = 5\mu bar$). The thickness of the adhesion layer has to be properly chosen since too thin layers do not assure good adhesion whereas to thick ones can cause various defects during the etching. Figure 4.18a shows the effects of 50nm thick Cr adhesion layer on the etched structures. The surface defects are probably caused by penetration of the etchant into the thick adhesion layer, causing degradation of surface quality. Moreover, etching geometry was disturbed, i.e, the pyramidal structure appeared in the underetched area[3]. The optimal result was obtained with thin 10nm thick Cr adhesion layer deposited with same parameters set as other layers composing the mask.

Summarizing, in the performed experiments two different masking materials were used. The first one is the double layer composed of SiN (150nm) deposited on SiO_2 (500nm). Whereas the second one was the metallic mask composed of Cr/Au/Cr/Au multilayer. In consequence two different, patterning processes where used: positive photography and RIE etching for SiN based mask (4.15a) and described above lift-off process for metal mask patterning (figure 4.15b). The isotropic etching were performed in the same conditions for both types of masks.

[1] Those two parameters defines the energy of metal atoms reaching the substrate: higher the pressure and larger the travel distance more collision sputtered particle encounters in consequence it loose the energy that allows relaxation on the substrate.

[2] time of argon cleaning cannot be too long in order to avoid damaging of the resist pattern.

[3] Similar faceting is often observed in glass wet-etching when adhesive layer is etched at similar speed as glass substrate [184], or when adhesion layer delaminates because of low adhesive force or high tensile stress [204]

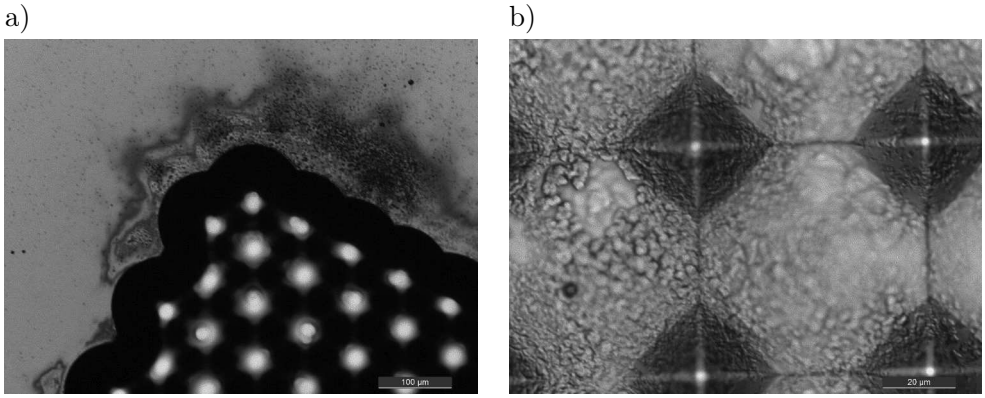


Figure 4.18: Adhesion layer defects - Thick metal adhesion layer (50nm Cr) caused deterioration of quality surface of the etched structure a), geometry of the structure is also affected when adhesion layer is not properly chosen b)

Agitation. As it was discussed before, agitation of etching solution can significantly improve the sphericity of generated structures. Then, the method of agitation is also important when geometry control is crucial. Different agitation methods can be applied. The most common are based on magnetic stirrer, rotational table or ultrasonic bath. The magnetic stirring is difficult to apply when small quantity of the solution is used. Rotational table tends to negatively impact the symmetry of the structure since the usual one-directional rotation privileges specific direction. In our system, since we use small quantity of the etching solution (100ml), we employ specific agitator that allows to perform nearly random agitation of the solution without negative influence on generated structure. The agitator (Programmable 3D-sunflower-shaker from BIOSAN figure 4.19) continuously moves the etching baker, but with a complex motion. The agitation can be composed of three basic movements: orbital rotation, reciprocal rotation and vibrating rocking. The platform of the agitator is also slightly tilted (7^o) so that in case of rotational movement (orbital or reciprocal) it cause relatively complex (quasi-chaotic) movement of the fluid contained in the baker. In described experiments the agitation is programmed as follows: 6 seconds of reciprocal rotation at 8rpm with 360^o turning period, following by 4seconds of rocking movement with 2^o amplitude. These steps lasting 10 seconds are repeated during the whole etching process. It allows sufficient degree of agitation without introducing negative effects to the process like breaking metal mask or introducing asymmetry to the generated structures.

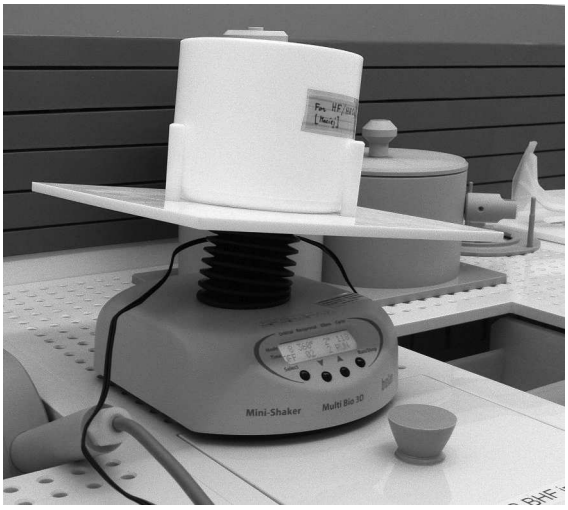


Figure 4.19: Agitation setup for isotropic silicon etching - The Agitator [205] allows quasi-random movement of the etching baker. This is needed to improve aspect ratio of etched structures without introducing asymmetrical effects that can be caused by classical monotonic agitation systems. The agitator from BIOSAN was adapted to the need of etching station by replacing original platform by a PTFE one to provide holder for the etching baker[1].

Process control. The standard method of the process definition is the etching time. However, since the process is very sensitive on several factors difficult to control accurately, such as mixture composition or agitation etching time is not always the best parameter to control the etching process. Consequently, we investigated an alternative method for *in situ* etching progress control. The method based on so-called "etching flags" allows to define the time moment when desired etch depth is reached. This approach, suitable mostly for prototyping, allows achieving more repeatable results despite changes in etching conditions such as: inaccuracy of mixture preparation, aging of the solution or when comparing different agitation programs. The idea of the method is schematically sketched on figure 4.20a. The flags are the additional patterns added to the mask design. They takes the form of long rectangular mask island which are during the etching process underetched. When specific underetch is reached, the island is released to the solution.

The release moment is visible[2] and indicates that designed underetch has been reached so that the process should be stopped. The practical realization of the flag structure relies on the design of the island structure, that should well reflect the etching progress. The two main parameters of the flag geometry are inner rectangle width a_m and the outer-frame width b_m (figure 4.20a). In

[2]Etching mixture has to be under careful visual inspection, the flags are few mm length but less than $100\mu m$ width

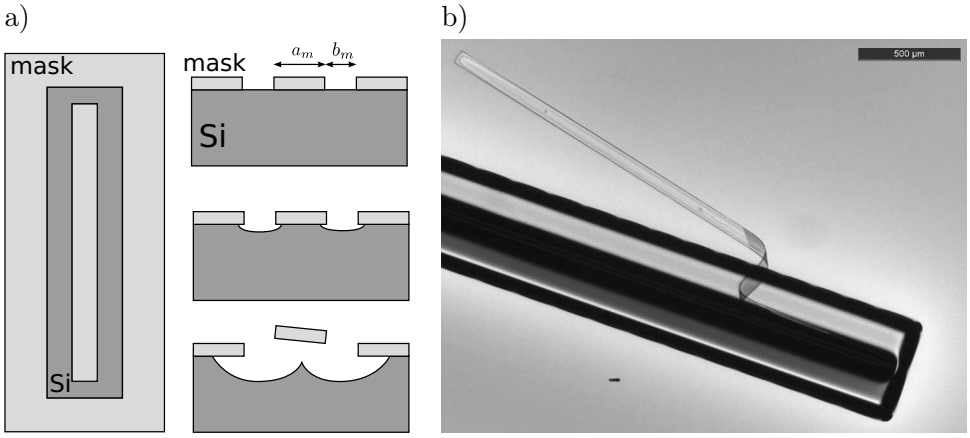


Figure 4.20: Etching flags - a) the mask layout of a flag structure and a working principle; b) image of a realized flag structure after the etching process in this case the flag was not fully detached from the silicon wafer.

practice, in order to assure good visibility of flags releasing point, many structures are necessary (20). They take the form of few mm long rectangles with width $a_m \in (70, 200)\mu m$ and frame size $b_m = 200\mu m$ depending on the desired etching depth. Example flag structure is presented on figure 4.20b at the moment where the flag is not yet fully released from the Si substrate.

Microlenses molds and micromirrors. Generation of spherical cavities, by means of silicon etching in aqueous solution of HF/HNO_3, is achieved by etching through circular openings in mask. According to the theoretical analysis, it is preferable to use small apertures and long etching times if good sphericity of the structure is required. In practice, the mask apertures can range from 2microns for the smallest structures to 300microns for the largest. As far as there is no technological limitations for the maximal size of the mask window, the main limit of acids-based etching is the process duration. The aggressive etching solution (except for etching silicon) attacks the mask material, thus limiting the maximal process time. Within performed experiments, the longest etching performed with Cr/Au multilayer was 120 minutes, while with SiO_2/SiN masking it was 40 minutes. This limitation defines the ranges of structures that can be generated as ranging from about 20 to 500 microns in diameter.

The small structures takes the form of hemispheres whereas the larger ones exhibit more flatten form (positive conic constant). The optical properties of generated structures are investigated by the characterization system described in chapter 3 of this thesis. The measurement results are

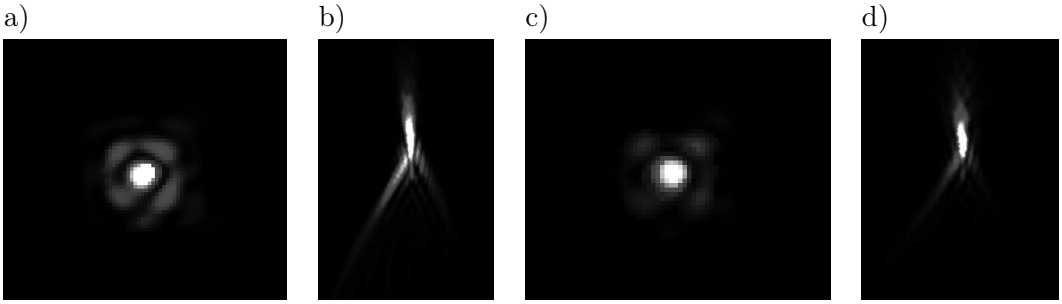


Figure 4.21: Optical measurements of micromolds: small mask window - Focal spot measured in confocal imaging configuration of two molds: (a) and (b) 130μm diameter mold generated by etching (120min) through 20μm diameter mask window; (c) and (d) mold diameter 200μm obtained within same process with mask diameter of 50μm. (a) and (c) corresponds to the xy image of a focal plane while (b) and (d) are the slices along the propagation directions (xz). Focus dimensions are summarized in table 4.2.

d_0 [μm]	t [min]	d_t [μm]	δx^{fwhm} [μm]	δz^{fwhm} [μm]	ROC [μm]
20	120min	130	1.2	11.5	63.75
50	120min	200	1.0	10.0	96.5
110	40min	265	1.7	56	559
350	40min	525	2.9	222	785

Table 4.2: Summary of IPSF measurements of isotropically etched mirrors - Summarized characteristics of IPSF presented in figures 4.21 and 4.22, d_0 - diameter of mask opening, t - etching time , d_t - diameter after etching, δx^{fwhm} - lateral spot size at focus, δz^{fwhm}-axial spot extension, ROC- radius of curvature.

presented in the figures 4.21 and 4.22. In the case of etching through small windows (20 and 50 μm), the resulted structures have nearly the spherical shapes (focal spot is small and short in axial direction), however, they are slightly asymmetric (fig. 4.21a and c) due to the residual anisotropy of the etching solution ([100] Si wafer was used). The structures generated from large mask openings (110 and 350 μm) generate focal spot with better axial symmetry (fig. 4.22a and c). However, the resulting geometry is less spherical than the previously discussed structures. As the consequence, the focal spot posses strong rings around the central peak. Moreover, the focus is strongly stretched in the axial direction. This behavior can be attributed to the oblate ellipsoid form of the cavity that provokes spherical aberration of the observed beam.

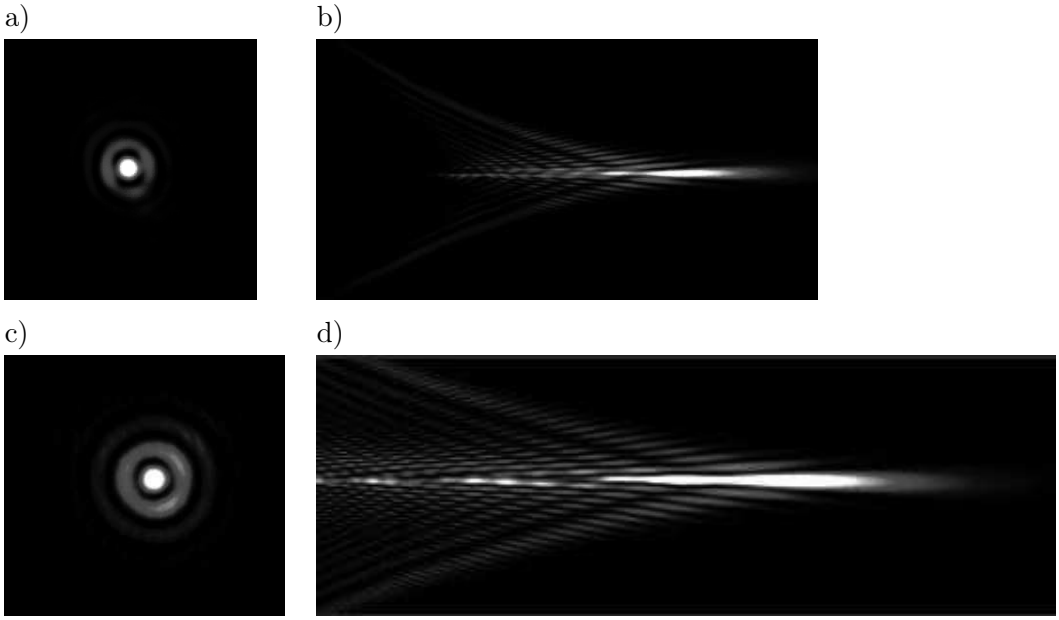


Figure 4.22: Optical measurements of micromolds: large mask window - Similar measurements to figure 4.21 in the case of two structures etched 40minutes through masks of diameters 110μm (a),(b) and 350μm (c),(d). Focus dimensions are summarized in table 4.2.

The small crystallography dependent asymmetry of smaller ($< 150\mu m$) structures was confirmed by comparing the etching of differently oriented wafers. In figure 4.23, IPSF measured in reflection for similar structures produced within silicon substrates with different crystallographic orientation, are compared. In the case of the structure etched in (100) oriented substrate, the IPSF has visibly four-fold symmetry (fig. 4.23a,b) while (111) orientation leads to tri-fold symmetrical IPSF. This results correlates with crystallographic symmetry of two considered substrates.

The investigations of anisotropy of silicon etching in HF/HNO_3 mixtures was made in [197]. They were based on analysis of cavity footprint and demonstrated that (111) oriented wafers exhibits lower degree of crystallographic dependence then (100) or (110) wafers. However, analysis of the footprint cannot fully describe the impact of anisotropy on etched geometry. In here, we presented our first results of investigation etching anisotropy in the context of 3D geometry. In the investigated cases, i.e. etching through small circular windows (12-50μm) etched for 30 minutes, the anisotropy is clearly visible for both types of wafers and its degree is very similar. However, quantitative comparison could not be done because slightly different etching conditions of the discussed samples.

The fabrication of spherical micromirrors and micromolds by isotropic etching of silicon require

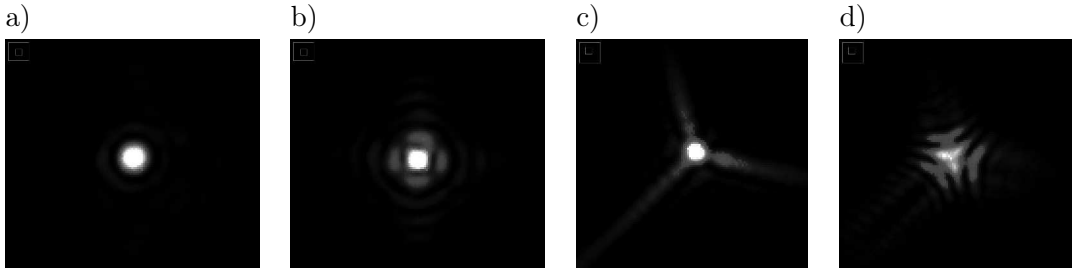


Figure 4.23: Impact etched wafer orientation on reflection IPSF - Residual anisotropy of the etching process observed as asymmetry of IPSF. (a), (b) and (c),(d) correspond to structures etched in (100) and (111) oriented wafers respectively. (a) and (c) correspond to focal planes while (b) and (d) to slightly defocused planes.

special attention in choosing process parameters. The window mask opening from one the hand has to be small to be able to generate well spherical geometry, and from other hand etching through small mask windows provokes small degree of asymmetry in the generated structures. The etching time as main limiting factor of this constraints need to be maximized that can be achieved by using multilayer metallic mask.

Arrays. One of the advantage of the wafer-level fabrication approach is the possibility of generation densely packed structures. In this section investigates the possibility of using wet isotropic etching for generation of high fill-factor arrays of microlenses molds. Microlens arrays have already found many application in beam shaping, 3D imaging, displays, wavefront-sensors or beam scanning systems [206]. In here, we investigate generation of dense arrays of micromolds in silicon aiming at simplification of integration array-based optical systems within silicon based MEMS. One of impor-

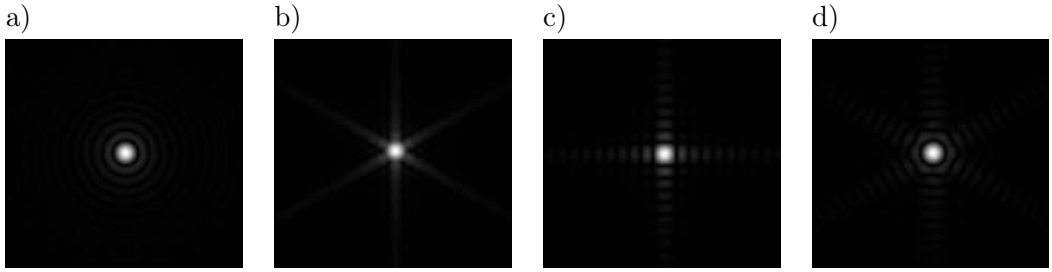


Figure 4.24: Focal spots generated by lenses with different footprints - Four apertures considered: (a) circular; (b) triangular; (c) square and (d) hexagonal, respectively.

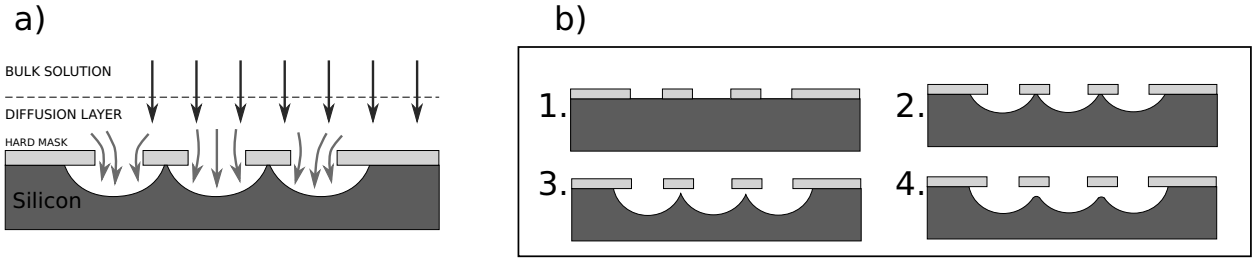


Figure 4.25: Scheme of the etching dense matrices of micromolds - (a) mass-transfer effects in the case etching closely placed structures and (b) profile evolution of etched array.

tant issue is the density or filling-factor of the arrayed structures. In particular when light efficiency is an important factor. Circular structures (mirrors/molds) cannot yield 100% surface covering. In order to obtain full-fill factor microlenses molds, the footprint of the structures need to be adjusted. The most common footprints allowing to generate 100% fill-factor are square, hexagonal or triangular (figure 4.26). Changing the footprint form of a lens slightly changes its optical characteristics. The most important change is the different shape of the focal spot generated by lenses with different footprints (apertures). In figure 4.24, the focal spots generated by lenses with different apertures are presented. The effect of straight edges composing triangular, square and hexagon apertures manifest themselves in the focal spot as the linear diffraction pattern perpendicular to the footprint edges.

Circular mask openings arranged in a dense array generates a matrix of etched cavities with the footprint shape defined by matrix periodicity. Etching of closely packed structures changes the mass-transfer conditions (figure 4.25a), moreover the etching time has to be well adjusted if the spherical shape of the structure is required. If, etching time is not long enough cavities would not fully connect (figure 4.25b step 2), in the opposite if the etching is to long the connection borders "collapse" (figure 4.25b step 4). The effect of etching silicon below the mask defines the 3D geometrical shape of the generated structures. In figure 4.27 three different structures in the different etching stadium are presented. In first stage of the process (figure 4.27a) the structure is not etched enough and vertical pillars are still present. Continued etching suppress the pillars (figure 4.27b) and the structure in this moment is uniformly spherical on the whole area. When the molds array is "over etched" (figure 4.27c) the corners of the structures started to collapse producing visible deviation from spherical shape near the corners of the mold edges.

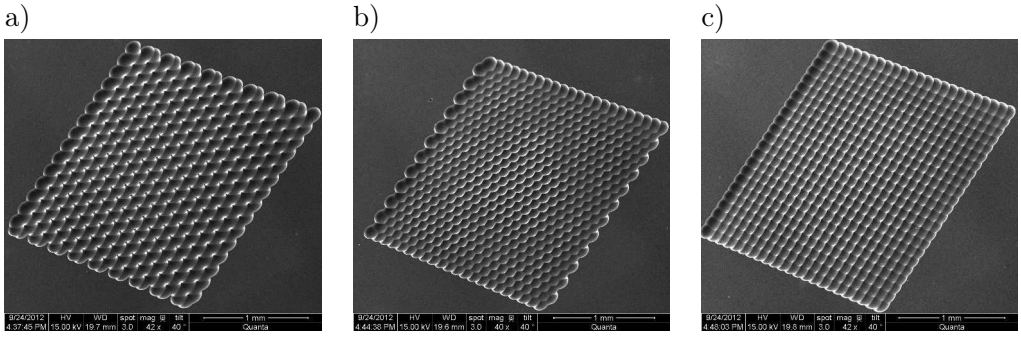


Figure 4.26: SEM images of realized molds for high fill-factor microlenses molds - Three matrices composed of elements of different footprints that assure 100% fill factor in the array: (a) triangular; (b) hexagonal and (c) square.

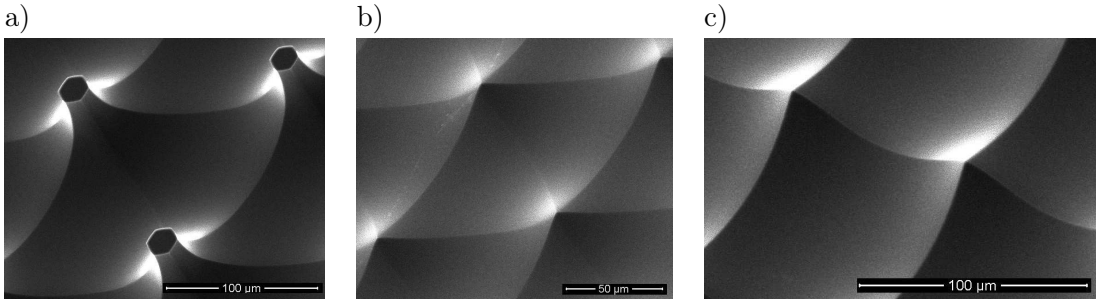


Figure 4.27: Different etched geometries in wet etching of dense molds array - (a) triangular structure etched not enough, (b) optimal etch of triangular mold and (c) over-etched square structure.

4.1.2.3 HF/HNO_3 etching: conclusions

The isotropic wet etching is well adapted for fabrication of microlens molds or micromirrors of high numerical aperture, since the process tends to generate hemispherical cavity in silicon. The technological limitations of the process are the resistivity of mask material and residual anisotropic dependence of the process. The first one limits the maximal possible process time, that in consequence limits the maximal size of the structures that can be generated with well spherical profile. The second limitation, i.e., anisotropy observed in the etching process is manifested mainly in smaller structures, so that they are slightly asymmetrical.

In addition, generation of micromirrors and micromolds the isotropic etching allows to generate matrices that are densely packed in an 100% fill factor array. For these structures, resulted geometry

is dependent not only of window size and etching time but also on the pitch and periodicity of the array.

4.1.3 Silicon etching in SF_6 plasma

As it was discussed in the previous sections, the wet etching technologies are limited in terms of the possible geometries and sizes of generated structures. Moreover, in the context of the miniature confocal microscope project, the better control of microlens geometry as well as the possibility to obtain more advanced aspherical shapes of microlens are highly desired. Then, this section describes very first results of plasma silicon etching, which was developed in order to generate similar structures as obtained previously by means of silicon wet etching (i.e. spherical shapes). Nevertheless, we investigate particularly the possibility to generate larger spherical shapes or structures characterized by negative conic constants that are difficult to make by use of wet etching techniques.

4.1.3.1 Basic etching mechanisms in plasma process

Etching in plasma is performed in a vacuum chamber where special gas is supplied and ionized by means of time varying electric (capacitively coupled plasma - CCP) or magnetic (inductively coupled plasma - ICP) fields. Basically, plasma etching can rely on two different mechanisms: reactive ion etching and radical etching [207]. The reactive ion etching (RIE) is based on etching by energetic ions that physically attack the material to be etched. The second mechanism, radical etching (RE), relies on chemical process between the reactive species (radicals) present in the plasma and the etched substrate. In real systems, the two mechanisms are present and, depending on the plasma conditions, one mechanism can dominate the other, leading to large variation of geometries generated by different plasma processes. Moreover, both mechanisms can impact each other, hence, theoretical predictions of geometrical shapes that can be generated by plasma process are relatively difficult [208, 209].

In MEMS fabrication, the most commonly used plasma processes aim anisotropic, i.e. vertical, etching[1] of silicon. The etching is governed by so-called physical etching, realized by ions that are accelerated towards the etched surface by an electric field (figure 4.28).

In consequence, the plasma process naturally exhibits the etching anisotropy. However, in order to fabricate spherical-like cavities with smooth surfaces, lateral etching is also necessary. In this work, the chemical etching mechanism present in the plasma system is employed to generate rounded structures.

[1] the term "anisotropy" is used here as directional in respect to the wafer surface and do not refer to the crystallography

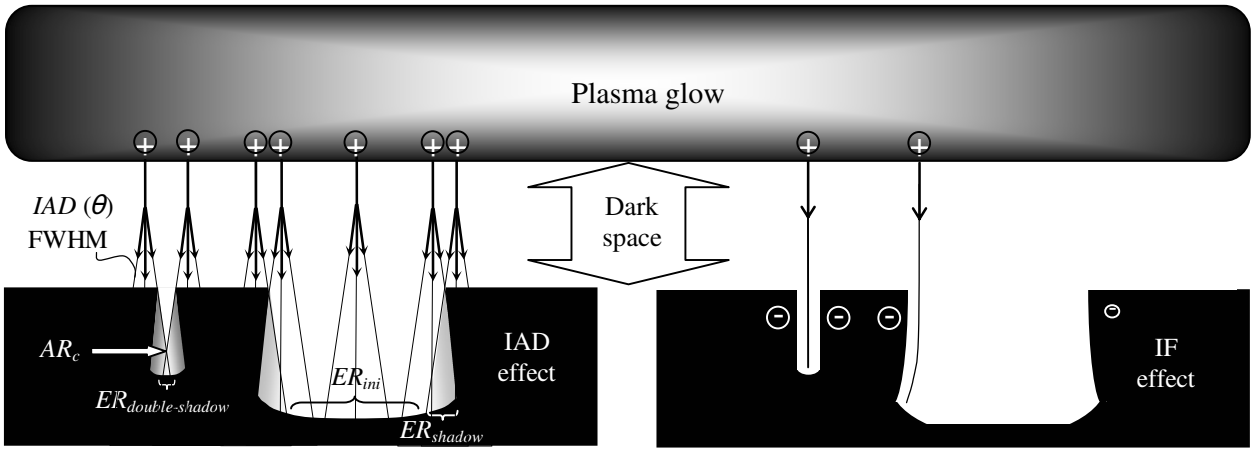


Figure 4.28: Scheme of plasma etching process - Geometry of etched structures by RIE depends on ions angular distribution (IAD), electrical interaction of ions and grounded etched surface (image force - IF). The different phenomena are usually highly dependent on the scale and aspect ratio of the etched structures [210].

4.1.3.2 Plasma etching of silicon for mirrors/mold fabrication

Several approaches of fabrication of mirrors or microlens molds by silicon plasma etching have been already investigated. Larsen et al. [124] proposed a two-step process based on the combination of isotropic etching in SF6 plasma followed by a maskless etching step serving as a thinning process. The latter allows to enlarge the spherical zone obtained within first masked etch. In the same time, maskless etch eliminates the non-spherical parts of the structure produced by the first etching process.

Another approach was employed in [211] where two-step etching is also used, however for a different aim and by use of different processes. The convex silicon mirror was generated by use of a mask having the form of a dense grid of rectangles of varying sizes. The first anisotropic (DRIE) etching process, based on classical Bosch process, generates a structure made of a grid of vertical walls where depth of the etching is spatially varying and defined by the microloading effect. The second etching step is a maskless etch in SF_6 plasma that transform the grid-like structure in the smooth convex structure.

However, both approaches consider only small structures with relatively small numerical apertures of the final mirrors or microlenses. In here, we are focused on the investigation of single step, masked plasma process for generation of relatively large structures (diameter$>$ $300\mu m$) and the possibility of more advanced control of the geometry of generated structures.

4.1.3.3 Experiment

The experiments were carried out in Pegasus-Rapier ICP-DRIE system (SPTS) using SF6 plasma. Test pattern contained circular openings with diameter in the range of $10\mu m$ to $600\mu m$. The pattern was transferred in standard photolithography process into $12\mu m$-thick AZ9260 photoresist, serving as the etching mask. The characterization of generated structure was made with precise wafer dicing and SEM imaging. The process parameters were based on the following recipe: ICP generator power: $P_{ICP} = 2000W$, CCP generator power: $P_{Bias} = 20W$, pressure: $40mTorr$, wafer temperature $T_{Si} = 0°C$, SF_6 gas flow $fl_{SF_6} = 500sccm$, and etching time $t = 900seconds$.

In order to find correlation between process parameters and generated geometry, different process parameters (i.e. mask diameter, gas pressure, substrate temperature) were separately varied. The obtained silicon structures were then diced and observed under SEM. Processing of SEM micrographs allowed the visual investigation of etched surfaces as well as the extraction of their shape profile. This analysis led to identify the role of each process parameter in the etching process.

Figure 4.29 presents the cross sections of etched structures generated by the plasma process. In here, the important dependence of the size scale on the geometry of etched structures are clearly visible. Small structures (figure 4.29 a,b) are relatively uniformly curved whereas larger structures geometry differs in the bottom and in the underetched zone. This effect could be explained by shadowing phenomena (figure 4.28), i.e. etching of the bottom part is enhanced by ion bombardment (physical etching) whereas underetching is generated by radicals (chemical etching). The different mechanism of etching that are present within single structures are responsible for double curvature visible in the large structures (figure 4.29 c,d). Although the generated shape is not spherical when considering the whole structure, its bottom part is characterized by a spherical profile.

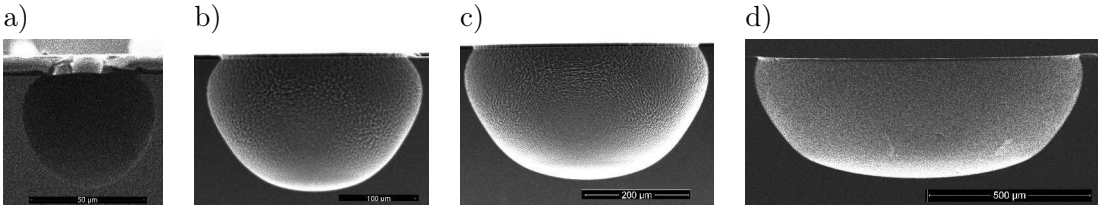


Figure 4.29: Geometry of etched cavity for different size of mask opening - Profiles of etched structures obtained by plasma etching, different mask openings etched within a single wafer: (a) $10\mu m$, (b) $100\mu m$, (c) $200\mu m$ and (d) $600\mu m$ diameter (etching performed under pressure p=100mTorr).

Gas pressure. The pressure of the gas in the plasma chamber can impact the etching in different ways. Firstly, if power is kept constant, the increase of the pressure reduces the ionization efficiency - there is more particles in the chamber so the mean energy per particle is lower. Consequently, the ratio of ions to radicals in the plasma should decrease[1] and etching should be more chemical. Secondly, pressure affects ions angular distribution, i.e. ions directions are more spread in higher pressure [213]. This means that physical etching should be less anisotropic so that it can reach larger zones under the shadowing mask (figure 4.28). In figure 4.30, experiments of etching with three different pressures are summarized. As expected, higher gas pressure results in increased lateral etching (mask underetching). Nevertheless, crystallographic-based anisotropy of the etching is also revealed. This indicates that chemical mechanism is mostly responsible for the lateral etching. Similarly to the case of HF/HNO_3 wet etching process, crystallography has a larger impact on smaller structures than on larger ones.

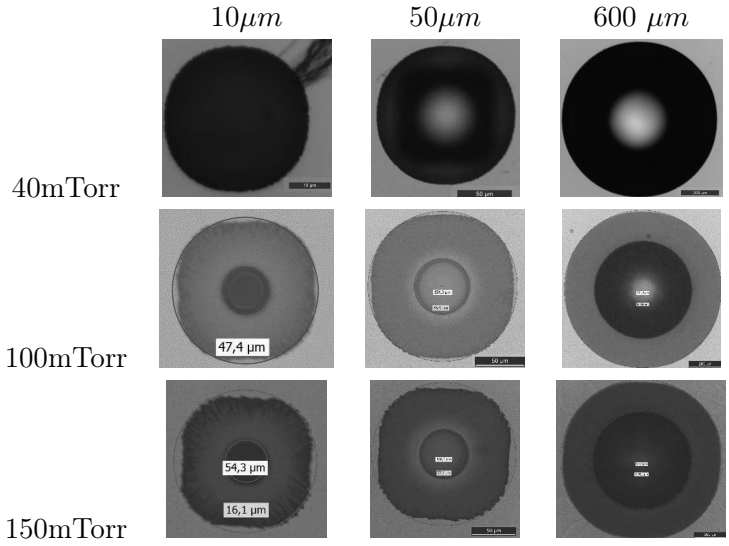


Figure 4.30: Impact of gas pressure on the footprint of etched structures - Three different pressure levels were investigated: 40mTorr, 100mTorr, and 150mTorr while all other process parameters were fixed. With increased pressure, underetching is faster, but new phenomena in the form of crystallography dependence appears.

Substrate temperature. In the etching reactor, the sample is placed on a wafer chuck that allows to control the etched substrate temperature. Since the considered process is partially a chemical

[1] ionization in general requires more energy than generation of radicals [212]

process, the sample temperature can impact the etching characteristics. Moreover, as etching is governed by the two mechanisms, i.e. ion etching and radical etching, different temperatures could be use to act on the geometry of the etched structures. Indeed, radical etching, that can be understood as a chemical etching, is supposed to be more dependent on temperature than physical one. In figure 4.31, two similar structures were etched in the same conditions except the wafer temperature. Sample etched at temperature $T = 0°C$ shows smaller underetching than sample processed at $T = 20°C$. Since the temperature dependence of lateral etching is much stronger than vertical one, the 3-D geometry is also changed. In consequence, the structure etched at higher temperature has a more spherical profile than the one etched at lower temperature. However, as chemical etching is accelerated when substrate temperature is increased the anisotropy and surface roughness of generated structures also increase.

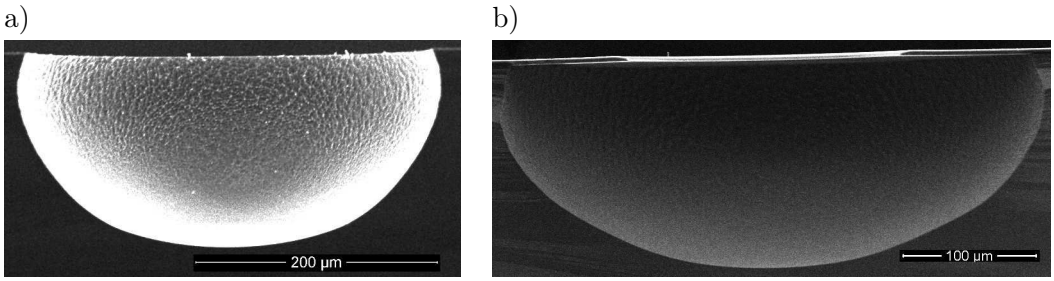


Figure 4.31: Effect of substrate temperature on etched profile - Two structures etched with the same plasma parameters but different temperatures of substrate (set by wafer chuck cooling system), two cases are compared: (a) $T = 0°C$ and (b) $T = 20°C$.

Aspherical Structures. The geometries generated by plasma process can be divided into two categories. The first one consists in structures obtained by etching through relatively large mask opening (diameter $> 100\mu m$). Those structures are characterized by relatively well spherical part at the bottom of the etched cavity. As the curvature is relatively low, they could be used as low power micromirrors. The second category of generated geometries are structures etched through relatively small mask openings (diameter $< 100\mu m$). In this case, the whole surface of the structure can be used since the etched surface is smooth and continuous. There is no visible border between differently, i.e. chemically or by ions, etched parts, such as in the case of etching through large mask windows. Figure 4.32 presents a profile of such structure. This profile obtained by SEM imaging (4.32a), was fitted until a diameter of $120\mu m$ to the conic section equation. It reveals

that the structure can be described by conic section $k = -0.35$, and $ROC = 55.5\mu m$. As it was discussed in the chapter 2, microlenses with such negative conic constant are highly desirable for the construction of micro-optical scanner.

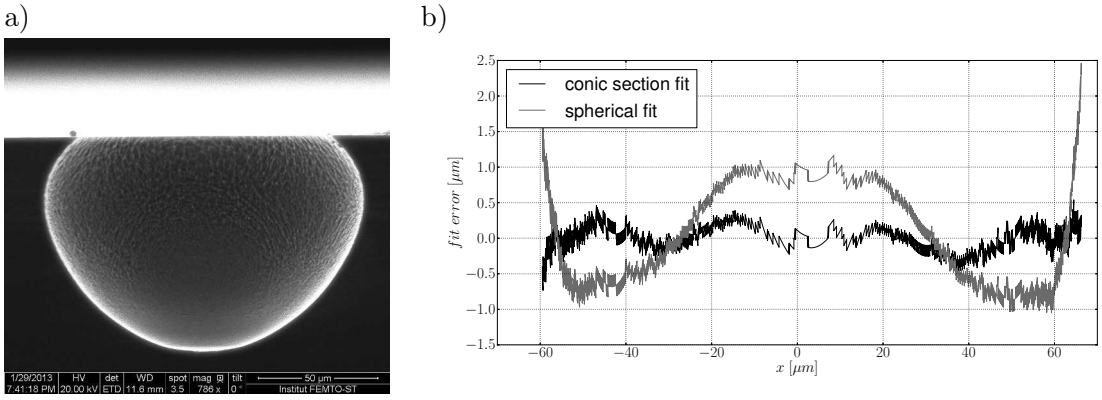


Figure 4.32: Negative conic constant profile - Generated ($p = 40mTorr$,$t = 1800s$,$d_{mask} = 30\mu m$) structure of aspect ratio slightly higher than a hemisphere, results in a profile that can be described as a conic section with negative conic constant. (a) SEM image of diced structure and (b) results of the fitting the profile to: conic section (black line) and to a sphere (red line), resulted fit parameters of the conic sections: $k = -0.35$, $ROC = 55.5\mu m$ $RMS_{fit} = 0.18\mu m$.

Surface roughness. The investigated process produces structures characterized by some level of roughness. The surface quality of the etched structure is not uniform, being much better on the bottom of the structure than on the edges (figure 4.33). High quality surface at the bottom of the etched cavity correlates with the mask opening diameter. This could indicate that roughness accompanies the chemically driven etching that takes place on the mask shadowed area. However, as roughness formation in plasma processes is a complex phenomenon [214, 215], it could be minimized by appropriate process parameters choice. Additionally, a so-called "plasma polishing" process, proposed by [216] and applied by [217] for improvement of silicon micromirrors surface quality, may be used in our case.

4.1.3.4 Conclusions and future work

The preliminary results concerning fabrication of micro-molds and micromirrors by use of SF_6 plasma are promising. The main advantage of this process is in principle more possibilities for generated geometries. Moreover, plasma etching systems can provide better process reliability, in

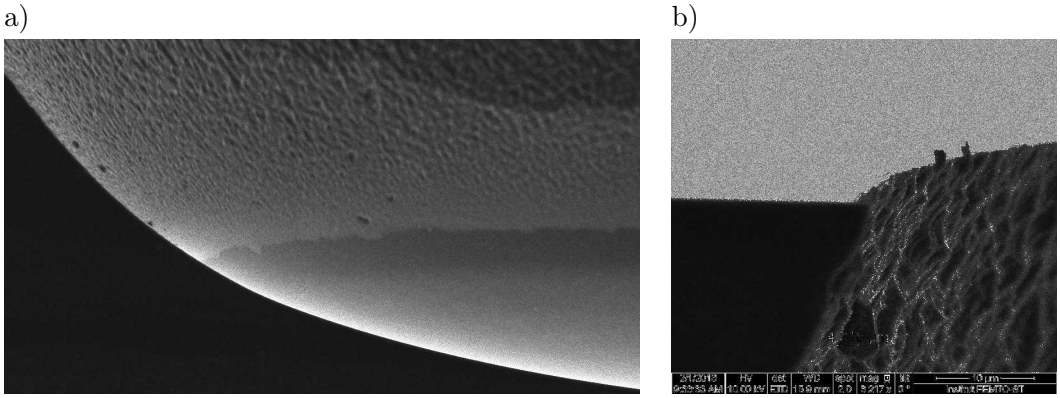


Figure 4.33: Roughness in SF_6 plasma etched structures - (a) variation of roughness within etched structure, (b) zoom on the edge of the cavity where surface roughness is the largest.

the form of process repeatability and uniformity over wafer, than in the case of wet etching based techniques.

In this work, the performed experiments were only the first attempts in order to investigate the physics of the plasma process and determine the range of structures that could be fabricated. Nevertheless, they demonstrated a clear potential of this technique for the generation of more complex shapes than the one that can be produced by wet-etching based techniques. In particular, possibility of creating aspherical shapes with desirable negative conic constant and high aspect ratio (and consequently high NA of corresponding optical elements) were presented. In addition, when considering plasma etching through larger mask openings, such process can be used for the generation of large spherical depressions. In this case, although only the central part of the etched structure is optically usable, fabrication of relatively large mirrors is possible. Such mirrors are needed as primary mirrors in the construction of micromachined Schwarzschild objective (that will be presented later in this chapter).

Then, future work needs to deeper explore the process in order to better understand the etching process. In particular, precise correlation of temperature impact on the etched geometry in a wider range of etching parameters has to be determined. The minimization of both surface roughness and crystallography dependence is also necessary.

4.1.4 Molding

Cavities etched in silicon, by the different wet or dry etching processes previously presented, can be used directly as micro-mirrors. But, transformation of these silicon concave structures into microlenses requires a replication process. Replication is a procedure of transfer of shape from a mold (which is made in silicon in this specific case) to another material. In the context of micro-optics, replication is made into an optically transparent material, e.g. glass or polymer.

4.1.4.1 Glass replication

Transfer of silicon structure into glass is made by combination of silicon-glass bonding and glass reflow techniques [123]. The scheme of the process is presented on figure 4.34. A glass wafer (Borofloat 33 from Schott) is bonded under vacuum condition to the silicon wafer with etched structures (step 1). Then, the created sandwiched structure is heated in the furnace up to $850°C$ (step 2). During this step, soft glass fills the silicon cavity. One effect of glass reflow is also to bend the backside surface of the glass wafer. Thus, in order to planarize it, a mechanical grinding of glass is applied. In addition, the optical quality of grinded surface is restored by a polishing step (step 3). Finally, the generated glass structure is released by silicon etching from the silicon wafer backside (step 4). This step can be made by wet etching (KOH) or dry etching (DRIE). In both cases, silicon can be etched whether selectively to keep a silicon frame around the glass structure or completely to let the replicated structure as a single glass wafer.

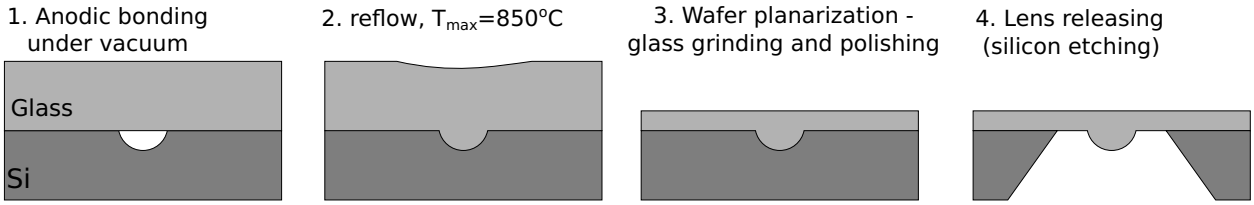


Figure 4.34: Scheme of molding process - Combination of glass silicon bonding and glass thermal reflow used for generation of glass microlens from silicon cavity via molding technique.

Glass molding technique is very interesting since it provides robust optical micro-components. The good optical, mechanical and thermal properties of glass makes it an appropriate material for micro-optics fabrication. This is especially important in the frame of complex microsystems where additional processing such as bonding or layer deposition can be required. However, the main disadvantage of glass molding is the resulting destruction of the mold.

4.1.4.2 Polymer replication

Consequently, for less demanding applications (in terms of robustness) or simply prototyping or testing of optical quality of produced molds, one alternative method is employed. This faster and cheaper method is the polymer-based replication. It uses mold as a multi-use stamp, since, in principle, replication procedure can be repeated many times (if molds are robust enough). Many different replication methods adapted to micro-optics exist[206]. In here, we employ a method based on UV-curable polymer that is relatively simple to use and does not require heavy dedicated equipments. In order to easily separate the replica from the mold, and to further achieve repeatable molding-demolding process, the surface of the mold is covered by an anti-adhesion layer. In here, the anti-adhesive layer is a fluorocarbon film, deposited from the C_4F_8 plasma discharge and performed in a silicon etching system (A601E by Alcatel). The polymer used for replication is NOA65 (Norlands Adhesive). The polymer is deposited in the form of a single drop on the Si substrate to be replicated. It is then slowly pressed by glass support wafer to fill all the structures. The polymerization is afterwards obtained by UV-irradiation. Such curing is performed with a UV-lamp whose exposition time is adjusted to reach recommended curing energy ($4.5 J/cm^2$). Demolding

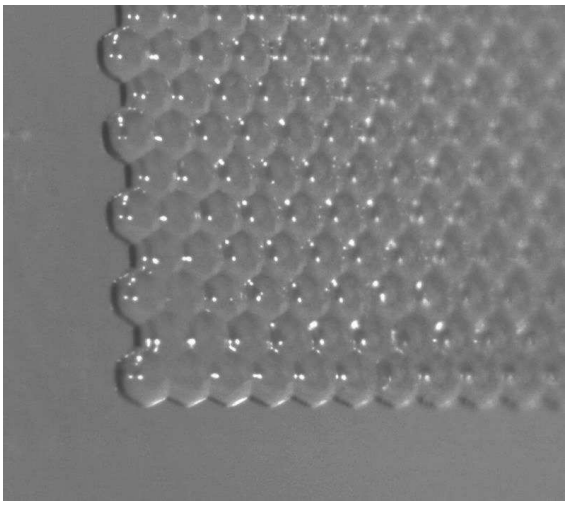


Figure 4.35: Example of a polymer replica - Replicated 100% fill-factor microlens array.

is performed via mechanical separation of silicon mold wafer and glass support wafer that host the replicated structures. Finally, the replicated structures are located on the glass wafer (figure 4.35). The polymer-based micro-structures create an additional layer on the host glass wafer whose thickness is in the order of 80-150microns. The replicated structures can be tested within transmissive

characterization bench that allows to measure their optical performance in the configuration that they are intended to be used.

4.1.5 Microlenses and Micromirrors: Conclusions

In this section, we discussed techniques for generation of micro-mirrors and microlenses molds by use of silicon etching. Although different methods for generation of micro-optical elements on the wafer-level can be used, the silicon-based techniques are especially attractive because they can be relatively easily integrated within silicon MEMS.

Hence, we discussed three different methods of etching, allowing generation of spherical-like cavities. The first considered technique, based on a two-step silicon etching in aqueous solution of KOH, allows generation of relatively large structures ($> 200\mu m$) but with low aspect ratio (sag/diameter< 0.02) resulting in low NA microoptical components.

The second investigated technique relies on isotropic wet-etching in aqueous solution of HF/HNO_3 mixture. This technique allows generation of hemispherical structures, i.e. characterized by high NA. Small anisotropy is pronounced within this etching solution, although it is much smaller than the one observed within KOH-based process. Moreover, it is present only on relatively small structures, i.e., generated by etching through small ($< 50\mu m$) mask apertures. When this technique is used to generate larger structures (typical diameter: $500\mu m$), the etching time has to be increased to obtain spherical shape. However, the process time is limited by resistance of the mask material. Consequently, isotropic etching can produce structures of high NA with diameters in a range of few hundreds micrometers. Future work on the optimization of the (chemical as well as mechanical) mask resistivity is required in order to increase the possible etching time and then the accessible structure sizes. We also demonstrated that isotropic etching can be used for generation of full fill-factor microlens arrays.

The third studied etching technique was SF_6 plasma etching. The preliminary aim was to study the possibility of generation of larger structures. In addition, it has been shown that it can be used to produce structures with aspherical geometries. This has been achieved by adjusting the etching parameters to balance the physical and chemical parts of the etching mechanisms, which are more vertical or lateral, respectively. Therefore, future work concerning silicon processing for microlenses and micromolds generation should be focused on SF_6 process for generation of aspherical components with wider spectrum of diameters.

The generation of microlenses from silicon molds was also presented. Two different techniques of replication were discussed. The first one is based on anodic bonding and glass reflow for generation

of glass microlenses, allowing their natural integration with silicon structures. The second one is based on polymer, and is used for prototyping and testing of generated structures.

4.2 Micro Schwarzschild Objective

Optical aberrations are usually encountered in micro-systems based on microlenses, especially when high numerical aperture microlenses or large spectrum of wavelengths are required. Such aberrations are responsible for a limitation of the system resolution. Besides, optical MEMS field also relies on reflective optical elements, such as plane mirrors or, in some cases, curved reflective surfaces for off-axis systems. In this paragraph, we investigate a reflective system, i.e., a two-curved-micro-mirrors integrated system, well known as a macro-component and so-called Schwarzschild objective. This sytem can be used in the analogous fashion than microlenses but with much lower three primary Seidel aberrations as well as an improved working distance. Thanks to molding from silicon, we show that miniaturization of this anastigmatic reflective objective is possible in order to generate low aberration and high numerical aperture (up to 0.6 for a diffraction limited system) micro-optical components with achromatic behavior.

4.2.1 Two-mirrors anastigmat

The elimination of optical aberration in micro-optical systems can be achieved by use of aspherical geometries [16], however not many micro-fabrication technologies allow arbitrary control of generated geometries of microlenses. Moreover, each microlenses fabrication technology has limitation in respect to possible materials and available microlenses sizes. For example, on the one hand, generation of the aspheric microlenses characterized by negative conic constant was developed by combination of resist reflow and reactive ion etching of fused silica [118].

On the other hand more MOEMS-friendly microlenses generation techniques allow produce spherical structures. However, spherical microlenses have limited performance in terms of optical aberrations. In particular, the spherical microlenses are inefficient when working in high NA systems, when intrinsic spherical aberration seriously deteriorate imaging/focusing ability of the microlens. For instance, in plano-convex spherical micro-lenses, optical aberrations limit their performance as soon as NA reaches 0.25. As the aspherical microlenses usually outperforms spherical ones, a simple aspheric structure (single plano-convex conic surface), is not a perfect imaging solution in case of high NA and large fields angles (like in configuration used in beam scanning confocal microscope) will also exhibit optical aberrations.

In the field of telescope optics and microscopy, K. Schwarzschild and C. Burch [143] have shown a century ago that a system made of two mirrors can be designed in order to eliminate optical

aberrations. Indeed, the reflective optical systems present naturally superior performances for wide-band optical applications than refraction- or diffraction-based systems, simply because reflective systems do not suffer from chromatic aberrations. In addition, when a system is arranged along the so-called "Schwarzschild configuration" (with proper choice of mirror geometries and of their relative separation, the three primary Seidel aberrations, namely spherical aberration, coma and astigmatism are eliminated making the system anastigmatic.

In this work, we investigated the use of a collective technique we employed in the past to fabricate microlenses [123] in order to generate a miniaturized anastigmatic reflective objective. The technique is based on wet-etching of silicon in order to fabricate the two micromirrors (directly or through molding). Because of this technology, we consider Schwarzschild Anastigmat composed of spherical only mirrors. The use of silicon and glass technology allows natural integration of generated micro-objective within complex micro-systems.

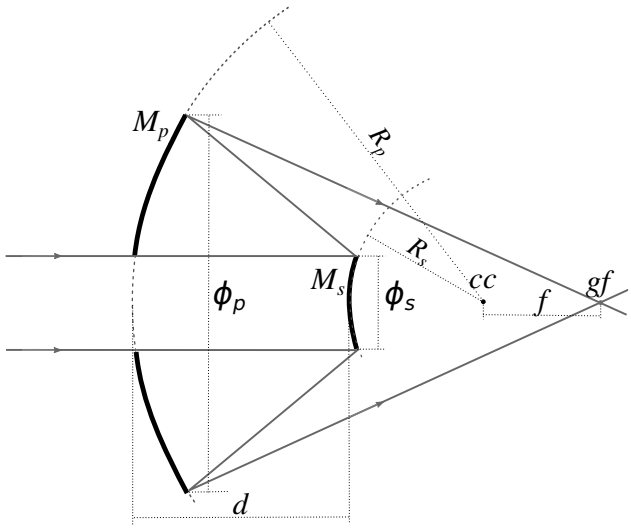


Figure 4.36: Geometry of the Schwarzschild anastigmat - $M_{p,s}$ Primary and Secondary mirror, cc common center of curvature, gf geometric focus, $R_{p,s}$ Mirror radii of curvature, $\phi_{p,s}$ Mirror diameters, d mirror separation, f effective focal length.

Figure 4.36 shows the principle of the reflective objective. Few rules have to be respected so that spherical and off-axis aberrations are eliminated. First, mirrors need to share the same center of curvature (COC) to create a point-symmetric system, avoiding the definition of an optical axis. In other terms, all incident rays are on-axis so that off-axis aberrations do not exist. Secondly, the ratios of curvature of the two mirrors are chosen so that their present spherical aberration contribution have opposite signs, leading to their compensation. Correction of the third order

spherical aberration is then achieved by a system composed from one convex and one concave mirror arranged in co-centric configuration. The main system parameters can be expressed as a function of the effective focal length (equations 4.13- 4.16):

$$R_p = \left(\sqrt{5}+1\right) f \tag{4.13}$$

$$R_s = \left(\sqrt{5}-1\right) f \tag{4.14}$$

$$d = 2f \tag{4.15}$$

$$\phi_p = \left(\sqrt{5}+2\right) \phi_s \tag{4.16}$$

where $R_{p,s}$ are the radii of curvatures of two mirrors, d is their relative separation and $\phi_{p,s}$ are their diameters. The important feature of the co-centrism employed in the Schwarzschild system eliminates the off-axis aberrations, however, co-centric condition has also important disadvantage that is a curved image plane. The curvature of the image plane is defined by the focal length ($R_{Ptz} = -f$) of the system and is usually referred as Petzval curvature R_{Ptz} [6]. Petzval curvature is usually considered as optical aberration (field dependent defocus). Thus, in the classical imaging systems, Schwarzschild systems are equipped with an additional "field flattener" lens, aimed at correcting the image curvature of the system. However, in the context of confocal systems with 3D-beam scanning, curvature in the image space does not impact the system resolution, the only effect is a geometric deformation of imaged volume that can be corrected in the post-processing step. In consequence, in here, we will not consider any additional elements than the mirrors. Moreover, in the aberration analysis we exclude the Petzval term from the total aberration of the system.

The aberration analysis of such system was performed with Zemax (EE version, nov. 2008, Zemax Development Corporation, USA) by means of Zernike polynomial wavefront expansion [6]. The optical quality of the system is evaluated by means of wavefront RMS which defines the wavefront deviation from ideal spherical reference at the system image plane.

Although several criteria exist for the "Diffraction Limited systems", one of them defining high quality optical systems says that aberration "free" optical systems are characterized by Strehl ratio $SR > 0.8$ [16], this condition translated (equation 3.4) into wavefront rms leads to $\sigma_{rms} < 0.02\lambda$.

If the incident light onto the system is collimated, then only axial aberrations, i.e., primary and secondary spherical aberrations, limit the optical performances. For the Reflective objective based on spherical mirrors, important contribution of such aberrations ($\sigma_{rms} \approx 0.02$) appears only for NA > 0.57 whereas they appear as soon as NA is equal to 0.26 for an hemispherical glass lens (figure 4.38);

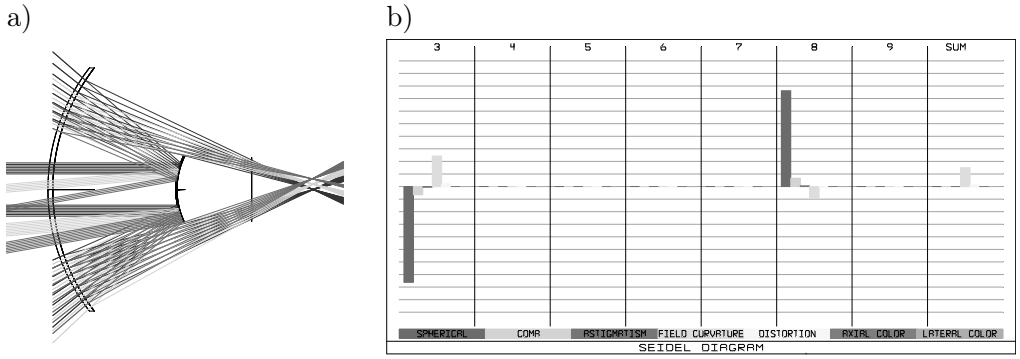


Figure 4.37: Two mirrors anastigmatic configuration - (a) light path (Zemax) of Schwarzschild system, (b) Seidel diagram of the system: surface 3 corresponds to secondary mirror, while surface 8 corresponds to primary mirror. The three principal Seidel aberrations are in exact balance resulting in corrected (aberration free) anastigmatic system.

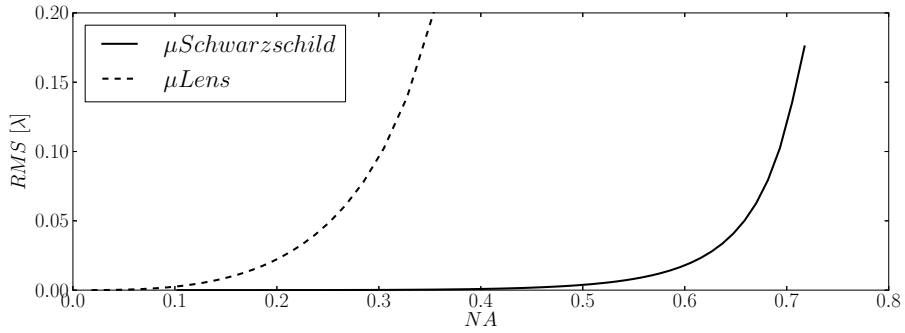


Figure 4.38: Axial aberrations of Schwarzschild system compared to a microlens - Theoretical comparison of microlens and schwarzschild micro-objective: the diffraction limited performance of anastigmatic reflective objective allow achieving much higher NA than a spherical refractive microlens. Analysis made with Zemax where input beams for both cases have been kept constant ($125\mu m$) and where the system focal length was varied to change NA.

Thus, the reflective objective remains diffraction limited for NA twice larger than an equivalent microlens. Concerning off-axial aberrations, and as it was mentioned earlier, high symmetry of the system tends to eliminate them. ZEMAX aberration analysis confirms the elimination of coma, and shows that only small traces of astigmatism (primary and secondary) remains in high NA systems, however it never reaches high values, i.e., bellow 0.02λ even for high angle (15^o) fields and high NA (0.5). Another feature of such system is an increased working distance compared to standard microlenses, because of the combination between positive and negative powers of the two mirrors

resulting in the principal plane location at the physical end of the system instead of its center in the case of microlens. This feature can be interesting in the case of MEMS based imaging systems, where space for packaging is often required.

Reflective objectives also suffer several drawbacks consecutive to the so-called obstruction. Indeed, the secondary mirror or the port in the primary mirror create circular shadow for incident light passing through the objective. It reduces the light efficiency of the system and changes the shape of the (3D) PSF of the setup, i.e. the airy disk is not anymore standard. In addition, obstruction is responsible for an increased depth of field (in the confocal system, it means deterioration of the axial resolution) in comparison with clear (not obstructed) systems.

4.2.2 Fabrication within Si/Glass μtechnologies

Construction of multi-component micro-objective using micro-fabrication technologies is a challenging task. From one side, precise fabrication of each component according to the specifications of the system has to be made, and from the other side, precise positioning of system elements is also required. Moreover, the physical realization of the system require additional elements such as mechanical support for the secondary mirror.

4.2.2.1 Architecture

Miniaturization and collective fabrication of the anastigmatic reflective objective is achieved through silicon/glass micromachining. The architecture is shown in figure 4.39 and the generic fabrication flow-chart in figure 4.40.

The primary concave mirror is formed directly in silicon (for example by wet etching), and its central input/output port is made by deep reactive ion etching (DRIE) (figure 4.40(II.2)). To increase reflectivity of silicon mirror, a metallic layer (Al) is deposited on the surface (PVD) (figure 4.40(II.3)).

The generation of secondary mirror is based on the replication of silicon molds in glass (section 4.1.4). For this purpose, the concave spherical cavity generated in silicon is replicated into a (anodically bondable) glass by means of anodic bonding under vacuum and thermal reflow technique (figure 4.40(I.2-I3)). The original Si wafer used for generation of molds for secondary mirror is then used as the separation wafer defining precisely the separation between the two mirrors. The mirror release is done from the backside of the Si wafer by means of dry etching (DRIE) or wet etching (KOH) (figure 4.40(I.5)). Since, the secondary mirror is made in glass and is suspended of glass substrate the reflective layer has to be deposited on the top of the mirror. It is important to notice

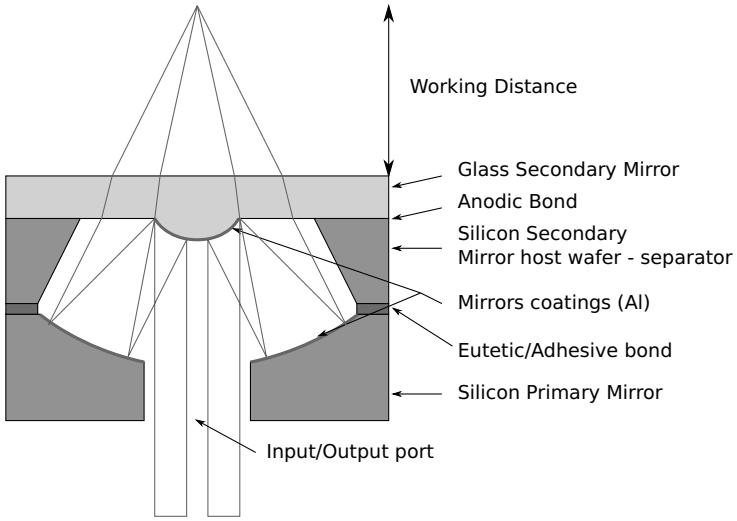


Figure 4.39: Architecture of Schwarzschild micro-objective within Si/Glass fabrication technology - Two mirror system fabricated withing Si/Glass technologies: the primary mirror is made in Silicon whereas the convex secondary mirror is formed by replication of a silicon concave mold into glass. The Si mold wafer used for generation of mold of secondary mirror serve as a separator defining the distance between mirrors.

that patterning the surface (metal coating on the mirror surface) on the bottom of the deep cavity is not straight-forward and needs special attention.

Finally, the two elements composing the system can be integrated together by means of wafer bonding techniques. Since two silicon interfaces have to be joined, eutectic (Au-based) or adhesive (SU8-based) bonding methods can be used.

4.2.2.2 Tolerances

The important issue about Optical Design (OD) of optical systems is their technical feasibility strictly related to the tolerances that OD needs to fulfill. Tolerances depend on the particular system. In the case of original Schwarzschild configuration, i.e. when equations 4.13-4.16 are fulfilled, the system depends on only a single parameter (from point of view of the aberration correction). However, when deviation from exact solution exist (perturbed system) the setup has 3 parameters: two radii of curvatures R_s, R_p and the mirrors separation d. According to 4.13-4.16, the aberration correction is based on two concepts: cocentrism (off-axial aberrations) and appropriate ratio of radii of curvature of two mirrors. Deviation from one of these two conditions produces aberrations in the system.

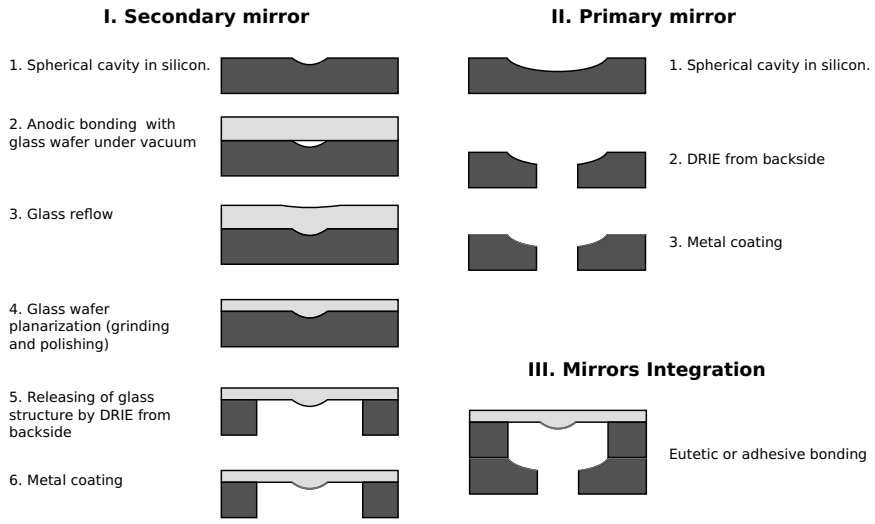


Figure 4.40: General flowchart of reflective micro-objective fabrication - (I) secondary mirror generation via combination of silicon etching and glass molding, (II) primary mirror is made in silicon whereas central port is etched by DRIE technology, (III) integration of elements on the wafer level is made via wafer bonding technologies.

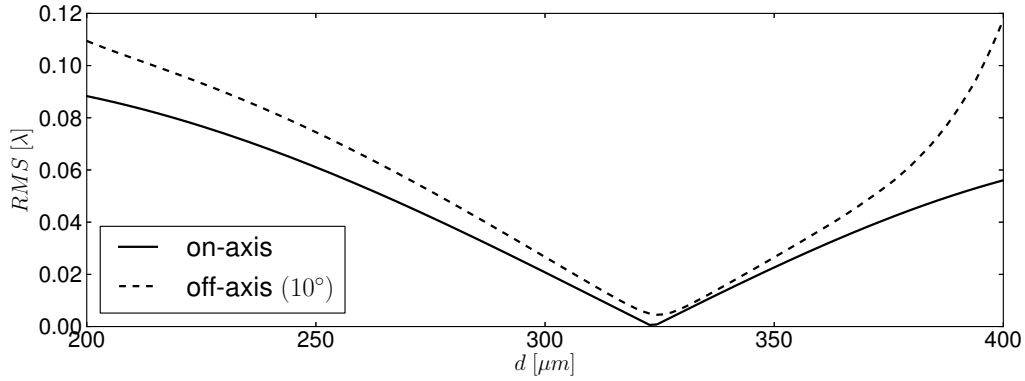


Figure 4.41: Impact of mirror separation on the aberration present in the system - The deviation of mirror separation rapidly increases spherical aberration (on-axis aberration), while off-axis components increase much slower. Solid curve represent on axis illumination (no off-axial aberration in the system), while dashed curve corresponds to off-axis illumination (10°) (in here both axial and off-axial aberrations are present).

In figure 4.41 impact of in-optimal separation on to aberrations present in the system is plotted. Considered system has the following parameters: $\phi_p = 600\mu m$, $\phi_s = 150\mu m$, $R_s = 200\mu m$ $R_p = 524\mu m$, $d_{exact} = 324\mu m$ resulting $NA \approx 0.35$. It is visible that axial misalignment mostly im-

pacts the spherical aberration while off-axial effects (mainly coma and astigmatism) increase much slower with deviation from the optimal value of mirror separation. In other terms, spherical aberration is dominant over the off-axial ones. In the considered system and from figure 4.41 a $50\mu m$ deviation from optimal separation distance provokes 0.05λ of wavefront aberration, value that can be considered as the tolerance of our system.

The two other parameters of the system, i.e., curvatures of mirrors also need to be precisely defined. In the figure 4.42 the impact of dispersion of mirrors ROC on the resulting wavefront aberrations is shown. In the case of on-axis illumination (figure 4.42a) the deviations of the two mirrors can compensate each other if there deviates accordingly (black zone in fig. 4.42a). However, when off-axis aberration are also considered (figure 4.42b), deviation of R_s or R_p, even if it is in the same direction, results in deviation from cocentrism of the two mirrors setup. The effects are in tightening of the tolerances compared to on-axis performance. However, it is important to notice that principal impact defining the tolerances in the system is the on-axis aberration, precisely due to the primary spherical aberration.

Compared to tolerance of mirror separation distance, tolerance of ROC seems to be more strict since in considered system, $20\mu m$ error leads to already non-negligible aberrations.

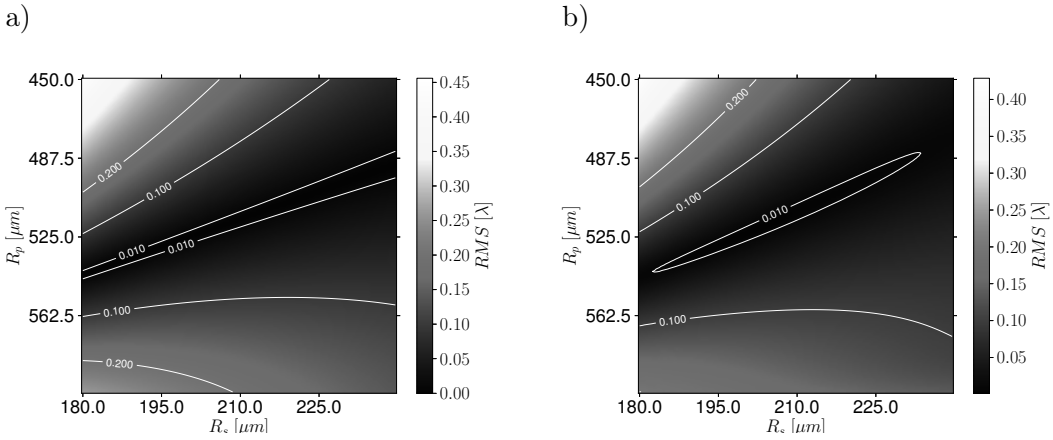


Figure 4.42: Radius dispersions impact on aberrations of Schwarzschild system - (a) on-axis case and (b) off-axis case (10°). For both cases, separation between mirrors is fixed as $d = 324\mu m$.

Furthermore, from the point of view of realization of the device, it is important to estimate the precision of mirror geometry needed by the system. In practice, various figure errors can appear depending on the fabrication process. In here, we analyze simple deviation from the spherical shape

of the mirrors by adding nonzero conic constant (A) to the mirror geometry definition. As it is a very specific deviation from the spherical shape, it can be used only as an estimation of the precision needed for mirror fabrication. To do so, the conic constant of two mirrors was varied and its impact on resulting wavefront was analyzed (figure 4.43a). It is clearly visible that secondary mirror sphericity precision affect less the system then the primary one. It can be attributed partially to the scale difference between the two cases.

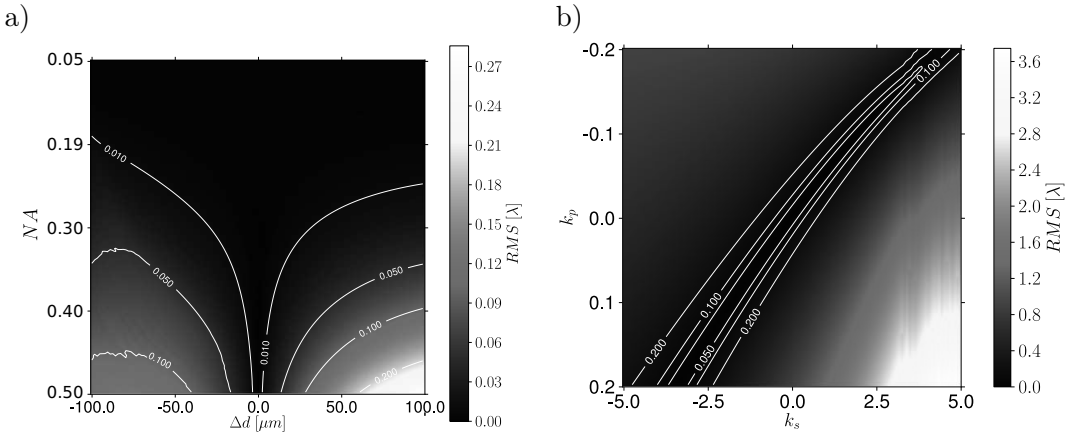


Figure 4.43: Tolerance dependence with NA of the system - (a) dependence of on-axis aberration as a function of mirror separation (Δd is a deviation from Schwarzschild condition) and NA of the system. In here, one system was analyzed (separation fixed as $d = 324\mu m$) - NA was varied by changing diameter of the input pupil. (b) The precision of mirror shape in the case where mirror has non zero conic constant, $k_{p,s}$ - conic constant of primary and secondary mirror respectively.

Finally, the tolerances are also highly dependent on the system NA. In general, higher NA requires higher precision than lower NA systems. In the figure 4.43b, the aberration dependence as a function of separation deviation and the system numerical aperture is drown. It can be seen that low NA systems are much more tolerant than high NA systems and that tolerances are not symmetric in respect to exact value of mirror separation. This effect applies to other system parameters as well so that tolerance analysis is strictly connected with the system NA.

4.2.2.3 Influence of Glass Support

The specific considered architecture based on Si/Glass technology uses a glass plate in the optical path as a support for the secondary mirror. As it is commonly known, transparent parallel-plate can add wavefront deformation to the convergent (or divergent) beam. The flat glass block in the

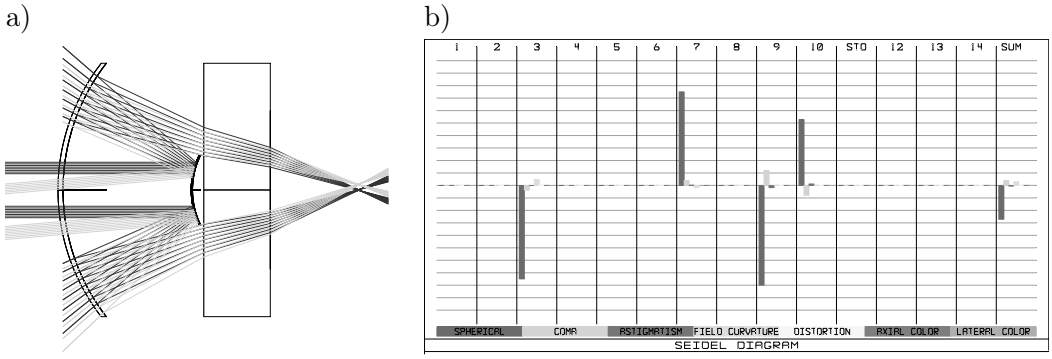


Figure 4.44: Schwarzschild system with added glass support - (a) Ray tracing of modified system and (b) Seidel diagram illustrating aberrations that originate from the additional glass plate in the light path, in here surfaces numbered: 3, 7, 9, 10 correspond to secondary mirror, primary mirror, first and second glass plate surface, respectively.

case of collimated light does not deform the beam only spatially shift it position, however in the case of convergent rays, various aberration are introduced. The source of aberration is that different rays composing the beam are shifted differently depending on their incidence angle with respect to the normal to the plate. Moreover, when polychromatic light is considered chromatic aberration may also appear. In the context of the point-symmetric Schwarzschild system, introducing parallel plate to the system naturally breaks its symmetry, and in consequence, exact correction of off-axis aberrations is not possible.

Thus, the glass support should be as thin as possible (figure 4.45). In addition, it is also possible to correct the unwanted effects of glass plate by changing the parameters of the mirror setup, viz. mirror separation d and curvature of the secondary mirror R_s.

The adjustment aiming at the compensation, is done thanks to Zemax, optimization runtime with RMS wavefront as merit function. The correction of influence of glass support $d_{glass} = 150\mu m$ was performed. By changing d from $324\mu m$ to $312\mu m$ and R_s from $200\mu m$ to $194\mu m$ compared to exact Schwarzschild configuration (NA=0.35), the RMS wavefront drops from 0.13λ (SR=0.56) to 0.03λ (SR=0.94). Interested feature of this modified system is a slightly smaller obstruction ratio of the corrected system when glass support is in the optical path.

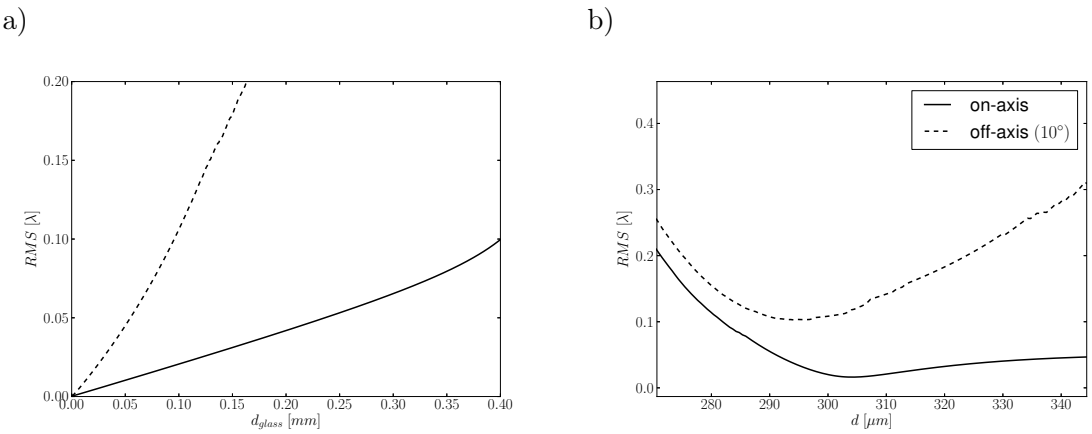


Figure 4.45: Aberration generated by glass support - (a) RMS wavefront deformation provoked by glass parallel plate in function of its thickness, (b) RMS aberration for glass support ($d_{glass} = 150\mu m$) in function of mirror separation (d) - simple change of separation distance cannot eliminate aberration generated by glass plate.

4.2.3 First Demonstrator

As it was discussed in previous sections of this chapter dealing with technologies of micro-lenses/mirrors in silicon/glass technology, isotropic wet etching process cannot generate well spherical structures above $300\mu m$ diameter. Though KOH-based process can be used for generation of larger mirrors but of lower focusing power (longer focal lengths).

Because, in the considered system the input/output port has to be made in the center of the primary mirror it is difficult to scale the system down. Scaling to much the system down is not appropriate in the considered system because the input/output port has to be made in the center of the primary mirror and should not truncate the incident beam. According to equation 4.16, the input port diameter should be around 4.2 times smaller than the primary mirror. Moreover, if the mirrors made by isotropic etching our current process (max $250\mu m$ diameter to have correct profile) tend to be used for the primary mirror the input port would have a diameter of $60\mu m$ which is too small for targeted application. Indeed, this size of the port would cause noticeable diffractive spreading of the beam inside the system that could affect the work of the system. Besides, characterization of the device would also be much more difficult.

For this reasons, the first attempt to fabricate the discussed reflective objective was made by using KOH wet etching for mirrors generation. In this case achievable NA of the system remains

small ($NA < 0.1$), however, it allows to test most of technology steps and validate the optical/technological concept[1].

4.2.3.1 Specifications

KOH double step etching process (presented in section 4.1.1) allows good control of radius of curvature of generated micro-mirrors, since geometry of mirrors is well defined by initial conditions of masked etching and etching conditions are well controllable. For the first demonstrator primary mirror was designed as: $R_p = 6200\mu m$ and $\phi_p = 800\mu m$ while secondary has mirror $R_s = 2370\mu m$ and $\phi_s = 190\mu m$, these define geometrical parameters of the system as: $d = 3832\mu m$, $NA = 0.05$, $f = 1916\mu m$. It can be mentioned that the complete integration of the system elements would be difficult since the separation of the two mirrors is larger ($d \approx 3.8mm$) than standard thicknesses of wafers used in the MEMS fabrication processes. However, the wafers with elements of the micro-objective could be easily aligned and tested on an optical test bench. Moreover, since in considered configuration NA is small, the impact of glass support ($d_{glass} = 200\mu m$) discussed before does not need to be included since it has negligible impact on the theoretical performance.

4.2.3.2 Fabrication

Both mirrors (primary and secondary) were generated with KOH techniques described in section 4.1.1 where initial apertures (circular mask windows) for masked etching step were $d_p^0 = 70\mu m$ and $d_s^0 = 10\mu m$ for primary and secondary mirrors, respectively.

The masked etching done in 10M KOH water solution at 80^oC was made within $t_p^m = 90min$ and $t_s^m = 15min$ with etching speed $v_{100} = 0.85\frac{\mu m}{min}$. The mask-less etching was performed in the same etching solution with following etching depths: $h_p^{ml} = 340\mu m$ ($t_p^{ml} = 400min$) and $h^{ml} = 120\mu m$ ($t_s^{ml} = 125min$), for primary and secondary mirrors, respectively.

The input port in the primary mirror is etched from the backside by DRIE process. Since etching is performed through wafer, mirror surface is protected by deposited 250nm layer of aluminum that serves as the etch-stop for etching performed from backside. The DRIE process performed through a resist mask (AZ-9260, $10\mu m$ thickness) that was and aligned to the mirror structures by use of the alignment marks created in backside nitride mask used in KOH etching and transferred to silicon (in the form of inverted pyramids during maskless etching step). DRIE etching is performed with an

[1] it is worth to mention that in parallel to fabrication of first demonstrator based on KOH-mirrors the development of large mirrors by isotropic wet etching and dry plasma etching are investigated in order to generate higher NA reflective objective.

additional silicon holding wafer temporary bonded (by thermo-conductive oil) to the etched wafer. The aim is to prevent a leakage in the cooling circuit as the wafer is etched through. The array of primary mirrors with etched input ports is presented on figure 4.46a.

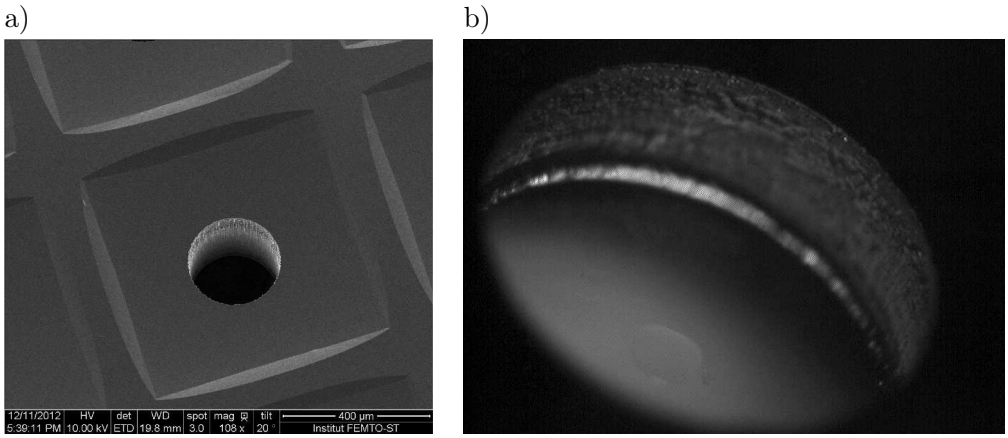


Figure 4.46: Realized mirrors for Schwarzschild micro-Objective - (a) SEM image of primary mirrors, (b) optical micrograph of secondary mirror within it silicon frame.

The wafer with molds for secondary convex mirror was bonded under vacuum condition with a borofloat 33 glass wafer ($525\mu m$ thickness), consequently thermal process was performed (section 4.1.4) to fill the silicon cavities with glass. The next step consisting glass planarization by use of grinding and polishing of front side (glass-side) of the two-wafer stack. During the grinding step, the thickness of the glass part of the sandwich can be precisely adjusted. In considered case glass substrate was grinded until the thickness of $200\mu m$.

The releasing of the secondary mirror, the etching of the silicon in the hybrid silicon/glass structure, is achieved by use of DRIE technology (Bosh process). For this purpose, the silicon (backside) was patterned with photoresist (AZ-9260, $10\mu m$ thickness) by means of UV-photolithography, where the pattern was aligned with structures located on the frontside (alignment marks were created in oxide mask on the backside after first KOH etching). The standard DRIE process was used (within A601E by Alcatel) for generation of through holes until the glass substrate. Only difference from the standard etching recipe was the periodic pauses in the process. The etching was made with 5minutes etching cycles followed by 3minutes of pause in order to compensate the low thermal conductivity of silicon/glass stack. That latter can cause overheating of the sample when the etching is continued for long time (through etching of silicon $450\mu m$ wafer takes approximately 110minutes).

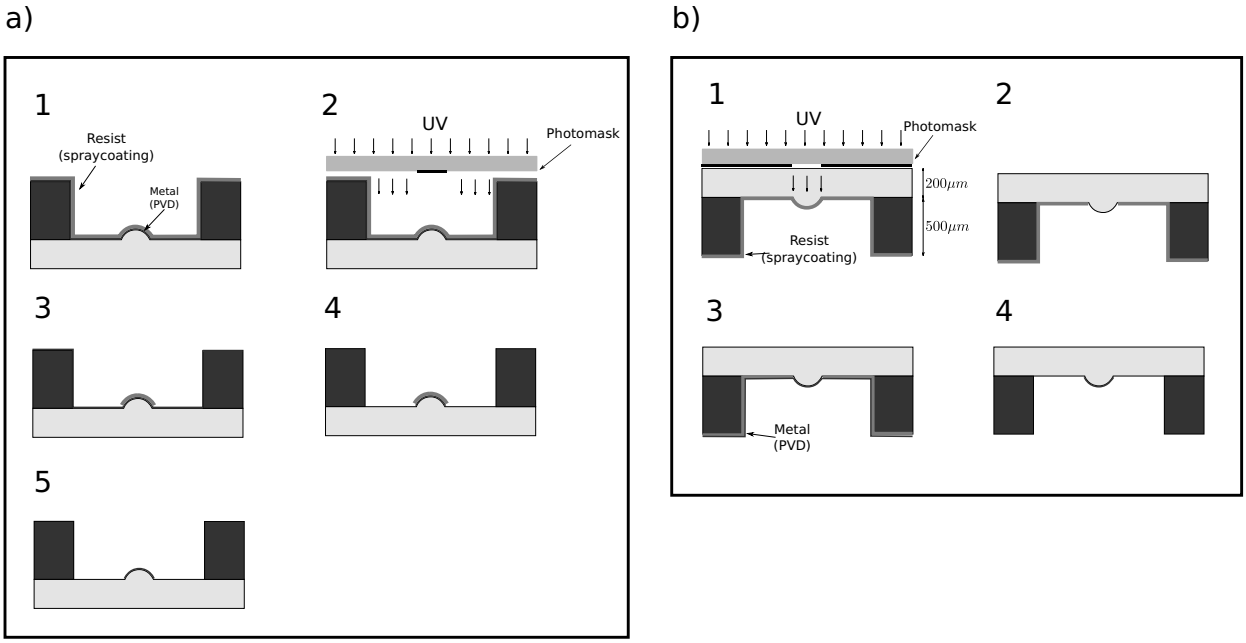


Figure 4.47: Deposition of reflective layer on secondary mirror - Two strategies considered for the selective deposition of metal on the mirror placed in deep silicon cavity: a) backside (Si-side) and b) frontside (glass-side) photolithography.

Once glass convex structures are released (figure 4.46b) they have to be covered with reflective metallic layer to generate the secondary mirror. In here, the patterning of bottom of Si cavity bottom can be a difficult task: firstly resist deposition cannot be performed within standard spin-coating process, secondly the photolithography, in particular UV-exposure, is also unusual (normally we employ contact exposition). In here, the mask used for UV-exposure is located at a significant separation (Si wafer thickness) from the interested structure. The third issue concerns the resist development: In the case of small and deep structures, the resist developer (water solution) does not well penetrate the cavities and the bottom of the structure remains undeveloped.

The first issue was addressed by using spray-coating system for resist deposition, the large separation structure-photomask did not cause visible pattern deterioration in the considered geometries ($450\mu m$ separation and $200\mu m$ structures sizes), however this could be a problem in the case of larger separations or smaller structures. The problem of poor wet-ability of cavities covered with photoresist requires the use of aggressive agitation during development (ultrasound bath).

Two process schemes are considered for this step. The first one is based on material deposition followed by selective metal etching made by backside photolithography (figure 4.47a), The alterna-

tive considered method is the UV-exposure through the glass wafer (figure 4.47b). In this scheme, the resist is first deposited onto the structure and the UV-exposition is performed from the glass side, i.e., through only $200\mu m$ thick glass. This approach requires finally a lift-off process so that reflective layer is deposited on the patterned resist. The important advantage of this process is minimization of the number of wet processes since only resist development is performed in water solution. Comparing to first scheme where in addition to development also metal etching has to be performed in the water solution, the number of wet processing is minimized. This is preferable since the specific geometry of the structure is not easy for wet processing.

4.2.3.3 Characterization

Characterization of the device is performed by IPSF measurement system described in the 3rd chapter. The two components of the system are not assembled together but tested on the optical bench so that distance between the wafers can be adjusted. The measured system response is presented on figure 4.48. The measurements does not match expected results. In particular, the focal spot is not axially symmetrical (figure 4.48a), and local side lobes (secondary, local maxima) are highly pronounced (inset in fig. 4.48a). Axial slice of the focus (figure 4.48b) also shows high asymmetry around the focal plane.

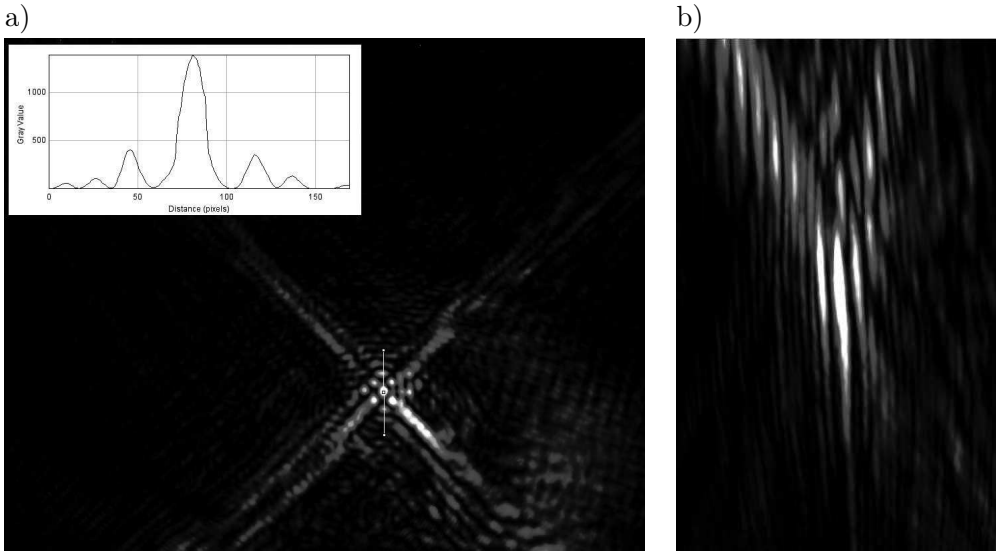


Figure 4.48: Measured focus spot of fabricated system - (a) focus plane and (b) ZX slice of focal volume.

In consequence, this 1^{st} demonstrator is not aberration free. The origin of the aberration present in the constructed system probably lies in geometry inaccuracy of composing mirrors. As was seen in section 4.1.1, used KOH technology does not generate mirror of very good spherical shapes. This appears to be clearly critical for reflective objective generation. Observed 4-fold symmetrical geometry corresponds to observed IPSF pattern of a single KOH mirror. Moreover, since two KOH-etched mirrors are used, the effect can be larger than for single surface elements (single lens, or single mirror). Finally, we have to conclude that mirror quality generated by the KOH-based technology is not sufficient for this compound system where optical quality is crucial.

4.2.4 Conclusions/Perspectives

The Schwarzschild objective is a very attractive optical architecture that in many aspects, outperforms single refractive lens. The 3 primary aberrations, namely: spherical aberration, coma, and astigmatism are completely eliminated. That means that within this system, high NA and high field of view can be achieved without resolution degradation. As a reflective element, it is also completely achromatic thus it can be employed for system employing wide-band spectrum or extreme wavelengths (e.g. X-rays, far IR) for which refraction-based elements are not adequate or available, respectively. From the point of view of the fabrication, this device can be made in batch process by stacking wafers with mirrors composing the system.

Future work will be linked to alternative mirror generation techniques (discussed in previous sections: HF/HNO_3 wet or SF_6 dry Si etching), that can allow to produce mirrors of better quality than the ones used here based on KOH wet etching.

4.3 Micro-Beam-Splitter

Many optical devices require beam splitting functionality. In macroscopic optical systems, beam splitting or beam division is achieved by use of beam-splitting cubes or tilted semitransparent mirrors. In micro-optical systems, micro-beam-splitters are necessary. Currently, beam-splitting structures for micro-optical devices rely on complicated pop-up-structures [218], complicated lithographic patterning of thick polymer films like angled UV-exposure SU8 layer [219, 220], or LIGA technology [221].

In the context of reflective confocal microscopy and in particular for the system designed in the frame of this thesis, beam-splitting is necessary to redirect the signal returning from the sample to the detector. In the miniature confocal systems, usual way to by-pass this requirement on the level of the micro-device is to employ fiber optics as the input and output of the system so that beam-splitting is performed within a fiber coupler [114, 125]. However, if miniaturization of the all parts of the system is needed, miniaturization of beam-splitters that can be easily integrated with microsystems has to be addressed. In this section, we describe the design and the fabrication of a micro beam-splitter made at the wafer-level by use of MEMS technologies.

4.3.1 Classical Beam-Splitting

Beam splitters (BS) are usually divided into two classes, i.e., polarizing and non-polarizing (polarization-insensitive). The non-polarizing BS is independent on polarization of incident beams, i.e., splits the beam in same power ratio whatever is its polarization state. Polarizing BS is normally understood as a polarizing element: on the two outputs of the BS, two orthogonal linear polarizations are present. In here, at first a more specific situation is considered: beam-splitting of a specific linear polarization state is targeted. This approach simplifies design and construction of the BS, although it still allows full use of the device in the confocal system when input polarization is well defined. Classical beam splitting devices are usually so-called beam splitting cubes, where a semi-transparent mirror is located at the diagonal plane of the glass cube (glass cube being formed by two right-handle prisms glued together). Most of BS characteristics depends on the semitransparent mirror embedded in the cube. For such mirror commonly used method is dielectric multi-layer deposition. The advantage of multilayers are low losses (comparing to metallic layers) and wide possibility of designs, i.e., appropriate stack can be chosen to obtain polarization control, achromatic or dichroic behavior.

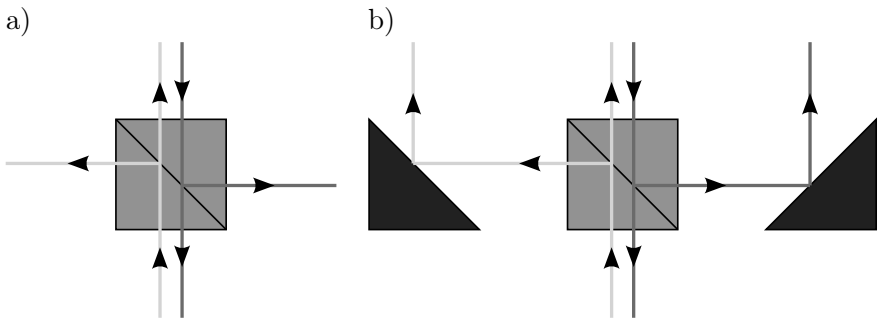


Figure 4.49: Beam splitting - (a) classical beam splitting cube and (b) arrangement of BS cube and 45^o mirrors allowing vertical two-way beam-splitting.

Typical beam-splitter separates the incident beam into two beams that propagate in two perpendicular directions (figure 4.49a). This standard configuration is not convenient in the case of miniature systems, where linear alignment of optical components is preferable, especially when they are vertically integrated. To achieve vertical beam splitting, micro-beam-splitter (MBS) has then to split the beam into two parallel laterally shifted beams. This can be achieved by arranging the beam splitter together with two "outcoupling" mirrors (figure 4.49b).

4.3.2 Wafer-Level Cube-Type Micro-Beam Splitter

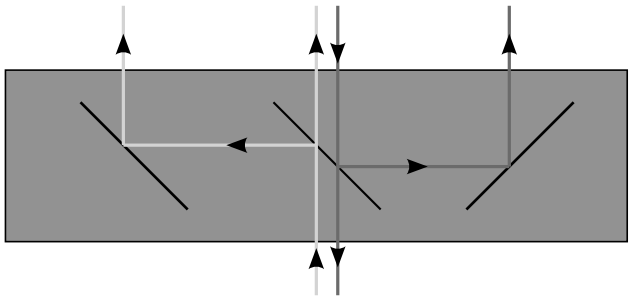


Figure 4.50: Conception of integrated vertical MBS - The integration of beam-splitting structure with two mirrors in a single component allows realization of "vertical" micro-beam-splitter, well adapted to the vertically integrated microsystems.

The scheme of targeted device is presented in figure 4.50. The main challenge for the realization of this concept is generation of 45° slanted mirrors, embedded in optically uniform medium. The fabrication is based on bulk micromachining, viz. saw-dicing of glass substrates with custom-made blades, to generate directly the 45° slanted mounts, combined with usual thin film deposition (mirror

surfaces) and embedding of the mirrors with optically appropriate (i.e. refractive index matching) UV-curing polymer (filling machined glass structure). The MBS structure is made of borosilicate glass wafer that is compatible with anodic bonding process[1] which allows easy wafer-level integration of MBS with silicon components, and particularly, thanks to wafer-level alignment/positioning possibility.

4.3.3 Realization of MBS

The technological realization of the device is based on wafer dicing process. Then the layer depositions employ standard technologies used in MEMS facilities such as physical layer deposition (PVD) for metal deposition and chemical layer deposition (CVD) for dielectric films deposition, respectively.

Structure embedding is performed with UV-curable polymer usually employed for creation of robust mechanical connections with high optical quality (transparency, uniformity). Although, employed fabrication techniques are well known and commonly applied in the MEMS community optimization of critical process steps was performed and dedicated design taking into account the fabrication accuracy was made.

Two designs are investigated: the first one is the 50/50 BS that works with a single incident polarization (TE), whereas the second design considers polarizing beam splitter. In the following, the first design was realized experimentally and demonstrated.

4.3.3.1 Architecture

The MBS is composed of two glass substrates. The bottom micromachined one is bonded together with a lid by use of UV-curable optical adhesive, as shown in figure 4.51. Thanks to refractive index precise match between UV-curable material (NOA 84, Norland Products, Inc.) and glass (borosilicate or fused silica), layers deposited onto the micromachined glass part are then embedded into an optically uniform volume, avoiding deflection of the beam due to refraction. In the demonstrator (figure 4.51), a dielectric multilayer is deposited onto central 45° surface of the structured cavity. It is designed to be, once embedded, semi-transparent to achieve beam splitting function. In addition, metallic layers are deposited onto two other inclined surfaces working as micromirrors for,

[1] It is important to note that the total structure composed from glass and polymer is not compatible with anodic bonding (temperature incompatibility of polymer), however if appropriate bonding order is chosen the device can be easily integrated by use of the standard anodic bonding process.

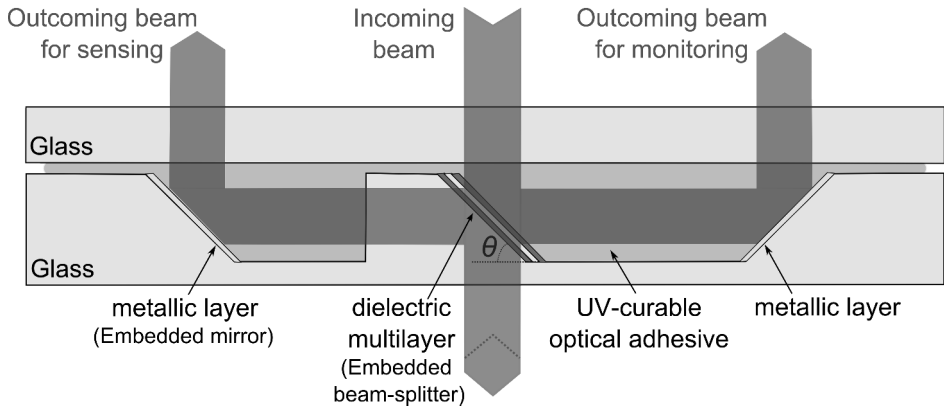


Figure 4.51: Integrated MBS architectures - System architecture allowing parallel beam splitting by use of immersed mirrors tilted at 45°.

reflecting on the one hand, the beam directly from the source and, on the other hand, the beam returned from the sample, for monitoring and sensing purposes, respectively. Thus, different types of multi-layer stacks can be deposited onto the central 45^o-inclined surface depending on the required beam-splitting function, i.e. to adapt the beam splitting ratio, the wavelength dependence or the polarization sensitivity. Such stack embedded in material of refractive index n=1.457 (borosilicate glass and UV-curing adhesive) takes the form of suspended semitransparent mirror.

Stack design The design of the stack is based on so-called quarter-wave layers. Single quarter-wave layer, composed of material of higher refractive index than the one of the substrate, can be used to increase the reflectivity of the optical interface [6]. The use of stacked quarter-wave layers allows increasing performance of the mirror. However, technological realization becomes more difficult when number of layers grows since the tolerances on the layers fabrication are more strict. In here, the quarter wave stack is composed from layers periodically deposited on the glass surface. The layer of lower index (n_L) of refraction is fixed as the same as the one of embedding medium, i.e. $n_L = 1.457$, the index of second layer (n_H) has to be larger than n_L. The thickness of both layers are defined as a quarter of considered wavelength (λ) (equation 4.17):

$$h = \frac{\lambda}{4n\ cos(\beta_n)} \tag{4.17}$$

where β_n is the incident angle at the layer interface (in our case $\beta_1 = 45^o$) and $\lambda = 632.8nm$. Condition 4.17 fixes the thickness of low index layer as $h_L = 153.6nm$. The choice of n_H, and number of layers was done by analyzing beam-splitting parameters of the stack and the tolerances

n_H	1.7	1.8	1.9	2.0	2.1
h_H [nm]	117.0	107.2	99.1	92.3	86.5
3 Layers:					
R_{TM}[%]	0.53	1.59	3.38	5.95	9.21
R_{TE}[%]	24.62	38.00	**49.63**	59.18	66.82
T_{TM}[%]	99.47	98.41	96.62	94.05	90.79
T_{TE}[%]	75.38	62.00	**50.37**	40.82	33.18

Table 4.3: Beam splitting performance of examples dielectric stacks - 3 layers stack scan assure 50/50 beam splitting only for TE polarization, TM polarization has always relatively high transmission through the stack. The exact 50/50 TE splitting can be achieved with $n_H = 1.904$.

required on the layers composing the stack. Table 4.3 shows beam splitting performance of several multilayer stacks for few different values of n_H (that can be reached with SiO_xN_y). As it can be seen TM polarization weekly interacts with the multilayer (relatively small reflection coefficient). Indeed, with considered geometry and principal material (glass with n=1.457) it is difficult to achieve 50/50 splitting ratio for both polarizations. In consequence, for the first realization of the MBS we have employed 50/50 beam splitting ratio for a single TE polarization only. From the table 4.3, it can be seen that 3 layers stack can assure desired reflectivity for $n_H = 1.904$ (and $h_H = 99.1nm$).

Finally, the 3 layer stack has to be constructed from 3 layers with refractive indices equal to 1.904/1.457/1.904 ($n_H/n_L/n_H$) and thicknesses equal to 99/154/99nm ($h_H/h_L/h_H$), respectively. Such stack embedded in material of refractive index n=1.457 (borosilicate glass and UV-curing adhesive) splits equally the incident beam (without absorption unlike metallic layers) if the latter is TE-polarized and if its angle to the stack normal is 45^o. If 1% splitting ratio deviation is considered whereas incident angle and refractive indices are well controlled, the thickness tolerances are ±20 nm and ±9nm for low and high refractive index layers, respectively. If thicknesses and refractive indices are well controlled, 1% splitting ratio deviation is encountered when incident angle differs by $\pm 0.7^o$ from 45^o.

Advanced polarizing MBS One efficient way to generate a PBS is to use property of the Brewster angle[1] - an angle for which TM polarized incident light is not reflected. The difficulty of

[1] Brewster angle is the angle defined for an optical interface for which TM polarization has null reflection coefficient, this particular phenomena is often use as principal method for controlling both polarization in most commercial polarizing BS [222].

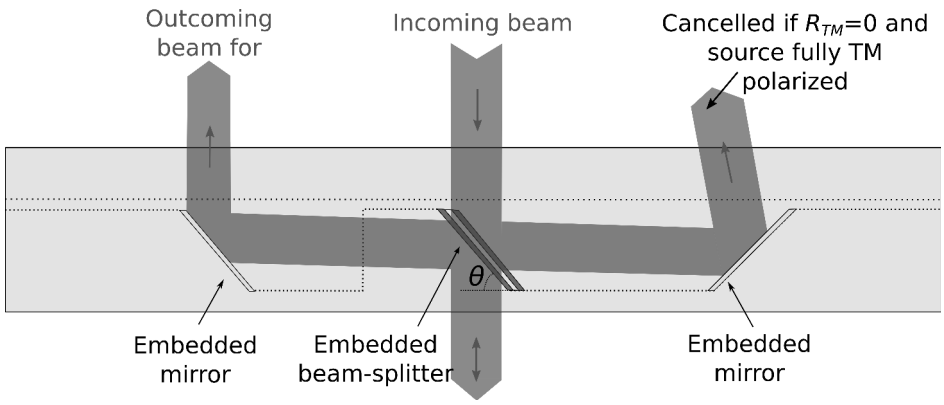


Figure 4.52: Modified architecture for polarizing MBS - Change of the angle of the mirror allow to employ the Brewser angle properties and add controllable polarization sensivity to the device.

controlling both polarization within considered system originates from fixed material of the base substrate, when using borofloat glass (to low refractive index) as a substrate Brewster angle property is not possible to employs in considered geometry. However, using a blade with a slightly different shape, can results in an angle close to the Brewster condition ($tan(\theta_B) = \frac{n_H}{n_L}$) for all slanted sidewalls ($\theta_B = 52.5^o$ with previously considered refractive indices). Then, polarizing beam splitting with high extinction ratio (>100 in reflection and transmission) can be reached with relatively simple stack based on only few layers (7 to 9). Furthermore, since higher refractive index substrates are not required to respect Brewster condition at 45^o, MPBS can be fabricated from borosilicate glass as well.

The modified geometry of the device is shown in figure 4.52 and considered stacks parameters are summarized in table 4.4. It is visible that increasing the number of layers improves its efficiency along TE. It is important to underline that in considered system when Brewster angle is required the choice of n_H defines the angle of the mirror ($\theta = \theta_B$) and in consequence the thickness h_L (via equation 4.17). Table 4.4 presents few performances of several possible stacks. Efficiency of polarization separation is in here reported through the transmission extinction ratio (TER) defined as a ratio of transmission coefficients for two perpendicular polarization, i.e. $TER = \frac{T_{TM}}{T_{TE}}$. For possible refraction indices of dielectric films (i.e. accessible n_H) deposited within standard techniques 7 or 9 layer stack can already provide efficient polarization separation.

n_H	1.7	1.8	1.9	2.0	2.1	2.2
θ_B [°]	49.40	51.01	52.52	53.93	55.25	56.49
h_L [nm]	166.9	172.6	178.5	184.5	190.6	196.7
h_H [nm]	122.6	113.1	105.0	97.9	91.7	86.3
7 Layers:						
R_{TE}[%]	71.2	87.3	94.4	97.5	**98.9**	**99.4**
TER	3.5	7.9	18.0	40.3	**87.3**	**183.4**
9 Layers:						
R_{TE}[%]	83.3	94.3	98.0	**99.3**	**99.7**	**99.9**
TER	6.0	17.7	51.1	**141.8**	**375.4**	**951.5**

Table 4.4: Multilayer stacks for polarizing MBS - The performances of different stacks expressed in terms of TE polarization reflective coefficient (R_{TE}) and extinction ration in transmission. The most efficient stacks are marked with bold font, TER reaching almost one thousand (like for $n_H = 2.2$, 9 layers stack) is close to performance achieved by commercial PBS.

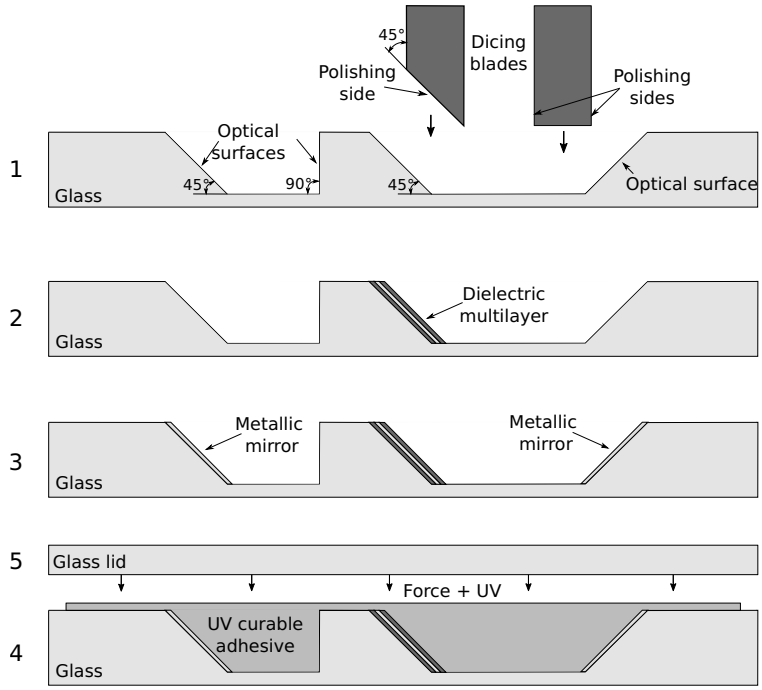


Figure 4.53: MBS fabrication flowchart - 1. dicing of glass; 2. deposition and patterning of dielectric multilayer; 3. deposition and patterning of metallic layers; 4. filling with refractive-index matching UV-curable adhesive; 5. sealing with glass lid and bonding by UV-exposure.

4.3.3.2 Fabrication

The fabrication process is shown schematically in figure 4.53. It combines saw-dicing-based micromachining of glass with deposition of thin-film dielectric and metallic layers. 0.7mm thick Borofloat 33 glass substrate (Schott) is first structurized by use of automatic high precision dicing saw DAD321 from DISCO (Step 1). After dicing, selective deposition of dielectric beam-splitting stack (Step 2) based on lift-off using spray-coated resist. For this step, three layers of SiO_xN_y are deposited by inductively coupled plasma-enhanced chemical vapor deposition (ICP-PECVD) at low temperature (80^oC), where refractive index is alternately changed between 1.45-1.95 by variation of each layer stoichiometry. Following (Step 3), selective metal deposition is performed by means of physical vapor deposition (PVD) for the outcoupling mirrors. The last, 4th step is the polymer deposition and closing the structure with glass lid by means of index matching UV-curable polymer (NOA 84).

Glass dicing. Dicing process is commonly used in the MEMS fabrication workflow, however only as a dicing method to separate/release the micro-structures fabricated within the wafer. The less conventional use of saw dicing as a bulk micromachining method was demonstrated in [223]. An interesting result, considering the use of dicing saw for generation of "optical grade" surfaces, was obtained in the case of processing of crystalline lithium niobate [224].

Dicing optimization Glass dicing process is commonly employed in microfabrication workflow but the quality of surface generated by the process is hardly ever considered. In the investigated process, and since saw-machined surfaces serve as optical elements, surface quality is of the most importance. The optimization of dicing process was performed in order to obtain smooth, flat surface with minimal quantity of defects (scratches, digs) that are generated in the standard dicing process.

Dicing procedure has been first optimized on vertical cuts (with polishing blade). Optimized dicing process schematically shown in figure 4.54, it includes conditioning of the blades with special DISCO plate and silicon wafer, then dicing of vertical groove at low speed (0.2 mm/s), followed by a second dicing (0.2mm/s) in order to improve the surface quality, dicing blade in all processing steps spins at the same speed of 15000rpm.

Figure 4.55 (a) and (b) show the improvement consecutive to the second blade travel ($60\mu m$ of the bottom encountered only one travel). The custom made dicing/polishing blades and optimized dicing procedure lead to surfaces characterized by four-times lower roughness than obtained typically

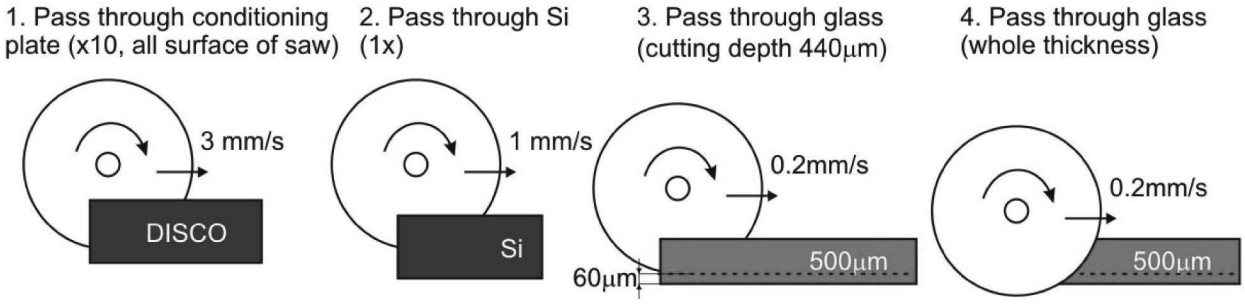


Figure 4.54: Scheme of optimized dicing process - Optimized procedure consists dicing blade conditioning and double passage of dicing blade with low speed over the machined surface.

after standard glass dicing/polishing process (roughness measured by stylus profilometer) as shown in figure 4.55 (c) and (d).

Similar procedure was employed to generate the 45^o inclined surface, for which a vertical groove is first diced at low speed (0.2 mm/s), followed by final dicing with 45^o-inclined custom made blade to form slanted surfaces. Figure 4.58 shows the resulting saw-diced glass structure. Height of the inclined surfaces is $400\mu m$. It can be noted that the 2mm lateral separation (requiring several adjacent saw cuts) is chosen to facilitate optical characterization, although they could be much closer if source and photodetector are closely located on the same chip.

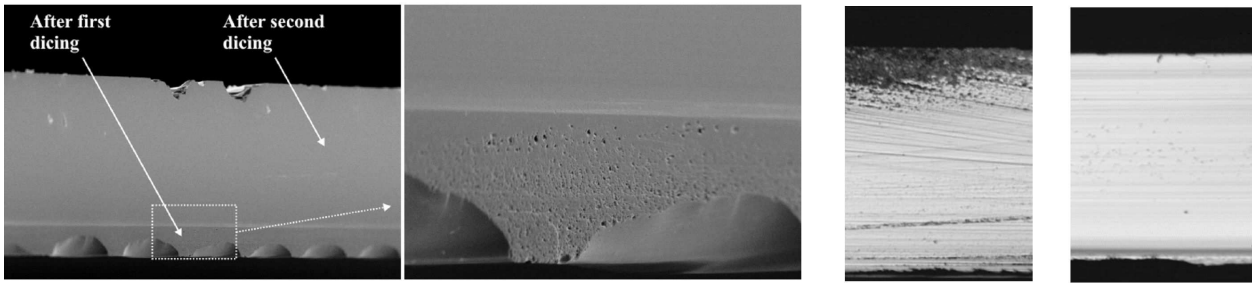


Figure 4.55: Illustration of Dicing optimization - a),b) effect of blade passing on surface quality in case of the substrate where the bottom part has encountered only one dice passage, c) example of diced surface after standard process and d) sample diced by optimized process.

Roughness impact. In any optimization process, it is important to have a simple merit function that allows comparing and guiding the optimization procedure. The standard merit function in the context of surface quality optimization is RMS surface roughness. RMS is calculated as the root mean squared deviation from filtered topography data (obtained via 1D or 2D profilometry). Filtering is applied to the data in order to extract and analyze only small scale topography details

(so-called high-frequencies). In general, quantitative absolute measurements of roughness measurement is a difficult task since it strongly depends on the used equipment and details of the data processing method. For these reasons, roughness measurement are often not directly comparable [225]. The process optimization was guided by comparative analysis of RMS obtained within contact profilometer (Alpha-Step IQ TENCOR: tip ROC: $5\mu m$; cone angle: 60^o; high-pass filter with cut-off at $80\mu m$). According to this measurement presented dicing procedure improve surface quality over 4 times over standard dicing process (figure 4.55).

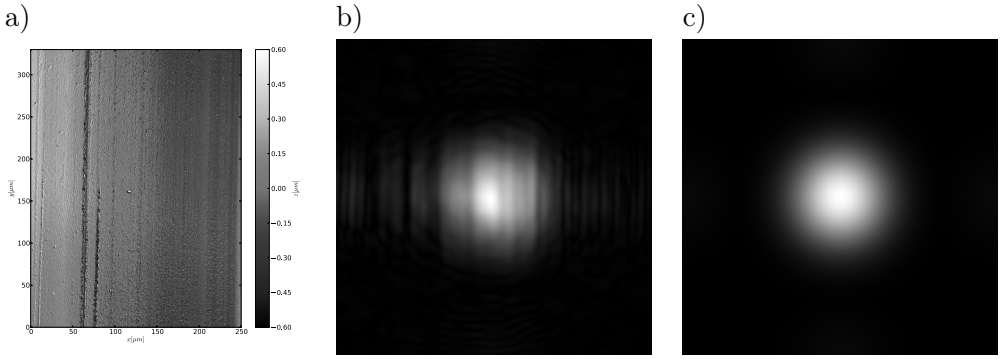


Figure 4.56: Optical impact of diced surface structure - (a) measured topography (white light interferometry) of mirror, (b) simulation of beam reflected from beam-splitter surface and (c) reference beam.

This comparative analysis of surface roughness is useful during optimization, however it does not provide the real measure of surface quality that can be translated to optical performance of the final device. Normally, surface quality measures (flatness, roughness etc.) in the context of optical application are compared to the operational light wavelength, that in our work is $\lambda = 633nm$. However, in the considered case when the mirror surfaces are embedded in a medium, the wavelength interacting with mirror is shortened so that $\lambda_n = \lambda/n$. In consequence tolerances for surface quality are tighten than in the case of free space optical mirrors.

The optical impact of residual surface imperfections of the diced structures at 45° was analyzed by use of 2D topography measurements performed by white-light interferometer (MSA-500 by Polytec). Based on the measurements, propagation of a Gaussian beam was simulated after reflection from the surface. The results are reported in figure 4.56 where measured topography, simulated beam after reflection (24mm after the mirror) and reference Gaussian beam (in the case of reflection from a perfect mirror) are presented. The roughness present on the surface of the mirror scatters

part of the reflected light out of the propagation direction. The power loss encountered by the beam can be used to quantify the surface quality. In the considered case, about 28% of light is lost due to imperfect surface of the diced surface. This is obtained by comparing energy in beams (fig. 4.56a and b) encircled by a circle of diameter equal to the reference beam waist.

Important observation is the asymmetrical scattering generated by the considered surface. This effect is a consequence of the specific structure of the surface defects. The scratches consecutive the dicing process diffract light in the direction perpendicular to the scratches direction. This effect is better visible in the figure 4.57 where cross-sections of beams from figure 4.56b and c are plotted. The y-section (along the scratches) is smooth and symmetrical while section in x-direction (perpendicular to the scratches) is perturbed with visible secondary peaks and thus wider and less symmetrical than the y-profile.

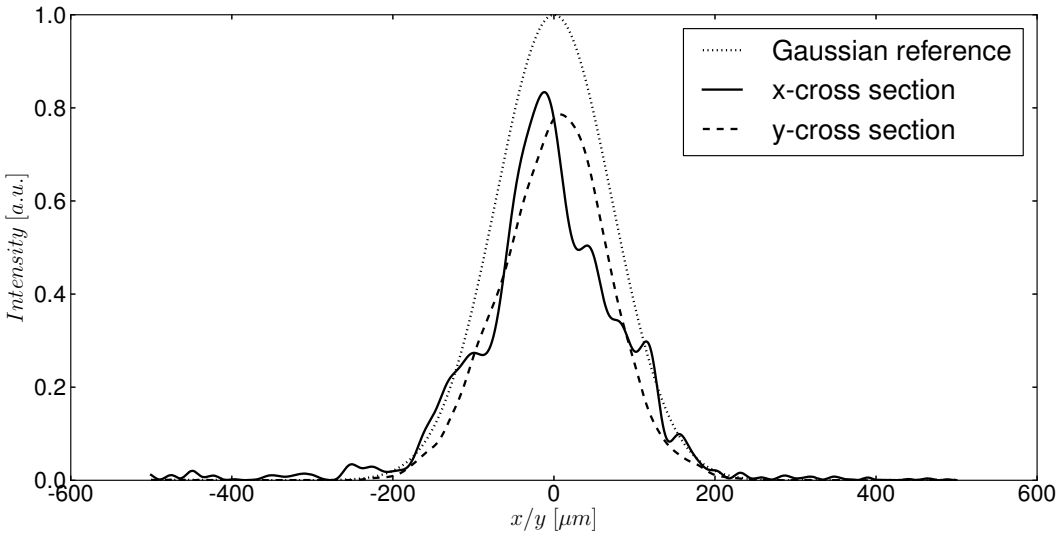


Figure 4.57: Cross sections of the beam reflected from diced surface - Two orthogonal cross sections have different structures, the difference originates from specific "anisotropic" defects of the machined surface.

The impact of surface quality is more pronounced after the reflection from the surface, than in the case of the transmission. Since non-perfect surface is embedded in index matching material, the surface roughness will not directly affect the beam propagation. In this case the roughness could affect the performance of the dielectric layer that inherits rough structure of the surface, however experiment does not show significant losses nor beam deformation in the beam transmitted through the structure.

	NH_3[sccm]	SiH_4[sccm]	O_2[sccm]	Ar[sccm]	P [W]	p[Pa]	n	rate [nm/min]
SiN_x	145	6.8	0	140	150	5	1.95	17.3
SiO_y	0	130	9	126	300	2	1.45	13.6

Table 4.5: IC-PECVD dielectric films deposition process parameters - Different condition in the deposition chamber results in different refraction indices of deposited layer the deposition was performed at temperature 80^{o}C.

Dielectric mirror The beam splitting functionality lies in the semitransparent dielectric mirror deposited in central 45° wall (figure 4.51). The beam-splitting mirror is constructed as a stack of thin films generated by use of chemical vapor deposition (CVD) technology. The parameters of MBS in terms of light transmission, reflection and polarization sensitivity largely depend on the design and realization of the stack. In here, we present a system rather simple to realize but showing sufficient performances to be deployed in considered miniature confocal system.

Stack multilayer is fabricated by means of inductively coupled - plasma enhanced chemical vapor deposition system (IC-PECVD). All the films composing the stack during a single sample load are fabricated at single sample load. Patterning of the structure can be performed by lift-off technique for which resist deposition on the structured wafer is made within spray coating system. The layers refractive index can be precisely controlled by adjusting process conditions. In general, refractive indices obtained within considered system ("ICPECVD SI 500 D" by SENTECH) can vary as the stoichiometry of the deposited material changes [226]. Process parameters used in the deposition are summarized in the table 4.5.

4.3.4 Characterization

Figure 4.59 shows a fabricated device during its characterization. It has to be noticed that the pictures display only the scattered light to illustrate the device principle, whereas the beams of interest are reflected perpendicularly to the device and not captured by the camera. Figure 4.59a shows the light path when the incident light hits the semi-transparent stack and is reflected by the facing mirror. In Figure 4.59b, transmitted light through the device is reflected onto an additional mirror (placed under the device) and returned into the device to be guided to the second mirror. From incident TE-polarized light, 48.5% is transmitted by the multi-layer stack (Fresnel reflections subtracted), i.e. close to the designed 50% splitting ratio. This value demonstrates the correct behavior of the stack. The measured reflected beam (left side of pictures in figure 4.59) is equal

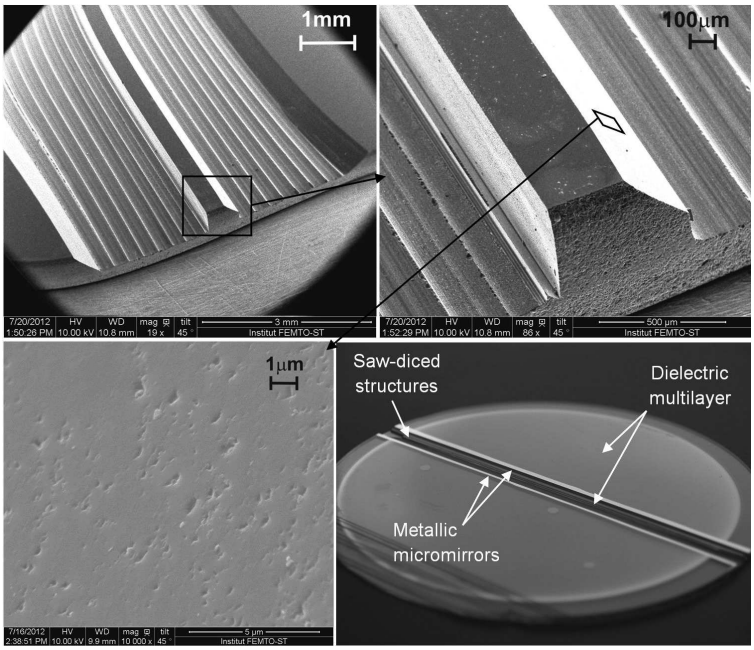


Figure 4.58: Fabricated MBS - a),b),c) - SEM micrographs of diced structure and d) MBS with deposited layers ready to be sealed with lid and UV-curable adhesive.

to 25.3% of the incident light (power-meter located at 6cm from the device). These measured efficiencies lead to a beam splitting ratio T/R=65.7/34.3 at λ=632.8 nm with 26.2% losses.

Losses of reflected light encountered at both multidielectric stack and gold mirror (totally near 20% of incident light) are attributed to gold absorption (5%) and mostly to scattering resulting from non-perfect quality of the two 45°-inclined surfaces.

As seen in section 4.3.3.2, compared to a perfect surface, the 45^o inclined saw-diced one realized for the demonstrator leads to 28% of losses due to scattering. Shape anisotropy of the reflected beam confirms that losses are mainly due to scratches oriented along the dicing travel (figure 4.56). Considering the complete device characterization, and when such losses are taken into account along with gold absorption, the ratio between reflected and incident light should be equal to 24.8%. This value is in very good agreement with the measured reflected light (25.3%).

4.3.5 Conclusions and Perspectives

This novel fabrication method for micro beam splitter (MBS) is based on saw-dicing of borosilicate glass substrate and on deposition of multidielectric layer. In order to avoid deflection of beams, the structure is filled with refractive index matching UV-curable adhesive. The demonstrator behaves

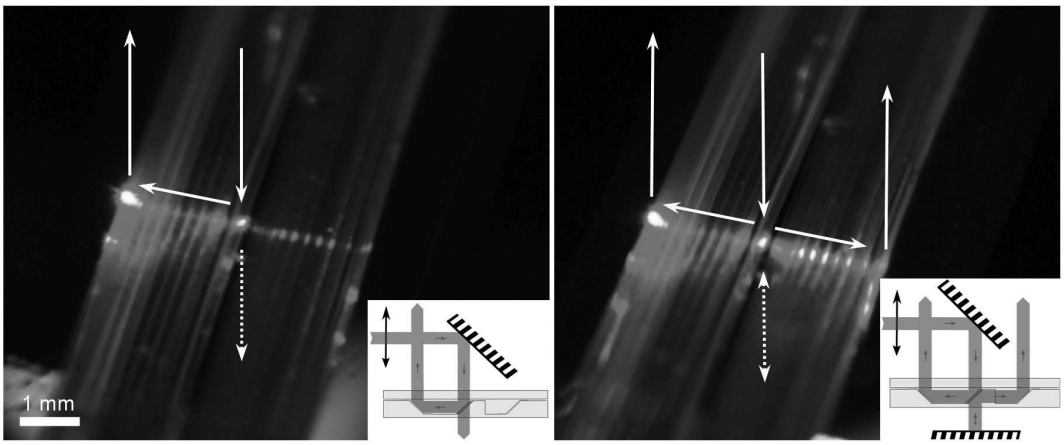


Figure 4.59: Characterization of constructed MBS - (a) device working in single pass mode (light-path in the inset), and (b) in the round-trip mode.

as a beam splitter for TE-polarized light. Concept for easily-manufacturable micro polarization beam splitter is also presented, reaching high extinction ratio with only few dielectric layers. The device was developed for application into the miniature confocal microscope, however, as it is a generic optical component, it can find applications in many different photonic micro-systems (interferometers, bio detection systems, data storage, etc.). This is strengthened thanks to its wafer-level fabrication methodology and consecutive integration and packaging capabilities as well its wafer-level alignment.

The future work will be focused on improving the quality of diced surface to suppress the losses due to scattering and eliminate the beam deformation due to imperfect surface. The optimization of the dicing process can be still improved, since in fabricated structure, dicing process was based on optimization made with vertical cuts. In practice, since slanted walls are generated with a blade of different geometry, mechanical behavior can be expected to be different, resulting in worst quality of slanted walls than vertical ones. Then, the improvement of dicing could be also achieved by using more mechanically stable dicing blade such as a symmetric v-shaped disc. The other possibility is to add a post-processing step aiming to improve quality of the surface. For instance thermal processing could be used for this step.

5

Toward first demonstrator of scanning confocal microscope

In this chapter, the general concept of scanning confocal microscope demonstrator, based on combination of MEMS 3-D optical microscanner and fiber-optics illumination/detection system, is described. The construction of the MEMS 3-D microscanner, which is a key sub-system of scanning confocal microscope, is presented. In particular, we emphasize the integration method of glass microlens with silicon microactuators as well as the overall wafer-level bonding/interconnecting strategy for 3-D microscanner.

5.1 Introduction

Realization of scanning confocal microscope on-chip, employing microlens transmissive 3D optical scanning, represents several technological difficulties and challenges. The optical design of 3D scanning mechanism, described in detail in Chapter 2, has to be implemented in a compact three-dimensional structure, which is built according to the rules of MEMS technology and follows numerous opto-mechanical constrains, compatibility requirements etc. Moreover, besides scanning system, some additional elements, such as light source, collimation block, beam splitter and photodetector are required. Thus, one of the main difficulties is the 3D integration of heterogeneous building blocks, especially fragile micromechanical components (microactuators) and micro-optical components (microlenses), both fabricated at wafer level. Another challenge lies in the optimal choice of monolithic or hybrid technologies to integrate glass microlenses on top of MEMS microactuators, allowing high-frequency scanning of optical beam as well as compatibility with batch

fabrication and bonding process (temperature, pressure). The last but not least demanding tasks are the efficient electrical interconnection for microscanner driving and overall protection of system from environment (dust, moisture).

The development of the scanning confocal microscope has therefore multidisciplinary character. Particularly, it requires expertise in state-of-the-art integration and packaging technologies. Hence, this part of work, concerning the MEMS 3D optical microscanner, was carried out in the frame of DWST-DIS project in cooperation with Fraunhofer Institute for Electronic Nanosystems ENAS (Group of System packaging, lead by dr Maik Wiemer) the world wide known specialist in micro/-nanosystems integration and packaging technologies. The chosen development strategy for the first demonstrator was based on the following assumptions:

- development in parallel of different building blocks of the 3-D microscanner and vertical integration technologies[1],
- simplification of illumination/detection blocks by use of fiber optics components,
- development of relatively simple hybrid method of integration of microlenses with silicon microactuators.

In consequence, the simplified version of the microscope, considered to be fabricated as a proof-of-concept demonstrator, consists of fully integrated MEMS 3-D microscanner (scanning doublet + focusing lens), whereas source, detector and collimation block are realized by use of commercially available optical fibers components.

5.2 General architecture

The scheme of hybrid scanning confocal microscope, utilizing MEMS 3D microscanner and optical-fiber components, is presented in figure 5.1. The illumination is provided by single mode optical fiber from pigtailed laser VCSEL source (λ=637nm). The collimated input light beam is provided by a GRIN lens that is apertured ($\phi = 150\mu m$) in front of the scanning system. The collection of the output light of the system is performed within the same components, where the fiber core serves as a confocal detector (confocal pinhole). In order to fulfill condition of optimal confocal imaging, for given size of the fiber core ($d_{core} = 4\mu m$), the focal length of GRIN lens should be

[1]this choice was also motivated by division of blocks development and integration technology to two project partners: FEMTO-ST and Fraunhofer/ENAS

$f_{grin} > 600mm$. In our system, the commercial GRIN lens (Edmunds Optics), characterized by focal length of f_{grin}=920mm and diameter of $D_{grin} = 1000\mu m$ is used. The 3D microscanner employs commercially available glass ball microlenses, which are assembled and bonded into the microscanner platforms.

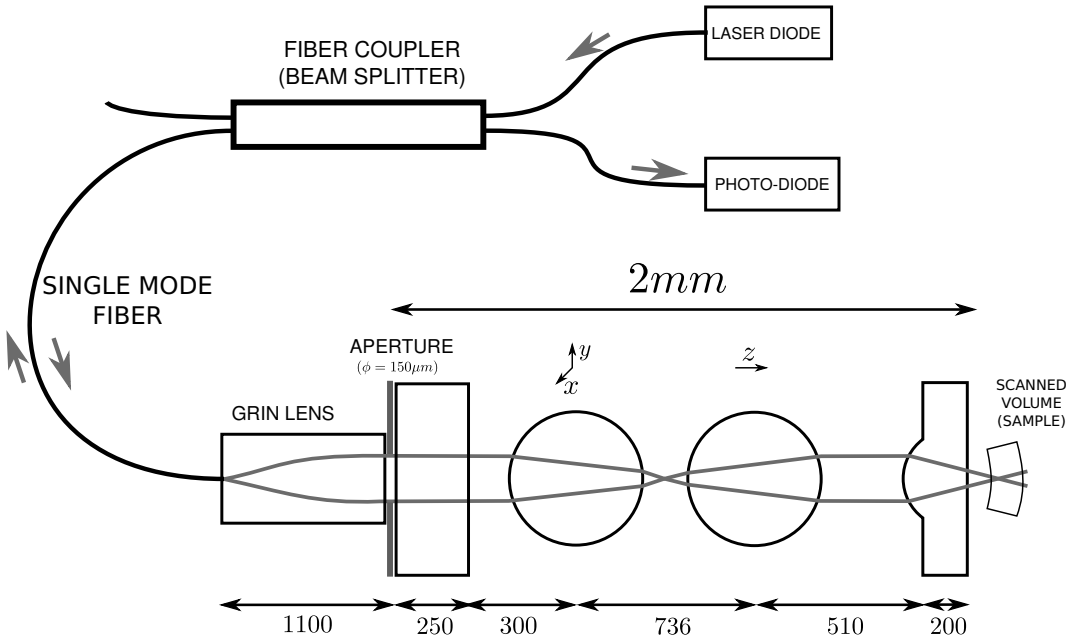


Figure 5.1: Scheme of optical design of hybrid confocal microscope - Scanner transformed into confocal microscope by providing illumination/collection blocks by fiber-optics components (all unitless numbers refer to distances in microns).

5.3 MEMS microscanner for confocal microscope

As it was discussed in detail in chapter 2, the working principle of the microscanner is based on a free-space transmission steering of a laser beam when it passes through two movable microlenses. The displacement of microlenses is provided by two electrostatic MEMS micro-actuators, in-plane (comb-drive X-Y-axis) and axial (parallel-plate Z-axis), which are stacked vertically (Figure 5.2). This type of MEMS-based scanning has been proposed by [127] as an alternative approach for micro-machined confocal microscopes, usually employing scanning micromirrors [125]. This architecture allows implementation of a compact and possibly array-type optical microsystems with simplified optical path and possibility of on-wafer packaging of sensitive components. It is also compatible

with multi-wafer integration, where all individual building blocks are wafer-level fabricated, stacked and mechanically/electrically connected by appropriate wafer bonding methods.

5.4 Opto-mechanical design

The construction of the 3-D microscanner is presented in the figure 5.3. The device is composed of 5 functional elements (building blocks) that are fabricated individually on five different wafers: top glass lid, silicon electrostatic comb-drive X-Y microactuator with integrated scanning microlens, spacer wafer, silicon electrostatic Z microactuators with integrated second scanning microlens, and bottom glass lid with integrated focusing microlens. The XY microactuator that has been the purpose of a former PhD work [132], is a translation microstage with frame-in-the-frame architecture, which provides an independent movement of microlens in the range of $\pm 35 \mu m$ using four comb-drive actuators and a system of straight spring suspensions. The Z microactuator is based on a electrostatic parallel-plate actuation principle, in which the microlens is located in the center of a movable electrode and allowing out-off plane microlens scanning in the range $\pm 20 \mu m$ [133]. All the building blocks of the microscanner are mechanically and electrically connected at the wafer level. Two glass lids, made of borosilicate glass, ensure an excellent optical transparency through the whole stack for incoming laser beam, providing at the same time hermetic sealing of the device. Thus, the sensitive microactuators and glass microlenses are protected from environmentally-induced degradation (dust, moisture). The MEMS microactuators that are the core of the scanning system are fabricated by double-side high-aspect-ratio DRIE of silicon on insulator (SOI) substrates. The both lids enclosing the system are fabricated in borosilicate glass, while separator wafer located between two scanners is made of bondable LTCC substrate. Although this system is heterogeneous in terms of materials used for generation of different blocks, only one anodic bonding technique is necessary to mechanically connect all the blocks. The illumination/collection system, realized by use of commercially available fiber-optics components is connected with the 3D microscanner by assembly of the GRIN lens onto the top glass lid using the optical UV glue. The aperture deposited on the top lid defines the stop of the optical system truncating the beam from relatively large GRIN lens.

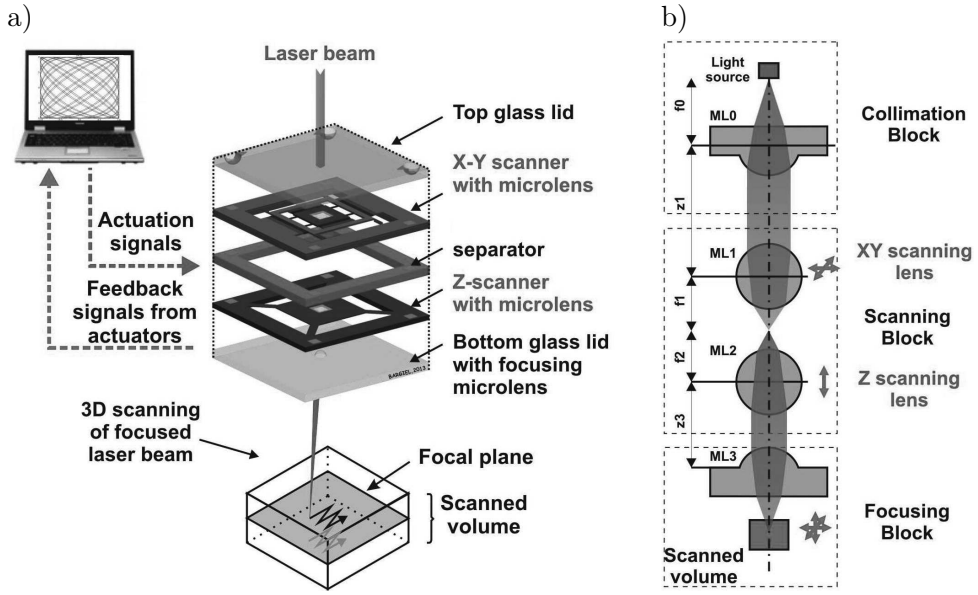


Figure 5.2: Vertically stacked MOEMS scanner: System conception - The idea of system is based on vertical architecture of the device that can be realized within integration method based on vertical-stacking of the functional wafers. (a) scheme of system composed of stacked functional blocks and (b) optical scheme of the system.

5.4.1 MEMS/Mechanical constraints, technological limitations

5.4.1.1 Bonding methods and materials selection

The borosilicate glass materials, such as Borofloat33 (Schott) or Pyrex (Corning) are commonly used in the M(O)EMS technology due to their excellent connection with silicon via anodic bonding method. The composition is borosilicate glass is based generally on silica mixed with boron oxide and doped with sodium. The possibility of reliable bonding is important parameter when considering heterogeneous micro-systems. Many different bonding techniques exist [227] from which anodic bonding is considered as one of the most reliable (hermetic packaging) and relatively simple bonding methods. As such, it is very convenient method for use in the considered microsystem. However, this specific bonding technique is limited to specific materials. The usual substrates that are anodically bonded to silicon are sodium containing, high quality borosilicate glass wafers, having coefficient of thermal expansion (CTE) adjusted to CTE of silicon. However, due to several technological reasons, the vertical interconnects are difficult to realize in glass wafers with thickness of several hundreds of micrometers. Recently, Nikko company [228] has developed low temperature co-fired

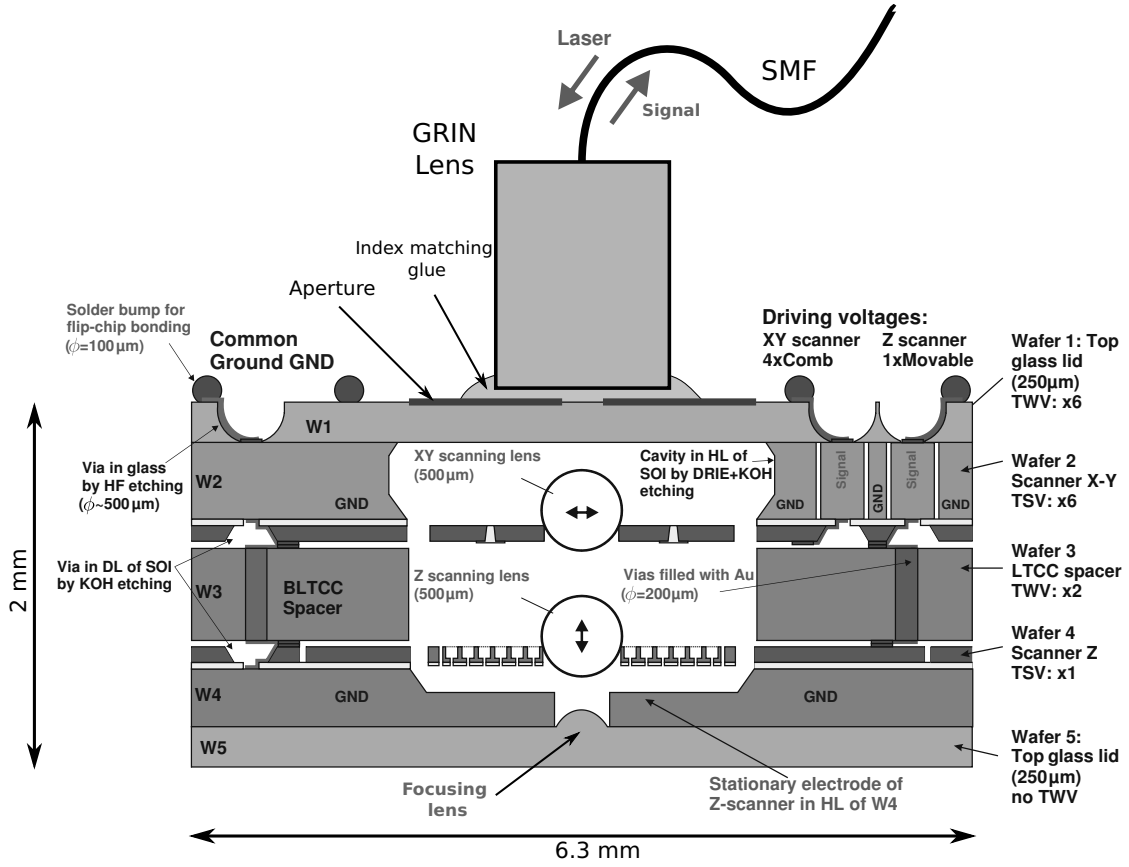


Figure 5.3: Construction scheme of vertically stacked MEMS confocal microscope - Architecture of the device realized within hybrid approach: vertical-wafer stacking approach used for scanner construction and fiber based system for illumination/detection block.

ceramic (LTCC) substrates, which can be anodically bonded to silicon due to matched CTE [229]. The important advantage of using LTCC substrate instead of more standard glass substrate, is the possibility of relatively easy integration of lateral and vertical electrical interconnections as well as embedded cavities during the substrate fabrication. Embedded structures and vias are created by pin punching of the green sheet, followed by screen printing of via materials, lamination and firing. Due to the relatively low sintering temperature of this LTCC (around 800°C to 900°), the vias can be filled with highly conductive materials such as Ag or Au. figure 5.48 is a SEM. cross-section photo of a LTCC substrate sample.

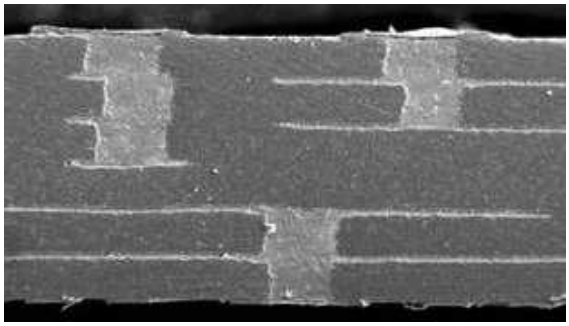


Figure 5.4: LTCC substrate - Cross section of anodically bondable LTCC substrate with through wafer electrical interconnects [229].

5.4.1.2 Thickness limitations

The basic MEMS material is silicon in the form of thin wafers. The thickness of Si wafers varies from typically 300-600μm (4 inch wafers) up to 1500-2000μm for special applications. The limitation of Si wafer thickness and generally planar fabrication principle (based on photolithography) , defines relatively small vertical dimensions of MEMS (up to few mm range) , while lateral dimensions are constraint mainly by wafer size.

5.4.1.3 Micromachining methods and process availability

The material applicability for construction of a specific device is not only defined by its integrability potential. Important limitations originate from the accessible fabrication processes that are highly dependent from considered material. For instance, silicon as the principal substrate used for microsystems fabrication has a wide range of developed micromachining processes. Various etching techniques exist, such as wet isotropic, wet anisotropic, deep vertical plasma etching (DRIE) and many others. Moreover, the equipment for silicon etching is easily accessible. However, the micromachining of other materials may be much more difficult. For instance, deep etching of glass can be only realized by wet techniques (HF/BHF) . In consequence, the creation of via structures presents a difficult task due to the limited mask selectivity and large under-etching accompanying wet processes.

5.4.2 Sensitive components, hermetic packaging

The electrostatic actuators used in the device are composed of fragile and precise micromechanical structures. The XY-stage contains 30μm-thick suspended platform, actuated by a set of four comb-

drives that are composed of dense array of $10\mu m$-wide combs, separated by tiny isolation gap (5 μm wide) . The second Z-axis parallel-plate actuator is fabricated within $15\mu m$ thick silicon platform. As the employed actuators are driven by electrostatic force, generated by applying of relatively high voltage (up to $\approx$ 100V), the system has to be protected from the environment (dust, moisture) . For this reason, protection of active components by hermetic packaging is crucial.

5.5 Components tolerance analysis

The optimal distances between optical elements are determined by the optical design. However, in the real structure, the distances are ensured by appropriate choice of wafers used for system construction. The thickness variation within wafer batch can vary from $\pm 5\mu m$ to $\pm 10\mu m$, depending on wafer type and the manufacture. Moreover, the substrates exhibit thickness variation (TTV$\approx 1-10\mu m$) that can also impact the deviation of positioning of system elements. As it was discussed in the chapter 2, the optical design was conceived to minimize the constraints for axial positioning of optical elements in the system. The collimated beams employed on the input and output of the system sets relatively large tolerances to the location of the scanning system in respect to neighborhood blocks. The scanning block designed as an afocal doublet has to be well arranged in respect to the afocal condition. Deviation from this position leads to axial displacement of the scanned volume in considered system, i.e. when axial magnification is close to 1, the separation error in the afocal doublet positioning causes the same error in axial position of the scanning zone. In the first demonstrator, two ball lenses are considered to be used in the scanning system. Their separation is defined as a sum of their focal lengths ($f_1 + f_2 = 734\mu m$) , which fixes necessary spacing (counted from centers of lenses) . The LTCC separator wafer has a thickness of $d_{ltcc} = (700 \pm 20)\mu m$. In the system based on ball lenses, the distance is not only defined by the spacer distance but also by the lens assembly method. Ball lenses are individually assembled into so-called assembly ports and subsequently bonded. Hence, additional positioning errors can arise. The diameter tolerance of ball lenses, specified by manufacturer, equals to $\Delta D = 3\mu m$. Diameter and following ROC inaccuracies provoke variation in focal length of the microlenses ($\Delta f = 2.2\mu m$).

However, positioning of ball lens has to be considered, the lens axial position can be very fragile on the small deviation of its diameter. The ball lens is assembled in the circular hole in the actuator stage, as shown schematically in figure 5.5a. Thus, the lens auto-align itself that its center lies directly above the center of the assembly port. The position of the lens center above the wafer level (h) substrate depends on the lens diameter and port size (figure 5.5a). Finally,the positioning error

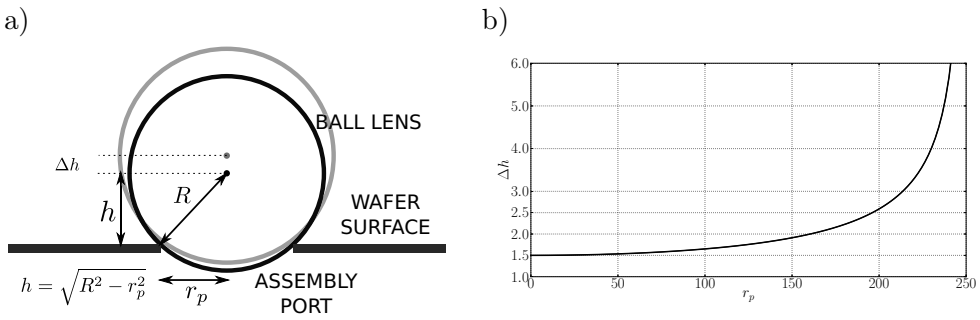


Figure 5.5: Assembly of ball lens in actuator platform - (a) positioning of the ball lens ($D = 2R = 500\mu m$) into a circular assembly port (of radius r_p), axial (in respect to wafer surface) position (h) of the lens center depends on lens radius and size of the port. (b) size dispersion's of microlenses cause error in axial positioning of the lens, the position error Δh strongly depends on assembly port size, plot of error assuming lens radius deviation as $1.5\mu m$, and port diameter error $1\mu m$.

(Δh) depends on: assembly port size, lens and assembly port diameter errors. Figure 5.5b presents dependence of assembly port size (its radius r_p) Finally, when the port size is defined as $r_p = 200\mu m$, the biggest contribution to the dispersion of separation distance originates from the LTCC wafer thickness inaccuracy. Since the total positioning in-accuracy is of the same order of magnitude as the axial scanning range of Z-scanner the optical performances the optical performance (optical resolution) would not be affected in an important degree. Finally, the main consequence of the positioning error of scanning lenses is an axial shift of scanned volume.

5.6 Integration methods

Wafer bonding of device components allow generation of whole device on the wafer level including wafer level hermetic packaging and interwafer electrical connections. In discussed system all wafer level bonding is achieved by anodic bonding technique. The special type of LTCC used as a separator wafer. This material, from the one hand allows to incorporate vertical VIAs within substrate fabrication, and from the other hand allows to use anodic bonding as a integration technique for creation of mechanical connection with silicon. Another bonding method employed consist a laser induced thermal bonding of discrete optical components employed within the system.

5.6.1 Ball lens bonding

As was discussed before ball lenses employed as the scanning lenses are assembled within circular ports made in actuators platforms. Bonding between glass (ball lens) and silicon (actuators) is achieved by laser induced thermal bonding. The bonding process relies on heating the platform by high power IR radiation (the used laser station consist 3Watt laser diode working at $\lambda = 608nm$). Since absorption of silicon is much larger than in glass, the laser radiation is mostly part absorbed by the silicon platform that leads to its efficient heating while lens is heated mostly in the contact points with silicon. The 30 seconds of exposure with power of 1.3W allows to generate permanent bond between lens and silicon platform. Figure 5.6 presents the scheme of the bonding process and SEM image of bonded structure.

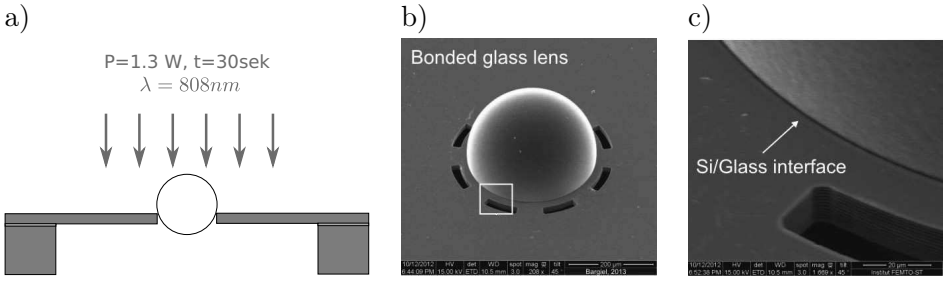


Figure 5.6: Ball lens assembly and laser bonding - (a) Ball lens placed in assembly port etched in the platform that is heated by high power infrared laser, (b) example of bonded ball lens and (c) zoom on the interface lens / silicon platform.

5.6.2 Electrical connections

The active elements of the system, i.e., electrostatic actuators are enclosed inside the wafer stack. The electrical connections through the wafers have to be provided to assure the control of two actuators. In order to simplify further integration with other components of confocal microscope on-chip, including external electronics board, all electrical inputs to the microscanner are made on its front side (Top Lid side). In consequence, the vertical electrical "wiring" through the stack up to 3-wafers have to be provided. The number of connections, required for driving of each of two microactuators is different. The XY comb-drive stage requires 4 driving lines (two lines for each direction), and the out-of plane scanner needs one driving line. In addition, both actuators share common ground that also needs to be connected to the driving electronics. The minimization of

the number of vertical interconnections is an important parameter in the system architecture choice due to high impact on technology involved as well as on overall costs of the device. From this perspective, it is preferable to place the comb-drive actuator close to the top of the structure.

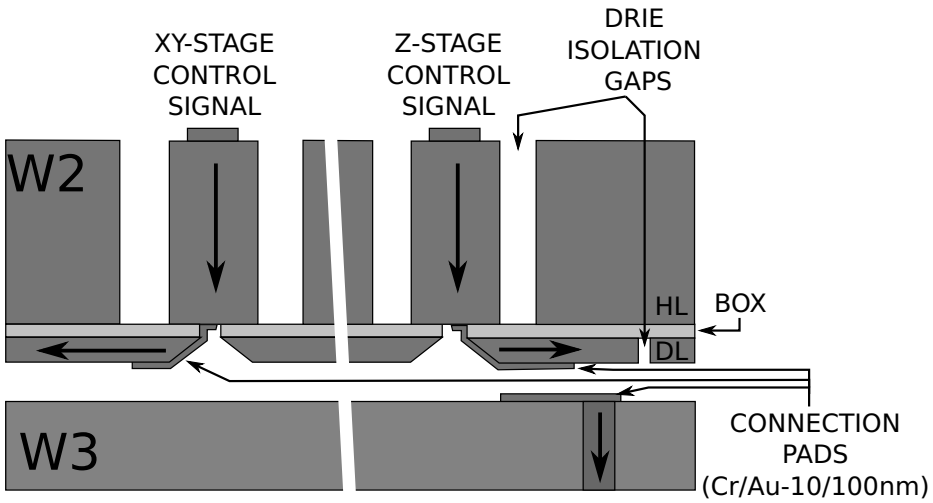


Figure 5.7: Electrical connections in the stacked system using through wafer vias technology - silicon columns, isolated by air gap, guide electrical signal through handle layer of W2. Access ports in device layer of SOI connects the TSVs with device layer that conduct the signal to comb-drives of XY-actuator. The signal driving Z-stage is guided also through LTCC wafer (W3) by embedded Au-filled VIA connection. Connection between wafers is achieved by compresivelly bonded gold pads, deposited on both wafers.

The construction of vertical through wafer vias, employed in the 3-D microscanner, is schematically shown in figure 5.7. Vertical electrical lines through wafers are made within each wafer fabrication workflow. Signal lines through silicon wafer (W2 in the figure 5.3) are accomplished by use of silicon columns, surrounded by air gap. Low resistivity silicon wafers are used for this purpose (ρ=0.01Ohm cm). The silicon columns, further called through silicon vias (TSVs), are generated by DRIE of narrow trenches ($30\mu m$ or $100\mu m$) into the $400\mu m$-thick handle layer of SOI wafer. TSVs are mechanically connected to the device layer of the SOI through insulating layer of buried silicon dioxide (BOX). The use of conductive properties of silicon for making vertical interconnects simplify the fabrication flow chart since no additional filling process (with conductive material) of TSVs is needed. Connection of columns with driving elements (comb-drives) of XY-actuator on the device layer is made by combination of wet etching (creation of access ports in device layer to the TSVs and etching the BOX) and metal layer deposition (PVD). On the level of device layer, the

electrical signals are guided by metal lines and by bulk silicon (e.g. spring suspensions) whereas different paths are isolated from each other by DRIE insulation air gaps.

The separation wafer (W3) is made of special type of LTCC [230], which allows incorporation of vertical metal paths into the substrate during substrate generation. The LTCC employed in the fabrication of 3-D microscanner contains circular vias with diameter of $100\mu m$, filled with gold. Electrical connections between stacked wafers are achieved during the system integration process. Anodic bonding used to create mechanical connection between blocks of the systems is used to form the (thermo)compressive bond between metal (Au) pads, creating electrical connections between wafers W2/W3 and W3/W4. Thin layer of gold (100nm deposited on 10nm adhesive layer of chromium) used for formation of connection pads does not affect the bonding quality. Moreover, Au-Au contact is made by high force and elevated temperature that accompanies anodic bonding process. Since gold is relatively soft, its allows generation of the high quality electrical connection between conductive VIA's of the stacked wafers. Preliminary tests, carried out at Fraunhofer/ENAS have shown that a temperature of at least 300°C is necessary to form a low ohmic contact (3.5-4.8Ωm for contact area $100 \times 100mm^2$ [231].

5.6.3 Multi wafer anodic-bonding

Considering that the anodic bonding can only be realized either between Si and glass or between Si and LTCC, the bonding sequence has been chosen in such a way that Si and glass or LTCC are used alternatively. In the first steps of the bonding sequence, two SOI wafers for electrostatic X-Y-axis and Z-axis microactuators are fabricated using silicon direct bonding process. This bonding process consists of three main steps, i.e. 1)surface pre-treatment with RCA1, RCA2 and again RCA1 followed by low pressure oxygen plasma, 2) a vacuum bonding process at low pressure ($<10^{-4}$mbar) using a standard bonding equipment, and 3) an annealing step at during 6h in nitrogen in a horizontal furnace. SOI wafer used for construction of XY stage is a standard substrates are used (purchased as complete SOI stack from Ultrasil, USA), the construction of Z-scanner is coupled with the fabrication of customized SOI structure, carried out at Fraunhofer/ENAS [231].

After the fabrication of the five building blocks (i.e. two wafers of top and bottom glass lids, one LTCC spacer wafer and two wafers of electrostatic microactuators), they are connected according to the sequence depicted in figure 5.8 [232]. First, the Z scanner is bonded anodically to LTCC spacer. The integration of scanning microlens ML2 into the Z scanner, based on laser-assisted bonding method, is performed before the anodic bonding step. During this bonding step, the electrical contacts are formed between Cr/Au pads by thermo-compression accompanying the wafer bonding

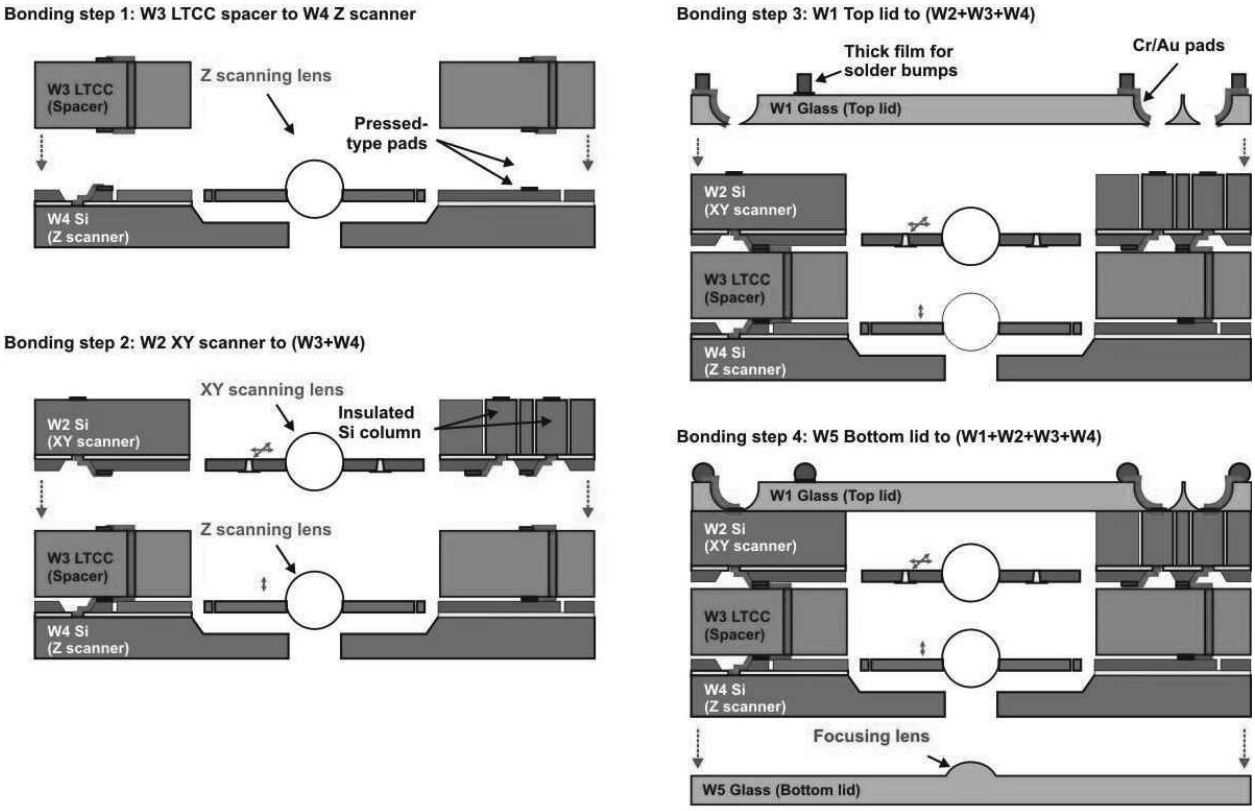


Figure 5.8: Bonding sequence of 5-wafer stack - Stack integration order starts with bonding Z-scanner with LTCC spacer (step 1), following by joining LTCC with XY-scanner (step 2) two last steps consit in bonding glass lids: firstly top lid (step 3), and bottom lid with focusing lens (step 4) [232].

process. In the step 2, the first stack must be bonded to the X-Y scanner with already assembled and bonded scanning microlens ML1. In this case, the interface consists of LTCC and device layer of SOI wafer. Similarly, the electrical contact is formed by thermo-compression of Cr/Au pads, deposited on separator wafer and the device layer of X-Y scanner. Step 3 starts the process of encapsulation of the microsystem by bonding the top glass lid. The top glass lid wafer contains isotropically etched holes for contacting the underlying layers. Thus, after a successful anodic bonding, the sputtering of 20/200nm Cr/Au layer is performed over the holes through a shadow mask. In the last step, a hermetic sealing is performed by anodic bonding of the bottom glass lid to the bottom side of the Z scanner.

5.7 Conclusions and perspectives

In this chapter, we have presented the concept of hybrid scanning confocal microscope, which combines fully integrated MEMS 3-D microscanner with external illumination/detection system, based on fiber-optics components. The design and realization concept of the millimeter-size MEMS 3-D microscanner has been also described. The 3-D microscanner employs several multi-wafer vertical integration technologies to bond and interconnects five deeply structurized wafers made of silicon, glass and LTCC ceramics. Presented approach allows space-effective integration of complex

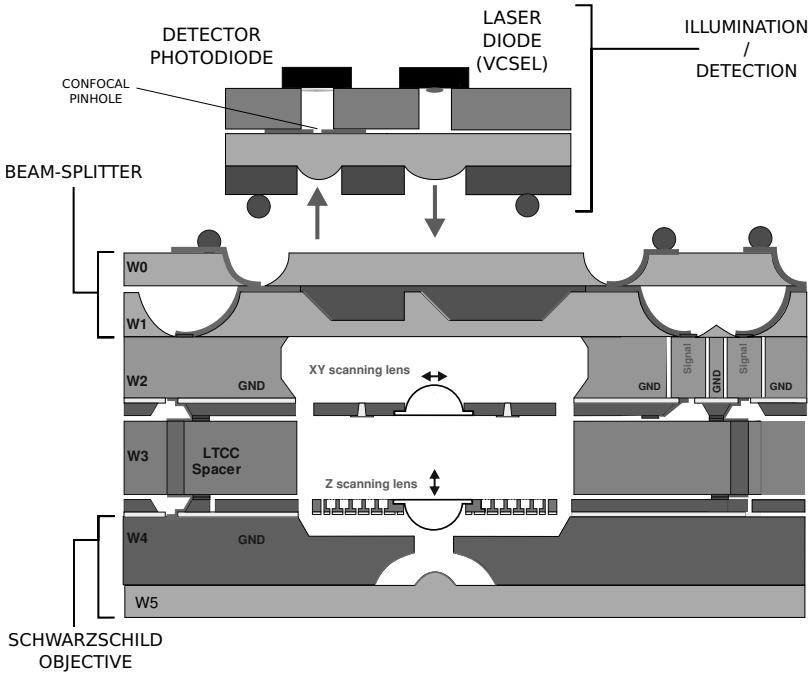


Figure 5.9: Scheme of advanced version of integrated scanner - Advanced version of the scanner including plano-convex batch fabricated scanning lenses, integrated beam splitter and Schwarzschild objective as focusing block and an additional block consisting illumination/detection block.

MOEMS devices, fabricated using various heterogeneous technologies. The first demonstrator of the MEMS 3-D microscanner is, in the moment of writing of this thesis, under fabrication in the frame of DWST-DIS project. The main goals here concern demonstration of successfully developed wafer-level integration technologies and to validate the opto-mechanical design of the microscanner. The future system would implement more optically optimal design (figure 5.9). Indeed, the use of plano-convex glass microlenses, fabricated within glass-silicon molding technique and integrated onto the actuators by wafer-level methods, could allow complete batch fabrication of the microscanner.

Replacing single lens in the focusing block by micro Schwarzschild objective allow increase the accessible resolutions and scanning zone of the system. Additional integration of beam-splitter, described previously in section 4.3 as well as collimation block would allow elimination of fiber-optics systems, creating complete confocal microscope on chip. In order to eliminate the bulk fiber elements, used in the first concept of microscope demonstrator, the illumination/detection block has also to be added. Since this block requires two opto-electronic components, i.e. light source (VCSEL) and photodetector (photodiode), complete integration with MOEMS scanner would be very complicated. One of the possible solutions would be to create this block as a separate sub-component, that can be fabricated within wafer level process, while assembly and bonding with the scanner could be performed on the chip level by means of e.g. flip-chip bonding.

Appendix A

SEM Profiles Analysis

The dicing is a common method of investigation of cross sections of generated microstructures. In particular, dicing coupled with SEM imaging allows relatively simple high resolution measurement of fabricated geometries. In case of optical structures like mirrors or lenses, line measurements (diameter, depth etc.) performed on acquired image are not sufficient. In particular, when qualitative geometry characterization is needed[1] a more precise geometry analysis is necessary. However, the precise profile analysis cannot be performed directly on the image. This appendix describes procedures used for extraction and analysis of profiles acquired by dicing and SEM imaging technique.

A.1 Profile extraction

The analysis is divided in two steps: profile extraction achieved with an image processing software (Fiji[2]) followed by the profile analysis done in Python[3].

The profile extraction algorithm presented in figure A.1 is composed from 4 steps: The first step is a pre-processing aiming at removing the noise from the image. To not affect the profile shape a median filter is used as it conserves the sharp edges present in the image. Then, the profile extraction is based on binarization of the image. For this purpose, a threshold value is set and the image is converted to a binary form. The choice of the threshold is the most important parameter of the procedure, and in most cases can be simply set as a mean value of image. However, when

[1] imho it is always needed

[2] Fiji is a clone of ImageJ [233], famous image processing open source software that is very popular in the area of scientific image processing. Especially, it is frequently used for microscope images analysis

[3] Python is general purpose programming language, however numerical packages (like NUMPY, SCIPY) make it a powerful open source numerical (data processing) environment (in some level Python equipped in numpy, scipy is very similar to better known commercial MATLAB environment)

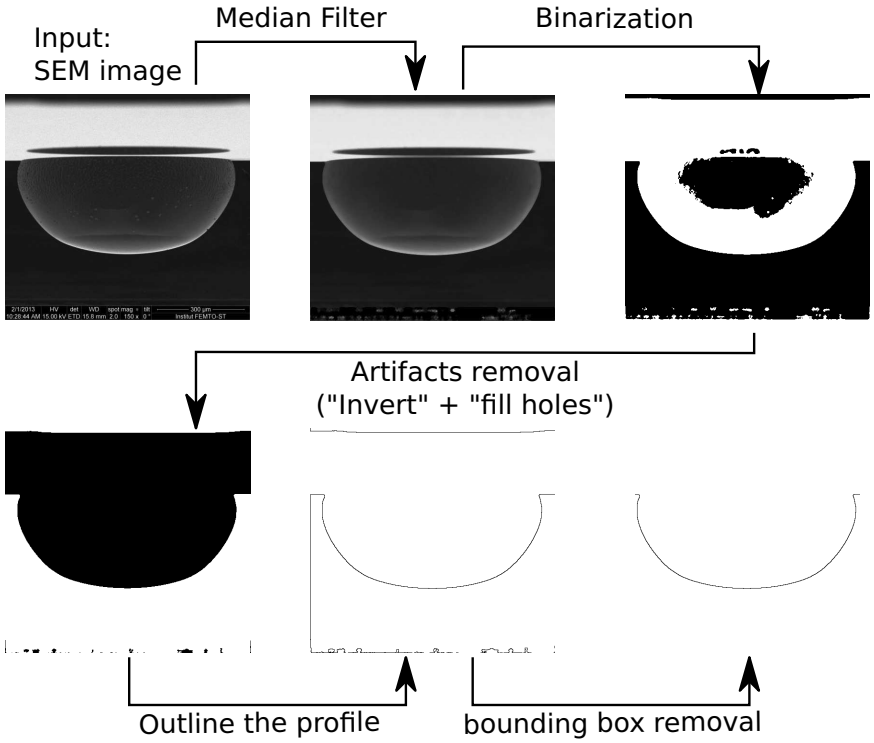


Figure A.1: Profile extraction algorithm - The input SEM image of diced structure is smoothed, transformed to binary image and cleaned from unwanted structures. Then, profile is outlined and cropped to the structure dimensions

images charcaterized by low contrast between observed sample and the background are analyzed, an alternative threshold value needs to be chosen. Binary image before outlining (profile extraction) is also processed to remove artifacts appearing in binarization process due to contrast variation in the image. The outline of the binary image produces a binary image with binary contour of the observed structure. The last step of the procedure consist in removing the frame generated by outlining algorithm (boundary effects) and saving the binary profile image as a coordinates set (a plain text file). The outcome of the described procedure is a text file with pixel coordinates of the structure profile. The text file can be read in any data analysis software. The implementation of presented procedure in Fiji macro language is presented in listing A.1. The profile coordinates are in pixel units, thus in order to transform profile to physical units, pixel resolution has to be known[1]. The profile extracted from image has the same quantization as the original image (figure A.2) It is then important to acquire high resolution images when profile analysis is considered to minimize

[1]when SEM images are registered in TIF format the resolution is written in image metadata and can be accessed directly from the image file

undesirable effects of discretization

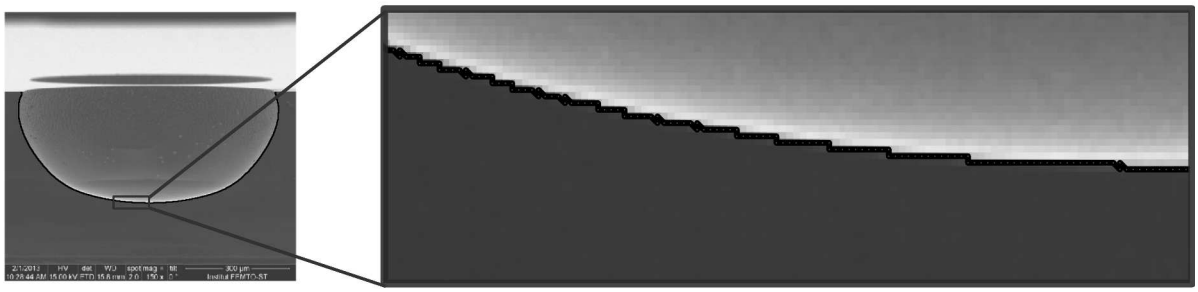


Figure A.2: Pixelized structure of extracted profile - Extracted profile superimposed with extracted profile on the left whole structure and magnified image on the left. visible step-like structure of the profile is due to the pixelization of the original image.

A.2 Profile analysis

The profile analysis is based on a standard curve fitting procedure, which requires the definition of the targeted geometry. In general, lenses or mirrors can take a form of a sphere, more generally of a conic section or an arbitrary aspheric [16]. The important assumption is that the lens is axis-symmetrical. This is an ideal case, however, not always fulfilled. In here, we analyze only the cross section and consequenly only the mirror symmetry can be verified, not the axial symmetry for which the 3D analysis is necessary. In the case of most common spherical lenses/mirrors, the geometry is described by equation A.1.

$$z(r) = R - \sqrt{R^2 - r^2} \tag{A.1}$$

where z is depth coordinate (sometimes called sag function), r is the radial coordinate and R is the radius of the sphere.

The more complex geometries are often described as conic sections that can be expressed as equation A.2.

$$z(r) = \frac{cr^2}{1 + \sqrt{1 - (k+1)\,c^2 r^2}} \tag{A.2}$$

where c is curvature at the vertex, curvature defined as an inverse of vertex radius of curvature $c = \frac{1}{R_{vert}}$, k is a conic constant that describe the geometry of the structure: for $k = 0$ is equivalent to a sphere, $k = -1$ is a parabola, $k < -1$ describes hyperbolas finally $k \in (0, -1)$ and $k > 0$ describes prolate and oblate ellipsoids respectively (figure A.3).

```
// ExtractProfile.ijm : profile extraction macro (for Imagej/Fiji)
// to be used with SEM images of diced molds/lenses
// program will fail to extract the profile if contrast sample/background is not high enough;
// the result is a profile writen to the text file (XY-coord in pixel coordiantes)
// author: maciej.baranski@femto-st.fr

// set fields in Result (Measure) table
run("Set Measurements...", "area min bounding fit shape display add redirect=None decimal=3");

// get data about image:
IJ.deleteRows(0, 100); // reset measure table
run("Measure")
w=getResult("Width", 0); h=getResult("Height", 0);
// Median Filter:
run("Median...", "radius=3");
// set Treshold for binarization:
setAutoThreshold("Mean dark");
//if automatic Tresholding does not produce good results adjust treshold manually:
//setThreshold(A,B); it can be done in GUI: Image->Adjust->Treshold...

// Binarization:
run("Make Binary", "thresholded remaining black");
// ARTFACTS REMOVAL
run("Fill Holes"); run("Invert"); run("Fill Holes");
// OUTLINE
run("Outline");
// ARTFACTS REMOVAL stage 2 (@ outline level)
run("Invert");
makeRectangle(0, 0, w, 2); run("Cut");
makeRectangle(w-2, 0, 2, h); run("Cut");
run("Fill Holes");
// Remove Frame (bounding box)
makeRectangle(w*0.05, h*0.1, w*0.9, h*0.8);
run("Make Inverse"); run("Cut");
// save the profile as XY coordiante set (.txt file)
run("Select All"); run("Invert");
run("Save XY Coordinates...", "background=255");
```

Listing A.1: ExtractProfile.ijm macro used for profile extraction from SEM images

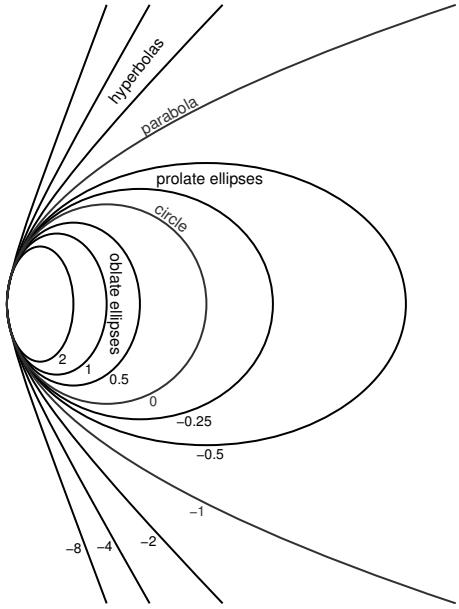


Figure A.3: Profiles of conic sections - Conic constant defines different shapes from different kinds of ellipses, circle, parabola and hyperbolas, numbers on the figure correspond conic constant of the specific curves, image retrieved from [234]

The description of optical surfaces as conic sections is usual in optics, since it provides simple translation of surface geometry parameters (conic constant, curvature) into optical properties (focal length, aberration performances). However, conic section is not general enough to describe all the possible geometries that are obtained. The most general form of description of any axially symmetrical geometry is a general polynomial: $z(r) = \sum_{i=0}^{N} \alpha_i r^i$. High order polynomial can describe arbitrary geometry, although the polynomials coefficients are difficult to interpret. For this reason, the usual way to deal with more complex geometries than conic sections, is to use the polynomials only as correction term to the conic equation:

$$z(r) = \frac{cr^2}{1 + \sqrt{1 - (k+1)\, c^2 r^2}} + \sum_{i=n_0}^{N} \alpha_i r^i \tag{A.3}$$

where α_i are the polynomials coefficients.

The fitting of profiles is performed on Cartesian coordinate system ($r \to x$). The parameters of the fit define not only the parameters of model shape (R, or k) but also the location of the structure vertex ($x0, z0$). Finally, in most considered cases, we limit our fitting model to 3 geometry models: parabolic, spherical and general conic. The fiting equations used for fiting in Cartesian system are

written as equations A.5-A.6:

$$z(x;a,b,c) = Ax^2 + Bx + C \tag{A.4}$$

$$z(x;R,x_0,z_0) = z_0 + R - \sqrt{R^2 - (x-x_0)^2} \tag{A.5}$$

$$z(x;c,k,x_0,z_0) = z0 + \frac{c(x-x_0)^2}{1+\sqrt{1-(k+1)\,c^2(x-x_0)^2}} \tag{A.6}$$

In general, vertex location (x_0,z_0) can be set as explicit parameters of the geometry model. However, in the case of a parabola, it is advantageous to fit the corresponding equation in classical polynomial form (eq. A.5) and calculate the vertex position from polynomial coefficients: $x0 = -\frac{B}{2A}$ and $z_0 = C - \frac{B^2}{4A}$. The polynomial form of the fitting function sets linear relation of model parameters and the z value. In consequence, linear methods of curve fitting can be used for finding the model parameters. In the case of equation of circle and conic, the linear form does not exist and nonlinear curve fitting algorithms have to be employed. The nonlinear fitting in general is more complicated than linear fitting, we will not discuss here the detail of the fitting algorithms, however it is important to be aware of the practical differences between linear and nonlinear fitting algorithms that are used. The linear fitting is based on the linear least squares minimization, which has always single, unique solution[1]. In the case of nonlinear fitting problem, the least squares solution in general can have more than one minimal solution. In this case, and to obtain physically meaningful solution of nonlinear problem special solving methods have to be used. In practice, the good solution can be easily found if the minimum search is performed close to the optimal result. To achieve this, an initial set of model parameters (so-called initial guess) has to be chosen and nonlinear fitting is performed in the vicinity of the starting point. In the case of considered spherical-like structures, the fitting procedure is as follow: first fitting of a parabola is performed (linear least squares can be applied here and unique solution is ensured), in the second step, the parabola coefficients are used to calculate the parameters of adequate circle or adequate conic, then nonlinear fitting of circle or conic section with initial guess obtained from parabolic fit is performed. The relations between parabola coefficients and adequate circle and general conic parameters are summarized in equations

[1] curve fitting can be seen as error minimization problem, the minimized function is an error function defined by the difference of data and fitting model as a function of the model parameters (p), the error function: $S(p) = \sum_i^{data\ points}(z_i - f(x_i;p))^2$ - it is visible that $S(p)$ has unique minimum for model parameters only if $f(x;p)$ is linear in p.

```
def fit_parabolaLin(x,z):
  """ linear least square parabolic fit
  z = c+bx+ax**2 """
  import numpy as np
  # matrix of base vectors:
  A= np.zeros((z.shape[0],3))
  A[:,0] = np.ones_like(x)
  A[:,1] = x
  A[:,2] = x**2
  # SOLVE matrix eq (A*cfs=z)
  # for the cfs of the polynomial by *LINEAR* least squares:
  cfs, res, rank, sing = np.linalg.lstsq(A,z)
  # evaluate fitted parabola (A*cfs):
  zfit=A.dot(cfs)
  return cfs,zfit,zfit-z
```

Listing A.2: Python function for linear fitting of a parabola to the profile data, the function input x,z are the profile coordinates obtained by profile extraction from SEM image or any other profilometry method.

A.7-A.11

$$R = \frac{1}{2A} \tag{A.7}$$

$$x_0 = -\frac{B}{2A} \tag{A.8}$$

$$z_0 = C - \frac{B^2}{4A} \tag{A.9}$$

$$c = 2A \tag{A.10}$$

$$k = -1 \tag{A.11}$$

The Python implementation of fitting procedures are presented on listings A.2, A.3, A.4. The used engine for parabolic fit linear least squares is a part of numpy.linalg package, nonlinear fit was performed within scipy.optimize package [235].

A.3 Example

The demonstration of fitting procedure was performed on a sample SEM image (figure A.4) of diced silicon structure (microlens mold). The profile extraction was performed according to the procedure described in the first section of this appendix. Three fittings are performed: first fitting a parabola,

```
def fit_circle(x,z):
    """ nonlinear least square CIRCLE (2D sphere) fit
    z = z0 + R-sqrt(R**2-(x-x0)**2) """
    import numpy as np
    from scipy.optimize import curve_fit
    def f(x,r,x0,z0):
        """fitting function definition"""
        z=z0+r-np.sqrt(r**2-(x-x0)**2)
        z[np.isnan(z)]=1e6
        return z
    # Linear parabola "pre-fit" (for init guess for nonlin fit):
    cfs,zf,err=fit_parabolaLin(x,z)
    # re-calculate fited parabola coefs to
    # get circle params (R,x0,z0):
    R  = 0.5/cfs[2]
    x0 = -cfs[1]/(2*cfs[2])
    z0 = cfs[0]-cfs[2]*x0**2
    print x0,z0,R
    # fit:
    cfs,cv =curve_fit(f,x,z,p0=(R,x0,z0))
    # evaluate fitted circle:
    zfit=f(x,cfs[0],cfs[1],cfs[2])
    return cfs,zfit,zfit-z
```

Listing A.3: Python function performing fitting of a circle to the profile data.

```
def fit_conic(x,z):
    """ nonlinear least square  CONIC fit
    z=z0+c*(x-x0)**2/(1+sqrt(1-(k+1)*c**2*(x-x0)**2 )) """
    import numpy as np
    from scipy.optimize import curve_fit
    def f(x,c,k,x0,z0):
        """fitting function definition"""
        z=z0+c*(x-x0)**2/(1+sqrt(1-(k+1)*c**2*(x-x0)**2 ))
        z[np.isnan(z)]=1e6 # kill nans if appeared
        return z
    # Linear parabola "pre-fit" (for init guess for nonlin fit):
    cfs,zf,err=fit_parabolaLin(x,z)
    # re-calculate fited parabola coefs to
    # get conic params (c(=1/R),x0,z0):
    R  = 0.5/cfs[2]
    x0 = -cfs[1]/(2*cfs[2])
    z0 = cfs[0]-cfs[2]*x0**2
    # fit:
    cfs,cv =curve_fit(f,x,z,p0=(1/R,-1,x0,z0))
    # evaluate fitted tilted conic:
    zfit=f(x,cfs[0],cfs[1],cfs[2],cfs[3])
    return cfs,zfit,zfit-z
```

Listing A.4: Python function performing fitting of a conic section to the profile data.

second a circle and third a general conic section. The three models more or less correctly fits the investigated profile. However, precise quantification of the obtained fits allows to extract optically meaningful data describing the structure.

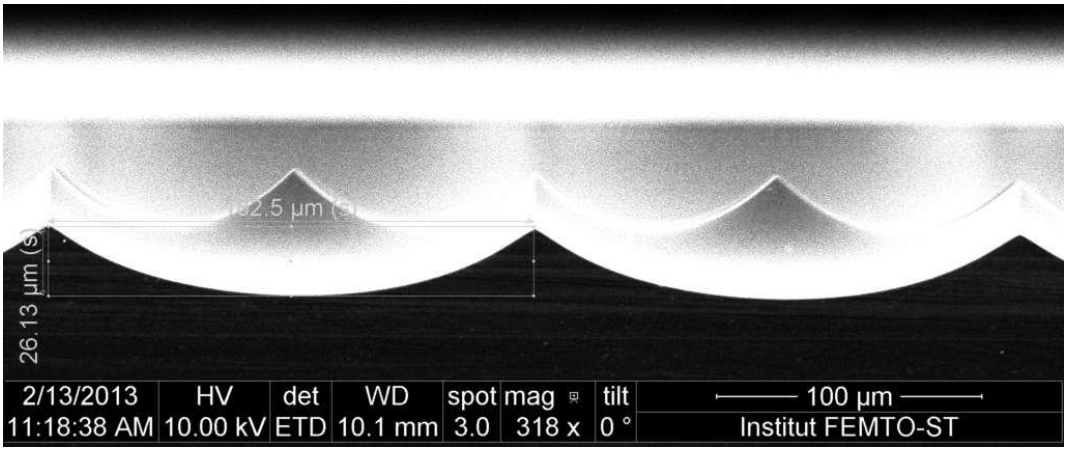


Figure A.4: SEM image used for demo - Sample SEM image of fabricated structure (Si wet etching) used for demonstrating profile analysis. In the image two structures are visible only the one on the left was considered in the example.

The most important results of performed fits are the geometry parameters obtained. In table A.1 the results of fitting to 3 considered geometries are summarized. Different geometry models lead to slightly different R (15% maximal difference), whereas the vertex positions are consistent for all 3 performed fits. The quality of fit are characterized as RMS error or PV error between fitted function and the data. It is visible that conic model describes best the geometry of investigated structure. In this case, the RMS fit error is in order of 1px that is the resolution of the used data. Figure A.5 illustrates the results of the fits by plotting the difference of fitted data and the fitted curves.

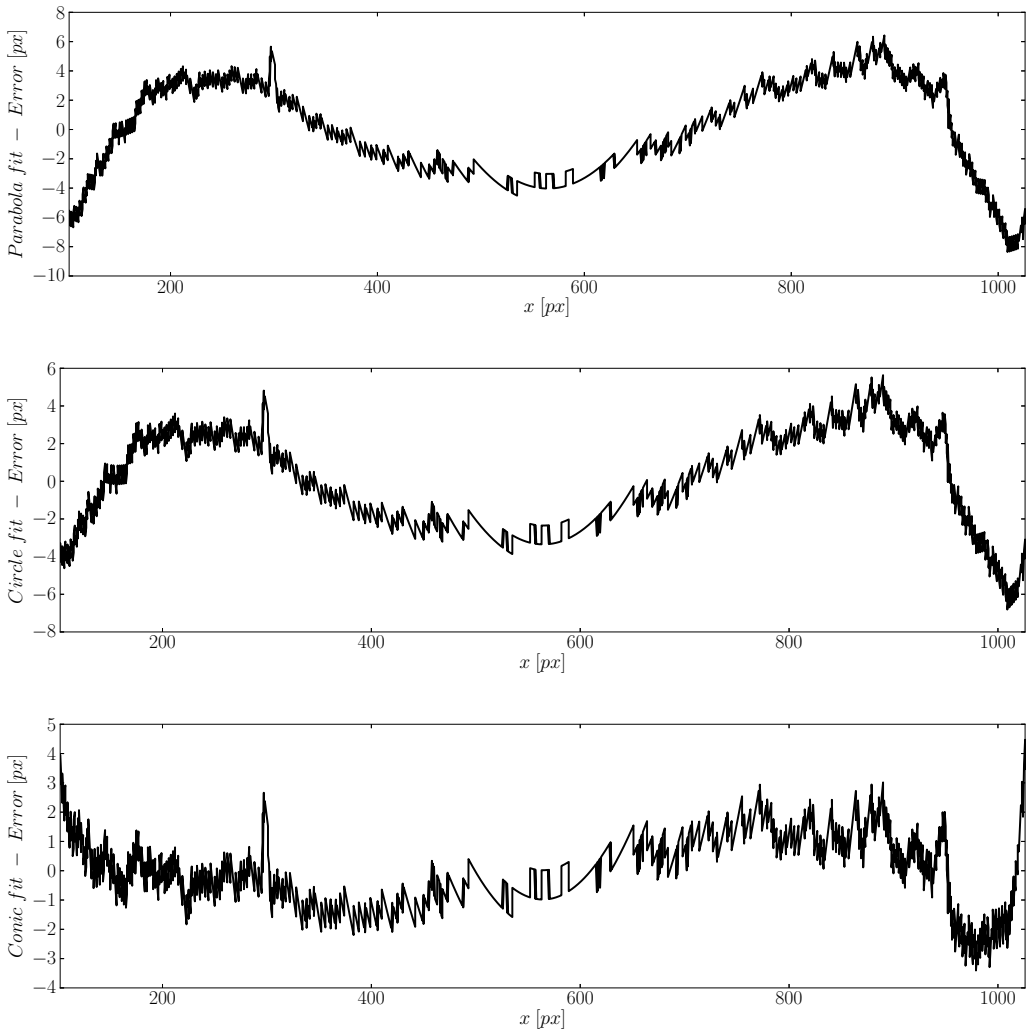


Figure A.5: Example fits difference: model - data - The parabola and circle fits yields to relatively similar shape of the difference profile, whereas the fitted conic describes much better the measurement data. Small residual deviation could be fitted employing aspheric equation, however the difference is in order of the resolution of profile data. For this reason using more complicated model is doubtful. The data that originate from pixelized image are clearly visible on the plots (especially in the center of the structure) however the precision of the data is sufficient to notice asphericity of the structure (positive conic constant).

	R [px]	k	x_0 [px]	z_0 [px]	RMS [px]	PV [px]
PARABOLA	860.3	(-1)	564.8	876.0	3.25	14.8
CIRCLE	912.1	(0)	564.7	876.7	2.60	12.4
CONIC	1071.9	2.9	564.3	879.1	1.26	7.9

Table A.1: Comparison of fitted parameters for 3 different model geometries - All parameters are in pixel units except k which is unit-less. Rescaling to physical units can be done by multiplying by pixel size (in this case $\Delta x = 0.192\mu m$). Values in parenthesis are not the fit parameters but are defined by geometry model.

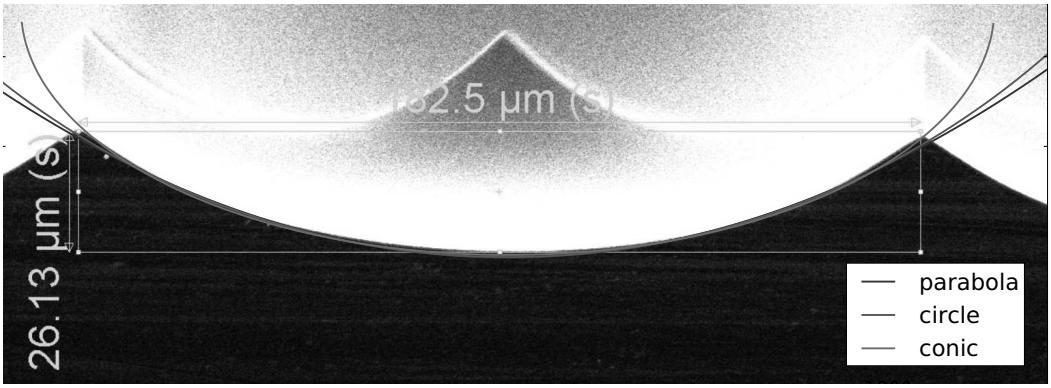


Figure A.6: Graphical comparison of fitted curves and raw SEM image - The original image superimposed with curves representing three fitted models: parabola (blue), circle (green) and conic (red).

General Conclusions and Perspectives

Biological imaging requires nowadays compact, low-cost and high resolution imaging tools to improve quality, modularity, portability and cost of medical instrumentation. Small metrology devices offering sub-cellular resolution are particularly needed for real time *in vivo* imaging. Among all the different methods, confocal microscopy is able to perform high resolution imaging and optical sectioning in both reflectance and fluorescence modes.

The goal of this PhD thesis is then to design and to develop the different building blocks of a miniaturized confocal microscope based on MOEMS technologies.

For this purpose, two challenging aspects have been mainly addressed. First, the miniature confocal microscope has been optically designed in the framework of specific technological constraints. The latter were the compatibility to wafer-level fabrication of planar components and to their vertical assembly, in order to ensure affordability and array-ability of the resulting microsystem. These conditions are crucial for reaching new and maybe unpredicted applications in the future. Secondly, several building blocks of the miniature confocal microscope were developed, according to design requirements. A strong effort has been made to increase the optical quality of micro-optical components.

The proposed optical design, reported in the **Chapter 2**, is based on beam-scanning achieved by microlens displacements. Specific constraints of planar wafer-level fabrication, such as limited accuracy of axial positioning, needs for microsystem encapsulation and minimization of system elements, were taken into account. As a result, the proposed architecture is composed of three blocks, namely a collimation block, a scanning block and a focusing block, rather independent from each other. Three different versions of this last architecture have been proposed, depending on the micro-optical components that are employed. The first configuration was targeted for the demonstration of proof-of-concept of the integrated micro-optical scanner proposed in the frame of the DWST-DIS

project. It is based on discrete optical components (ball lenses) to be assembled on micro-scanners by pick-and-place methodology. Moreover, since optical performances of the first version are limited, two more advanced versions have been also proposed. They are focused on the improvement of optical performance in terms of accessible resolution in the whole field of view. This optimization was obtained by use of aspherical plano-convex scanning lenses, whereas, even better performances have been predicted by adding an anastigmatic reflective objective as the focusing block. These two upgrades allow the reduction of off-axis aberrations and thus, improving resolution within the whole scanned volume.

Concerning the development of building blocks for on-chip microscopy (Contribution of **Chapter 4**), the technologies of fabrication of micro-lenses and micro-mirrors have been investigated. Three different types of silicon wet-etching were studied for the generation of spherical cavities, usable as concave micromirrors or microlens molds.

The first considered technique, based on a two-step silicon etching in aqueous solution of KOH, allows generation of relatively large structures ($> 200\mu m$) with low aspect ratio (sag/diameter$<$ 0.02) resulting in low NA microoptical components. It has been demonstrated that this fabrication method produces structures characterized by residual anisotropy which is correlated with the crystallography of the etched silicon substrate. This last effect is dependent of the aspect ratio of the etched structures, i.e. anisotropic effects become smaller for structures of lower aspect ratio. If this non-perfect sphericity can be neglected when the structure is used as microlens mold, it is not anymore the case when the structure is used as a mirror because of the doubled wavefront deformation. This was highlighted during the first attempt to demonstrate a micromachined Schwarzschild objective based on two KOH-etched mirrors. Consequently, this technique should be restricted to low NA microlenses generation.

The second investigated technique relies on isotropic wet-etching in aqueous solution of HF/HNO_3 mixture. This technique allows generation of hemispherical structures, i.e. characterized by high NA. It has been noticed that it shows also anisotropic effects, although much smaller and mostly present on structures obtained by etching through small ($< 50\mu m$) mask apertures. We demonstrated to an extent that it can be interesting for generation of full fill-factor microlens arrays. At the other extreme of the possible size range (typical diameter: $500\mu m$), generation of large structures is limited by resistance of the mask material to the etching solution since they require relatively long etching time. Moreover, enlarging the window mask size leads to ellipsoidal profile of etched structures. Consequently, isotropic etching can produce structures of high NA with diameters in a

range of few hundreds micrometers. Future work on the optimization of the (chemical as well as mechanical) mask resistivity is required in order to increase the possible etching time and then the accessible structure sizes.

The third studied etching was dry etching in SF_6 plasma. The preliminary aim was to study the possibility of generation of larger structures. In addition, it has been shown that it can provide structures with aspherical geometries, unlike wet-etching which is restricted to spherical geometries at best. This has been achieved by adjusting the etching parameters to balance the physical and chemical parts of the etching mechanism, which are more vertical or lateral, respectively. Although surface roughness is not yet optimal, structures characterized by negative conic constant, that are very attractive from the optical point of view, have been produced. Therefore, future work concerning silicon processing for microlenses and micromolds generation should be focused on SF_6 process for generation of aspherical components with wider spectrum of diameters. Moreover, it would be in my opinion interesting to consider a hybrid approach, combining wet etching for generation of well-spherical pre-structures that are enlarged via ionic etching within SF_6 plasma.

As it was just mentioned, large spherical molds are also required for the Schwarzschild objective. The latter was proposed to be integrated as the focusing block because it allows a significant improvement of the optical performances of the confocal microscope thanks to its anastimagtic character. This component would increase the possible system NA (and its 3D resolution) and would allow much larger lateral scanning, since it does not generate off-axis aberrations. The design of such objective and a preliminary demonstrator (in the so-called Schwarzschild configuration) fabricated by Si-Glass processes have been done. However, it was found that quality of the two KOH-etched mirrors was not sufficient to demonstrate the aberration compensation and then the high optical performances of this component. Future work on the second demonstrator will be based on the generation of a large primary mirror. This fact is one of the motivations for study of SF_6 plasma etching.

In order to build the fully integrated confocal microscope, illumination and detection blocks are also necessary. In particular, for reflective confocal microscope, a beam splitting element is needed. In consequence, an integrated beam-splitter fabricated within wafer-level machining was developed. It consists of one semi-transparent (beam-splitting) and two out-coupling mirrors in order to ensure vertical architecture of the microscope. The construction is based on saw-dicing for 45° slanted walls generation in the glass substrate. One advantage is the possibility to perform the alignment at the wafer-level.

It can also be noticed that all these components require to be characterized. Thus, **Chapter 3** was dedicated to present employed characterization methods. In particular, a dedicated bench for quality assessment of these optical elements was developed. This system, based on the direct measurement of impulse response (IPSF), allows quality assessment by a simple analysis of the focal spot extension (lateral and axial). Depending on the operation mode, both transmissive objects (e.g. microlenses, Schwarzschild micro-objective, MEMS scanner) and reflective components (e.g. silicon molds, mirrors) can be characterized. Future developments of this system will be made to improve the analysis of 3D IPSF data in order to distinguish particular aberrations generated by the tested components.

Finally, **Chapter 5** shows the procedure of realization of the MEMS 3-D micro optical scanner. This first demonstrator is, at the moment of writing this manuscript, under fabrication in the frame of DWST-DIS project. The 3-D microscanner employs several multi-wafer vertical integration technologies to bond and interconnect five structurized wafers made of silicon, glass and LTCC ceramics. Presented approach allows space-effective integration of complex MOEMS devices that are fabricated using various heterogeneous technologies. The main goals of this first system concern the demonstration of wafer-level integration technologies and the validation of the opto-mechanical design of the microscanner. The upgrade of this microscanner into a first hybrid confocal microscope will be achieved by the addition of an illumination/detection system based on fiber-optics components.

Once this demonstration achieved, the next step will concern the realization of the fully integrated miniature confocal microscope. It will incorporate the collectively integrated microlenses onto the scanners, the integrated beam-splitter and the reflective objective (Schwarzschild anastigmat). Indeed, wafer-level integration of scanning optics is necessary in order to achieve fully batch-fabricated system. This integration can be made by alternative methods: Either based on the generation of microlens directly in the SOI wafer used for fabrication of actuators. Or by a lens transfer, i.e., generation of lenses on one substrate followed by their transfer and bonding to a substrate with pre-fabricated actuators. Both approaches will be investigated in a near future.

As it was already mentioned, such optical architecture for confocal microscopy is very demanding in terms of optical components quality and numerical aperture when fine optical sectioning is considered. Moreover, it has been shown that high optical quality microlenses are easier to produce

when they remain relatively small. Nevertheless, demands for system encapsulation, long working distance and large field of view avoid a strong miniaturization of the optical elements.

Consequently, as a further perspective of this work, we could imagine benefit from these conclusions and employ arrays of small microlenses. These arrays, arranged specifically, could mimic larger scale systems. This idea is displayed on the figure A.7a.

Another perspective that could be an interesting option for the future architecture of miniature confocal system is the theta configuration. By using two separated channels for illumination and detection that have tilted optical axes (figure A.7b), it should be possible to increase the axial resolution without the need of high NA. Such configuration would lead to an increased working distance.

Finally, it has to be noticed that these last two perspectives are compatible with the requirements of vertically integrated optical architectures. Moreover, several concepts, approach of microoptical design as well as the developed building blocks are today contributions to new projects of the MOEMS group at FEMTO-ST Institute (e.g. European collaborative project VIAMOS of FP7).

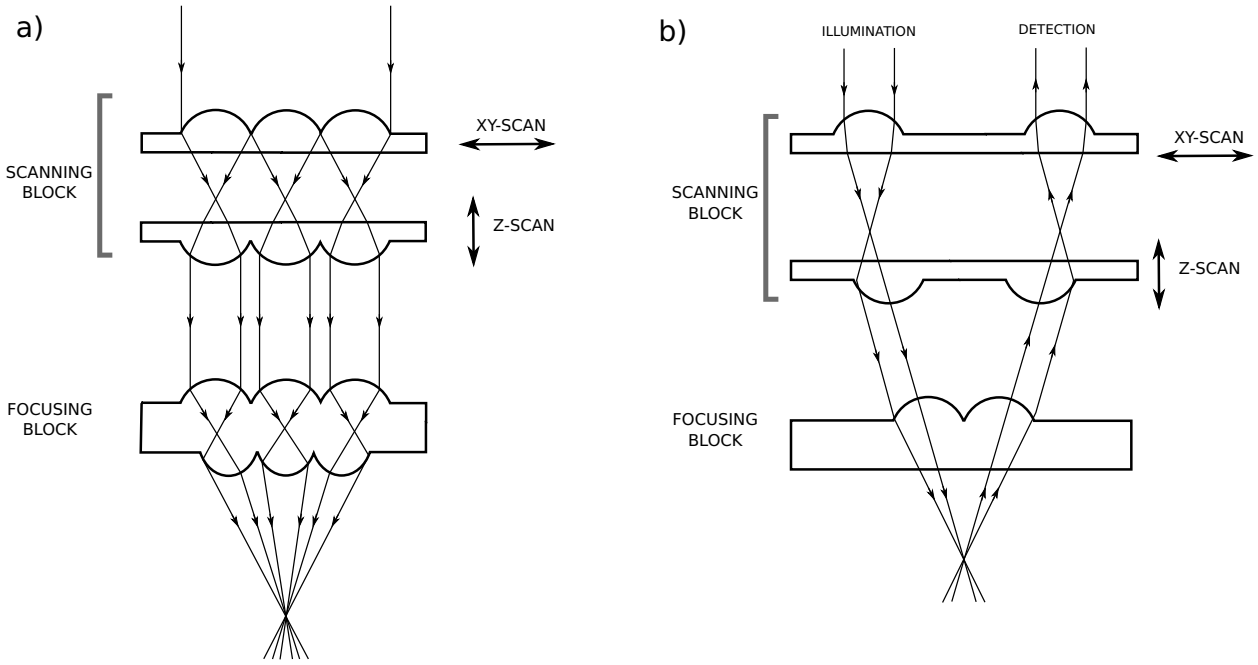


Figure A.7: Alternative ideas of optical configurations for μconfocal - (a) micro-lens array used in focusing and scanning block, (b) theta configuration implemented with transmissive scanning block.

Bibliography

[1] M. Minsky, "Microscopy apparatus," US Patent 3013467 (1961). 5

[2] S. Baer, "Optical apparatus providing focal-plane-specific illumination," US Patent 3547512 (1970). 5

[3] T. Wilson, Confocal Microscopy (Acad. Press, 1990). 5, 7, 9, 17

[4] R. H. Webb, "Confocal optical microscopy," Reports on Progress in Physics **59**, 427–471 (1996). 5, 20

[5] J. Goodman, Introduction To Fourier Optics, McGraw-Hill physical and quantum electronics series (Roberts & Company Publishers, 2005). 7, 16, 20, 22, 73

[6] M. Born, E. Wolf, and A. Bhatia, Principles of Optics: Electromagnetic Theory of Propagation, Interference and Diffraction of Light (Cambridge University Press, 1999). 8, 16, 19, 67, 85, 92, 146, 163

[7] A. A. Tanbakuchi, A. R. Rouse, J. A. Udovich, K. D. Hatch, and A. F. Gmitro, "Clinical confocal microlaparoscope for real-time in vivo optical biopsies." Journal of biomedical optics **14**, 044030 (2009). 11, 39, 46

[8] C.-h. Lee and J. Wang, "Noninterferometric differential confocal microscopy with 2-nm depth resolution," Optics Communications **135**, 233–237 (1997). 12

[9] W. Zhao, J. Tan, and L. Qiu, "Bipolar absolute differential confocal approach to higher spatial resolution," Optics Express **12** (2004). 12

[10] J. Liu, J. Tan, H. Bin, and Y. Wang, "Improved differential confocal microscopy with ultrahigh signal-to-noise ratio and reflectance disturbance resistibility." Applied optics **48**, 6195–6201 (2009). 12

[11] J. Rayleigh, "On the theory of optical images, with special reference to the microscope." Lord Rayleigh Scientific papers **5**, 118–125 (1902). 13

[12] C. M. Sparrow, "Spectroscopic resolving power," Astrophysical Journal **44**, 76–86 (1916). 13

[13] E. H. K. Stelzer, "Contrast, resolution, pixelation, dynamic range and signal-to-noise ratio: fundamental limits to resolution in fluorescence light microscopy," Journal of Microscopy **189**, 15–24 (1998). 14, 15

[14] P. Duffieux, The Fourier transform and its applications to optics: second edition, A Wiley-Interscience publication (John Wiley & Sons Australia, Limited, 1983). 16

[15] E. Abbe, On the Estimation of Aperture in the Microscope, vol. 1 (Royal Microscopical Society., 1881). 16

[16] W. Smith, Modern Optical Engineering, 4th Ed., McGraw Hill professional (Mcgraw-hill, 2007). 19, 144, 146, 193

[17] J. T. C. Liu, M. J. Mandella, N. O. Loewke, H. Haeberle, H. Ra, W. Piyawattanametha, O. Solgaard, G. S. Kino, and C. H. Contag, "Micromirror-scanned dual-axis confocal microscope utilizing a gradient-index relay lens for image guidance during brain surgery." Journal of biomedical optics **15**, 026029 (2010). 20, 29

[18] R. Barakat, "Application of Apodization to Increase Two-Point Resolution by the Sparrow Criterion. I. Coherent Illumination," Journal of the Optical Society of America **52**, 276–283 (1962). 21

[19] M. Martínez-Corral, M. Kowalczyk, C. J. Zapata-Rodríguez, and P. Andrés, "Tunable Optical Sectioning in Confocal Microscopy by use of Symmetrical Defocusing and Apodization." Applied optics **37**, 6914–21 (1998). 21

[20] M. Kowalczyk, C. J. Zapata-Rodríguez, and M. Martínez-Corral, "Asymmetric apodization in confocal scanning systems." Applied optics **37**, 8206–14 (1998). 21

[21] B. Davis, W. Karl, A. Swan, M. Unlu, and B. Goldberg, "Capabilities and limitations of pupil-plane filters for superresolution and image enhancement." Optics express **12**, 4150–6 (2004). 21

[22] M. Martinez-Corral, P. Andres, C. Zapata-Rodriguez, and C. J. Sheppard, "Improvement of three-dimentional resolution in confocal scanning microscopy by combination of two pupil filters," Optik **107**, 145–148 (1998). 22

[23] E. H. K. Stelzer and S. Lindek, "Fundamental reduction of the observation volume in far-field light microscopy by detection orthogonal to the illumination axis: confocal theta microscopy," Optics Communications **111**, 536–547 (1994). 23

[24] T. D. Wang, M. J. Mandella, C. H. Contag, and G. S. Kino, "Dual-axis confocal microscope for high-resolution in vivo imaging." Optics letters **28**, 414–6 (2003). 23, 24

[25] P. J. Dwyer, C. A. DiMarzio, and M. Rajadhyaksha, "Confocal theta line-scanning microscope for imaging human tissues." Applied optics **46**, 1843–1851 (2007). 24

[26] L. Wong and M. Mandella, "Mie scattering model for dual-axes confocal architecture," in "Proc. SPIE 6443, Three-Dimensional and Multidimensional Microscopy: Image Acquisition and Processing XIV," (2007), M. 24

[27] R. H. Webb and F. Rogomentich, "Confocal Microscope with Large Field and Working Distance," Applied optics **38**, 4870 (1999). 24

[28] S. Lindek, T. Stefany, and E. H. K. Stelzer, "Single-lens theta microscopy - a new implementation of confocal theta microscopy," Journal of Microscopy **188**, 280–284 (1997). 24

[29] T. D. Wang, C. H. Contag, M. J. Mandella, N. Y. Chan, and G. S. Kino, "Confocal fluorescence microscope with dual-axis architecture and biaxial postobjective scanning." Journal of biomedical optics **9**, 735–42 (2004). 24

[30] W. Zhao, Q. Jiang, L. Qiu, and D. Liu, "Dual-axes differential confocal microscopy with high axial resolution and long working distance," Optics communications **284**, 15–19 (2011). 24

[31] S. Lindek, J. Swoger, and E. H. K. Stelzer, "Single-lens theta microscopy: resolution, efficiency and working distance," Journal of modern optics **46**, 843–858 (1999). 24

[32] M. J. Mandella, J. T. C. Liu, W. Piyawattanametha, H. Ra, P.-L. Hsiung, L. K. Wong, O. Solgaard, T. D. Wang, C. H. Contag, and G. S. Kino, "Compact optical design for dual-axes confocal endoscopic microscopes," Proceedings of SPIE **6443**, 64430E–64430E–9 (2007). 24

[33] C. J. Sheppard, W. Gong, and K. Si, "The divided aperture technique for microscopy through scattering media." Optics express **16**, 17031–8 (2008). 24

[34] W. Gong, K. Si, and C. J. Sheppard, "Optimization of axial resolution in a confocal microscope with D-shaped apertures." Applied optics **48**, 3998–4002 (2009). 24

[35] ScanLab AG, "Galvanometer scanners," "http://www.scanlab.de/en/-/products/dynAXIS" (2013). [Online; accessed 16-July-2013]. 26

[36] Fraunhofer Photonic Microsystems, IPMS, "Mems scanners," "http://www.ipms.fraunhofer.de/en/applications/mems-scanners.html" (2013). [Online; accessed 16-July-2013]. 26

[37] L. Beiser, Unified Optical Scanning Technology (Wiley, 2005). 25, 26

[38] J. Pawley, Handbook Of Biological Confocal Microscopy (Springer London, Limited, 2006). 25, 216

[39] H. Miyajima, K. Murakami, and M. Katashiro, "MEMS Optical Scanners for Microscopes," IEEE Journal of Selected Topics in Quantum Electronics **10**, 514–527 (2004). 25

[40] U. Breng and T. Gessner, "Electrostatic micromechanic actuators," Journal of Micromechanics and Microengineering **2**, 256–261 (1992). 25, 34

[41] C. Tsou, W. T. Lin, C. C. Fan, and B. C. S. Chou, "A novel self-aligned vertical electrostatic combdrives actuator for scanning micromirrors," Journal of Micromechanics and Microengineering **15**, 855–860 (2005). 25, 34

[42] L. Wu and H. Xie, "A large vertical displacement electrothermal bimorph microactuator with very small lateral shift," Sensors and Actuators A: Physical **145-146**, 371–379 (2008). 25, 56

[43] Z. Z. J. Glazowski, C. Wang, Reflectance Confocal Microscopy for Skin Diseases, chap. Experimantal Applications and Future Directions, in [91] (2012). 26

[44] Y. Shao and D. L. Dickensheets, "MOEMS 3-D scan mirror for single-point control of beam deflection and focus," Journal of Microlithography, Microfabrication, and Microsystems **4**, 041502 (2005). 26

[45] G. D. Reddy and P. Saggau, "Fast three-dimensional laser scanning scheme using acousto-optic deflectors." Journal of biomedical optics **10**, 064038 (2005). 27

[46] P. A. Kirkby, K. M. N. Srinivas Nadella, and R. A. Silver, "A compact Acousto-Optic Lens for 2D and 3D femtosecond based 2-photon microscopy." Optics express **18**, 13721–45 (2010). 27

[47] M. Petráň, M. Hadravský, M. D. Egger, and R. Galambos, "Tandem-Scanning Reflected-Light Microscope," Journal of the Optical Society of America **58**, 661 (1968). 27

[48] "Till photonics", "Solutions and components for fluorescence microscopy," "http://www.till-photonics.com/" (2013). [Online; accessed 16-July-2013]. 27

[49] Cambridge Technology, "Resonant scanners," "http://www.camtech.com/index.php?option=com_content&view=article&id=103&Itemid=100" (2013). [Online; accessed 16-July-2013]. 28

[50] Hamamatsu, "Electromagnetic mems micromirrors s12236/s12237/s12238 series," "http://www.hamamatsu-news.eu/issues/hamamatsu_news_01_2013/files/assets/basic-html/page6.html" (2013). [Online; accessed 16-July-2013]. 28

[51] Olympus, "Confocal microscope scanning systems," "http://www.olympusconfocal.com/theory/confocalscanningsystems.html" (2009). [Online; accessed 16-July-2013]. 28

[52] Wikipedia, "Lissajous curve — wikipedia, the free encyclopedia," "http://en.wikipedia.org/w/index.php?title=Lissajous_curve&oldid=559765732" (2013). [Online; accessed 16-July-2013]. 29

[53] U. Hofmann, J. Janes, and H.-J. Quenzer, "High-Q MEMS Resonators for Laser Beam Scanning Displays," Micromachines **3**, 509–528 (2012). 29, 32

[54] D. L. Dickensheets and G. S. Kino, "Micromachined scanning confocal optical microscope." Optics letters **21**, 764–6 (1996). 29, 43

[55] F. Helmchen, M. S. Fee, D. W. Tank, and W. Denk, "A miniature head-mounted two-photon microscope: High-resolution brain imaging in freely moving animals." Neuron **31**, 903–12 (2001). 29

[56] Y. Wang, S. Bish, J. W. Tunnell, and X. Zhang, "MEMS scanner based handheld fluorescence hyperspectral imaging system," Sensors and Actuators A: Physical **188**, 450–455 (2012). 29

[57] T. Tuma, J. Lygeros, V. Kartik, A. Sebastian, and A. Pantazi, "High-speed multiresolution scanning probe microscopy based on Lissajous scan trajectories." Nanotechnology **23**, 185501 (2012). 29

[58] H. C. Nathanson and R. a. Wickstrom, "a Resonant-Gate Silicon Surface Transistor With High-Q Band-Pass Properties," Applied Physics Letters **7**, 84 (1965). 29

[59] S. Beeby, MEMS Mechanical Sensors, Artech House MEMS Library (Artech House, 2004). 29

[60] K. Petersen, "Micromechanical light modulator array fabricated on silicon," Applied Physics Letter **31**, 521–523 (1977). 29

[61] K. Petersen, "Silicon Torsional Scanning Mirror," IBM Journal of Research and Development **24**, 631–637 (1980). 29

[62] E. Motamedi, MOEMS: Micro-opto-electro-mechanical Systems, Press Monographs (SPIE Press, 2005). 29

[63] C. Gorecki, F. Chollet, E. Bonnotte, and H. Kawakatsu, "Silicon-based integrated interferometer with phase modulation driven by surface acoustic waves." Optics letters **22**, 1784–6 (1997). 30

[64] H. L. Kung, S. R. Bhalotra, J. D. Mansell, D. A. B. Miller, and J. S. Harris, "Standing-Wave Transform Spectrometer Based on Integrated MEMS Mirror," IEEE Journal on selected topics in quantum electronics **8**, 98–105 (2002). 30

[65] J. Correia, M. Bartek, and R. Wolffenbuttel, "Bulk-micromachined tunable Fabry–Perot microinterferometer for the visible spectral range," Sensors and Actuators A: Physical **76**, 191–196 (1999). 30

[66] C. Madsen, J. Walker, J. Ford, K. Goossen, T. Nielsen, and G. Lenz, "A tunable dispersion compensating MEMS all-pass filter," IEEE Photonics Technology Letters **12**, 651–653 (2000). 30

[67] M. Tuohiniemi and M. Blomberg, "Surface-micromachined silicon air-gap Bragg reflector for thermal infrared," Journal of Micromechanics and Microengineering **21**, 075014 (2011). 30

[68] B. H. Weigl, R. L. Bardell, and C. R. Cabrera, "Lab-on-a-chip for drug development," Advanced Drug Delivery Reviews **55**, 349–377 (2003). 30

[69] Y.-C. Toh, C. Zhang, J. Zhang, Y. M. Khong, S. Chang, V. D. Samper, D. van Noort, D. W. Hutmacher, and H. Yu, "A novel 3D mammalian cell perfusion-culture system in microfluidic channels." Lab on a chip **7**, 302–9 (2007). 30

[70] B. Kuswandi, Nuriman, J. Huskens, and W. Verboom, "Optical sensing systems for microfluidic devices: a review." Analytica chimica acta **601**, 141–55 (2007). 30

[71] P. Nussbaum and R. Völkel, "Design, fabrication and testing of microlens arrays for sensors and microsystems," Pure and Applied ... **6**, 617–636 (1997). 30, 43

[72] E. Verpoorte and N. De Rooij, "Microfluidics meets MEMS," Proceedings of the IEEE **91**, 930–953 (2003). 30

[73] C. Yi, C.-W. Li, S. Ji, and M. Yang, "Microfluidics technology for manipulation and analysis of biological cells," Analytica Chimica Acta **560**, 1–23 (2006). 30, 36

[74] M. Gad-el Hak, MEMS: Design and Fabrication, Mechanical and Aerospace Engineering Series (Taylor & Francis, 2010). 31, 50

[75] R. Ghodssi and P. Lin, Mems Materials and Processes Handbook, MEMS reference shelf (Springer US, 2010). 31

[76] F. Chollet and H. Liu, "A (not so) short introduction to micro electro mechanical systems," `http://memscyclopedia.org/introMEMS.html` (2012). This is an electronic document published under Creative Commons Attribution-NonCommercial 3.0 License (`http://creativecommons.org/licenses/by-nc/3.0/legalcode`). 32

[77] T. Hsu and I. of Electrical Engineers, Mems Packaging, EMIS Processing Series (Institution of Engineering and Technology, 2004). 32

[78] J. Mireles, M. Garcia, and R. Ambrosio, "Packaging Investigation and Study for Optical Interfacing of Micro Components with Optical Fibers, part I," Revista Superficies y Vacío **20**, 21–33 (2008). 32, 65

[79] A. Tabbert, B. Goushcha, Springer Handbook of Lasers and Optics (Springer Berlin Heidelberg, 2012), chap. Optical Detectors. 33

[80] J. Art, Handbook Of Biological Confocal Microscopy, chap. Photon Detectors for Confocal Microscopy, in [38] (2006). 33

[81] H. Baltes, O. Brand, A. Hierlemann, D. Lange, and C. Hagleitner, "CMOS MEMS - present and future," in "Technical Digest. MEMS 2002 IEEE International Conference. Fifteenth IEEE International Conference on Micro Electro Mechanical Systems (Cat. No.02CH37266)," (Ieee, 2002), i, pp. 459–466. 34

[82] C.-M. Sun, C. Wang, M.-H. Tsai, H.-S. Hsieh, and W. Fang, "Monolithic integration of capacitive sensors using a double-side CMOS MEMS post process," Journal of Micromechanics and Microengineering **19**, 015023 (2009). 34

[83] K.-Y. Hung, F.-G. Tseng, and H.-S. Khoo, "Integrated three-dimensional optical MEMS for chip-based fluorescence detection," Journal of Micromechanics and Microengineering **19**, 045014 (2009). 34

[84] B. Reig, T. Camps, V. Bardinal, D. Bourrier, E. Daran, J. B. Doucet, J. Launay, and J. Y. Fourniols, "Fabrication of polymer-based optical microsystem arrays suited for the active focusing of vertical laser diodes," Journal of Micromechanics and Microengineering **22**, 065006 (2012). 34

[85] M. Allen, M. Scheidl, R. Smith, and A. Nikolich, "Movable micromachined silicon plates with integrated position sensing," SensorSensors and Actuators A: Physical **21** (1990). 34

[86] J. Judy and R. Muller, "Magnetically actuated, addressable microstructures," Journal of Microelectromechanical Systems **6**, 249–256 (1997). 34

[87] K. H. Kim, B. H. Park, G. N. Maguluri, T. W. Lee, F. J. Rogomentich, M. G. Bancu, B. E. Bouma, J. F. de Boer, and J. J. Bernstein, "Two-axis magnetically-driven MEMS scanning catheter for endoscopic high-speed optical coherence tomography." Optics express **15**, 18130–40 (2007). 34

[88] A. Jain, H. Qu, S. Todd, and H. Xie, "A thermal bimorph micromirror with large bi-directional and vertical actuation," Sensors and Actuators A: Physical **122**, 9–15 (2005). 34

[89] F. Filhol, E. Defaÿ, C. Divoux, C. Zinck, and M.-T. Delaye, "Resonant micro-mirror excited by a thin-film piezoelectric actuator for fast optical beam scanning," Sensors and Actuators A: Physical **123-124**, 483–489 (2005). 34

[90] K. H. Koh, T. Kobayashi, F.-L. Hsiao, and C. Lee, "A 2-D MEMS Scanning Mirror Using Piezoelectric PZT Beam Actuators," Procedia Chemistry **1**, 1303–1306 (2009). 34

[91] R. Hofmann-Wellenhof, G. Pellacani, J. Malvehy, and H. Soyer, Reflectance Confocal Microscopy for Skin Diseases (Springer, 2012). 35, 36, 212

[92] A. Agero, K. Busam, M. Rajadhyaksha, Y. Patel, A. Scope, Benvenuto-Andrade, C. Gill, A. Marghoob, S. González, and A. Halpern, "Reflectance confocal microscopy for imaging pigmented basal cell cancers in vivo," in "Biomedical Topical Meeting," (2006), pp. 5–7. 35

[93] A. a. Tanbakuchi, J. a. Udovich, A. R. Rouse, K. D. Hatch, and A. F. Gmitro, "In vivo imaging of ovarian tissue using a novel confocal microlaparoscope." American journal of obstetrics and gynecology **202**, 90.e1–9 (2010). 35

[94] C. Liu, C. Q. Li, X. L. Zuo, R. Ji, X. J. Xie, Y. S. Yang, and Y. Q. Li, "Confocal laser endomicroscopy for the diagnosis of colorectal cancer in vivo." Journal of digestive diseases **14**, 259–65 (2013). 35

[95] I. Jalbert, F. Stapleton, E. Papas, D. F. Sweeney, and M. Coroneo, "In vivo confocal microscopy of the human cornea." The British journal of ophthalmology **87**, 225–36 (2003). 35

[96] M. Tavakoli, P. Hossain, and R. a. Malik, "Clinical applications of corneal confocal microscopy." Clinical ophthalmology (Auckland, N.Z.) **2**, 435–45 (2008). 35

[97] "Optiscan Pty Ltd", ""Optiscan Five I"," "http://www.optiscan.com/Products/FIVE1.asp" (2013). [Online; accessed 16-July-2013]. 35, 39, 46

[98] Caliber I.D., "Imaging & diagnosis on a cellular level," "http://www.caliberid.com/about.html" (2012). [Online; accessed 16-July-2013]. 35, 46

[99] M. Rajadhyaksha, R. R. Anderson, and R. H. Webb, "Video-Rate Confocal Scanning Laser Microscope for Imaging Human Tissues In Vivo," Applied Optics **38**, 2105 (1999). 35

[100] S. Liu, S. Xu, X. Wu, and W. Liu, "Iterative method for in situ measurement of lens aberrations in lithographic tools using CTC-based quadratic aberration model." Optics express **20**, 14272–83 (2012). 35, 36

[101] K. S. Kim, S. Kim, S. Beack, J.-A. Yang, S. H. Yun, and S. K. Hahn, "In vivo real-time confocal microscopy for target-specific delivery of hyaluronic acid-quantum dot conjugates." Nanomedicine : nanotechnology, biology, and medicine **8**, 1070–3 (2012). 36

[102] R. Liu, Q. Huang, B. Li, C. Yin, and C. Jiang, "Extendable, miniaturized multi-modal optical imaging system: cortical hemodynamic observation in freely moving animals," Optics express **21**, 2521–2523 (2013). 36

[103] A. Ashkin, "Forces of a single-beam gradient laser trap on a dielectric sphere in the ray optics regime." Biophysical Journal **61**, 569–582 (1992). 36

[104] M. MacDonald, G. Spalding, and K. Dholakia, "Microfluidic sorting in an optical lattice," Nature **426**, 421–424 (2003). 36

[105] A. N. Rubinov, V. M. Katarkevich, and T. S. Éfendiev, "Gradient-Field Sorting of Microparticles," Journal of Applied Spectroscopy **70**, 753–757 (2003). 36

[106] D. G. Grier, "A revolution in optical manipulation." Nature **424**, 810–6 (2003). 37

[107] J. Enger, M. Goksör, K. Ramser, P. Hagberg, and D. Hanstorp, "Optical tweezers applied to a microfluidic system." Lab on a chip **4**, 196–200 (2004). 37

[108] A. F. Gmitro and D. Aziz, "Confocal microscopy through a fiber-optic imaging bundle." Optics letters **18**, 565 (1993). 38

[109] C. Liang, M. Descour, K. B. Sung, and R. Richards-Kortum, "Fiber confocal reflectance microscope (FCRM) for in-vivo imaging." Optics express **9**, 821–30 (2001). 38

[110] K. Grattan and B. Meggitt, Optical Fiber Sensor Technology: Fundamentals (Springer, 2000). 38

[111] M. Gu, C. J. Sheppard, and X. Gan, "Image formation in a fiber-optical confocal scanning microscope," JOSA A **8**, 1755–1761 (1991). 38, 39

[112] C. L. Arrasmith, D. L. Dickensheets, and A. Mahadevan-Jansen, "MEMS-based handheld confocal microscope for in-vivo skin imaging," Optics Express **18**, 3805 (2010). 40

[113] K. Kumar, K. Hoshino, and X. Zhang, "Handheld subcellular-resolution single-fiber confocal microscope using high-reflectivity two-axis vertical combdrive silicon microscanner." Biomedical microdevices **10**, 653–60 (2008). 41

[114] K. Kumar, K. Hoshino, and X. Zhang, "Handheld subcellular-resolution single-fiber confocal microscope using high-reflectivity two-axis vertical combdrive silicon microscanner." Biomedical microdevices **10**, 653–60 (2008). 41, 160

[115] H. Xie, "MEMS-based 3D optical microendoscopy." Annual International Conference of the IEEE Engineering in Medicine and Biology Society. IEEE Engineering in Medicine and Biology Society. Conference **2009**, 6703–5 (2009). 41, 42

[116] H. Ra, W. Piyawattanametha, M. J. Mandella, P.-L. Hsiung, J. Hardy, T. D. Wang, C. H. Contag, G. S. Kino, and O. Solgaard, "Three-dimensional in vivo imaging by a handheld dual-axes confocal microscope." Optics Express **16**, 7224–7232 (2008). 41, 42, 46

[117] W. Piyawattanametha, H. Ra, M. Mandella, K. Loewke, T. Wang, G. S. Kino, O. Solgaard, and C. Contag, "3-D near-infrared fluorescence imaging using an MEMS-based miniature dual-axis confocal microscope," IEEE Journal of selected topics in quantum electronics **15**, 1344 – 1350 (2009). 41

[118] R. Voelkel, K. J. Weible, and M. Eisner, "Wafer-Level Micro-Optics: Trends in Manufacturing, Testing and Packaging," in "SPIE," , vol. 8169, A. Duparré and R. Geyl, eds. (2011), vol. 8169, pp. 81690C–81690C–12. 43, 144

[119] D. Daly and R. Stevens, "The manufacture of microlenses by melting photoresist," Measurement Science and Technology **1**, 759–766 (1990). 43

[120] A. Schilling, R. Merz, C. Ossmann, and H. P. Herzig, "Surface profiles of reflow microlenses under the influence of surface tension and gravity," Optical Engineering **39**, 2171 (2000). 43

[121] V. Fakhfouri and N. Cantale, "Inkjet printing of SU-8 for polymer-based MEMS a case study for microlenses," in "IEEE 21st International Conference on Micro Electro Mechanical Systems, 2008. MEMS 2008.", (2008), pp. 407–410. 43

[122] V. Bardinal, T. Camps, B. Reig, D. Barat, E. Daran, and J. B. Doucet, "Collective Micro-Optics Technologies for VCSEL Photonic Integration," Advances in Optical Technologies **2011**, 1–11 (2011). 43

[123] J. Albero, L. Nieradko, C. Gorecki, H. Ottevaere, V. Gomez, H. Thienpont, J. Pietarinen, B. Päivänranta, and N. Passilly, "Fabrication of spherical microlenses by a combination of

isotropic wet etching of silicon and molding techniques." Optics express **17**, 6283–92 (2009). 43, 79, 113, 119, 140, 145

[124] K. P. Larsen, J. T. Ravnkilde, and O. Hansen, "Investigations of the isotropic etch of an ICP source for silicon microlens mold fabrication," Journal of Micromechanics and Microengineering **15**, 873–882 (2005). 43, 79, 134

[125] D. Dickensheets and G. S. Kino, "Miniature scanning confocal microscope," US Patent 5,742,419 (1998). 43, 46, 160, 177

[126] S. Kwon and L. P. Lee, "Stacked two dimensional micro-lens scanner for micro confocal imaging array," Technical Digest. MEMS 2002 IEEE International Conference. Fifteenth IEEE International Conference on Micro Electro Mechanical Systems (Cat. No.02CH37266) pp. 483–486 (2002). 44

[127] S. Kwon and L. P. Lee, "Micromachined transmissive scanning confocal microscope." Optics letters **29**, 706–8 (2004). 44, 46, 177

[128] K. C. Maitland, H. J. Shin, H. Ra, D. Lee, O. Solgaard, and R. Richards-Kortum, "Single fiber confocal microscope with a two-axis gimbaled MEMS scanner for cellular imaging." Optics express **14**, 8604–12 (2006). 46

[129] J. Knittel, L. Schnieder, and G. Buess, "Endoscope-compatible confocal microscope using a gradient index-lens system," Optics Communications **188**, 267–273 (2001). 46

[130] R. S. Pillai, D. Lorenser, and D. D. Sampson, "Deep-tissue access with confocal fluorescence microendoscopy through hypodermic needles." Optics express **19**, 7213–21 (2011). 46

[131] H. Mansoor, H. Zeng, K. Chen, Y. Yu, J. Zhao, and M. Chiao, "Vertical optical sectioning using a magnetically driven confocal microscanner aimed for in vivo clinical imaging." Optics express **19**, 25161–72 (2011). 46

[132] K. Laszczyk, S. Bargiel, C. Gorecki, J. Krężel, P. Dziuban, M. Kujawińska, D. Callet, and S. Frank, "A two directional electrostatic comb-drive X–Y micro-stage for MOEMS applications," Sensors and Actuators A: Physical **163**, 255–265 (2010). 51, 178

[133] S. Bargiel, C. Gorecki, T. Verdot, K. Laszczyk, J. Albero, and L. El Fissi, "Electrostatically driven optical Z-axis scanner with thermally bonded glass microlens," Procedia Engineering **5**, 762–765 (2010). 51, 178

[134] H.-C. Park, C. Song, and K.-H. Jeong, "Micromachined lens microstages for two-dimensional forward optical scanning." Optics express **18**, 16133–8 (2010). 50

[135] A. Lohmann, "Scaling laws for lens systems," Applied optics **28**, 4996–4998 (1989). 51

[136] A. Gerrard and J. Burch, Introduction to Matrix Methods in Optics, Dover Books on Physics (Dover, 1994). 59

[137] K. Schwertz and J. H. Burge, "Relating axial motion of optical elements to focal shift," in "SPIE Optical Engineering+ Applications. International Society for Optics and Photonics," (2010), pp. 779306–779306–14. 64

[138] S. Bargiel, C. Jia, M. Baranski, J. Frömel, N. Passilly, C. Gorecki, and M. Wiemer, "Vertical Integration Technologies for Optical Transmissive 3-D Microscanner based on Glass Microlenses," Procedia Engineering **47**, 1133–1136 (2012). 65

[139] M. Sasaki, F. Nakai, K. Hane, K. Yokomizo, and K. Hori, "Absolute micro-encoder using image obtained by ball lens assembled inside wafer," Journal of Optics A: Pure and Applied Optics **8**, S391–S397 (2006). 65

[140] C. T. Pan, "Silicon-based coupling platform for optical fiber switching in free space," Journal of Micromechanics and Microengineering **14**, 129–137 (2004). 65

[141] Y. J. Fan, Y. C. Wu, Y. Chen, Y. C. Kung, T. H. Wu, K. W. Huang, H. J. Sheen, and P. Y. Chiou, "Three dimensional microfluidics with embedded microball lenses for parallel and high throughput multicolor fluorescence detection," Biomicrofluidics **7**, 044121 (2013). 65

[142] R. Voelkel, "Wafer-scale micro-optics fabrication," Advanced Optical Technologies **1**, 135–150 (2012). 70, 79

[143] C. Burch, "Reflecting microscopes," in "Proceedings of the Physical Society," , vol. 41 (1947), vol. 41, pp. 41–48. 73, 144

[144] P. Nussbaum, R. Voelkel, H. P. Herzig, M. Eisner, and S. Haselbeck, "Design, fabrication and testing of microlens arrays for sensors and microsystems," Pure and Applied Optics **6**, 617–636 (1997). 79

[145] D. W. de Lima Monteiro, O. Akhzar-Mehr, P. M. Sarro, and G. Vdovin, "Single-mask microfabrication of aspherical optics using KOH anisotropic etching of Si." Optics express **11**, 2244–52 (2003). 79, 104

[146] R. Leach, Optical Measurement of Surface Topography (Springer, 2011). 81

[147] W. Osten, Optical Inspection of Microsystems, Optical Science and Engineering (SPIE, 2006). 82

[148] S. Petitgrand, B. R. Courbet, and A. Bosseboeuf, "Characterization of static and dynamic optical actuation of Al microbeams by microscopic interferometry techniques," Journal of Micromechanics and Microengineering **13**, S113–S118 (2003). 82

[149] A. Bosseboeuf and S. Petitgrand, "Characterization of the static and dynamic behaviour of M(O)EMS by optical techniques: status and trends," Journal of Micromechanics and Microengineering **13**, S23–S33 (2003). 82

[150] M. Józwik, C. Gorecki, A. Sabac, P. Delobelle, and M. Kujawińska, "Evaluation of micromechanical properties of buckled SiOxNy-loaded membranes by combining the Twyman–Green interferometry with nanoindentation and point-wise deflection technique," Optics and Lasers in Engineering **41**, 703–716 (2004). 82

[151] P. Sandoz and G. Tribillon, "Profilometry by zero-order interference fringe identification," Journal of Modern Optics **40**, 1691–1700 (1993). 82

[152] J. Albero, S. Bargiel, N. Passilly, P. Dannberg, M. Stumpf, U. D. Zeitner, C. Rousselot, K. Gastinger, and C. Gorecki, "Micromachined array-type Mirau interferometer for parallel inspection of MEMS," Journal of Micromechanics and Microengineering **21**, 065005 (2011). 82

[153] P. Jacquot, "Speckle Interferometry: A Review of the Principal Methods in Use for Experimental Mechanics Applications," Strain **44**, 57–69 (2008). 82

[154] P. Aswendt, R. Hoefling, and K. Hiller;, "Testing microcomponents by speckle interferometry," in "SPIE 3825, Microsystems Metrology and Inspection," (1999). 82

[155] M. Jacquot, P. Sandoz, and G. Tribillon, "High resolution digital holography," Optics communications **190**, 87–94 (2001). 82

[156] S. Seebacher, W. Osten, T. Baumbach, and W. Jüptner, "The determination of material parameters of microcomponents using digital holography," Optics and Lasers in Engineering **36**, 103–126 (2001). 82

[157] G. Coppola, P. Ferraro, M. Iodice, S. D. Nicola, A. Finizio, and S. Grilli, "A digital holographic microscope for complete characterization of microelectromechanical systems," Measurement Science and Technology **15**, 529–539 (2004). 82

[158] S. Reichelt and H. Zappe, "Combined Twyman-Green and Mach-Zehnder interferometer for microlens testing." Applied optics **44**, 5786–92 (2005). 83

[159] P. Nussbaum and H. Herzig, "Low numerical aperture refractive microlenses in fused silica," Optical Engineering pp. 1412–1414 (2001). 83

[160] T. Kozacki, K. Liżewski, and J. Kostencka, "Holographic method for topography measurement of highly tilted and high numerical aperture micro structures," Optics & Laser Technology **49**, 38–46 (2013). 84

[161] D. Malacara, Optical Shop Testing, Wiley Series in Pure and Applied Optics (Wiley, 2007). 84, 91

[162] M.-S. Kim, T. Scharf, and H. P. Herzig, "Small-size microlens characterization by multiwavelength high-resolution interference microscopy." Optics express **18**, 14319–29 (2010). 84

[163] J. L. Beverage, R. V. Shack, and M. R. Descour, "Measurement of the three-dimensional microscope point spread function using a Shack-Hartmann wavefront sensor." Journal of microscopy **205**, 61–75 (2002). 84

[164] J. Braat, S. V. Haver, A. Janssen, and P. Dirksen, "Assessment of optical systems by means of point-spread functions," Progress in Optics **51**, 349–468 (2008). 84, 85, 100

[165] E. Botcherby, R. Juškaitis, M. Booth, and T. Wilson, "An optical technique for remote focusing in microscopy," Optics Communications **281**, 880–887 (2008). 84

[166] R. W. Cole, T. Jinadasa, and C. M. Brown, "Measuring and interpreting point spread functions to determine confocal microscope resolution and ensure quality control." Nature protocols **6**, 1929–41 (2011). 84

[167] N. Bobroff and a. E. Rosenbluth, "Evaluation of highly corrected optics by measurement of the Strehl ratio." Applied optics **31**, 1523–36 (1992). 84, 96, 97

[168] T. E. Oliphant T., "Python for scientific computing," Computing in Science & Engineering **9**, 10–20 (2007). 88

[169] T. Schmitz, C. Evans, A. Davies, and W. Estler, "Displacement uncertainty in interferometric radius measurements," CIRP Annals - Manufacturing Technology pp. 2–5 (2002). 91

[170] W. Zhao, R. Sun, L. Qiu, and D. Sha, "Laser differential confocal radius measurement." Optics express **18**, 2345–60 (2010). 91, 92, 93, 94

[171] L. C. Roberts, Jr., M. D. Perrin, F. Marchis, A. Sivaramakrishnan, R. B. Makidon, J. C. Christou, B. a. Macintosh, L. a. Poyneer, M. a. van Dam, and M. Troy, "Is That Really Your Strehl Ratio?" in "Advancements in Adaptive Optics," , vol. 5490, D. Bonaccini Calia, B. L. Ellerbroek, and R. Ragazzoni, eds. (SPIE, Bellingham, 2004), vol. 5490, pp. 504–515. 96

[172] V. N. Mahajan, "Strehl ratio for primary aberrations: some analytical results for circular and annular pupils," Journal of the Optical Society of America **72**, 1258 (1982). 97

[173] V. Gerbig and A. Lohmann, "Is lens design legal?" Applied optics **28**, 5198–5199 (1989). 97

[174] Radiant Zemax, "Optical Design Program User's Guide," Tech. rep., ZEMAX Development Corporation (2008). 99

[175] G. Kovacs, N. Maluf, and K. Petersen, "Bulk micromachining of silicon," Proceedings of the IEEE **86**, 1536–1551 (1998). 102

[176] D. L. Kendall, G. R. de Guel, S. Guel-Sandoval, E. J. Garcia, and T. a. Allen, "Chemically etched micromirrors in silicon," Applied Physics Letters **52**, 836 (1988). 102

[177] D. L. Kendall, "A new theory for the anisotropic etching of silicon and some underdeveloped chemical micromachining concepts," Journal of Vacuum Science & Technology A: Vacuum, Surfaces, and Films **8**, 3598 (1990). 102, 103, 104

[178] K. Sato, M. Shikida, T. Yamashiro, K. Asaumi, Y. Iriye, and M. Yamamoto, "Anisotropic etching rates of single-crystal silicon for TMAH water solution as a function of crystallographic orientation," Sensors and Actuators A: Physical **73**, 131–137 (1999). 104

[179] X. Zhang, Electrochemistry of Silicon and Its Oxide (Springer, 2001). 104

[180] M. Koefferlein, "High performance layout viewer and editor," "http://www.klayout.de/" (2013). [Online; accessed 10-September-2013]. 106

[181] P. Rangsten, C. Hedlund, I. V. Katardjiev, and Y. Bäcklund, "Etch rates of crystallographic planes in Z -cut quartz - experiments and simulation," Journal of Micromechanics and Microengineering **8**, 1–6 (1998). 110

[182] I. Steingoetter and H. Fouckhardt, "Deep fused silica wet etching using an Au-free and stress-reduced sputter-deposited Cr hard mask," Journal of Micromechanics and Microengineering **15**, 2130–2135 (2005). 110, 123

[183] C. Iliescu, B. Chen, and J. Miao, "On the wet etching of Pyrex glass," Sensors and Actuators A: Physical **143**, 154–161 (2008). 111

[184] N. Pekas, Q. Zhang, M. Nannini, and D. Juncker, "Wet-etching of structures with straight facets and adjustable taper into glass substrates." Lab on a chip **10**, 494–8 (2010). 111, 123

[185] H. Robbins and B. Schwartz, "Chemical etching of silicon I," Journal of the electrochemical society **106**, 505–508 (1959). 112, 113

[186] H. Robbins and B. Schwartz, "Chemical etching of silicon II," Journal of the electrochemical society **107**, 108–111 (1960). 112

[187] B. Schwartz and H. Robbins, "Chemical etching of Silicon III," Journal of The Electrochemical Society **108**, 365–372 (1961). 112, 117, 118

[188] B. Schwartz and H. Robbins, "Chemical etching of silicon IV," Journal of The Electrochemical Society **123**, 1903–1909 (1976). 112, 113

[189] M. Steinert, J. Acker, S. Oswald, and K. Wetzig, "Study on the Mechanism of Silicon Etching in HNO 3 -Rich HF / HNO 3 Mixtures," J. Phys. Chem. C **111**, 2133–2140 (2007). 112

[190] M. Steinert, J. Acker, M. Krause, S. Oswald, and K. Wetzig, "Reactive species generated during wet chemical etching of silicon in HF/HNO3 mixtures." The journal of physical chemistry. B **110**, 11377–82 (2006). 112

[191] J. Acker, A. Rietig, M. Steinert, and V. Hoffmann, "Mass and Electron Balance for the Oxidation of Silicon during the Wet Chemical Etching in HF/HNO3 Mixtures," Journal of Physical Chemistry C **116**, 20380–20388 (2012). 112

[192] M. Steinert, J. Acker, and K. Wetzig, "New Aspects on the Reduction of Nitric Acid during Wet Chemical Etching of Silicon in Concentrated HF/HNO3 Mixtures," Journal of Physical Chemistry C **112**, 14139–14144 (2008). 112

[193] M. S. Kulkarni, "A Review and Unifying Analysis of Defect Decoration and Surface Polishing by Chemical Etching in Silicon Processing †," Industrial & Engineering Chemistry Research **42**, 2558–2588 (2003). 113

[194] R. Noek, C. Knoernschild, J. Migacz, T. Kim, P. Maunz, T. Merrill, H. Hayden, C. S. Pai, and J. Kim, "Multiscale optics for enhanced light collection from a point source." Optics letters **35**, 2460–2 (2010). 113

[195] H. K. Kuiken, "Etching through a slit," Proc. R. Soc. Lond. A **396**, 95–117 (1984). 114

[196] H. K. Kuiken, "A mathematical model for wet-chemical diffusion-controlled mask etching through a circular hole," Journal of engineering mathematics **45**, 75–90 (2003). 114

[197] V. B. Svetovoy, J. W. Berenschot, and M. C. Elwenspoek, "Precise Test of the Diffusion-Controlled Wet Isotropic Etching of Silicon via Circular Mask Openings," Journal of The Electrochemical Society **153**, C641 (2006). 115, 117, 119, 128

[198] M. Baranski, J. Albero, R. Kasztelanic, and C. Gorecki, "A Numerical Model of Wet Isotropic Etching of Silicon Molds for Microlenses Fabrication," Journal of The Electrochemical Society **158**, D681 (2011). 116, 117

[199] Z. Yifan and C. Sihai, "Deep Wet Etching in Hydrofluoric Acid, Nitric Acid, and Acetic Acid of Cavities in a Silicon Wafer," Japanese Journal of ... **52**, 1–7 (2013). 118

[200] J. Albero, "Mise au point d'une filière de fabrication de microlentilles par moulage silicium : Application à l' instrumentation optique miniature," Ph.D. thesis, Universite de Franche-Comte (2010). 119

[201] Z. Moktadir, E. Koukharenka, M. Kraft, D. M. Bagnall, H. Powell, M. Jones, and E. a. Hinds, "Etching techniques for realizing optical micro-cavity atom traps on silicon," Journal of Micromechanics and Microengineering **14**, S82–S85 (2004). 119

[202] J. K. Lee, J. C. Choi, W. I. Jang, H.-R. Kim, and S. H. Kong, "Electrowetting Lens Employing Hemispherical Cavity Formed by Hydrofluoric Acid, Nitric Acid, and Acetic Acid Etching of Silicon," Japanese Journal of Applied Physics **51**, 06FL05 (2012). 119

[203] K. Williams, K. Gupta, and M. Wasilik, "Etch rates for micromachining processing-Part II," Journal of Microelectromechanical Systems **12**, 761–778 (2003). 123

[204] Y. Mourzina, A. Steffen, and A. Offenhäusser, "The evaporated metal masks for chemical glass etching for BioMEMS," Microsystem technologies **11**, 135–140 (2005). 123

[205] Biosan, "Rockers, shakers, rotators," "http://biosan.lv/" (2013). [Online; accessed 20-October-2013]. 125

[206] H. Herzig, Micro-Optics: Elements, Systems And Applications (Taylor & Francis, 2012). 129, 141

[207] H. Jansen, H. Gardeniers, M. D. Boer, M. Elwenspoek, and J. Fluitman, "A survey on the reactive ion etching of silicon in microtechnology," Journal of Micromechanics and Microengineering **6**, 14–28 (1996). 133

[208] V. Singh, "Simulation of profile evolution in silicon reactive ion etching with re-emission and surface diffusion," Journal of Vacuum Science & Technology B **10** (1992). 133

[209] O. Ertl and S. Selberherr, "Three-dimensional level set based Bosch process simulations using ray tracing for flux calculation," Microelectronic Engineering **87**, 20–29 (2010). 133

[210] H. V. Jansen, M. J. de Boer, S. Unnikrishnan, M. C. Louwerse, and M. C. Elwenspoek, "Black silicon method: X. A review on high speed and selective plasma etching of silicon with profile control: an in-depth comparison between Bosch and cryostat DRIE processes as a roadmap to next generation equipment," Journal of Micromechanics and Microengineering **19**, 033001 (2009). 134

[211] T. Takahata, E. Iwase, K. Matsumoto, and I. Shimoyama, "Three-dimensional silicon fabrication using microloading effects with a rectangular aperture mask," Journal of Micromechanics and Microengineering **20**, 075022 (2010). 134

[212] Y. Tanaka, Y. Yokomizu, M. Ishikawa, and T. Matsumura, "Particle composition of high-pressure SF_6 plasma with electron temperature greater than gas temperature," IEEE Transactions on Plasma Science **25**, 991–995 (1997). 136

[213] Z.-L. Dai, X. Xu, and Y.-N. Wang, "A self-consistent hybrid model of a dual frequency sheath: Ion energy and angular distributions," Physics of Plasmas **14**, 013507 (2007). 136

[214] H.-C. Liu, Y.-H. Lin, and W. Hsu, "Sidewall roughness control in advanced silicon etch process," Microsystem Technologies **10**, 29–34 (2003). 138

[215] E. Gogolides, "Si etching in high-density SF6 plasmas for microfabrication: surface roughness formation," Microelectronic Engineering **73-74**, 312–318 (2004). 138

[216] K. P. Larsen, D. H. Petersen, and O. Hansen, "Study of the Roughness in a Photoresist Masked, Isotropic, SF[sub 6]-Based ICP Silicon Etch," Journal of The Electrochemical Society **153**, G1051 (2006). 138

[217] A. Laliotis, M. Trupke, J. Cotter, and G. Lewis, "ICP polishing of silicon for high quality optical resonators on a chip," J. Micromech. Microeng **22**, 1–6 (2012). 138

[218] C.-H. Lee, Y. Chiu, and H.-P. D. Shieh, "High-extinction-ratio micro polarizing beam splitter for short wavelength optical storage applications." Optics express **13**, 10292–301 (2005). 160

[219] F. Wang, F. Liu, and A. Adibi, "45 Degree Polymer Micromirror Integration for Board-Level Three-Dimensional Optical Interconnects." Optics express **17**, 10514–21 (2009). 160

[220] Y.-J. Chuang, S.-H. Huang, Y.-C. Chen, and K.-Y. Hung, "Application of the inclined exposure and molding process to fabricate a micro beam-splitter with nanometer roughness," Microsystem Technologies **19**, 461–470 (2012). 160

[221] K. H. Brenner, M. Kufner, S. Kufner, J. Moisel, a. Müller, S. Sinzinger, M. Testorf, J. Göttert, and J. Mohr, "Application of three-dimensional micro-optical components formed by lithography, electroforming, and plastic molding." Applied optics **32**, 6464–9 (1993). 160

[222] S. M. Macneille, "Beam Splitter," US Patent US2403731 A (1946). 164

[223] N. Baron, J. Passave, B. Guichardaz, and G. Cabodevila, "Investigations of development process of high hollow beveled microneedles using a combination of ICP RIE and dicing saw," Microsystem Technologies **14**, 1475–1480 (2008). 167

[224] N. Courjal, B. Guichardaz, G. Ulliac, J.-Y. Rauch, B. Sadani, H.-H. Lu, and M.-P. Bernal, "High aspect ratio lithium niobate ridge waveguides fabricated by optical grade dicing," Journal of Physics D: Applied Physics **44**, 305101 (2011). 167

[225] A. Duparré, J. Ferre-Borrull, S. Gliech, G. Notni, J. Steinert, and J. M. Bennett, "Surface characterization techniques for determining the root-mean-square roughness and power spectral densities of optical components." Applied optics **41**, 154–71 (2002). 169

[226] E. Herth, H. Desré, E. Algré, C. Legrand, and T. Lasri, "Investigation of optical and chemical bond properties of hydrogenated amorphous silicon nitride for optoelectronics applications," Microelectronics Reliability **52**, 141–146 (2012). 171

[227] P. Ramm, J. Lu, and M. Taklo, Handbook of Wafer Bonding (Wiley, 2012). 179

[228] Nikko company, "Nikko: functional ceramics," "http://www.nikko-company.co.jp/ceramics/index.php" (2013). [Online; accessed 30-September-2013]. 179

[229] E. Gusev, E. Garfunkel, and A. Dideikin, Advanced Materials and Technologies for Micro/Nano-Devices, Sensors and Actuators, NATO Science for Peace and Security Series B: Physics and Biophysics (Springer, 2010). 180, 181

[230] M. Mohri and N. Kidani, "Anodic bondable porcelain and composition for the porcelain," US Patent 2011/0108931 A1 (2011). 186

[231] M. Wiemer, D. Wuensch, J. Frömel, T. Gessner, S. Bargiel, M. Baranski, and N. Passilly, "Multi-wafer bonding , stacking and interconnecting of integrated 3-D MEMS micro scanners," in "14th International Symposium in Microwave and Optical Technology," (Kuala Lumpur, 2013), pp. 28–31. 186

[232] S. Bargiel, C. Gorecki, M. Baranski, N. Passilly, M. Wiemer, C. Jia, and J. Frömel, "3D micro-optical lens scanner made by multi-wafer bonding technology," in "SPIE MOEMS-MEMS," , W. Piyawattanametha and Y.-H. Park, eds. (International Society for Optics and Photonics, 2013), pp. 861605–861605–10. 186, 187

[233] M. D. Abràmoff, I. Hospitals, P. J. Magalhães, and M. Abràmoff, "Image Processing with ImageJ," Biophotonics international **11**, 36–42 (2004). 191

[234] Wikipedia, "Conic section — wikipedia, the free encyclopedia," "http://en.wikipedia.org/w/index.php?title=Conic_section&oldid=574663036" (2013). [Online; accessed 1-November-2013]. 195

[235] E. Jones, T. Oliphant, P. Peterson et al., "SciPy: Open source scientific tools for Python," "http://www.scipy.org/" (2001). 197

Author's publications

1. M. Baranski, J. Albero, R. Kasztelanic and C. Gorecki, *A Numerical Model of wet Isotropic Etching of Silicon Molds for Microlenses Fabrication*, Journal of Electrochemical Society, vol. 158, D681-D688 (2011).

2. R. Chutani. N. Passilly, J. Albero, M. Baranski and C. Gorecki, *Deep wet-etched silicon cavities for micro-optical sensors: Influence of masking on 111 sidewalls surface quality*, to be published in IEEE Journal of Microelectromechanical Systems (2013). Digital Object Identifier: 10.1109/JMEMS.2013.2285575

3. M. Baranski, S. Bargiel, N. Passilly, B. Guichardaz, E. Herth, C. Gorecki, C. Jia, J. Froemel and M. Wiemer, *Wafer-level fabrication of micro Cube-typed beam-splitters by saw-dicing of glass substrates*, to be published in IEEE Photonics Technology Letters (2013). Digital Object Identifier: 10.1109/LPT.2013.2289981

Author's proceedings

1. M. Baranski, R. Kasztelanic, J. Albero, L. Nieradko, C. Gorecki, *Level set method for microfabrication simulations*, Proc. SPIE 7716, 77161W (2010).

2. R. Kasztelanic, M. Baranski, *Semi-derivative real filter for the measurement of the wavefront distortion*, Proc. SPIE 7718, 77181L (2010).

3. M. Baranski, N. Passilly, J. Albero and C. Gorecki, *Fabrication of 100% fill factor arrays of microlenses from Silicon molds*, Proc. SPIE 8428, 84281G 1-7 (2012).

4. S. Bargiel, C. Jia, M. Baranski, J. Froemel, N. Passilly, C. Gorecki, M. Wiemer, *Vertical integration technologies for optical transmissive 3-D microscanner based on glass microlenses*, Proc. Eurosensors XXVI, Procedia Eng., vol. 47, pp. 1133-1136 (2012). ***Award for an outstanding poster***

5. C. Jia, J. Froemel, M. Wiemer, T. Gessner, S. Bargiel, N. Passilly, M. Baranski, C. Gorecki, *A hierarchic bonding procedure for the assembly of micro confocal microscope*, Proc. 3rd IEEE International workshop on Low Temperature Bonding for 3D integration (LTB-3D) pp. 187-189, (2012).

6. M. Wiemer, J. Froemel, C. Jia, S. Bargiel, M. Baranski, N. Passilly, C. Gorecki, *Bonding and contacting of vertically integrated 3-D microscanners*, Proc. 9th International Wafer-Level Packaging Conference IWLPC, San Jose, USA, 5-8 November 2012.

7. S. Bargiel, C. Gorecki, M. Baranski, N. Passilly, M. Wiemer, C. Jia, J. Froemel, *3D micro-optical lens scanner made by multi-wafer technology*, Proc. SPIE 8616, 861605 (2013).

8. S. Bargiel, M. Baranski, N. Passilly, B. Guichardaz, E. Herth, C. Gorecki, C. Jia, J. Froemel, M. Wiemer, *wafer-level fabricated micro beam splitter based on 45-degree saw dicing of glass substrate*, Solid-State Sensors, Actuators and Microsystems (Transducers & Eurosensors XXVII), pp. 534-537, (2013).

9. M. Jozwik, T. Kozacki, K. Lizewski, M. Baranski, C. Gorecki, *Topography Measurements of High Gradient and Reflective Micro-structures by Digital Holography*, In Fringe 2013, Springer Berlin Heidelberg, pp. 623-628 (2013).

10. M. Wiemer, D. Wuensch, J. Froemel, T. Gessner, S. Bargiel, M. Baranski, N. Passilly, C. Gorecki, *Multi-wafer Bonding, Stacking and Interconnecting of Integrated 3-D MEMS Micro Scanners*, ISMOT 2013 - 14th International Symposium in Microwave and Optical Technology, Kuala Lumpur, Malaysia, October, 28-31 2013.

Abstract:

The thesis manuscript concerns optical design and development of a vertically integrated MEMS-based confocal microscope. Different optical architectures have been proposed that aim to combine optimal optical design and the numerous technological constraints linked to the batch fabrication of the different building blocks. The latter, made by hybrid technologies, and packaged by vertical assembly using multi- wafer bonding, allow the construction of a complete microsystem for instrumentation. Special emphasis is placed on the minimization of optical aberrations generated by the different microoptical components to ensure good resolution of measurement. For these purposes, different building blocks have been developed, namely a batch-fabricated cube-typed beamsplitter, different silicon moulded refractive microlenses and a miniature reflective objective. Dedicated characterization system for quality assessment of the fabricated micro-components was also developed. Moreover, different processes of silicon-based micromachining for generation of micromirrors and microlenses (wet anisotropic and isotropic etch, dry isotropic etch of silicon) have been compared. Finally, procedures of vertical assembly including all electrical interconnection technologies have been developed. The thesis work was performed in the frame of the DWST-DIS (The Development of Multi Wafer Stacking 3D Technology for Displays and Imaging MicroSystems) project funded by the Programme Inter Carnot Fraunhofer (PICF) – an ANR project between FEMTO-ST and ENAS - Fraunhofer Institute.

Keywords: mems,moems, micro-optics, confocal microscopy, microlenses, microfabrication, vertical integration

Résumé :

Les travaux de thèse concernent le design optique et le développement d'un microscope confocal miniature MEMS intégré verticalement. Différentes architectures optiques ont été proposées afin de combiner un design optique optimal aux nombreuses contraintes technologiques liées à la fabrication collective des différents blocs élémentaires du microscope sur puce. Ceux-ci, réalisés avec des technologies hybrides, sont encapsulés par assemblage vertical de wafers utilisant les technologies de soudure «multi-wafer», et permettent la construction d'un microsystème complet d'instrumentation. Un accent particulier a été mis sur la minimisation des aberrations optiques générées par les différents composants microoptiques pour permettre une résolution de mesure élevée. Pour satisfaire ces besoins, différentes briques élémentaires ont été développées : un cube semi-transparent micro-fabriqué, différentes microlentilles réfractives basées sur le micro-moulage silicium et un micro-objectif réflecteur. Un montage expérimental de caractérisation dédié à l'évaluation de la qualité de ces microcomposants a également été proposé. De plus, les différents procédés de micro-usinage silicium (gravure humide anisotrope et isotrope, gravure sèche isotrope du silicium) pour la génération de micro-miroirs et de microlentilles ont été comparés. Enfin, les procédures d'assemblage vertical, incluant toutes les technologies d'interconnexion électrique ont été développées. Le travail de thèse a été réalisée dans le cadre du projet DWST-DIS (The Development of Multi Wafer Stacking 3D Technology for Displays and Imaging MicroSystems), programme financé par le programme Inter Carnot Fraunhofer (PICF) - un projet ANR entre FEMTO-ST et l'institut Fraunhofer ENAS.

Mots-clés : mems, moems, micro optique, microscopie confocal, micro-lentilles, micro-usinage, intégration verticale

SPIM

■ École doctorale SPIM 16 route de Gray F - 25030 Besançon cedex
■ tél. +33 (0)3 81 66 66 02 ■ ed-spim@univ-fcomte.fr ■ www.ed-spim.univ-fcomte.fr

UFC
UNIVERSITÉ DE FRANCHE-COMTÉ